ON THE DYNAMIC FREQUENCY SUPPORT OF ACTIVE DISTRIBUTION GRIDS AND THEIR AGGREGATION

Dem Fachbereich Elektrotechnik und Informationstechnik
der Technischen Universität Darmstadt

TECHNISCHE
UNIVERSITÄT
DARMSTADT

etit

zur Erlangung des akademischen Grades
eines Doktor-Ingenieurs (Dr.-Ing.)
vorgelegte und genehmigte Dissertation von

ANNA PFENDLER, M.SC.

Erstgutachterin: Prof. Dr.-Ing. Jutta Hanson
Zweitgutachter: Prof. Dr.-Ing. Bernd Engel

Darmstadt 2024

Anna Pfendler
On the Dynamic Frequency Support of Active Distribution Grids and their Aggregation
Darmstadt, Technische Universität Darmstadt
Jahr der Veröffentlichung der Dissertation auf TUprints: 2024
URN: urn:nbn:de:tuda-tuprints-278328
URI: https://tuprints.ulb.tu-darmstadt.de/id/eprint/27832
Tag der Einreichung: 5. März 2024
Tag der mündlichen Prüfung: 17. Juli 2024

Für meine Familie.

Lass dich nicht unterkriegen,
sei frech und wild und wunderbar!
Astrid Lindgren

DANKSAGUNG

Die vorliegende Dissertation ist während meiner Zeit als wissenschaftliche Mitarbeiterin am Fachgebiet Elektrische Energieversorgung unter Einsatz Erneuerbarer Energien (E5) der Technischen Universität Darmstadt entstanden. Ich bedanke mich von Herzen bei allen, die mich auf diesem Weg begleitet und unterstützt haben.

Zunächst bedanke ich mich bei meiner Doktormutter Prof. Dr.-Ing. Jutta Hanson für die Möglichkeit und Ermutigung meine Doktorarbeit am Fachgebiet E5 zu schreiben. Danke für das langjährige entgegengebrachte Vertrauen, die gewährten Freiheiten und die gegebene Unabhängigkeit meiner Forschungsarbeit. Mein Dank gilt auch Herrn Prof. Dr.-Ing. Bernd Engel für die Übernahme des Korreferats und das Interesse an den Inhalten meiner Arbeit. Außerdem bedanke ich mich bei den Mitgliedern meiner Prüfungskommission Prof. Dr.-Ing. Gerd Griepentrog, Prof. Dr.-Ing. Herbert De Gersem und Prof. Dr.-Ing. Tran Quoc Khanh für die anregende Diskussion.

Allen aktuellen und ehemaligen Kolleginnen und Kollegen sowie dem Sekretariat am Fachgebiet E5 danke ich für die vertrauensvolle Zusammenarbeit, den fachlichen Austausch, den regelmäßigen IT-Support als auch die angenehme und freundschaftliche Atmosphäre - in Mittagspausen, bei Spieleabenden oder Kickerrunden. Allen, die mit mir auf der ein oder anderen Dienstreise waren danke ich für die unvergessliche Zeit. Für das Korrekturlesen meiner Dissertation bedanke ich mich bei meinen Kollegen Soham Choudhury, Rafael Steppan, Aaron Hebing und meinem Schwiegervater Wolfgang Huber.

Ich bedanke mich außerdem bei allen Studierenden, die sich im Rahmen von Seminaren und Abschlussarbeiten oder als studentische Hilfskräfte nicht von netzdynamischen Themen abschrecken lassen haben und zu meiner Forschung beigetragen haben. Insbesondere sei hier Lukas Jung genannt, der mich über drei Jahre lang in meiner Forschung unterstützt hat.

Abschließend gilt mein Dank meiner Familie und meinem Freundeskreis, die mir stets mit Verständnis und einem offenen Ohr für meine Sorgen und Gedanken beigestanden haben. Ein besonderer Dank gilt meinen Eltern Bärbel und Jürgen Pfendler, die mir bedingungslos den Rücken gestärkt haben. Mein größter Dank gilt meinem Mann Stephan, der während all der Höhen und Tiefen fest an meiner Seite stand und unerschütterlich an mich glaubt. Mit ihm freue ich mich darauf, das nächste Kapitel aufzuschlagen.

ERKLÄRUNG LAUT PROMOTIONSORDNUNG

§8 Abs. 1 lit. c PromO

Ich versichere hiermit, dass die elektronische Version meiner Dissertation mit der schriftlichen Version übereinstimmt.

§8 Abs. 1 lit. d PromO

Ich versichere hiermit, dass zu einem vorherigen Zeitpunkt noch keine Promotion versucht wurde. In diesem Fall sind nähere Angaben über den Zeitpunkt, Hochschule, Dissertationthema und Ergebnis dieses Versuchs mitzuteilen.

§9 Abs. 1 PromO

Ich versichere hiermit, dass die vorliegende Dissertation selbstständig und nur unter Verwendung der angegebenen Quellen verfasst wurde.

§9 Abs. 2 PromO

Die Arbeit hat bis jetzt noch nicht zu Prüfungszwecken gedient.

Darmstadt, März 2024

Anna Pfendler

ERKLÄRUNG ZUR NUTZUNG KI-BASIERTER HILFSMITTEL

Bei der Erstellung dieser Dissertation wurden die folgenden Hilfsmittel basierend auf Künstlicher Intelligenz (KI) verwendet:

DeepL

ChatGPT

Die KI-basierten Textwerkzeuge wurden ausschließlich zur Übersetzung, Verbesserung von Satzbau, Grammatik und Rechtschreibung verwendet. Stellen, an denen Inhalte dieser Arbeit mithilfe KI-basierter Werkzeuge bearbeitet wurden, sind durch die Autorin geprüft. Hiermit versichere ich, dass keine generative Nutzung von KI zum Erstellen von schriftlichen Inhalten für die Erstellung der vorliegenden Dissertation verwendet wurde.

Darmstadt, März 2024

Anna Pfendler

ABSTRACT

The growing integration of renewable energy power plants strongly influences the dynamic behaviour and thus the stability of interconnected power systems. Disturbances leading to rapid and severe frequency fluctuations gain significance, as for instance shown by the system separation event in continental Europe in 2021. Conventional power plants inherently counteract such frequency deviations, leveraging the inertia of rotating machines to slow down frequency changes by absorbing or releasing kinetic energy. Conversely, renewable energy power plants and emerging technologies, such as battery storage, predominantly connect to the grid through inverters — power electronic devices that inherently lack mechanical inertia.

With the increasing share of inverter-based generation, it becomes imperative to assess their potential role in maintaining the stability of power systems, particularly in low-inertia power systems. The distributed generation in many small units shifts the power generation from the transmission to the distribution grids. This thesis investigates the contribution of active distribution grids to the dynamic short-term frequency stability through comprehensive numeric simulations in the time domain. Results show that, especially under conditions of high inverter-based generation and low system inertia, active distribution grids can play a significant role in contributing to the short-term frequency stability. Different implementations of the fast frequency response control for inverter-based generation are applied and compared in a medium-voltage and high-voltage benchmark grid.

The modelling of distributed inverter-based generation plants in power system studies presents unique challenges due to their vast numbers. For large power systems, this thesis proposes reduced dynamic equivalent models based on a measurement-based approach. The dynamic equivalent or aggregation models can replicate the dynamic frequency response of active distribution grids for various settings and help including the changing structure of generation plants into power system frequency stability studies. The results also indicate which parameters are relevant to consider for dynamic equivalents of active distribution grids.

KURZFASSUNG

Die zunehmende Integration von Erzeugungsanlagen basierend auf erneuerbaren Energien beeinflusst stark das dynamische Verhalten und damit die Stabilität des elektrischen Energiesystems. Störungen, die zu schnellen und starken Frequenzänderungen führen, gewinnen an Bedeutung, wie beispielsweise das Ereignis der Systemauftrennung in Kontinentaleuropa im Jahr 2021 gezeigt hat. Konventionelle Kraftwerke wirken solchen Frequenzabweichungen inhärent entgegen, da die Trägheit der rotierenden Maschinen Frequenzänderungen durch das Aufnehmen oder Freisetzen von kinetischer Energie verlangsamt. Im Gegensatz dazu sind Erneuerbare-Energie-Anlagen und aufkommende Technologien, wie Batteriespeicher, überwiegend über Wechselrichter mit dem Netz verbunden – leistungselektronische Komponenten, die grundsätzlich keine mechanische Trägheit aufweisen.

Mit dem zunehmenden Anteil wechselrichterbasierter Erzeugung wird es unerlässlich, ihre mögliche Rolle bei der Aufrechterhaltung der Stabilität von elektrischen Energiesystemen zu bewerten, insbesondere in Systemen mit geringer Trägheit. Die dezentrale Erzeugung in vielen kleinen Einheiten verlagert die Stromerzeugung von den Übertragungs- zu den Verteilnetzen. Diese Arbeit untersucht den Beitrag aktiver Verteilnetze zur dynamischen kurzfristigen Frequenzstabilität durch umfassende numerische Simulationen im Zeitbereich. Die Ergebnisse zeigen, dass aktive Verteilnetze, insbesondere bei hohem Anteil wechselrichterbasierter Erzeugung und geringer Systemträgheit, eine bedeutende Rolle bei der kurzfristigen Frequenzstabilität spielen können. Verschiedene Implementierungen einer schnellen Frequenzregelung (engl. fast-frequency response) für wechselrichterbasierte Erzeugungsanlagen werden angewendet und in einem Mittelspannungs- und Hochspannungs-Benchmark-Netz verglichen.

Die Modellierung von verteilten kleineren wechselrichterbasierten Erzeugungsanlagen in Studien des elektrischen Energiesystems stellt aufgrund ihrer großen Anzahl einzigartige Herausforderungen dar. Für große Energiesysteme schlägt diese Arbeit reduzierte dynamische Aggregationsmodelle basierend auf Messungen vor. Die dynamischen Äquivalente oder Aggregationsmodelle können die dynamische Frequenzantwort aktiver Verteilungsnetze für verschiedene Einstellungen nachbilden und helfen dabei, die sich ändernde Struktur von Erzeugungsanlagen in Studien zur Frequenzstabilität einzubeziehen. Die Ergebnisse zeigen auch auf, welche Parameter für dynamische Äquivalente aktiver Verteilungsnetze zu berücksichtigen sind.

CONTENTS

I FUNDAMENTALS

1 INTRODUCTION 1
- 1.1 Motivation and Background . . . 2
- 1.2 State of the Art . . . 3
- 1.3 Research Questions and Thesis Overview . . . 6

2 FREQUENCY DYNAMICS 9
- 2.1 Power System Dynamics and Modelling . . . 9
- 2.2 Electrical and Angular Frequency . . . 10
- 2.3 Frequency Stability and Control . . . 12
  - 2.3.1 Power System Stability Definitions . . . 12
  - 2.3.2 Power System Frequency Control . . . 14
  - 2.3.3 Fast Frequency Response . . . 16
- 2.4 Frequency Estimation . . . 17
  - 2.4.1 Phase-Locked Loop . . . 18
  - 2.4.2 Further Frequency Estimation Methods . . . 19
- 2.5 Summary . . . 20

3 INVERTER-BASED GENERATION 21
- 3.1 Basic Characteristics of Power Inverters . . . 21
- 3.2 Inverter Model Classes . . . 23
- 3.3 Control Concepts for Inverter-Based Generation . . . 26
  - 3.3.1 Control Levels . . . 26
  - 3.3.2 Grid-following, grid-supporting and grid-forming control 27
- 3.4 Grid Codes and Ancillary Services . . . 28
- 3.5 Summary . . . 30

4 DYNAMIC SYSTEM EQUIVALENTS 33
- 4.1 Overview of Dynamic Aggregation Approaches . . . 34
- 4.2 Aggregation of Overlying External Grid . . . 36
- 4.3 Greybox Aggregation . . . 36
  - 4.3.1 Particle Swarm Optimisation . . . 38
  - 4.3.2 Differential Evolution Algorithm . . . 39
- 4.4 Summary . . . 42

II MODELLING OF ACTIVE DISTRIBUTION GRIDS

5 DYNAMIC MODELLING OF GRID COMPONENTS 45
- 5.1 Generic Medium-Voltage Testbench . . . 45
- 5.2 Synchronous Generator Model . . . 46

5.3 Frequency-Dependent Load Model 52
5.3.1 Static Load Models 53
5.3.2 Dynamic Load Models 55
5.3.3 Composite Load Models 56
5.4 Passive Components 59
5.5 Summary 60
6 INVERTER-BASED GENERATION MODEL 61
6.1 Electrical Model 61
6.2 Grid-Supporting Control Model 63
6.2.1 Signal Processing 63
6.2.2 Outer Control 65
6.2.3 Inner Control 66
6.2.4 Current Limiter 67
6.2.5 Voltage Limiter 70
6.3 Direct Voltage Control Model 70
6.4 RMS and EMT Modelling 73
6.5 Summary 74
7 DISTRIBUTION GRID MODELS 77
7.1 Medium-Voltage Benchmark Grid 77
7.2 High-Voltage Benchmark Grid 81
7.3 Dynamic Equivalent Models 83
7.4 Model Parameter Fitting 84
7.5 Summary 85

III DYNAMICS OF ACTIVE DISTRIBUTION GRIDS
8 DYNAMIC FREQUENCY RESPONSE OF AN INDIVIDUAL IMVERTER-BASED GENERATOR 89
8.1 Medium-Voltage Testbench in Default Parametrisation 90
8.2 Frequency Metrics Evaluation 92
8.3 Sensitivity Analysis 93
8.3.1 External Grid 94
8.3.2 Loadstep Size 97
8.3.3 Load Type 99
8.3.4 Distance of the External Grid 100
8.3.5 Frequency Support of the Inverter-Based Generation . . . 100
8.3.6 Energy requirements for the fast-frequency response . . . 104
8.4 Summary 105
9 FREQUENCY DYNAMICS OF ACTIVE DISTRIBUTION GRIDS 107
9.1 Medium-Voltage Benchmark Grid 107
9.1.1 Frequency Control 111
9.1.2 Grid-Supporting vs. Direct Voltage Control 117

9.1.3 Impact of the External Grid 120
9.1.4 Impact of the Load Modelling 121
9.2 High-Voltage Grid 123
9.2.1 Power System Inertia 124
9.2.2 Spatial Distribution 125
9.3 Summary 125
10 DERIVATION OF DYNAMIC AGGREGATED MODELS FOR FREQUENCY INVESTIGATIONS 129
10.1 Parameter Limits 129
10.2 Scenario Definition 131
10.3 Equivalent Medium-Voltage Grid 132
10.3.1 Comparison of Aggregation Approaches 132
10.3.2 Optimisation settings 137
10.3.3 Aggregation results for varying inertia constant 139
10.3.4 Inhomogeneous inverter control 140
10.4 Equivalent High-Voltage Grid 144
10.4.1 High-voltage benchmark grid with dynamic equivalent medium-voltage grids 144
10.4.2 Reduced-order active distribution grid 145
10.5 Summary 148

IV CONCLUSION AND OUTLOOK
11 SUMMARY AND CONCLUSION 151
12 OUTLOOK AND FURTHER RESEARCH 153

V APPENDIX
A APPENDIX xxv
A.1 Synchronous Generator Model Parameters xxv
A.1.1 Medium-Voltage Synchronous Generator Model xxvi
A.1.2 High-Voltage Synchronous Generator Model xxvii
A.1.3 Ultra-High-Voltage Synchronous Generator Model . . . xxviii
A.2 Load Model Parameters xxix
A.3 Line Parameters xxxi
A.4 Inverter-Based Generation Model Parameters xxxii
A.5 Benchmark Model Parameters xxxiii
A.5.1 Medium-Voltage Benchmark Model Parameters xxxiii
A.5.2 High-Voltage Benchmark Model Parameters xxxv
A.6 Supplementary Results to Chapter 8 xxxvi
A.7 Supplementary Results to Chapter 9 xxxviii
A.8 Supplementary Results to Chapter 10 xl

BIBLIOGRAPHY xliii

LIST OF FIGURES

Figure 1.1	Installed renewable energy power per voltage level	2
Figure 2.1	Power system dynamic phenomena and time frames	10
Figure 2.2	Power system stability definitions	13
Figure 2.3	Typical dynamic underfrequency course	14
Figure 2.4	Time scales of power system frequency control	16
Figure 2.5	Implementation of the fast-frequency response control	17
Figure 2.6	Standard synchronous reference frame (SRF) PLL	19
Figure 3.1	Overview of a six-pulse bridge inverter	23
Figure 3.2	Pulse-width modulation (PWM) with triangular carrier	24
Figure 3.3	Control levels for inverter-based generation	27
Figure 3.4	Requirement on the frequency ride-through of generators	29
Figure 4.1	Schematic of the internal and external system	34
Figure 4.2	Overview of dynamic system equivalents	35
Figure 4.3	Schematic process of the greybox aggregation	37
Figure 4.4	Overview of the differential evolution algorithm	40
Figure 5.1	Overview on the generic medium-voltage testbench	46
Figure 5.2	Equivalent circuit of the synchronous generator	47
Figure 5.3	Overview of the synchronous generator (SG) control	48
Figure 5.4	Influence of SG parameters on the frequency curve	51
Figure 5.5	Load model active and reactive power consumption	58
Figure 6.1	Electrical and control model for IBG	62
Figure 6.2	Frequency estimation with variation of the PLL parameters	64
Figure 6.3	Current limiting for the inverter-based generator model	67
Figure 6.4	Comparison of current limiters	69
Figure 6.5	Overview of the direct voltage control	71
Figure 6.6	Current limit of direct voltage and grid-supporting control	72
Figure 6.7	Comparison of MV testbench results in RMS and EMT	74
Figure 7.1	Medium-voltage benchmark grid	78
Figure 7.2	High-voltage benchmark grid	81
Figure 7.3	Windfarm model in string configuration	83
Figure 7.4	Fitting model for the greybox aggregation	84
Figure 8.1	Overview of investigations in the medium-voltage testbench	89
Figure 8.2	Dynamic IBG reaction in the medium-voltage testbench	91
Figure 8.3	Impact of external grid parameters on IBG dynamics for a loadstep $\Delta P_{\mathrm{L0}} = 5$ MW	95

Figure 8.4 Impact of external grid parameters on IBG dynamics for a loadstep $\Delta P_{L0} = 15$ MW 96
Figure 8.5 Impact of the loadstep size on the IBG current infeed . . 98
Figure 8.6 Impact of the load model type on the IBG current infeed 99
Figure 8.7 Impact of the cable length on the IBG dynamics 101
Figure 8.8 Impact of the FFR implementation on the dynamics . . . 102
Figure 8.9 Impact of the FFR droop and deadband on the dynamics 103
Figure 9.1 Dynamic frequency response for different IBG scenarios in the medium-voltage benchmark grid (case 1) 108
Figure 9.2 Dynamic frequency response for different IBG scenarios in the medium-voltage benchmark grid (case 2) 110
Figure 9.3 Impact of the FFR droop and deadband on the frequency metrics 112
Figure 9.4 Dynamics of the MV benchmark grid for different shares of IBG with constant FFR 114
Figure 9.5 Impact of the constant FFR parametrisation with a delay $T_{\mathrm{delay}} = 1$ s 115
Figure 9.6 Impact of the constant FFR parametrisation with a delay $T_{\mathrm{delay}} = 100$ ms 116
Figure 9.7 Homogeneous and inhomogeneous distribution of linear and constant FFR 118
Figure 9.8 Comparison of grid-supporting and direct voltage control in the MV benchmark grid 119
Figure 9.9 Grid-supporting and direct voltage control frequency metrics varying inertia constant and FFR 120
Figure 9.10 Impact of the external grid inertia and loadstep size . . . 121
Figure 9.11 Dynamics of the MV benchmark grid for different static and dynamic load models 122
Figure 9.12 Dynamics of the HV grid for different shares of IBG . . . 124
Figure 9.13 Frequency metrics for varying system inertia and FFR implementations 125
Figure 9.14 Frequency metrics depending on the connection point of the windfarm 126
Figure 10.1 Dynamics of the MV benchmark grid aggregation for the max IBG scenario with linear FFR 133
Figure 10.2 Distribution of the relative absolute error (AE) for the different aggregation methods of the MV benchmark grid 136
Figure 10.3 Comparison of the objective function for PSO and DE . . 137
Figure 10.4 Distribution of the relative mean absolute error for the aggregation of the MV benchmark grid using DE/best . 138

Figure 10.5 Dynamics of the MV benchmark grid aggregation for a varying inertia constant 140
Figure 10.6 Adaptation of the IBG control for aggregating inhomogeneous scenarios 141
Figure 10.7 Dynamics of the MV benchmark grid aggregation for mixed FFR scenarios 143
Figure 10.8 Dynamics of the MV benchmark grid aggregation using the direct voltage control 144
Figure 10.9 Dynamics of the detailed HV benchmark grid aggregation including aggregated MV grids 146
Figure 10.10 Dynamics of the HV benchmark grid aggregation 147
Figure 10.11 Frequency dynamics of the HV benchmark grid aggregation147
Figure A.1 Dynamic active power sharing in the medium-voltage testbench xxxvi
Figure A.2 Impact of the FFR droop and deadband with standard PLL parameters on the dynamics xxxvii
Figure A.3 Frequency curves in a low-inertia system for different FFR implementations xxxviii
Figure A.4 Dynamics of the HV grid for different shares of IBG . . . xxxix
Figure A.5 Distribution of the absolute error for the aggregation of the MV benchmark grid using DE/best xl
Figure A.6 Distribution of the absolute error for the aggregation of the MV benchmark grid using DE/best xli

LIST OF TABLES

Table 1.1 Overview of aggregation models applied in literature . . 5
Table 3.1 Classification of inverter models 25
Table 3.2 International grid codes including fast-frequency response 30
Table 5.1 Parameters of the generic medium-voltage testbench . . . 46
Table 5.2 Aggregated parameters of the overlying external medium-voltage grid 50
Table 5.3 Parameters for static and composite load models 59
Table 6.1 Parametrisation of the phase-locked loop (PLL) 64
Table 7.1 Default parameters of the medium-voltage benchmark grid 79
Table 7.2 Scenario definition for the medium-voltage benchmark grid 79
Table 7.3 FFR variations for the medium-voltage benchmark grid . 80
Table 7.4 Default parameters of the high-voltage benchmark grid . 82
Table 7.5 Scenario definition for the high-voltage benchmark grid . 83
Table 8.1 Frequency metrics of the MV testbench 93
Table 8.2 Energy requirement for the FFR 105
Table 9.1 Frequency metrics of the MV benchmark grid 111
Table 10.1 Parameter limits for the aggregation models 130
Table 10.2 Optimised parameters for the dynamic equivalent of the medium-voltage benchmark grid 134
Table A.1 Parameters of the synchronous generator PSS and excitation xxv
Table A.2 Medium-voltage synchronous generator model xxvi
Table A.3 Parameters of the MV synchronous generator governor . xxvi
Table A.4 Parameters of the high-voltage SG model xxvii
Table A.5 Parameters of the HV synchronous generator governor . xxvii
Table A.6 SG machine transformer parameters xxvii
Table A.7 Parameters of the ultra-high-voltage SG model xxviii
Table A.8 Parameters of the UHV synchronous generator governor xxviii
Table A.9 SG machine transformer parameters xxviii
Table A.10 Parameters for the static exponential load model xxix
Table A.11 Parameters for the static ZIP load model xxix
Table A.12 Parameters for the dynamic exponential load model . . . xxx
Table A.13 Parameters for the dynamic induction motor load model xxx
Table A.14 MV Line parameters xxxi
Table A.15 Default parameters of inverter-based generator (IBG) model xxxii
Table A.16 Default parameters of the medium-voltage testbench . xxxiii
Table A.17 Load parameters of the MV benchmark grid xxxiv

Table A.18 Parameters of the MV benchmark model xxxiv
Table A.19 Cable parameters of the MV benchmark grid xxxiv
Table A.20 Parameters of the HV benchmark grid components . . . xxxv

ACRONYMS

AC	alternating current
AE	absolute error
AVM	average-value model
AVR	automatic voltage regulator
CIGRÉ	International Council on Large Electric Systems
CO_2	carbon dioxide
DC	direct current
DE	differential evolution
DFIG	doubly-fed induction generator
EA	evolutionary algorithm
emf	electromotive force
EMT	electromagnetic transients
FCR	frequency containment reserve
FFR	fast frequency response
FRT	fault ride-through
FSM	frequency sensitive mode
HV	high-voltage
HVDC	high-voltage direct current
IBG	inverter-based generation
IEC	International Electrotechnical Commission
IEEE	Institute of Electrical and Electronics Engineers
IGBT	insulated-gate bipolar transistor
IM	induction motor
LFSM	limited frequency sensitive mode
LV	low-voltage
MAE	mean absolute error
MPPT	maximum power point tracking
MV	medium-voltage

oe	overexcited
PCC	point of common coupling
PI	proportional-integral
PLL	phase-locked loop
PSO	particle swarm optimisation
PSS	power system stabiliser
PST	power system transients
PV	photovoltaic
PWM	pulse-width modulation
REI	radial equivalent independent
RMS	phasor or root-mean square
RoCoF	rate of change of frequency
SCR	short-circuit ratio
SG	synchronous generator
SRF	synchronous reference frame
TSO	transmission system operator
ue	underexcited
UHV	ultra-high-voltage
VSC	voltage-source converter
WECC	Western Electricity Coordinating Council

SYMBOLS

Latin Symbols

c	acceleration coefficient for PSO	-
C	capacitance	F
CR	crossover probability for DE algorithm	-
d_{pr}	active power frequency droop, primary control	Hz/MW
D	dimension, number of elements of a vector	-
E	electromotive force	V
f	electrical frequency	Hz
F	mutation factor for DE algorithm	-
f_{cutoff}	filter cutoff frequency	Hz
f_{est}	PLL frequency estimation before filtering	Hz
f_{inst}	instantaneous electrical frequency	Hz
$\mathbf{g}_{IT}$	global best position for iteration IT	-
H	inertia constant	s
i	AC current	A
I	DC current	A
I_{f}	field current	A
IT	current iteration	-
J	moment of inertia	$\mathrm{kg} \cdot \mathrm{m}^2$
k	counting variable for vector elements, $k \in [1 \;\; D]$	-
k_{D}	derivative gain	s
k_{I}	integral gain	s^{-1}
k_{P}	proportional gain	-
l	counting variable for particles, $l \in [1 \;\; POP]$	-
p	number of pole pairs of machines	-
P	active power	MW
P_{G}	generated active power	MW
P_{L}	consumed active power (load)	MW

$\mathbf{p}_{l,IT}$	best position of particle l for iteration IT	MW
P_{loss}	active power losses	MW
POP	population (swarm size), number of particles	-
r	uniformly distributed random number	-
RL	rate limit for frequency	Hz/s
$RoCoF$	frequency gradient, rate of change of frequency	Hz/s
S	apparent power	MVA
t	time	s
S_{r}	rated power	MVA
T_{delay}	FFR time delay of additional active power infeed	s
T_{dur}	time duration of the FFR active power infeed	s
$\mathbf{u}_{k,l,IT}$	trial vector	-
v	time-variant voltage	kV
V	time-invariant voltage	kV
$\hat{V}$	voltage amplitude	kV
$\mathbf{v}_{l,IT}$	velocity vector for particle l and iteration IT	-
$\boldsymbol{v}_{\text{max}}$	velocity bound vector	-
v_{carrier}	PWM carrier voltage	kV
w	PSO weight factor for velocity	-
$\mathbf{x}$	parameter vector for dynamic equivalent	-
X	reactance	Ω
X'	transient reactance	Ω
X''	subtransient reactance	Ω
$\mathbf{x}^{\text{L}}$	lower limits of parameter vector $\boldsymbol{x}$	-
$\mathbf{x}^{\text{U}}$	upper limit of parameter vector $\boldsymbol{x}$	-
Z	impedance	Ω

Greek Symbols

Δ	difference	-
$\epsilon(\mathbf{x})$	objective function for greybox aggregation	-
φ_{v}	voltage phase angle	-
τ	torque	Nm
τ_{el}	electromagnetic torque	Nm

τ_{T}	turbine torque	Nm
θ	voltage phase	-
χ	constriction coefficient for the PSO algorithm	-
ω	electrical angular or rotational velocity	rad/s
ω_{m}	mechanical angular or rotational velocity	rad/s

Subscripts

$()_{\mathrm{abc}}$	three-phase signal in abc coordinates	-
$()_{\mathrm{agg}}$	aggregated value	-
$()_{\mathrm{dq}}$	dq coordinates with rotating reference frame	-
$()_{\mathrm{dc}}$	inverter-based generation (IBG) DC side	-
$()_{\mathrm{est}}$	estimation	-
$()_{\mathrm{FFR}}$	fast-frequency response	-
$()_{\mathrm{F}}$	filter	-
$()_{\mathrm{G}}$	generation	-
$()_{\mathrm{Gov}}$	governor	-
$()_{\mathrm{line}}$	line	-
$()_{\mathrm{L}}$	load	-
$()_{\mathrm{lim}}$	limited	-
$()_{\mathrm{meas}}$	measured	-
$()_{\mathrm{n}}$	nominal quantity	-
$()_{\mathrm{out}}$	output	-
$()_{\mathrm{r}}$	rated quantity	-
$()_{\mathrm{R}}$	rotor quantity	-
$()_{\mathrm{ref}}$	reference	-
$()_{\mathrm{S}}$	stator quantity	-
$()_{\mathrm{SC}}$	short-circuit	-
$()_{\mathrm{SG}}$	synchronous generator	-
$()_{\mathrm{Tur}}$	turbine	-
$()_{\mathrm{T}}$	transformer	-
$()_{\alpha\beta}$	signal in rotating $\alpha\beta$ coordinates	-

Part I

FUNDAMENTALS

1 INTRODUCTION

A major cause of nowadays environmental pollution, global warming and climate change is the release of carbon dioxide (CO_2) to the atmosphere. To reduce CO_2 emissions and make the whole energy system more sustainable, fossil fuels are being replaced by renewable energy sources. As renewable energy plants are connected to the electrical power system, other energy sectors, e.g. heat or mobility, are gradually being electrified. These changes in the power generation are at the heart of many of the current challenges in modern power systems.

Conventional large-scale power plants based on nuclear and coal energy, which are usually connected to the grid via a synchronous generator (SG), are gradually being phased out. To become more sustainable and climate-friendly, the power system is largely supplied by renewable energy plants, including wind power and photovoltaic (PV) systems in particular.[1] This new generation structure poses fundamental challenges because of its physical and technical characteristics: The power system must become more flexible due to the volatile feed-in characteristics. The energy feed-in of solar and wind power plants is highly dependent on wind and radiation conditions, so renewable energy plants are also being developed on a large scale away from load centers, i.e. remote - an example being offshore wind energy.

In order to achieve ambitious climate targets, the enormous potential of renewable energy plants must be exploited. This results in both centralised structures remote from load centers, such as large onshore and offshore windfarms, and more decentralised installations, such as rooftop PV systems, smaller PV plants and windfarms. The majority of renewable energy plants are connected at distribution level [2]. The large number of smaller distributed generation units in distribution grids requires a high level of coordination and design of the power system, e.g. in case of power flow reversal. Only very large windfarms are directly connected to the transmission grid. Figure 1.1 depicts an overview of the installed power of renewable energy plants across the different voltage levels in Germany. It shows that a vast majority of the renewable energy plant installed power is allocated to the distribution grid, consisting of low-voltage (LV), medium-voltage (MV) and high-voltage (HV) grids. A notably smaller proportion of renewable energy is fed in directly into the transmission grid, i.e. into the ultra-high-voltage (UHV) transmission grid and high-voltage/ultra-high voltage

1 Hydroelectric is the prevalent renewable energy source worldwide [1] and can provide consistent and reliable power generation, but is highly dependent on local geographic conditions.

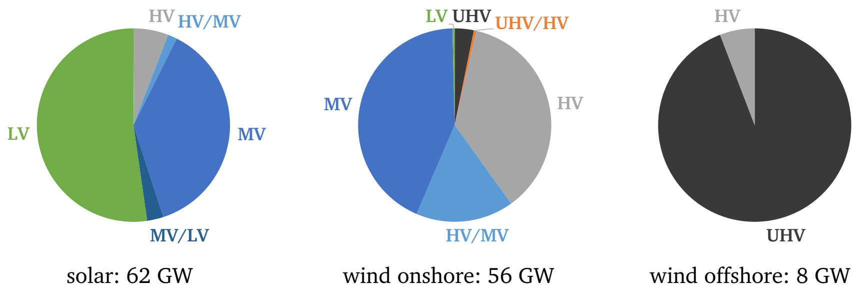

Figure 1.1: Installed renewable energy power per voltage level in Germany in 2022 based on [3].

(HV/UHV) substations with an exception of offshore-windfarms. Wind and solar power plants differ from conventional power plants not only because of their volatile feed-in characteristics. The technology used to connect them to the power system is also fundamentally different from that of SG. The large rotating masses of the SG store kinetic energy, the so called mechanical inertia, which slows down dynamic processes in the power system. SG are successively shut down and replaced by inverter-based generation (IBG). The latter are connected via power electronic inverters and do either have no rotating parts, e.g. PV applications or are fully or partly connected through power electronics for control puposes, as is the case for most wind turbines. Control methods for IBG plants are an important topic of current research. Grid-forming control methods have emerged, which actively form the grid voltage and frequency and, for example, emulate the behaviour of SG from a control point of view.

1.1 MOTIVATION AND BACKGROUND

Historically, public power distribution grids were designed as passive networks with a unidirectional power flow from centralised generation sources to end-users. However, the proliferation of decentralised IBG such as solar PV, wind turbines, and energy storage systems has introduced a new paradigm – the active distribution grid. These distribution grids enable bi-directional power flows, giving rise to local energy generation, consumption, and trading. The dynamic interaction of these IBG with the distribution grid creates a complex and evolving environment that necessitates innovative control strategies to ensure stability and efficient operation. The term *active distribution grid* is used in this work to describe distribution grids that are based to a large extent on IBG with the ability to contribute to frequency stability through appropriate control. It is important to distinguish the term *active distribution grid* from the terms *microgrid* and *grid cell*, both of which envisage a self-sufficient or partially self-sufficient operation of the distribution grid. Here, the active distribution grid is part of the interconnected power system.

The power system frequency is a critical indicator of its stability, determined by the delicate balance between power generation and consumption. The frequency can be deflected from its steady state due to disturbances in the system, such as a change in the load, the failure or tripping of a generator or, a system split. In traditional power systems, centralised SG provide inertia that helps maintain stable frequencies. The growing integration of IBG challenges this inertia and calls for advanced dynamic frequency control techniques. These techniques include demand response, energy storage management, and smart load shedding, which collectively contribute to stabilising the grid frequency in the face of frequency fluctuations. In this work, the fast frequency response (FFR) of IBG is investigated in detail and the impact of frequency dependent loads is discussed. As the power generation shifts from transmission to distribution grids due to the increased IBG integration, the interactions between distribution and transmission grids gain prominence [4, 5]. The contribution of active distribution grids to the dynamic frequency stability cannot be neglected for high penetrations of IBG [6] or represented as steady-state models for dynamic studies. However, the many different manufacturers and plant specifics of decentralised IBG cannot be modelled individually. Generic models are used to present typical characteristics of the static and dynamic behaviour [7].

The large number of decentralised IBG leads to further challenges: The issue of coordinating a vast number of individual plants remains complex. The combination of several plants to form virtual power plants may provide an answer. Moreover, the reduced modelling of distribution grids for transmission grid studies requires simple, but correct dynamic equivalents of the underlying grids. Aggregating the behaviour of active distribution grids and studying their impact on the transmission grid's frequency dynamics becomes crucial. This aggregation can offer insights into the effects of diverse IBG penetration levels, grid architectures, and control strategies on system-wide frequency stability. These investigations aid in formulating effective dynamic equivalents that reproduce the frequency support from active distribution grids.

1.2 STATE OF THE ART

The modelling of IBG in the form of generic models refers to a simplified representation that allows power system studies without the need for highly detailed and specific data. Generic models for IBG are developed e.g. by the International Electrotechnical Commission (IEC) [8, 9] and the Western Electricity Coordinating Council (WECC) [10]. Further research is conducted on the simplified modelling of IBG for large scale power systems, e.g. in [7, 11–13]. In addition, the generic models are also increasingly validated with more detailed models [14] or with field testing results [15, 16] in order to achieve a match between reality and simulation.

For the IBG control, grid-forming and grid-supporting control concepts arise, which can provide ancillary services to the power grid. An overview of control concepts is given in [17] and specifically for grid-forming control concepts in [18]. To date research questions include the placement and size of grid-forming units [19, 20] and to which extent grid-supporting IBG can stabilise the frequency [21, 22]. For further details on IBG control concepts, the reader is referred to Chapter 3.3. Regarding the frequency support control of IBG, two main approaches can be distinguished. The first one is based on the emulation of an inertia-like behaviour through grid-forming control, the so called virtual inertia provision [23, 24]. The second frequency support control relies on the FFR control [25, 26], i.e. the fast adjustment of the IBG output power, which can be realised much faster than is the case for conventional SG-based generation. The provision of positive control energy means that IBG must either be operated with throttling or additional storage units, e.g. in the DC link, must provide the additional energy. This topic is discussed in [27–29].

Most of the studies carried out in interconnected active distribution grids are focussed on the voltage and reactive power control of IBG, e.g. [30–32]. Frequency investigations are usually carried out in transmission systems, e.g. [33, 34] or in microgrids, e.g. [35, 36]. In [37] the issue of implementing the power sharing for many small IBG units in active distribution grids is tackled, which is classified as long-term frequency stability. A broad analysis of the influence of IBG in active distribution grids on short-term dynamics in superimposed voltage levels is given in [38]. Here, the effects of a phase jump, a frequency jump and a short circuit are evaluated. However, a detailed consideration of the frequency and a comprehensive sensitivity analysis are not carried out.

Regarding a summerised or reduced-order modelling of active distribution grids, different approaches under the terms equivalent modelling, e.g. [39] and aggregation or aggregated models, e.g. [6] exist. An overview of studies is given in Table 1.1. The studies are divided into static and dynamic equivalents and the latter are subdivided into linearised small-signal and nonlinear large-signal disturbances. As of the author's awareness, there exists a notable gap in the current literature regarding comprehensive investigations into the dynamic short-term large-disturbance frequency behaviours within interconnected active distribution grids, along with their aggregation for system-wide frequency stability studies.

Table 1.1: Overview of aggregation models applied in literature, based on [40].

aggregation type	modelling approach	references
steady state	whitebox	[41–44]
	greybox	[39, 45–48]
	blackbox	[49–51]
dynamic linearised	whitebox	[52, 53]
	greybox	[54, 55]
	blackbox	[56–62]
dynamic nonlinear	whitebox	[63]
	greybox	[55, 64–68]
	blackbox	[69–73]

The steady-state aggregation models simplify the distribution grid by assuming steady-state conditions and constant parameters over time. These models are used for initial system analysis and planning, but are not suitable for capturing the dynamic behaviour of active distribution grids. Linearised dynamic aggregation models extend the steady-state models by including linear approximations of the system dynamics around the operating point. These models are used for small-disturbance stability analysis. For the nonlinear large-signal dynamic equivalents presented in Table 1.1, in [55, 64–70, 72, 73] the dynamic frequency and frequency control of IBG is not investigated. The authors of [63] focus on doubly-fed induction generator (DFIG) wind turbines and do not include full-power inverter-based generators nor FFR control. In [71], the dynamic frequency is investigated with a focus on microgrids in islanded mode.

Three different modelling approaches exist for the derivation of aggregation models. The whitebox approach uses detailed knowledge of the distribution grid to be aggregated and circuit theory for a reduced-order representation. For the blackbox approach, the grid to be aggregated is not known and the focus is solely on the input-output relationship without considering physical principles. The greybox approach blends the whitebox and blackbox approaches and models some basic components, which are to be parametrised.

This work presents a nonlinear greybox dynamic equivalencing method. The identification is carried out by applying system operating constraints and without assuming any linearisation of the model in order to maintain an effective relation with the real configuration of the active distribution grid. The prior understanding of the active distribution grid's structure can be effectively incorporated into the identification process in this way. The result is a model that can be effectively modified to fit various active distribution grid setups and operational circumstances before being integrated into a simulation of the transmission grid. Furthermore, all model parameters retain a physical meaning thanks to the use of a nonlinear structure based on physical principles. [66]

1.3 RESEARCH QUESTIONS AND THESIS OVERVIEW

In the context of the state-of-the-art, this thesis answers the following research questions:

1. **How can frequency analyses be carried out in the distribution grid?** How can the frequency support of individual IBG be studied on distribution grid level? Which requirements apply for the modelling of grid and component simulation models? How can the external grid be modelled in order to represent the characteristics of interconnected low-inertia power systems?
2. **How do IBG impact the dynamic frequency stability?** Which contribution can IBG make to frequency stability and control? Which sensitivities, e.g. IBG control concepts, share of IBG, external grid strength and inertia, have an impact on their contribution?
3. **How can the contribution of IBG within the active distribution grid be summarised?** How can active distribution grids and their contribution to frequency stability be aggregated in a reduced-order model for frequency studies in the transmission grid?
4. **How can inhomogeneities in the IBG control be included in the reduced-order model?** The knowledge of which parameters from the distribution grid facilitates the aggregation?

This thesis is structured as follows: Chapter 2 discusses power system frequency dynamics, control, stability and the challenges of frequency measurements in low-inertia systems. Chapter 3 presents the basics of IBG and IBG modelling as well as its control. In Chapter 4, fundamentals of dynamic system equivalents with a focus on the greybox approach are introduced. Chapter 5 provides an overview of the simulation methodology, and individual grid component models and Chapter 6 introduces the IBG model with a focus on the applied IBG controls. Chapter 7 presents the distribution grid models and scenarios used to explore frequency stability dynamics. Chapter 8 delves into the analysis of simulation results, focussing on the interplay of individual components in a simplified testbench. In Chapter 9, the results of investigations carried out in distribution grids are presented. Chapter 10 presents the results of the dynamic aggregation models. Finally, Chapter 11 concludes by discussing the implications of the findings for reduced active distribution grid modelling and Chapter 12 gives a short outlook on further research topics in the field.

2 FREQUENCY DYNAMICS

Annotation: Parts of this chapter have already been published in [74] and [75]. To improve the reading flow, self-citations are omitted.

In power systems, frequency is a key factor to balance power generation and load consumption. In steady state, the frequency of the continental European synchronous area is approximately the same and is kept in a narrow tolerance band. The balance can be affected by events in the system that disturb the active power balance, e.g. the failure of generating plants or the switching of loads. Transient processes then affect the frequency. This chapter describes the general definition of power system dynamics, defines the electrical frequency during transients and gives an overview over frequency stability and its control. Finally, the chapter closes with different methods to estimate the electrical frequency in power systems.

2.1 POWER SYSTEM DYNAMICS AND MODELLING

Power systems incorporate an immense number of components that act together and impact each other. For power system studies, the components are usually represented as mathematical models and are simplified for the phenomena to be studied. Due to the power system's complexity, the models represent only some characteristics of the physical elements to achieve the required accuracy. In order to derive a power system model, a system state and state variables are defined. The system state describes the operating conditions of the system, e.g. the power consumption of loads. The state variables, which are usually the voltage magnitudes and phase angles, are the minimum set of variables defining the system state. [76]

During normal operation, power systems are in a stable or steady state and the state variables are invariant over time. This steady state is a mathematical assumption only as loads are continuously connected and disconnected and the power infeed needs to be adapted accordingly [77]. In contrast, in case of a disturbance, the state variables are functions of time, i.e. the system is dynamic [76]. Due to the characteristic of electrical power systems as oscillating circuits, the changes of state variables following a disturbance in the system do not take place abruptly, but in the form of transient processes [77].

The disturbances and power system reaction can be divided into small signal and large signal phenomena. Small signal disturbances reflect only a small

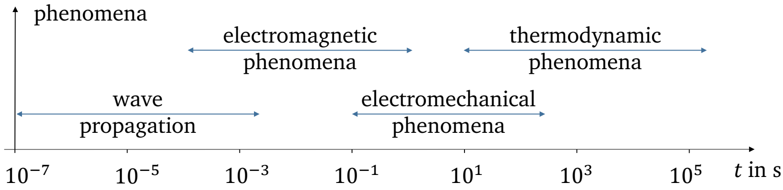

Figure 2.1: Power system dynamic phenomena and according time frames based on [82].

deviation from the operating point, such as e.g. load fluctuations. If the deviation is sufficiently small, the system can be linearised around the operating point and linear system theory can be applied [76]. Large signal disturbances result in highly dynamic and non-linear changes of the system variables that are usually analysed using numerical simulations in the time domain [78]. Typical scenarios include short circuits, failures of large power plants or system splits. A large excursion of the system variables from their setpoint can occur and countermeasures are taken. These large-scale disturbances in the power system occur much less frequently than smaller fluctuations, but are gaining relevance, e.g. recently for system splits [79–81]. This thesis is devoted to the analysis of large disturbance power system dynamics.

Various phenomena in the power system can be classified based on the time frame following a disturbance, as illustrated in Figure 2.1. Wave phenomena occur within microseconds to few milliseconds and are typically triggered by lightning propagation, surge switching, or the rapid switching of power electronic devices. Electromagnetic phenomena involve slower IBG controls and machine transients taking several hundred milliseconds. In contrast, electromechanical phenomena are caused by the frequency and voltage control of machines as the large rotating masses take up to several seconds to adapt. Lastly, thermodynamic phenomena occur over the slowest time frame, ranging from a few seconds to several hours and involve boiler control actions of steam power plants. This work focusses on electromagnetic and electromechanical phenomena.

2.2 ELECTRICAL AND ANGULAR FREQUENCY

According to [83], frequency can be divided into the frequency of a repeating pattern of events f, e.g. evaluating the zero crossings of an alternating voltage and the electrical angular frequency of machines ω, which evaluates the angular displacement of the rotor with a mechanical frequency ω_{m} and the number of pole pairs per phase p. In the following, a number of pole pairs $p = 1$ is assumed. In case of a sinusoidal signal, the frequency of a repeating pattern f and the electrical angular frequency ω can be linked as

$$\omega = 2\pi f = p \cdot \omega_{\mathrm{m}}. \tag{2.1}$$

Historically, synchronous generators are responsible to maintain the balance between generated and consumed active power in the system. In interconnected power systems, all rotating machines can be summarised with their moments of inertia J in a torque equilibrium according to (2.2), where losses are neglected. [76]

$$J \cdot \frac{\mathrm{d}\omega_{\mathrm{m}}}{\mathrm{d}t} = \tau_{\mathrm{Tur}} - \tau_{\mathrm{el}} \tag{2.2}$$

J, τ_{Tur} and τ_{el} are the total inertia of all rotating machines being connected to the system, the turbine torque and the counteracting electromagnetic torque, respectively. The moment equilibrium (2.2) can be converted in a power equilibrium (2.3) using the relation $P = \omega_{\mathrm{m}} \cdot \tau$.

$$\omega_{\mathrm{m}} \cdot J \cdot \frac{\mathrm{d}\omega_{\mathrm{m}}}{\mathrm{d}t} = P_{\mathrm{G}} - P_{\mathrm{L}} - P_{\mathrm{loss}} \tag{2.3}$$

With ω_{m}, P_{G}, P_{L} and P_{loss} being the mechanical rotor speed, the generated active power, the consumed active power (load) and the active power losses, e.g. line losses. In a perfectly balanced system with $P_{\mathrm{G}} = P_{\mathrm{L}} + P_{\mathrm{loss}}$, there is no change in rotor speed $\mathrm{d}\omega_{\mathrm{m}}/\mathrm{d}t = 0$, the state variables are invariant over time and the system is in steady state. In contrast, a power imbalance leads to a change of the rotor speed $|\mathrm{d}\omega/\mathrm{d}t| > 0$ and the power equilibrium must be restored through appropriate measures.

With the shutdown of conventional power plants and corresponding SG, determining the elctrical frequency f becomes more relevant. Unlike the mechanical rotation of machines, the electrical frequency cannot be measured directly. It must be derived by measuring an electrical alternating variable, such as the three-phase alternating current (AC) voltage or current. However, non-perfect sinusoids during power system transients cannot be evaluated that easily. Both in nature and in signal processing, dynamic events occur where the frequency changes over time. Here, the changing frequency of the AC voltage in the power system is considered. Thus, the problem of defining an instantaneous electrical frequency arises, which is described in [84] as a generalisation of the definition of constant frequency: The rate of change of the phase angle per time unit. The same result is achieved by the procedure where the signal of a harmonic oscillation, in this case of a sinusoidal voltage *v(t)* is defined as

$$v(t) = \hat{V} \cdot \sin[\int_0^t 2\pi \cdot f_{\mathrm{inst}}(t)\mathrm{d}t + \varphi_{\mathrm{v}}] = \hat{V} \cdot \sin(\theta(t)) \tag{2.4}$$

with the amplitude $\hat{V}$, the instantaneous frequency $f_{\text{inst}}(t)$, the phase $\theta(t)$ and the voltage phase angle φ_{V}. From the voltage phase $\theta(t)$, which is the argument of the sine function, the instantaneous frequency f_{inst} is defined as

$$f_{\text{inst}}(t) = \frac{1}{2\pi} \cdot \frac{\mathrm{d}\theta(t)}{\mathrm{d}t} \tag{2.5}$$

The electrical frequency f and the angular frequency ω are relevant quantities for the evaluation of the system state and for the control of power plants, which is described in the following section.

2.3 FREQUENCY STABILITY AND CONTROL

Frequency is a global quantity in the power system and frequency stability is key to maintain a stable operation. With the increasing share of power electronics, frequency control becomes more relevant and challenging as the inherent inertial response of synchronous generators decreases. Among the multiple phenomena related to frequency, e.g. harmonics and subfrequent oscillations, this work focuses on evaluating the fundamental frequency.

2.3.1 *Power System Stability Definitions*

According to [85], power system stability is defined as the ability of a system to regain a stable equilibrium state for given initial conditions after the system has been subjected to a physical disturbance. In the new equilibrium state, the system variables must be constrained over time, i.e., quasi-constant. Although in principle all phenomena of stability are related, they can be divided into categories.

The classical stability definitions of Institute of Electrical and Electronics Engineers (IEEE) and International Council on Large Electric Systems (CIGRÉ) [85] divide the power system stability into rotor angle stability, frequency stability and voltage stability, cf. Figure 2.2. Here, rotor angle stability describes the ability of synchronous machines in an interconnected system to remain synchronous or restore synchronism after a disturbance. For this purpose, a balance of electromagnetic and mechanical torque must prevail at each machine. Voltage stability describes the ability of the electrical power system to maintain a stable voltage on all busbars after a disturbance. In steady-state operation, the voltage tolerance bands are at most within a range of $\pm$ 10 % of the nominal voltage V_{n}. Voltage and rotor angle stability can each be subdivided into small and large signal stability, whereby the large-signal rotor stability is referred to as transient stability. According to the names, these are related to either small or large disturbances in the system, see Chapter 2.1.

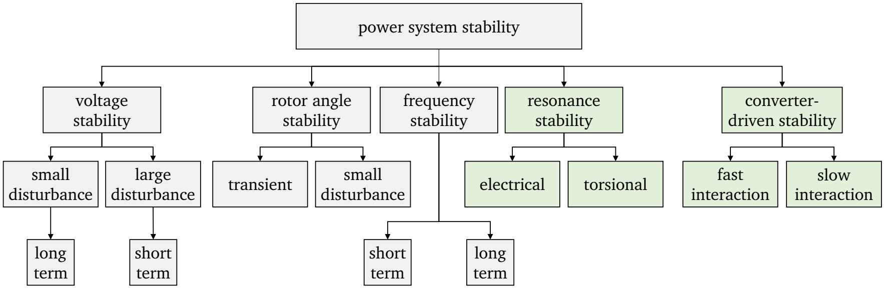

Figure 2.2: Power system stability definitions according to IEEE and CIGRÉ [82]. Grey: Classical stability definitions. Green: New categories since 2021.

Since 2021, two additional stability categories are added, which take into account the major changes in the generation structure: Resonance stability and converter-driven stability. Resonance generally occurs when there is a periodic exchange of energy in an oscillatory form. These oscillations can grow without sufficient dissipation of energy, leading to increasing voltage, current or torsional amplitudes. Resonance instability is defined as exceeding a threshold value of these amplitudes. A distinction is made between torsional resonance and electrical resonance. Torsional resonance refers to subsynchronous resonances for frequencies below 50 Hz, which can be caused by subsynchronous mechanical eigenmodes of a generator shaft. In the case of electrical resonance, a resonant circuit is excited at the natural frequency. This occurs, for example, in DFIG, which are used for connecting wind turbines. The resonance occurs when the filter and the inductance of the asynchronous generator form a resonant circuit in the subsynchronous range. [82]

Inverter-driven stability takes into account the fundamentally different dynamic intrinsic behaviour of IBG and SG or rotating machines in general. In this context, the control of IBG plays a crucial role and interactions can occur both between different IBG or between IBG and the electromechanical dynamics of rotating machines. These interactions can be divided into fast and slow phenomena. Fast phenomena in the high-frequency range from several hundred Hertz to several kilohertz and high-frequency oscillations are also called harmonic instability. Slow interactions with frequencies below 10 Hz can also occur and are similar to the subsynchronous resonances described above. [82]

Frequency stability describes the maintenance of a constant frequency throughout the interconnected power system. This depends on whether there exists a balance between generated and consumed active power according to (2.3) or whether it can be restored after a disturbance with a minimum unintentional loss of load. Disturbances include the tripping of generating plants and/or loads, system split scenarios or unintentional islanding. Frequency stability can be divided into short-term stability in the time frame of a few seconds and long-term stability ranging from tens of seconds to several minutes. Typical short-term phenomena are the splitting of the power system into two or more subsystems or the failure of large power plants. Long-term phenomena can consist of poorly tuned steam turbine controls or boiler protections. In the European interconnected power system, the nominal frequency is 50 Hz with a tolerance band of $\pm$ 200 mHz.

2.3.2 *Power System Frequency Control*

Keeping the power system frequency within a narrow tolerance band means that the active power equilibrium must be kept or restored by the power system control. This work examines underfrequency scenarios, in which due to a disturbance more active power is consumed than produced and the frequency decreases. In order to counteract the frequency drop, different controls - mainly in the generating plants - are activated and increase the active power infeed, also called the frequency containment reserve (FCR) or primary control. The typical frequency curve after a disturbance can be divided into different sections and is shown in Figure 2.3.

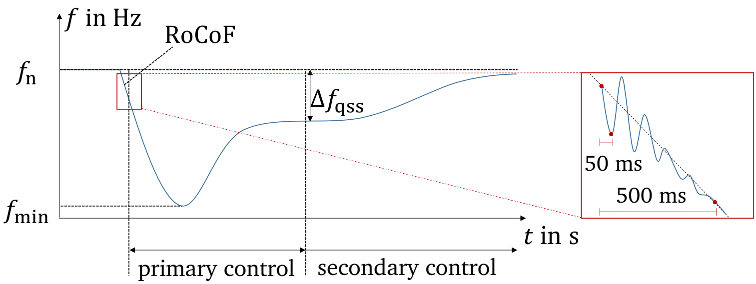

Figure 2.3: Typical dynamic underfrequency course and relevant metrics, based on [82] and zoom into the transient time range based on [86].

In the transient time range, the kinetic energy stored in the rotating masses of SG, i.e. the initial inertial response, compensates the power imbalance. As a result, the generators slow down due to the increased active power consumption and the corresponding increased electrical momentum, see (2.2),(2.3) and rotate with reduced speed - the grid frequency drops. To which extent the individual generators are decelerated depends on their inertia and during the short-term range can be influenced by the electrical distance to the disturbance [87]. The initial inertial response also determines the rate of change of frequency (RoCoF) [76]. The RoCoF can be calculated by (2.6) for a power system relying on n synchronous generators with f_n, ΔP, H_i and S_i being the nominal frequency, the active power mismatch, the inertia constant and the rated apparent power of the i-th generator. As the share of IBG without inertial behaviour increases, the additional term $S_\mathrm{SG}/P_\mathrm{L}$ in (2.6) is added to base the calculation only on the plants contributing to the system inertia. Power electronic devices do not inherently provide an inertial response to the power system. A reduced share of SG and a reduced system inertia H lead to faster and more severe frequency excursions following a disturbance. Thus, the RoCoF increases with decreasing share of SG or other sources of instantaneous inertia provision. However, the fast control of IBG can partly compensate for the reduced inertia, see Chapter 2.3.3.

$$\mathrm{RoCoF} = \frac{\mathrm{d}f_\mathrm{inst}(t)}{\mathrm{d}t} \approx \frac{f_\mathrm{n}\Delta P}{2 \cdot \frac{S_\mathrm{SG}}{P_\mathrm{L}} \cdot \sum_{i=1}^{n} H_i \cdot S_i} \approx \frac{f(t_0 + \Delta t) - f(t_0)}{\Delta t} \tag{2.6}$$

The RoCoF can also be calculated from a given frequency curve and serves as a measure of how severe a disturbance in the power system is. Protection systems [88, 89] or load shedding mechanisms [90] can rely on a RoCoF evaluation. So far, a uniform rule on how to evaluate the RoCoF from a measured frequency curve is missing [91]. This gap is partly closed in [92], where the minimum requirements for frequency and RoCoF measurements are presented with a focus on the performance, but definitions e.g. on the RoCoF calculation time window Δt are missing. The RoCoF, essentially representing the tangential line or instantaneous derivative at any point on a frequency curve, is usually approximated by taking two frequency measurements $f(t_0 + \Delta t)$, $f(t_0)$ within a brief time span Δt [26]. Recommendations range from a moving average window of $\Delta t = 100...1000$ ms [26, 91] or the maximum slope between two consecutive frequency measurements [26]. The choice of the time window Δt has a significant impact on the RoCoF calculation as can be seen in Figure 2.3.

As soon as a frequency deviation $|\Delta f| > 10$ mHz occurs, the primary frequency control in SG is activated and counteracts the frequency deviation by adjusting the injected active power within a range of ± 5 % of the rated power [76]. The frequency nadir f_min denotes the overall minimum frequency. As with the RoCoF, the shutdown of conventional power plants based on SG leads to more severe frequency deviations and in turn to a smaller frequency nadir f_min for underfrequency scenarios. The primary control – a proportional control – leads the frequency to a new steady-state value, which differs from the pre-fault condition. While SG typically run in frequency sensitive mode (FSM), which means that the primary control is activated at small frequency deviations, further plants are set to limited frequency sensitive mode (LFSM) and supply additional active power during severe disturbances with large frequency deviations.

The quasi-steady-state frequency deviation Δf_{qss} that occurs after activation of the primary control, is derived from the average active power frequency droop d_{pr} and the active power mismatch ΔP by (2.7). The droop control is described in more detail in the next section.

$$\Delta f_{\mathrm{qss}} = \Delta P \cdot \frac{d_{\mathrm{pr}}}{100\ \%} \tag{2.7}$$

Secondary frequency control compensates the deficit of generated energy by the power plants of the balancing group and returns the frequency back to its nominal value. Tertiary control ensures that sufficient control energy is available in the event of another fault [76]. Finally, rescheduling or dispatch of power plants can be necessary to adapt to new operational requirements. The frequency controls work on different time scales as depicted in Figure 2.4. The fast control of IBG can quickly adapt to frequency changes and therefore play a major role in the power system frequency control as described in the next section.

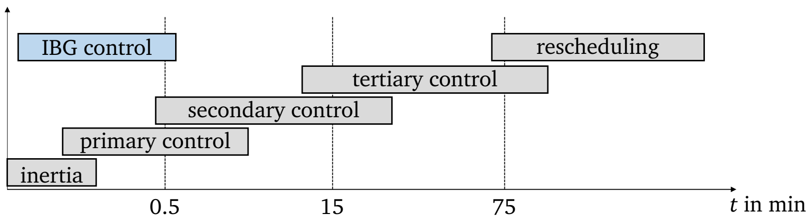

Figure 2.4: Time scales of power system frequency control based on [93].

2.3.3 *Fast Frequency Response*

Additionally to the ancillary services of conventional power plants with relatively slow time constants, IBG can adapt the active power infeed according to the grid frequency on a much faster time scale [93]. Fast frequency control, also referred to as FFR, can be defined as a fast active power support, which responds to frequency deviations Δf and contributes to arrest or slow down the frequency change [94–96]. The disconnection or reduction of the power demand of loads can also provide FFR. However, this work focusses on the provision of FFR only by generation plants. Different countries include FFR in the national grid codes [94] and thereby two different implementations emerge: The additional active power provision or withdrawal ΔP_{FFR} can be realised as a proportional change $k_{\mathrm{P,FFR}}$

according to the change in the system frequency with or without deadband db_{FFR} as depicted in Figure 2.5 a). The proportional dependency of the additional active power infeed ΔP_{FFR} on the frequency deviation Δf is typically expressed as a droop $d_{\text{FFR}} = 1/k_{\text{P,FFR}} = \Delta f/\Delta P_{\text{FFR}}$. The availability of additional active power from generation plants is highly dependent on the pre-fault feed-in and the dimensioning of the converter or in case of storages additionally depends on the state of charge. Therefore, the additional active power infeed might be limited, whereas reducing the active power infeed usually is less critical. The second implementation according to Figure 2.5 b) sets a defined additional active power ΔP_{FFR} that must be maintained constant for a defined time duration T_{dur} and uses the frequency deviation Δf as a trigger to start providing the predefined additional active power. The time delay T_{delay} until the additional active power starts adapting and the slope of the active power change $k_{\text{P,FFR}}$ are predefined by the system operator. Different levels or tariffs of FFR take into account different time constants for the additional active power T_{delay}, different frequency deviations as trigger or different durations T_{dur} [95].

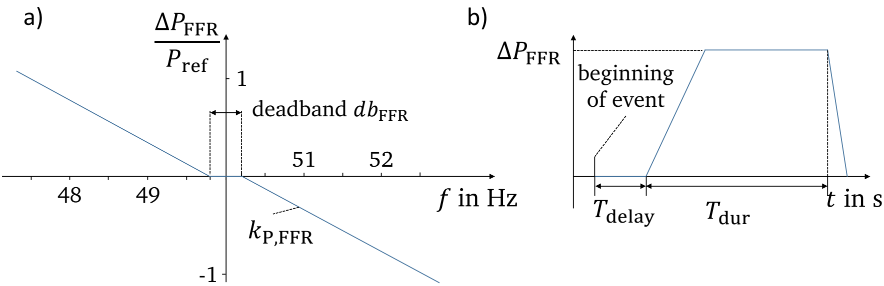

Figure 2.5: Implementation of the fast frequency response (FFR) control, based on [97]:
a) Linear power-frequency correlation (linear FFR) and
b) constant additional power infeed (constant FFR).

2.4 FREQUENCY ESTIMATION

Due to the increasing share of IBG in the power system, the relevance of frequency measurement and estimation increases, as the frequency is an input for the control [98] and synchronisation [99, 100] of IBG. As shown in the previous section, frequency is a derived quantity that can only be measured indirectly. This is done by measuring the voltage $v(t)$, because unlike the electric current $i(t)$, it is the more significant and steadier unit in power systems. This section presents the phase-locked loop (PLL) and some further frequency estimation methods to determine the frequency of the power system from a measured AC voltage v_{abc} in real time during the simulation.

2.4.1 *Phase-Locked Loop*

A PLL is a closed loop whose output signal is the estimated voltage phase θ_{est}, which is synchronised with the input three-phase voltage signal v_{abc} in phase and frequency. Due to the increasing share of IBG, PLL are increasingly applied in the power system with the main task being to synchronise the converters with the power systems frequency. A byproduct of this control loop is an estimate of the angular frequency ω_{est} [12].

The scheme of a conventional three-phase synchronous reference frame (SRF) PLL is shown in Figure 2.6. The phase detector performs the Clarke's and Park's transformation of the measured three-phase voltages v_{a}, v_{b} and v_{c} to $\alpha\beta$ and dq reference frame. Assuming the measured three-phase input voltages given in (2.8) with amplitude $\hat{V}$, the Clarke's and Park's transformation lead to the transformed voltages in the rotating dq reference frame (2.9) with the measured and estimated voltage phase θ and θ_{est} [101]. The linearised terms in (2.9) indicate that the signal v_{d} contains the voltage amplitude $\hat{V}$ and the signal v_{q} contains the phase error information $(\theta - \theta_{\mathrm{est}})$. A more detailed analysis can be found in [102].

$$v_{\mathrm{a}} = \hat{V} \cdot \cos(\theta), \quad v_{\mathrm{b}} = \hat{V} \cdot \cos(\theta - \frac{2\pi}{3}), \quad v_{\mathrm{c}} = \hat{V} \cdot \cos(\theta + \frac{2\pi}{3}) \tag{2.8}$$

$$v_{\mathrm{d}} = \hat{V} \cdot \cos(\theta - \theta_{\mathrm{est}}) \approx \hat{V}, \quad v_{\mathrm{q}} = \hat{V} \cdot \sin(\theta - \theta_{\mathrm{est}}) \approx \hat{V} \cdot (\theta - \theta_{\mathrm{est}}) \tag{2.9}$$

The phase detector passes the q axis output v_{q} to the loop filter, which is realised as a tracking controller, usually a PI controller [93]. Instead of using a PI controller, a proportional-integral-derivative (PID) controller, with the proportional gain $k_{\mathrm{P,PLL}}$, the integral gain $k_{\mathrm{I,PLL}}$ and the derivative gain $k_{\mathrm{D,PLL}}$, provides an additional degree of freedom to adjust the controller's performance [101]. The output of this controller is the estimated angular frequency deviation $\Delta\omega_{\mathrm{est}}$ in rad/s. The voltage-controlled oscillator integrates the estimated angular frequency ω_{est} to the estimated voltage phase angle θ_{est}. A feedback loop passes the estimated voltage phase angle θ_{est} back to the Park's transformation block for calculation of the voltages in dq reference frame v_{d}, v_{q}.

From the angular frequency estimation ω_{est}, the electrial frequency $\hat{f}_{\mathrm{est}}$ can be calculated using (2.1). A rate limiter RL limits the first derivative of the estimated frequency $\hat{f}_{\mathrm{est}}$, i.e. the RoCoF, to a defined value. Here, the derivative between two consecutive time steps is evaluated. The limiter compares the RoCoF of each

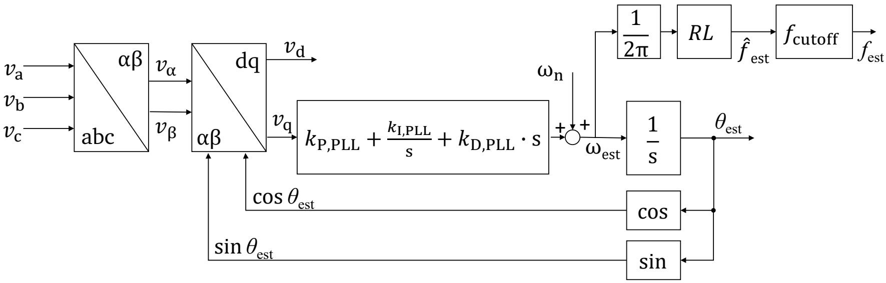

Figure 2.6: Standard synchronous reference frame (SRF) phase-locked loop (PLL) with rate limiter and low-pass filter, based on [8].

time step with the rate limit RL. If the RoCoF is larger than the rate limit RL, the output of the block is calculated as

$$\hat{f}_{est}(i) = \Delta t \cdot RL + \hat{f}_{est}(i-1) \tag{2.10}$$

with $\hat{f}_{est}(i)$ and Δt being the frequency of the i-th time step and the time between two consecutive time steps, respectively. In case the rate is smaller than the rate limit, the rate limiter does not affect the frequency estimation. Finally, an additional low-pass filter is implemented as a second-order filter with the cutoff frequency f_{cutoff} and with the filtered estimated electrical frequency f_{est} as output. Additional features can extend the standard PLL in order to cope with different challenges and improve the quality of the frequency estimation. Most of the advanced PLL with enhanced disturbance rejection capability are based on the basic scheme described in this subsection. Further details about advances in PLL can be found in [101].

2.4.2 *Further Frequency Estimation Methods*

Apart from the PLL frequency estimation, further algorithms and solutions are presented in literature to estimate the electrical frequency. Algorithms that evaluate the three-phase AC voltage in time domain are the zero crossing and the recursive Gauss-Newton algorithm. The first one evaluates the zero crossings of the voltage signal thereby calculating its period and frequency [103]. The zero crossings are identified by a change of sign and an additional interpolation between two consecutive samples of different sign is done to minimise the quantisation error. The recursive Gauss-Newton algorithm iteratively optimises the parameters of a sinusoidal AC voltage signal using a least-square approach [104].

Both algorithms are proven to lead to similar results as the PLL [74], but are more complex to model.

The concept of the center of inertia [105] calculates an average frequency from different bus measurements, the power system admittance matrix and parameters of the connected SG and requires communication between the buses and the IBG control. A local frequency measurement is strived for, which is why the center of inertia is not considered in this work.

The Fourier transform converts the time-domain signal into the frequency domain and decomposes it into the constituent frequency components. In [106], the Fourier transform method is implemented for dynamic frequency estimation, but leads to a time delay and therefore is disregarded in this work.

2.5 SUMMARY

Power systems are complex and involve mathematical models to represent their many components. These models simplify the system for analysis purposes. The system state and state variables define the power system model. Normal operation refers to a stable system in steady state, but disturbances can result in a time-varying or dynamic system, leading to transient processes. Disturbances are categorised into small-signal phenomena that can be linearised and large-signal phenomena, where dynamic non-linear processes are investigated.

Power system stability refers to the ability of a power system to regain a stable equilibrium state after experiencing a disturbance. Frequency stability is related to maintaining a constant frequency across the interconnected power system and is crucial for the power system active power balance. The frequency control includes mechanisms on different time scales: Inertial response, primary, secondary and tertiary controls work together to restore the power system frequency after being subjected to a disturbance. For inverter-based plants, the concept of the fast frequency control (FFR) quickly adjusts the active power infeed in response to a frequency deviation.

Frequency estimation in power systems relies on indirect measurements through the evaluation of voltage and current signals. This task becomes particularly challenging during transient processes. A commonly employed technique for estimating three-phase voltage phase and frequency is the phase-locked loop (PLL). This method involves comparing the estimated voltage with the measured voltage. In addition to the PLL, various other frequency estimation methods find application in both simulation and real-world applications. Examples include the zero crossing method, Gauss-Newton method, and the Fourier Transform.

3 INVERTER-BASED GENERATION

Power systems are to become more sustainable and climate-friendly by replacing conventional power plants with renewable ones, e.g. solar and wind generation units. These renewable sources are primarily connected to the grid through power electronics, which are chosen due to the physical and technical characteristics [107]. However, this shift leads to a weakening of the power system [93] due to the increasing presence of voltage-source converter (VSC) based resources, such as IBG, battery storage systems and loads, and due to the loss of mechanical inertia provided by the rotating masses of SG [93, 108]. The transition to low-inertia power systems results in rapid frequency changes following disturbances such as generation outages or significant load events, as described in Chapter 2.3. To address this issue, it is crucial for VSC-based resources to increasingly contribute to power system stability.

IBG, as an active component with various implementations across different voltage levels, gains significant relevance in power system studies. It encompasses both centralised remote generation, such as large offshore and onshore windfarms, as well as decentralised generation like rooftop PV installations and smaller PV plants and windfarms. Power electronic devices are not only used for connecting generation plants to the power system but also for applications such as high-voltage direct current (HVDC) transmission and energy storage. The majority of IBG installations are connected at the distribution grid level [2]. The presence of numerous smaller generation plants at this level requires careful coordination and the design of power systems capable of handling reverse power flows.

In this chapter, basic characteristics of power inverters in IBG applications in distribution grids are shown, model classes for the mathematical representation of inverters in simulations are introduced, control concepts for IBG and grid codes that apply for IBG on distribution grid level are presented.

3.1 BASIC CHARACTERISTICS OF POWER INVERTERS

Basically, the power inverter of IBG converts a direct current (DC) voltage v_{dc} into an AC three-phase voltage v_{abc} with a power flow from the DC to the AC side. On the DC side, an arbitrary energy source - PV, wind or battery storage system - is connected to the AC power system through a full power inverter. In wind turbines, usually a back-to-back converter is used, which consists of a machine-side rectifier and a grid-side inverter. In contrast, PV or battery storage systems that directly supply a DC voltage require a grid-side inverter only. The grid-side inverter and the DC voltage link of an IBG are depicted in Figure 3.1, while the energy-generating system connected to the DC link is not shown. For simplification, a two-level topology is assumed for the grid-side inverter, and the DC link consists of a single DC link capacitor C_{dc} with the DC link voltage V_{dc}. The power flow from the energy source to the AC system is controlled by the DC link voltage V_{dc}, which is increased or decreased by altering the active power injection from the energy source. The grid-side inverter responds to these changes by controlling the DC link voltage V_{dc} and thereby controlling the active power output to the AC system with the three-phase voltage v_{abc} [14, 109].

The DC link serves as an energy storage to the power system whose size is determined by the size of the DC link capacitor C_{dc}. For short-term dynamic studies, this energy storage decouples the grid-side from the side of the energy source [14, 110]. This is why the grid-side inverter and its control determine the dynamic behaviour of IBG during short-term dynamic studies. The specific characteristics of IBG and the energy source side components are less significant in terms of short-term dynamics. For the purposes of this work, when modelling IBG, the focus is on the grid-side converter while simplifying the side of the energy generation. If a fast chopper is used in the DC link, these assumptions apply to large signal disturbances like short circuits or large load disturbances [14]. These simplifications align with current recommendations for modelling IBG, see [111, 112].

Depending on the inverter topology, the DC link of an inverter can either have a central DC link capacitor C_{dc} or be cascaded or modular with distributed cells [113]. The configuration of power semiconductors in the inverter can be in a half-bridge or full-bridge topology. These characteristics result in various circuit topologies, each with its own advantages and disadvantages. Multilevel topologies offer the advantage of generating an output voltage with multiple discrete levels, allowing for low-harmonic reproduction of a sinusoidal voltage reference [114]. This helps reduce or even eliminate the need for AC-side filtering, see [113]. For a more comprehensive overview of common inverter topologies, refer to [102, 113, 115]. As the topology shown in Figure 3.1 is a two-level implementation, additional filtering on the AC side of the IBG is applied. VSC inverters in the MV and HV grid primarily use insulated-gate bipolar transistor (IGBT) semiconductors [113]. In principle, both a power flow from DC to AC side in inverter mode and vice versa in rectifier mode is possible. This work focuses exclusively on three-phase two-level inverters in a half-bridge topology with IGBT as power semiconductors.

The electrical configuration of a three-phase two-level inverter in a half-bridge configuration is shown in Figure 3.1 and consists of the DC link with a DC link voltage V_{dc} and a DC link capacitor C_{dc}, the half-bridge circuit comprising six IGBT switches (S1 to S6) with antiparallel freewheeling diodes (D1 to D6) and an AC-side LCL filter for smoothing and harmonic filtering of the inverter's output voltage v_{abc}. The control part, which is responsible for generating the control signals for the IGBT is not shown here, but is described in Chapter 3.3 and Chapter 6.2. For convenience, the active sign convention is applied to IBG so that the power flow from the IBG to the power system is defined as positive.

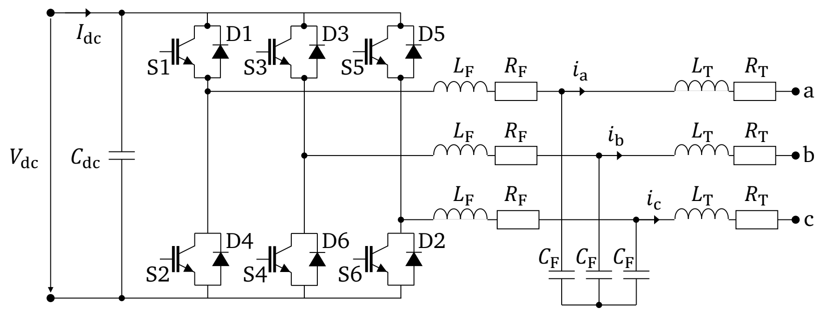

Figure 3.1: Overview of a three-phase two-level inverter in half-bridge configuration, based on [14].

The shape of the AC-side fundamental output voltage v_{abc} of a VSC inverter is achieved by switching between discrete voltage levels using the power semiconductors. The firing pulses for turning on and off each IGBT switch are obtained from a modulation. The carrier-based pulse-width modulation (PWM) compares the sinusoidal reference voltage $v_{abc,ref}$ to a repetitive or carrier waveform $v_{carrier}$ [116]. Figure 3.2 shows an exemplarily PWM using a triangular carrier. The upper switch of each arm is turned on while the lower switch is turned off if the reference voltage $v_{abc,ref}$ is larger than the carrier $v_{carrier}$ and vice versa if the reference voltage $v_{abc,ref}$ is smaller than the carrier $v_{carrier}$. The timing and duration of these pulses determine the output voltage v_{out} and the fundamental component of the output voltage v_{abc} of the inverter. Further modulation techniques are presented in [117, 118]. A detailed description of the functioning of power electronics is provided in [119, 120].

3.2 INVERTER MODEL CLASSES

Modern power systems are dynamic high-order multivariable systems based on numerous components with different characteristics and response rates [85]. As many basic components that have been in use for decades are well understood

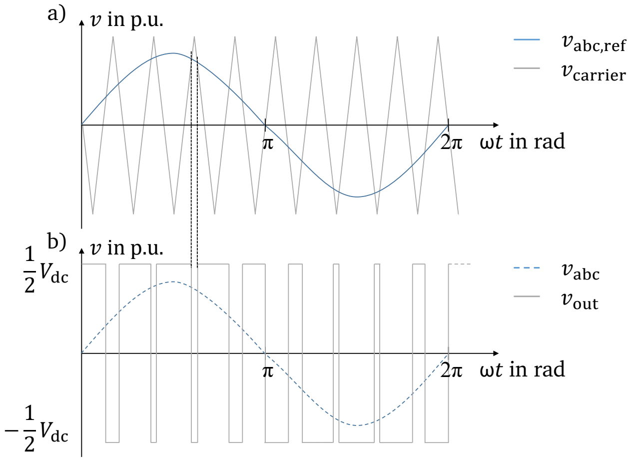

Figure 3.2: Pulse-width modulation (PWM) with triangular carrier based on [118].
a) Comparison of reference voltage $v_{\text{abc,ref}}$ and triangular carrier v_{carrier}.
b) Output voltage v_{out} and fundamental frequency output voltage v_{abc}.

and can be mathematically modelled according to the relevant characteristics [111], this is not yet the case for inverters. Attempts at modelling inverters with the model complexity adjusted to account for the physical phenomena being investigated are made in [111, 121].

Due to the large variety of IBG technologies and manufacturers, a uniform generic representation is widely used in power system studies. These generic IBG models are based on literature and standards. First uniform models are described for wind turbines in [109, 122]. Developments of generic PV systems and wind turbines are presented in [8, 123–125]. Further models are described e.g. in [7, 126] and are available in commercial simulation software.

Mathematical inverter models can be classified according to the level of detail of the inverter model and the study of interest, cf. Table 3.1. The seven inverter model classes are based on [121] and described for HVDC applications, but can be applied to IBG. With increasing model class, the simplifications made in the model increase and the simulation effort decreases. Models of type 1 and type 2 take into account the detailed physical processes of power electronics, e.g. switches and diodes. Type 1 models represent the power electronic switches by differential equations, whereas type 2 models rely on simplified nonlinear models of the switches [121]. The detailed modelling of switches is mainly used for inverter design studies and requires a certain computational burden, which makes them not suitable for power system simulations. Models of type 3 and type 4 simplify the power electronic switches to switchable resistances. The two-value resistors account for the open and closed state of the switches. Additionally, type 4 models reduce multi-level topologies, which are not of interest in this work. The model types using switchable resistances are used in studies on the inner control design of the inverter, DC transient analysis and for validating models of type 5 to type 7. Type 5 and type 6 models are based on an average-value model (AVM) representation, which reduces the switching process through averaged values over time. This assumption allows for the representation as controlled current or voltage sources on the AC and DC side. In type 5 models the sources are modelled with harmonic content, while type 6 models model the fundamental frequency only. AVM are widely used for large-signal power system dynamic studies [111] and the outer control design. Models of type 7 are phasor or root-mean square (RMS) load-flow models for the steady-state analysis.

Table 3.1: Classification of inverter models [121].

CLASS	DESCRIPTION	SIMULATION	TYPICAL STUDIES
Type 1	full physics based model	-	n/a for power systems
Type 2	full detailed model	EMT	inverter design
Type 3	switchable resistances	EMT	inverter analysis
Type 4	as type 3 with aggregation	EMT	control design
Type 5	average value model (AVM)	EMT	control design
Type 6	simplified AVM	RMS/EMT	large power systems
Type 7	RMS load-flow model	load flow	steady-state analysis

There exist two commonly used simulation models for dynamic power system investigations: EMT models and RMS models. While type 1 to type 5 models are implemented in EMT simulations, type 6 models can be either modelled in EMT or RMS. In RMS simulations, further simplifications are applied, e.g. neglecting of the inner control. Even though, studies on the choice of simulation are carried out [111, 127–129], the choice of simulation is not clear for low-inertia power systems with high shares of IBG. Although the increasing number of decentralised IBG must be modelled in a reduced and easy way with low computational burden, the faster dynamics in low-inertia power systems can lead to the need of EMT models. More details about EMT and RMS modelling can be found in [111].

In this work, IBG models of type 6 are modelled. A comparison between RMS and EMT models is given in Chapter 6.4.

3.3 CONTROL CONCEPTS FOR INVERTER-BASED GENERATION

The behaviour of inverters is largely dependent on the applied control. With a switching frequency of the inverters in the kilohertz range and the frequency of some controllers in the single-digit hertz range, the dynamic behaviour of the inverters covers several orders of magnitude. In low-inertia power systems, the fast dynamics in particular gain importance as discussed in Figure 2.4. Since a majority of the inverters in use are four-quadrant controllers that can exchange active and reactive power with the power system very quickly through appropriate control, new forms of grid stabilisation are emerging.

IBG increasingly have to take over control tasks that SG used to perform. However, IBG plants have characteristics that pose challenges for control and power system stabilisation: The short-circuit current contribution is within the order of the rated current [93] because the semiconductors can only be overloaded to a limited extent. In addition, unlike SG, IBG lack inherent inertial behaviour that slows down dynamics. To provide positive control energy, IBG plants must either decrease the power injection during normal operation or be oversized. Both options have a negative impact on the economics of the IBG plants.

3.3.1 *Control Levels*

The classification made in this chapter is based on [14] and divides the IBG control into three levels: The system level includes requirements of the responsible system operator or plant operator and contains the power setpoint as well as voltage and frequency control requirements. Here, the primary control or the FFR is implemented and the system operator can actively intervene in this control during operation. The output of the system level control usually are the active and reactive power setpoints P_{ref}, Q_{ref}. The inverter level control realises a voltage and current control loop to meet the setpoint specifications for active and reactive power [109]. This is done by comparing the power setpoints with the measured power at the point of common coupling (PCC) behind the LCL filter. The grid-side inverter is responsible for the DC voltage control [17, 109], synchronises with the grid and includes further functions, such as fault detection and fault ride-through (FRT) control. The energy source-side converter takes over the control of the primary source infeed, which can include maximum power point tracking (MPPT) or pitch angle control for wind turbines. Figure 3.3 gives an overview of the levels of IBG control. The energy source-side converter can either be a rectifier for wind turbines or a DC-DC converter for PV systems. Finally, the output of the inverter level control, which is the voltage setpoint, is

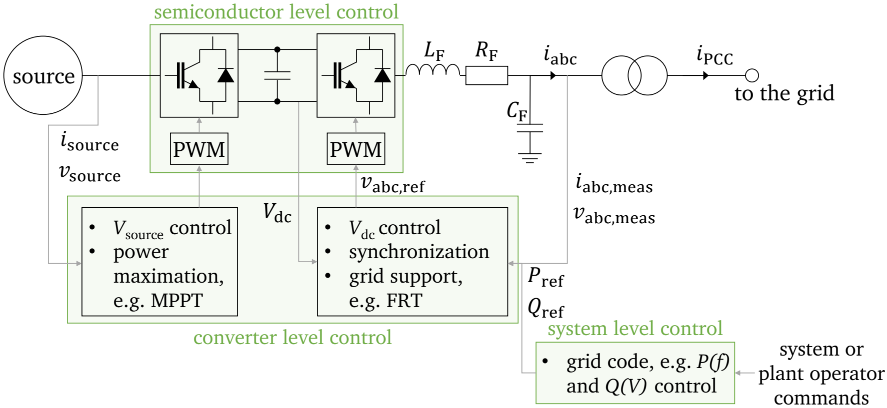

Figure 3.3: Overview of control levels for inverter-based generation.

As the grid-side inverter determines the dynamic behaviour of the IBG, the energy source-side converter as well as the energy source itself are neglected with the following assumptions:

1. The power infeed from the energy source is constant for the time interval of interest.

2. The DC voltage V_{dc} is constant for the time interval of interest.

3.3.2 *Grid-following, grid-supporting and grid-forming control*

Historically, with only small shares of IBG, inverters are controlled using a grid-following also known as grid-feeding concept that supplies the active power generated by the IBG to the grid. Inverters achieve synchronisation with the existing electrical grid by continuously monitoring and adjusting the power infeed to match the voltage and frequency of the grid. These inverters align the output voltage and frequency to be in line with the grid's signals. For this pupose, the active and reactive current fed to the grid is controlled in accordance with the existing grid voltage and a maximum power extraction from the energy source is in focus, e.g. a MPPT control.

Grid-supporting inverters provide additional functionalities beyond the grid-following control. These inverters actively control specific grid parameters. Grid-supporting inverters can control the active and reactive power infeed, thereby contributing to frequency and voltage control, and help mitigate fluctuations in these parameters. The FFR is one example of the additional functionalities. An important characteristic of the grid-supporting control concept is that the inverter continues to be synchronised, usually via a PLL, and the response to a change in the system occurs with a certain time delay. For this reason, the provision of synthetic inertia is not possible with this control concept. However, the IBG control discussed in Chapter 2.3.3 can act much faster than the one of SG. The grid-following and grid-supporting control concepts rely on a stable grid for the voltage and frequency references.

The grid-forming control concept is first implemented in offshore grids and microgrids with the goal to create an own stable grid-like condition and therefore operate in standalone mode or in weak grids. However, the application in parallel operation in interconnected power systems gains interest as the share of IBG increases. Unlike grid-following and grid-supporting inverters, grid-forming inverters can independently establish and maintain the voltage and frequency and thereby actively form the grid voltage. Grid-forming inverters find application in weak-grid scenarios, providing precise control over voltage and frequency to ensure a stable and reliable power supply within the power system. Different definitions of the grid-forming control exist, the most widely applied being the representation as voltage source with internal impedance or the representation as a virtual SG. Both approaches include the ability to indepently form a voltage without the existence of an external voltage signal, while self-synchronising with other voltage sources or SG. In the case of disturbance, the grid-forming control inherently counteracts voltage or frequency deviations by providing short-circuit currents and synthetic inertia. Further details on the control concepts applied in this work are given in Chapter 6.2.

3.4 GRID CODES AND ANCILLARY SERVICES

For the connection of IBG plants to the power system, certain requirements must be met, which are usually given in the grid connection codes. The latter specify the minimum technical requirements all connected power plants must meet to be granted grid access [130]. These requirements include active and reactive power control, voltage and frequency operating ranges, power quality, FRT capability and protection concepts. As an example, overfrequency active power reduction (LFSM-O) is required in many European grid codes [130].

In Germany, the VDE Forum Network Technology/Network Operation (VDE-FNN) provides the minimum technical requirements for the connection of power plants to the low-voltage grid VDE-AR-N 4105 [131], to the medium-voltage grid VDE-AR-N 4110 [132] and to the high-voltage grid VDE-AR-N 4120 [133]. All three grid connection codes distinguish between type-1 generation plants, which are connected to the grid via synchronous generators, and type-2 plants, which include all generating plants that are not of type 1. IBG therefore belong to type-2 plants.

An important aspect of the grid connection codes in the context of this work is the adaptation of the active power output during over- and underfrequency events. In case of a frequency deviation $\Delta f > 200$ mHz from the nominal frequency f_n, all generation units must contribute to the frequency support and ride through rapid frequency changes up to a RoCoF $= 2$ Hz/s for a 500 ms moving time window without disconnecting from the grid. If the system operator does not specify otherwise, the generation plants must be able to adjust the active power operating point at overfrequency starting from 50.2 Hz. The droop of the frequency-dependent active power feed-in $d = \frac{\Delta f}{f_\mathrm{n}} / \frac{\Delta P}{P_\mathrm{ref}}$ must be adjustable between 2 % and 12 %. This corresponds to a power-frequency $(P - f)$ droop of $0.167 \cdot P_\mathrm{ref}/\mathrm{Hz}$ $(d = 12\ \%)$ to $1 \cdot P_\mathrm{ref}/\mathrm{Hz}$ $(d = 2\ \%)$ for a nominal frequency $f_\mathrm{n} = 50$ Hz. If the system operator does not specify otherwise, a gradient of $d = 5$ % is to be set. Above 51.5 Hz, the generating plants may disconnect from the grid for reasons of self-protection.

During underfrequency events, a deficit of generation power is opposed to a surplus of load. During underfrequency, generating plants must not reduce the reference active power output for frequency curves in the dynamic short-term range between 50 Hz and the curve shown in Figure 3.4. Within the green area in Figure 3.4, the active power output of the IBG must not be reduced. In addition, generation plants must be able to adjust the active power operating point if the frequency drops below 49.8 Hz.

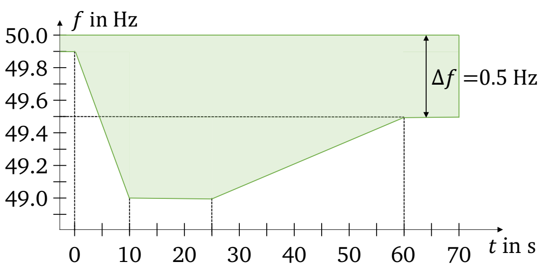

Figure 3.4: Requirement on the frequency ride-through of generating plants during underfrequency events, based on [132].

As for the overfrequency scenarios, the droop of the frequency-dependent active power feed-in must be adjustable from 2 % to 12 %. As discussed in Chapter 3.3, the underfrequency scenario is the more critical for IBG as the additional active power infeed requires overdimensioning of the inverter or additional storage solutions. Therefore, the maximum value of additional power output is determined by the available primary energy supply and the currently usable storage capacity. At grid frequencies $f < 47.5$ Hz, the generation plants are allowed to disconnect from the grid.

The German grid connection codes for the connection of power plants to the distribution grid do not (yet) consider FFR control. However, FFR is included in the German grid connection code for HVDC VDE-AR-N-4131 [134] and in other countries' grid codes, e.g. in UK, Ireland or Australia. Further updates of grid codes can include the provision of synthetic inertia or grid-forming behaviour of IBG. In Germany, the grid connection code for HVDC [134] includes a supplement for grid-forming behaviour. An overview of FFR requirements in international grid codes is given in Table 3.2. The constant additional active power infeed is considered in these examples as described in Figure 2.5. The frequency deadband specifies the starting signal of the FFR. The additional active power infeed ΔP begins after the time delay T_{delay} at the latest and is kept for the time duration T_{dur}.

Table 3.2: International grid codes including fast-frequency response (FFR), based on [97].

Country	deadband	ΔP	T_{delay}	T_{dur}
Australia	± 50...150 mHz	N/A	0.5...1 s	6 s
Ireland dynamic FFR	± 15...200 mHz	1...5 MW	2 s	8...10 s
Ireland static FFR	± 200...700 mHz	1...75 MW	2 s	8...10 s
United Kingdom	± 15...50 mHz	1...50 MW	1 s	15 min

3.5 SUMMARY

Power inverters play a crucial role in converting DC voltage from sources like photovoltaic panels, wind turbines and battery storage systems into three-phase AC voltage for grid connection. The DC link serves as short-term energy storage and decouples the grid-side from the energy source side during dynamic studies.

Modelling inverters for power system studies requires careful choice of the necessary degree of detail and can be divided into different model classes. The range covers detailed physical models (model class 1) to average-value models (class 5/6), which simplify the power-electronic switches to reduce the computational burden and load-flow models (class 7). The selection of the model class remains a topic of ongoing discussion in low-inertia systems.

The dynamic behaviour of Inverter-Based Generation Plants is highly dependent on the applied control. Different control levels can be distinguished on system level, converter level and semiconductor level. Only the grid-side converter of generation plants is considered in this work as it mainly determines the dynamic behaviour for system studies. Inverter-based generation plants can adapt their active power as a response to a frequency deviation much faster than conventional power plants. This fast-frequency response is already implemented in grid codes for countries with low inertia. In Germany, an active power-frequency droop must be adjustable between 2 % and 12 % in order to counteract frequency deviations.

4 DYNAMIC SYSTEM EQUIVALENTS

The deployment of distributed IBG in the power system brings new challenges in terms of transitioning from passive to active distribution grids [135]. While historically, large SG contributed to power system stability in a top-down hierarchy, volatile IBG and the control of associated power electronics need to increasingly provide ancillary services to the system on distribution grid level. Studies on the impact of IBG and their control concepts on power system stability are mainly carried out in simulation software. Three categories of investigations can be defined:

1. Islanded microgrid investigations without connection to the interconnected power system, e.g. [36, 136].
2. Investigations on distribution system level in interconnected power systems, e.g. [137, 138].
3. Investigations on transmission system level with aggregated distribution systems, e.g. [139–142].

In microgrid investigations, the entire system can be modelled in detail as it inherently consists only of a limited quantity of components. Recent research investigates the transition between islanded mode and interconnected mode. In contrast, for investigations in interconnected grids, only the part of the system that is of interest, i.e. the internal part can be modelled in detail. The external part must be reduced to keep the simulation effort reasonable and to deal with a possible lack of available data. The third case investigates the impact of IBG on the transmission system and requires a reduced order model of the underlying distribution grids, which can be done in aggregation models.

This study focuses on the second type of investigation with the active distribution grid being of interest. As power systems belong to the critical infrastructure, detailed data is usually not provided by the system operators. In addition, modern distribution systems and the detailed mathematical models have enormous system dimension, which leads to a large computational effort and long simulation time. Thus, the simulation effort must be reduced to a computationally feasible size. Due to the complexity and interconnectivity of power systems, for most investigations the part of the system that is not the focus is replaced by an equivalent reduced-order model. Those equivalents represent a compromise between computation effort and accuracy.

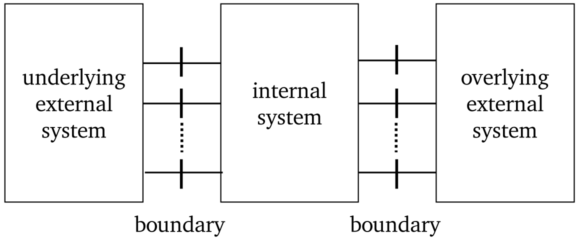

Figure 4.1: Schematic of the internal and external system for studies on the medium-voltage and high-voltage level.

In general, reduced-order models can be derived horizontally, i.e. neigbouring grids on the same voltage level are reduced, or vertically, if the underlying or overlying voltage level is to be reduced. Figure 4.1 shows the three parts for a vertical aggregation when studying medium-voltage and high-voltage grids. Since e.g. the medium-voltage grid is connected to the underlying low-voltage grid and to the overlying high-voltage grid, two external systems are defined. The external systems are connected to the internal system via tie lines. The external system model needs to provide a good approximation of the real system at the boundary while keeping the simulation effort low. Different steady-state and dynamic external system modelling approaches have been developed, e.g. the Ward [143], Zhukov [76] or radial equivalent independent (REI) method [144, 145]. An overview is given in [146] for load flow applications using steady-state equivalents and in [147] for dynamic equivalents.

According to [67] dynamic network equivalents should have the following properties:

1. The aggregation model is capable of reproducing discrete events and large disturbances in the system.

2. When the operating point of the system changes with respect to the load and the control of the IBG, the update in the aggregation model should be simple.

3. The aggregation model can be used in a wide range of operating conditions.

4.1 OVERVIEW OF DYNAMIC AGGREGATION APPROACHES

In accordance with [14, 148, 149], two main approaches for the dynamic aggregation of active distribution grids can be defined, namely the analytical and the measured value-based approaches, cf. Figure 4.2. The analytical or whitebox approach requires the knowledge of the entire data of the power system to be reduced. To reduce the passive components, network theory is applied on the basis of the admittance matrix. The active components can be reduced by modal analysis [52] or by the coherency criterion [145, 150]. The approach using modal analysis uses a linearised state space model of the network whose eigenvalues are to be identified [148]. Coherent generators can be combined by an equivalent machine in case they have a comparable oscillation behaviour following the disturbance [147, 148].

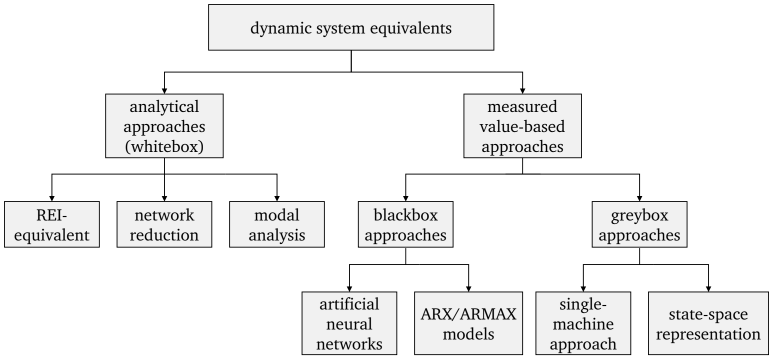

Figure 4.2: Overview of dynamic system equivalents based on [148].

Measured value-based approaches use the measurement or simulation data at the boundary between internal and external system. For this purpose, a suitable model structure is to be selected first, so that the dynamic behaviour of the original detailed system can be reproduced. Then, the appropriate parameters can be optimised until the difference between the measured or simulated data of the aggregated and the real detailed grid is minimal. Finally, the model structure and parameters are checked whether they can reconstruct various dynamic processes of the detailed system model. The selection of the model structure and the determination of parameters are called as identification process according to [148]. For this purpose, two approaches namely the greybox and the blackbox approach exist in practice. The main difference between those approaches is that the blackbox approach assumes that no relevant data of the system to be reduced is available except for the measurement at the boundaries, while the greybox approach assumes the availability of limited data such as a rough estimate of the installed load and generation power.

For the blackbox approach neither model structures nor parameters are known, so that they are determined by the identification process. The known methods in practice are approaches based on generalised input-output functions and approaches based on artificial neural networks [147, 148]. This approach is not considered further here, as the basic model structure of power systems, e.g. lines, transformers, loads, is known and the corresponding parameters are to be investigated.

The single-machine approach is chosen in this work and described in more detail in the next section.

4.2 AGGREGATION OF OVERLYING EXTERNAL GRID

For the investigation of active interconnected distribution grids, the overlying external grid, which is the system on the next higher voltage level, needs to be reduced, cf. Figure 4.1. In dynamic studies focusing on voltage stability, e.g. FRT of power plants, a generic overlying external grid model consisting of a voltage source in series with an internal impedance and constant frequency can be found, e.g. in [138, 151]. This model offers a basic solution for the studies mentioned, but cannot be used for frequency studies in the time domain as the voltage source uses a constant frequency. Instead, either a synthetic frequency curve or a synthetic phase jump can be applied to the voltage source, so that the reaction of the system to the frequency change can be investigated or a SG or a grid-forming IBG is modelled to replicate the grid-forming behaviour of the overlying external grid. In this work, a SG is modelled and different future scenarios are developed by adapting the parametrisation of the machine and control model.

For the overlying external grid, it is assumed that there are still SG or other grid-forming units, which provide the inertia and control tasks of SG to the grid. Thus, the dynamics of the overlying external grid are mainly defined by the short-circuit power S''_{SC}, the inertia constant H and the governor droop d_{Gov}. A derivation of the aggregated model based on the single-machine approach is given in Chapter 5.2.

4.3 GREYBOX AGGREGATION

The greybox approach uses prior knowledge of the power system to be aggregated to select the model structure and the optimisation algorithm to determine the model parameters. An overview of the greybox approach procedure is given in Figure 4.3. First, the structure of the equivalent model is selected. Thereafter, the objective function for determining the model parameters can be chosen. Usually, the objective function corresponds to a least-square minimisation problem [152]. During the optimisation, the dynamic responses of the original and the aggregated model are compared and the corresponding objective function $\epsilon(x)$ as the difference or error between the measurements of the original and the aggregated grid is calculated. The optimisation algorithms presented in Chapter 4.3.1 and 4.3.2 initialise the model parameters and then iteratively search for the best solution respectively for the minimum objective function. Finally, the parametrised dynamic equivalent model is tested for different operating points to verify its robustness. According to [14], the following three variants of the greybox approach are to be distinguished:

1. State-space model of a parallel load and IBG, e.g. [64, 148].
2. Single-machine approach, e.g. [67, 153, 154].
3. Further development of the exponential recovery model, e.g. [58, 61].

The technique based on state-space models uses the parallel connection of a composite load and a composite generation plant, the latter being modelled as a SG and a parallel IBG. The state-space model consists of a linear and a nonlinear part, which allows the direct application of optimisers such as Levenberg-Marquardt algorithm. As a disadvantage for this method, the control of the grid-side inverter is not considered. In addition, modelling the nonlinear behaviour of current limiters is complex.

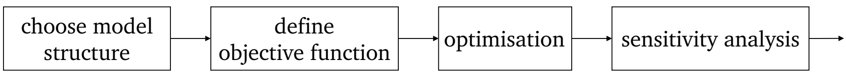

Figure 4.3: Schematic process of the greybox aggregation, based on [14].

In the single-machine approach, loads and IBG are combined into an equivalent load and IBG. This dynamic equivalent uses the detailed model of the corresponding components, in this case the load and the IBG. Thus it is possible to study the control and grid support of IBG in active distribution grids in detail. However, the disadvantage of this approach is that the objective function is not mathematically differentiable, so the use of optimisation methods is required as described in Chapter 4.3.1 and 4.3.2.

The last approach is the further development of the exponential recovery model according to [14]. This approach uses variable order transfer functions parameterised with vector fitting. While this approach has a generalised model structure that allows for studies of different controlled components, it is highly dependent on the operating point. Another disadvantage is that the nonlinear and discrete behaviour of the converter control is not accurately reproduced.

Due to the above reasons, a single-machine approach is chosen, which requires metaheuristic and derivative-free optimisation methods to find the near-optimal solution to the problem or objective function. This is due to the fact that the objective function of minimising the least-square minimisation problem in this approach is not differentiable and thus cannot be mathematically solved [152]. A metaheuristic optimisation algorithm is a general approach to solving optimisation problems. It is designed to be flexible and adaptable, and can be applied to a wide range of optimisation problems in different domains. It is often used when the optimisation problem to be solved is too complex or too difficult to solve using traditional mathematical optimisation methods. It is particularly effective for problems with multiple large or complex search spaces [155].

Metaheuristic algorithms including the evolutionary algorithm (EA), the differential evolution (DE) algorithm, and the particle swarm optimisation (PSO) are proposed for various real-world applications. In [156], these three optimisation methods are studied and compared in numerical benchmark problems. The DE algorithm is robust, easy to implement and converges relatively fast. Moreover, the PSO algorithm is typically the fastest in terms of convergence speed [157], while the EA algorithm is slowest. For this reason, the focus is on the use of the algorithms DE and PSO. In the following, these are described in detail.

4.3.1 *Particle Swarm Optimisation*

The PSO was introduced by Kennedy and Eberhart in 1995 and is inspired by the social behaviour of a swarm of birds or fishes [158]. This algorithm uses a simplified model of social behaviour to solve optimisation problems with the use of cooperative collaboration among individuals. Moreover, PSO is easy to implement, requires little memory and finds the optimal solution quickly [157]. The application of this algorithm in terms of power system such as coordination of relay protection and power management is described in [159].

According to [156], PSO principally consists of a swarm of particles or a population POP moving in a D dimensional real-value search space with possible solutions to the problem. Each particle has a position vector $\boldsymbol{x_{l,IT}}$, which has a proposed possible solution to the minimisation problem, and a velocity vector $\boldsymbol{v_{l,IT}}$. In addition, each particle has information about its own best position $\boldsymbol{p_{l,IT}}$ and a global best position $\boldsymbol{g_{IT}}$ obtained by communicating with neighboring particles. The indices IT and l refer to the iteration and particle number.

First, the parameter vector $\boldsymbol{x} = x_{1...D}$ to be optimised in each particle must be initialised within the given boundaries according to (4.1). The lower and upper limits x_k^{L}, x_k^{U} are chosen individually for each parameter $k \in [1,\ D]$. The parameter vector $\boldsymbol{x}$ of each particle $l \in [1,\ POP]$ and within each iteration IT must meet this condition. Moreover, in PSO the velocity $\boldsymbol{v}$ is limited to the bounds $[-\boldsymbol{v}_{\mathbf{max}}, \boldsymbol{v}_{\mathbf{max}}]$ given in [160] at which the particle is allowed to move maximally between two iterations IT and $IT+1$. The maximum velocity $\boldsymbol{v}_{\mathbf{max}}$ can be calculated for each parameter k by the difference of the upper and lower parameter limits $\boldsymbol{x}^{\mathbf{U}}$ and $\boldsymbol{x}^{\mathbf{L}}$ according to (4.2).

$$x_k^{\mathrm{L}} \leq x_{k,l,IT} \leq x_k^{\mathrm{U}} \tag{4.1}$$

$$\boldsymbol{v}_{\mathbf{max}} = v_{\max,k=1\ldots D} = 0.2 \cdot \left(\boldsymbol{x}^{\mathbf{U}} - \boldsymbol{x}^{\mathbf{L}}\right) \tag{4.2}$$

At each new iteration $IT+1$, the velocity vector $\boldsymbol{v}_{\boldsymbol{l},\boldsymbol{IT}+\mathbf{1}}$ is recalculated according to (4.3). Thus, the particle moves to a new position $\boldsymbol{x}_{\boldsymbol{l},\boldsymbol{IT}+\mathbf{1}}$, which is the sum of the previous position $\boldsymbol{x}_{\boldsymbol{l},\boldsymbol{IT}}$ and the new velocity $\boldsymbol{v}_{\boldsymbol{l},\boldsymbol{IT}+\mathbf{1}}$ according to (4.4).

$$\boldsymbol{v}_{\boldsymbol{l},\boldsymbol{IT}+\mathbf{1}} = w \cdot \boldsymbol{v}_{\boldsymbol{l},\boldsymbol{IT}} + r_1 \cdot c_1 \cdot \left(\boldsymbol{p}_{\boldsymbol{l},\boldsymbol{IT}} - \boldsymbol{x}_{\boldsymbol{l},\boldsymbol{IT}}\right) + r_2 \cdot c_2 \cdot \left(\boldsymbol{g}_{\boldsymbol{IT}} - \boldsymbol{x}_{\boldsymbol{l},\boldsymbol{IT}}\right) \tag{4.3}$$

$$\boldsymbol{x}_{\boldsymbol{l},\boldsymbol{IT}+\mathbf{1}} = \boldsymbol{x}_{\boldsymbol{l},\boldsymbol{IT}} + \boldsymbol{v}_{\boldsymbol{l},\boldsymbol{IT}+\mathbf{1}} \tag{4.4}$$

The inertia weight factor w is used to control the amplitude of the old velocity $\boldsymbol{v}_{\boldsymbol{l},\boldsymbol{IT}}$ when calculating the new velocity $\boldsymbol{v}_{\boldsymbol{l},\boldsymbol{IT}+\mathbf{1}}$. Moreover, r_1 and r_2 are uniformly distributed random numbers between 0 and 1. The coefficients c_1 and c_2 are called acceleration coefficients and determine the importance of the particle's best position $\boldsymbol{p}_{\boldsymbol{l},\boldsymbol{IT}}$ and global best position $\boldsymbol{g}_{\boldsymbol{IT}}$ in the computation [156].

In 2002, the ability of the PSO in finding the optimal solution to a problem is increased in [161]. The analysis derives modifications to the PSO algorithm that incorporate a set of constriction coefficients χ according to 4.5. To improve the convergence tendencies of the system, Φ, Φ_1 and Φ_2 are chosen so that it holds (4.6) with $\kappa = 1$ and $\Phi_1 = \Phi_2 = 2.05$.

$$\chi = \frac{2 \cdot \kappa}{2 - \Phi - \sqrt{\Phi^2 - 4 \cdot \Phi}} \tag{4.5}$$

$$\Phi = \Phi_1 + \Phi_2 > 4 \tag{4.6}$$

Thus, the inertia weight factor w and the acceleration coefficients c_1 and c_2 can be calculated by (4.7) to get the optimal result from the optimisation.

$$w = \chi, \qquad c_1 = \chi \cdot \Phi_1, \qquad c_2 = \chi \cdot \Phi_2 \tag{4.7}$$

4.3.2 *Differential Evolution Algorithm*

The DE algorithm was introduced in 1997 by Rainer Storn and Kenneth Price [162] and is a population-based search method based on an evolution process. In [163], the DE algorithm is further used for various optimisation problems related to power systems such as congestion management, power flow optimisation, and reactive power scheduling. As for the PSO, a parameter vector $\boldsymbol{x}$ is optimised for each particle of the population $l \in [1 \quad POP]$ within each iteration IT.

The DE algorithm consists of four steps according to Figure 4.4, namely the initialisation, the mutation, the crossover and the selection, and can be summarised as follows: The parameter vector to be optimised or target vector $\boldsymbol{x}_{l,IT}$ is initialised $\boldsymbol{x}_{l,0}$ and evaluated based on the provided objective function $\epsilon(\boldsymbol{x})$. For each target vector $\boldsymbol{x}_{l,IT}$ in the population, a trial vector $\boldsymbol{u}_{l,IT+1}$ is generated during the mutation and crossover step. The trial vector $\boldsymbol{u}_{l,IT+1}$ replaces the parent target vector $\boldsymbol{x}_{l,IT}$ if it yields a smaller objective function $\epsilon(\boldsymbol{x})$ in the selection step. Otherwise, the parent target vector $\boldsymbol{x}_{l,IT}$ survives and is passed to the next iteration $IT + 1$ of the algorithm. This whole process is executed until the termination criterion is met or the maximum number of iterations is reached. Finally, the parameter vector $\boldsymbol{x}$ with the smallest objective function $\epsilon(\boldsymbol{x})$ is returned as the solution. The following sections describe the four steps of the DE algorithm in more detail.

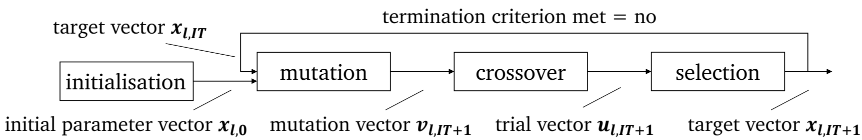

Figure 4.4: Overview of the differential evolution algorithm.

4.3.2.1 *Initialisation*

During the initialisation step, the first parameter vector for each particle of the population $\boldsymbol{x}_{l,0}$ is defined randomly according to the uniform probability distribution. The parameters of the initialisation vector $\boldsymbol{x}_{l,0}$ as well as any target vector $\boldsymbol{x}_{l,IT}$ are limited within the given lower and upper boundary $\boldsymbol{x}^{\mathbf{L}}$ and $\boldsymbol{x}^{\mathbf{U}}$, cf. (4.8).

$$\boldsymbol{x}^{\mathrm{L}} \leq \boldsymbol{x}_{l,IT} \leq \boldsymbol{x}^{\mathrm{U}} \tag{4.8}$$

4.3.2.2 *Mutation*

The mutation step is used to extend the search space of the algorithm. The corresponding donor or mutation vector $\boldsymbol{v}_{l,IT+1}$ can be calculated according to (4.9). Therefore, for each target vector $\boldsymbol{x}_{l,IT}$, three different parameter vectors $\boldsymbol{x}_{\mathbf{rand1},IT}$, $\boldsymbol{x}_{\mathbf{rand2},IT}$, $\boldsymbol{x}_{\mathbf{rand3},IT}$ are randomly selected from the existing population such that the integer indices l, rand1, rand2, and rand3 are different from each other. This is the reason why the population size POP must be at least four to compute the corresponding mutation vector. Ideally, POP lies in the interval $[5 \cdot D \ \ 10 \cdot D]$ according to [162]. In (4.9), the parameter vector $\boldsymbol{x}_{\mathbf{rand1},\boldsymbol{IT}}$ is added to the weighted difference of the two vectors $\boldsymbol{x}_{\mathbf{rand2},\boldsymbol{IT}}$ and $\boldsymbol{x}_{\mathbf{rand3},\boldsymbol{IT}}$. According to [162], the scaling factor F is a real factor $\in [0 \ \ 2]$ and sets the gain of the weighted difference. In the context of this work, the mutation factor F is randomly generated in the range $[0.5 \ \ 1]$ at each new iteration so that the convergence can be significantly improved.

$$\boldsymbol{v}_{\boldsymbol{l},\boldsymbol{IT}+\mathbf{1}} = \boldsymbol{x}_{\mathbf{rand1},\boldsymbol{IT}} + F \cdot \left(\boldsymbol{x}_{\mathbf{rand2},\boldsymbol{IT}} - \boldsymbol{x}_{\mathbf{rand3},\boldsymbol{IT}}\right) \tag{4.9}$$

4.3.2.3 *Crossover*

The crossover step allows combining the elements of the target vector $\boldsymbol{x}_{\boldsymbol{l},\boldsymbol{IT}}$ and the mutation vector $\boldsymbol{v}_{\boldsymbol{l},\boldsymbol{IT}+\mathbf{1}}$. At the end of this step, the trial vector $\boldsymbol{u}_{\boldsymbol{l},\boldsymbol{IT}+\mathbf{1}}$ is obtained. The crossover increases the variety of the perturbed target vector in the next iteration. Establishing each element in the trial vector $\boldsymbol{u}_{\boldsymbol{l},\boldsymbol{IT}+\mathbf{1}}$ from its parent vector $\boldsymbol{x}_{\boldsymbol{l},\boldsymbol{IT}}$ and the mutation vector $\boldsymbol{v}_{\boldsymbol{l},\boldsymbol{IT}+\mathbf{1}}$ is realised by the following specification:

$$u_{k,l,IT+1} = \begin{cases} v_{k,l,IT+1} & \text{if } \mathrm{rand}_{k,l} \leq CR \text{ or } k = \delta \\ x_{k,l,IT} & \text{if } \mathrm{rand}_{k,l} > CR \text{ or } k \neq \delta \end{cases} \tag{4.10}$$
$$k = 1, 2, 3, ..., D; l = 1, 2, 3, ..., IT$$

The elements of the mutation vector are included in the trial vector with the crossover probability CR. In accordance with [162], the crossover probability CR is in the range $[0 \ \ 1]$. In this work, the crossover probability CR is chosen to be in the range $[0.9 \ \ 1]$, as it leads to better results according to [164]. The random number $\mathrm{rand}_{k,l} \in [0 \ \ 1]$ is randomly chosen. The constant δ is a random integer in the range $[1 \ \ D]$ and ensures that the trial vector $\boldsymbol{u}_{\boldsymbol{l},\boldsymbol{IT}+\mathbf{1}}$ receives at least one element from the target vector $\boldsymbol{x}_{\boldsymbol{l},\boldsymbol{IT}}$ [162].

4.3.2.4 *Selection*

In the last step of the DE algorithm, the trial vector $\boldsymbol{u}_{\boldsymbol{l},\boldsymbol{IT}+\mathbf{1}}$ is evaluated with the target vector $\boldsymbol{x}_{\boldsymbol{l},\boldsymbol{IT}}$ using the objective function $\epsilon(\boldsymbol{x})$. If the trial vector $\boldsymbol{u}_{\boldsymbol{l},\boldsymbol{IT}+\mathbf{1}}$ has a smaller objective function value than the previous iteration, it is passed to the next iteration. Otherwise, the old target vector $\boldsymbol{x}_{\boldsymbol{l},\boldsymbol{IT}}$ is kept in the next iteration. The selection process can be formulated mathematically using (4.11).

$$\boldsymbol{x}_{\boldsymbol{l},\boldsymbol{IT}+\mathbf{1}} = \begin{cases} \boldsymbol{v}_{\boldsymbol{l},\boldsymbol{IT}+\mathbf{1}} & \text{if } \epsilon(\boldsymbol{v}_{\boldsymbol{l},\boldsymbol{IT}+\mathbf{1}}) \leq \epsilon(\boldsymbol{x}_{\boldsymbol{l},\boldsymbol{IT}}) \\ \boldsymbol{x}_{\boldsymbol{l},\boldsymbol{IT}} & \text{if } \epsilon(\boldsymbol{v}_{\boldsymbol{l},\boldsymbol{IT}+\mathbf{1}}) > \epsilon(\boldsymbol{x}_{\boldsymbol{l},\boldsymbol{IT}}) \end{cases} \tag{4.11}$$
$$l = 1, 2, 3, ..., POP$$

The DE algorithm described above is specified as the variant DE/rand/1/bin. This means that the vector $x_{\mathbf{rand1},IT}$ from (4.9) is chosen randomly (*rand*) and is implemented using a difference of two vectors (1). The binomial crossover (*bin*) generates the trial vector $u_{l,IT+1}$ from its parent vector $x_{l,IT}$ and its mutation vector $v_{l,IT+1}$. Further variants are described in the next section.

4.3.2.5 *Variants of the Differential Evolution Algorithm*

Two different variants of the DE algorithm are considered in this work in accordance with [162]. The variants differ in the number of vector differences used to calculate the mutation vector and the choice of the mutation vector. The first variant DE/rand/1/bin is described in the previous section. Here, the variant DE/best/2/bin is presented.

The variant DE/best/2/bin differs from the description in the previous sections in that two vector differences are considered to calculate the mutation vector $v_{l,IT+1}^{DE/best/2/bin}$. The use of two vector differences leads to the improvement of population diversity if the population size POP is sufficiently large. Additionally, the vector to be mutated $x_{\mathbf{best},IT}$ is based on the vector with the best objective function $\epsilon(x)$ from the previous iteration. Thus, (4.9) is replaced by (4.12).

$$v_{l,IT+1}^{DE/best/2/bin} = x_{\mathbf{best},IT} + F \cdot \left(x_{\mathbf{rand1},IT} + x_{\mathbf{rand2},IT} - x_{\mathbf{rand3},IT} - x_{\mathbf{rand4},IT}\right) \quad (4.12)$$

4.4 SUMMARY

Dynamic system equivalents summarise the part of the power system that is not in focus resulting in a simplified yet accurate representation of the power system dynamics of this external grid. Different approaches exist, namely the whitebox, i.e. analytical approach as well as the greybox and blackbox approach, which rely on measurements at the boundary between internal and external grid. The greybox aggregation based on a single-machine approach summarises similar components of a given power system in a single component of the same type. The dynamic course of the quantity of interest, e.g. the frequency of the aggregation model is compared against the course of the detailed model and a least-square approach is applied. The particle swarm and the differential evolution algorithms are implemented to find the global minimum of the optimisation problem. The particle-swarm optimisation is inspired by the social behaviour of birds and fish, where individuals (particles) in a swarm move through the search space based on their own experience and that of their neighbors. The differential evolution, on the other hand, mimics the process of natural selection and survival of the fittest, employing a population-based approach where individuals (vectors) evolve through mutation, crossover, and selection.

Part II

MODELLING OF ACTIVE DISTRIBUTION GRIDS

The statistician George E.P. Box famously said, "All models are wrong, but some are useful". This is not only true for statistics, but also for modelling the very complex power system. The models presented here are simplifications of the real world and implement state-of-the-art modelling approaches for dynamic power system simulations.

5 DYNAMIC MODELLING OF GRID COMPONENTS

Dynamic modelling of grid components plays a crucial role in power system simulations, enabling engineers and researchers to study and analyse the complex behaviour of power systems. These models provide valuable insights into the dynamic response of grid components, such as generators, transformers, lines and loads, and help in assessing system stability, transient performance, and fault analysis. As for the power system simulation models in general, dynamic grid components are modelled in a reduced or simplified way and take into account only the basic mathematical relations necessary for the individual study as described in Chapter 2.1. The dynamic behaviour of active distribution grids is mainly determined by its active components. These include SG, frequency-dependent loads and IBG. These components significantly impact the dynamic response of the active distribution grid. For testing purposes of the individual components, a medium-voltage testbench is introduced in Chapter 5.1. Subsequently, the models for the SG and load are described in Chapter 5.2 and Chapter 5.3.

For convenience, all loads are considered in the consumer-oriented or passive sign convention and generation plants in the generation-oriented or active sign convention. This means that both the power fed in from generation plants and the power consumed in loads are shown as positive values.

5.1 GENERIC MEDIUM-VOLTAGE TESTBENCH

The medium-voltage testbench for testing of the individual components is presented in Figure 5.1. The model consists of an IBG implemented as a full-size power converter as shown in Figure 3.3 and connected through a switch S1 to busbar BB1. A load L1 is also connected to busbar BB1. A SG with a parallel load L0 that takes into account the overlying interconnected power system is connected to busbar BB0. The two busbars are connected via a variable line with the line impedance $\underline{Z}_{\text{line}}$. The line models the electrical distance between the external grid at busbar BB0 and the internal grid at busbar BB1.

A disturbance in the form of a loadstep in the static load L0 is applied to the system, resulting in an active power mismatch and a dynamic underfrequency course, which is evaluated. The frequency estimation is done using a PLL based on a voltage measurement at busbar BB1 for testing purposes. The rated power and nominal voltage of the testbench components are given in Table 5.1. For

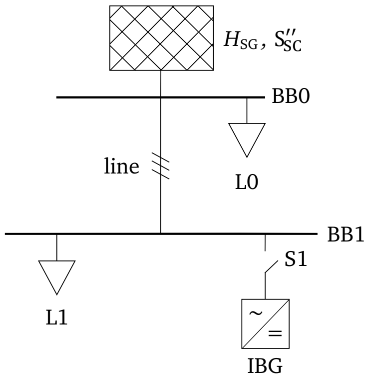

Figure 5.1: Overview on the generic medium-voltage testbench.

the investigations in this chapter, the switch S1 is open and only the dynamic behaviour of SG and load is investigated. The modelling of the IBG is described in Chapter 6.

Table 5.1: Parameters of the generic medium-voltage testbench.

parameter		default
nominal voltage	V_n	20 kV
SG rated power	$S_{r,SG}$	30 MVA
SG inertia constant	H_{SG}	6.5 s
load L0 apparent power	S_{L0}	8 MVA
load L0 power factor	$\cos\varphi_{L0}$	1
loadstep of load L0	ΔP_{L0}	5 MW
IBG rated power	$S_{r,VSC}$	3 MVA
load L1 apparent power	S_{L1}	5 MVA
load L1 power factor	$\cos\varphi_{L1}$	1

5.2 synchronous generator model

The model of the overlying external system used for the external MV, HV and UHV grid model for short-term frequency investigations is based on a sixth-order SG. The adaptation of the generator to emulate an external grid is done by modifying the parameters of the machine and its control. For this reason, the basic mathematical model used to implement the SG is shown here. The model is based on the SG's subtransient and transient electromotive force (emf) E, the corresponding time constants T and reactances X. The equivalent circuit is shown in Figure 5.2. For convenience, resistances R are neglected in this chapter. X_d, X_q, $X_\mathrm{d}^{'}$, $X_\mathrm{q}^{'}$, $X_\mathrm{d}^{''}$, $X_\mathrm{q}^{''}$ are the synchronous, transient and subtransient

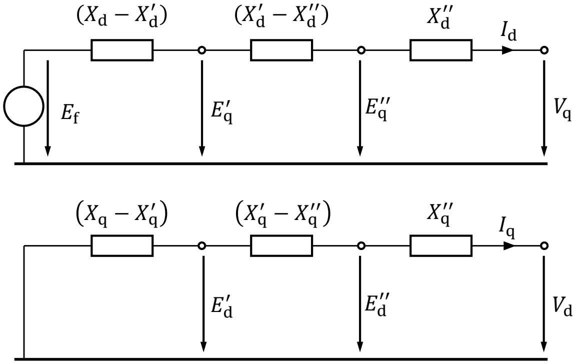

Figure 5.2: Equivalent circuit of the synchronous generator (SG) in d axis and q axis, based on [76].

reactances in d and q axis. E_f, $E_\mathrm{d}^{'}$, $E_\mathrm{q}^{'}$, $E_\mathrm{d}^{''}$, $E_\mathrm{q}^{''}$ are the field excitation emf, the transient and subtransient emf in d and q axis respectively and V_d, V_q and I_d, I_q are the d and q axis components of the generator terminal voltage and the armature current.

The sixth order SG model consists of four electrical and two mechanical states. The electrical states described in (5.1) to (5.4) take into account the armature flux that gradually enters the rotor during a fault and for this reason affects the emf. The mechanical states given in (5.5) and (5.6) describe the generator rotor swing. A detailed derivation of the equivalent circuit and the differential equations is given in [76].

$$T_\mathrm{d0}^{''} \cdot \frac{\mathrm{d}E_\mathrm{q}^{''}}{\mathrm{d}t} = E_\mathrm{q}^{'} - E_\mathrm{q}^{''} + I_\mathrm{d} \cdot (X_\mathrm{d}^{'} - X_\mathrm{d}^{''}) \tag{5.1}$$

$$T_\mathrm{q0}^{''} \cdot \frac{\mathrm{d}E_\mathrm{d}^{''}}{\mathrm{d}t} = E_\mathrm{d}^{'} - E_\mathrm{d}^{''} - I_\mathrm{q} \cdot (X_\mathrm{q}^{'} - X_\mathrm{q}^{''}) \tag{5.2}$$

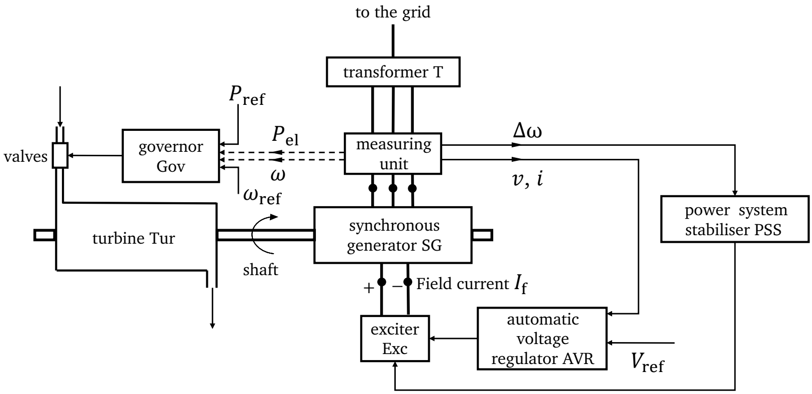

Figure 5.3: Overview of the synchronous generator (SG) control, based on [76].

$$T'_{\text{d0}} \cdot \frac{\text{d}E'_{\text{q}}}{\text{d}t} = E_{\text{f}} - E'_{\text{q}} + I_{\text{d}} \cdot (X_{\text{d}} - X'_{\text{d}}) \tag{5.3}$$

$$T'_{\text{q0}} \cdot \frac{\text{d}E'_{\text{d}}}{\text{d}t} = -E'_{\text{d}} - I_{\text{q}} \cdot (X_{\text{q}} - X'_{\text{q}}) \tag{5.4}$$

$$M \cdot \frac{\text{d}\Delta\omega}{\text{d}t} = P_{\text{m,Tur}} - P_{\text{e}} \quad \text{with} \quad M = \frac{2 \cdot H \cdot S_{\text{r}}}{\omega} = \omega \cdot J \tag{5.5}$$

$$\frac{\text{d}\delta}{\text{d}t} = \Delta\omega = \omega - \omega_{\text{n}} \tag{5.6}$$

with T'_{d0}, T'_{q0}, T''_{d0}, T''_{q0} being the d axis and q axis open-circuit transient and subtransient time constants, M the angular momentum, H the inertia constant, $\Delta\omega$ the rotor speed deviation, ω the electrical angular velocity of the generator, ω_{n} the nominal electrical angular velocity, $P_{\text{m,Tur}}$ the mechanical power of the turbine, P_{e} the electromagnetic air-gap power and δ the rotor angle.

An overview of the SG control is given in Figure 5.3. The SG control can be divided into the active power-speed (P-ω) control through the governor, which controls the steam supply to the turbine via valves and the voltage and excitation control, which adjusts the field current I_{f}.

The SG, automatic voltage regulator (AVR), power system stabiliser (PSS) and exciter models are standard models of the Matlab/Simulink library with the parameters given in Appendix A.1. The focus of this study is on the governor since it mainly determines the frequency behaviour of the SG. The governor control block is implemented as an active power-speed (P-ω) droop as presented in (5.7) and based on [76]. P_{ref} is the reference active power setpoint, k_{Gov} is the proportional gain of the speed control and the inverse of the governor droop d_{Gov}. In accordance with [142], the turbine dynamics are considered as a time delay with the time constant T_{Tur}, cf. (5.8). Further details on the derivation of the turbine as a first order delay are given in [76].

$$P_{\mathrm{Gov}} = P_{\mathrm{ref}} + k_{\mathrm{Gov}} \cdot (\omega - \omega_{\mathrm{n}}) \tag{5.7}$$

$$T_{\mathrm{Tur}} \cdot \frac{\mathrm{d}P_{\mathrm{Gov}}}{\mathrm{d}t} = P_{\mathrm{Gov}} - P_{\mathrm{m,Tur}} \tag{5.8}$$

For the overlying external grid (MV, HV, UHV), it is assumed that there are still SG or other plants, e.g. grid-forming units, which provide the inertia and control tasks of SG to the grid. Thus, the dynamics of the external grid are mainly defined by the rated power S_{r} of these plants, the inertia constant H_{SG} and the governor droop d_{Gov}. For simplification, the external grid model consists of a single SG, which is parametrised to represent an external grid and all grid-forming units available in this grid. According to the coherency method [145, 150, 165], the grid-forming units of the overlying grid are assumed to be coherent. This assumption is a simplification of the overlying external system. The aggregated model parameters can be derived from (5.9) to (5.11). The aggregated governor droop $d_{\mathrm{Gov,agg}}$ and the aggregated inertia constant H_{agg} are both calculated by the sum of the weighted values for each SG and referred to the total load of the system. Instead of the total installed generation power P_{G}, the total load active power P_{L} is used for the calculation to take into account that not all generating plants provide inertial behaviour and grid-forming control. The installed power of the aggregated generator $S_{\mathrm{r,agg}}$ is calculated using (5.11). The subtransient short-circuit power S''_{SC} is a typical measure of power systems and ranges between 105 and 225 MVA for medium-voltage grids and between 0.8 and 5.4 GVA for high-voltage grids [166]. The R to X ratio also depends on the voltage level and is typically 0.5...1 for medium-voltage grids and 0.1...0.3 for high-voltage grids [167]. The subtransient d axis reactance x''_{d} is given in p.u. and the maximum voltage factor is assumed to be $c_{\mathrm{max}} = 1.1$.

$$d_{\mathrm{Gov,agg}} = \frac{P_{\mathrm{L}}}{\sum_{i=1}^{N_{\mathrm{G}}} k_{\mathrm{Gov},i} \cdot P_{\mathrm{G},i}} \tag{5.9}$$

$$H_{\mathrm{agg}} = \frac{\sum_{i=1}^{N_{\mathrm{G}}} H_i \cdot S_{\mathrm{G},i}}{P_{\mathrm{L}}} \tag{5.10}$$

$$S_{\mathrm{r,agg}} = x''_{\mathrm{d}} \sqrt{1 + \left(\frac{R}{X}\right)^2} \cdot S''_{\mathrm{SC}} \tag{5.11}$$

Table 5.2: Aggregated parameters of the overlying external medium-voltage grid.

parameter		value range	default
governor droop	d_{Gov}	2 ... 12 %	2 %
inertia constant	$H_{\mathrm{agg}} = H_{\mathrm{SG}}$	1 ... 10 s	6 s
rated power	$S_{\mathrm{r,agg}} = S_{\mathrm{r,SG}}$	20 ... 50 MVA	30 MVA
turbine time constant	T_{Tur}	0.3 ... 0.9 s	0.3 s

N_{G}, H_i, $k_{\mathrm{Gov},i}$, $P_{\mathrm{G},i}$, $S_{\mathrm{G},i}$ are the number of grid-forming generators, the inertia constant, the governor gain, the momentary active and apparent power of the i-th generator. For the parameter derivation, typical machine parameters and power system characteristics are used based on [76, 141, 168, 169]. The aggregated default parameters used in this work as well as the parameter range applied for sensitivity studies in the medium-voltage testbench presented in Chapter 5.1 are given in Table 5.2 and are in line with current literature [170]. The detailed model parameters of the SG models for all voltage levels are given in the Appendix A.1, Tables A.1 to A.8. In the following, as the external grid is represented as a SG, the index 'agg' is replaced by 'SG' in order to attribute the parameters to the corresponding component.

The SG dynamic behaviour following a loadstep is shown in Figure 5.4. A sweep of each relevant parameter given in Table 5.2 is carried out with a disturbance being a loadstep $\Delta P_{\mathrm{L0}} = 5$ MW. Except for the variable to be varied, the parameters correspond to their default values given in Table 5.2. Using (2.6) and (2.7), the RoCoF and quasi-steady-state frequency deviation Δf_{qss} calculation for the default parametrisation is shown in (5.12) and (5.13). In (5.12), the term $S_{\mathrm{SG}}/P_{\mathrm{L}}$ is neglected as the SG is the only generation plant. For this reason, the entire generation is based on grid-forming control and provides inertia to the grid. A reduction of the inertia due to the infeed from grid-feeding or grid-supporting power plants is not necessary. The calculated RoCoF matches the simulation results in Figure 5.4. The quasi-steady-state frequency deviation can be calculated as $\Delta f_{\mathrm{qss}} = 0.17$ Hz and also aligns with the simulated frequency curves.

$$\mathrm{RoCoF}_{50\mu\mathrm{s}} \approx \frac{f_{\mathrm{n}} \cdot \Delta P}{2 \cdot \frac{S_{\mathrm{SG}}}{P_{\mathrm{L}}} \cdot \sum_{i=1}^{n} H_i \cdot S_i} = \frac{50\ \mathrm{Hz} \cdot 5\ \mathrm{MW}}{2 \cdot 6\ \mathrm{s} \cdot 30\ \mathrm{MVA}} = 0.7\ \mathrm{Hz/s} \tag{5.12}$$

$$\Delta f_{\mathrm{qss}} = \frac{\Delta P}{S_{\mathrm{r,SG}}} \cdot \frac{d_{\mathrm{Gov}}}{100\ \%} \cdot f_{\mathrm{n}} = \frac{5\ \mathrm{MW}}{30\ \mathrm{MVA}} \cdot \frac{2\ \%}{100\ \%} \cdot 50\ \mathrm{Hz} = 0.17\ \mathrm{Hz} \tag{5.13}$$

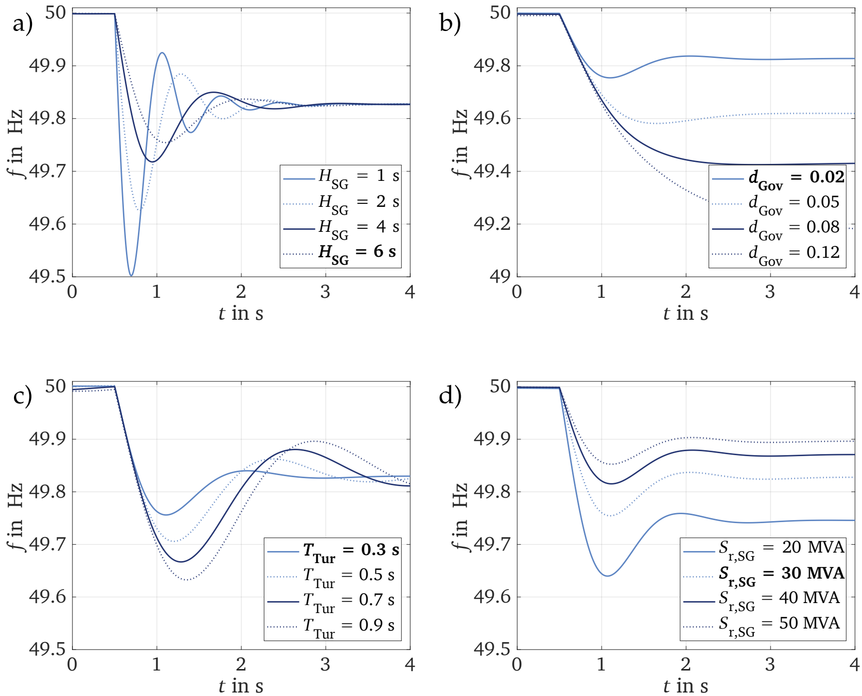

Figure 5.4: Influence of a) the inertia constant H_{SG}, b) the governor droop d_{Gov}, c) the turbine time constant T_{Tur} and d) the rated power $S_{r,SG}$ on the frequency behaviour of a synchronous generator (SG) with default parameters according to Table 5.2 and for a loadstep $\Delta P_{L0} = 5$ MW.

Figure 5.4 a) presents the variation of the SG inertia constant H_{SG}. Weak grids with little inertia $H_{SG} < 3$ s show the largest RoCoF and smallest frequency nadir. With increasing inertia constant H_{SG}, both, the RoCoF decreases and the frequency nadir f_{min} increases, which makes the frequency excursion less severe and slower. The inertia constant H_{SG} does not affect the quasi-steady-state frequency deviation Δf_{qss} after the disturbance as can also be seen in (5.13). When referring to the German grid code requirements shown in Figure 3.4, nowadays generation plants are only required to ride through a RoCoF≤ 0.09 Hz/s. In the scenarios shown here, a larger RoCoF occurs already for the inertia constant $H = 6$ s due to the very small turbine time constant. However, new requirements state that ride-through capabilities for frequency events with a RoCoF of up to 2 Hz/s arise [171], which take into account the faster frequency dynamics in low-inertia power systems. The results of this study show that the IBG is capable to handle very fast frequency dynamics.

Figure 5.4 b) presents the impact of the governor droop d_{Gov} on the frequency. The larger the governor droop, the larger becomes the quasi-steady-state frequency deviation Δf_{qss} with a proportional relation as shown in (5.13) following the loadstep ΔP. This is due to the proportional implementation of the primary control described in Chapter 2.3.2. The RoCoF remains unaffected as the primary control is implemented with a deadband and therefore does not act instantaneously following a disturbance. The frequency nadir decreases with increasing governor droop due to the reduced active power adaptation.

In Figure 5.4 c), the turbine constant T_{Tur} is varied. It can be seen that again, the RoCoF is not affected, but the frequency nadir as well as the settling time of the control worsen with increasing turbine constant T_{Tur}. The initial steady state before introducing the loadstep slightly differs for larger turbines also due to the larger time constant.

Finally, Figure 5.4 d) presents the frequency curves for a varying SG power $S_{\mathrm{r,SG}}$. The rated power $S_{\mathrm{r,SG}}$ effects all, the RoCoF, frequency nadir and quasi-steady-state frequency deviation Δf_{qss} with larger SG power having a positive effect on each parameter.

External Grid Model: The overlying external grid for dynamic frequency studies on distribution grid level is modelled as an aggregated synchronous generator in order to incorporate the dynamic frequency behaviour and inertia. A sixth order model is parametrised according to typical characteristics of German medium-voltage, high-voltage and transmission grids. The parameters to be chosen are the synchronous generator rated power $S_{\mathrm{r,SG}}$ and inertia constant H_{SG}, which determine the short-circuit power S''_{SC} and inertia of the external grid. Additionally, the governor droop d_{Gov} and the turbine time constant T_{Tur} determine the gradient and time delay of the primary frequency control and thus impact the frequency nadir f_{min} and quasi-steady-state frequency deviation Δf_{qss}.

5.3 FREQUENCY-DEPENDENT LOAD MODEL

In general, loads are characterised by how the power consumption behaves in relation to the power system voltage and frequency. When considering load models, an important distinction can be made between static and dynamic models. Static models establish a purely algebraic relationship between power, voltage and frequency, using separate equations for active and reactive power. On the other hand, dynamic models capture dependencies of power on preceding factors, e.g. machine dynamics and can be represented by a system of differential equations or a transfer function. Typically, loads are not modelled as individual components, but as an aggregated total load that is based either on the knowledge of the load components and parameters or based on field measurements. In both cases, loads with diverse characteristics are combined into composite models to more accurately represent the diverse behaviour. The aggregated total load is calculated as the sum of the individual aggregated loads of each type of load. Although these composite models are more complex, they tend to provide better accuracy [148].

The dependency of loads on the power system frequency is often neglected in load modelling [148], though different studies prove the importance to include the selfregulating effect of loads within power system studies [172–174]. The selfregulation of power system loads consists of the frequency dependency resulting from the torque characteristics of induction motor (IM) loads and further speed-controlled components. A load selfregulating effect of 1 % to 2 % power consumption adjustment per frequency deviation $\Delta f = 1$ Hz is typically assumed. However, some studies suggest the effect being significantly larger [172], whereas the field measurements in [175] show no significant active power change in response to a frequency change. In terms of dynamic frequency studies, the load selfregulation increases the impact of active distribution grids on the frequency support. For this reason, different static and dynamic as well as composite load models are described in the following sections.

A distinction is made between residential load sectors (res), commercial load sectors (comm) and industrial load sectors (ind). In addition, sectors can be divided according to season, since the resistive heating load predominant in winter (w) has a stronger influence on the behaviour compared to summer (s). If no such dependency on the season is applicable, data is provided for the whole year. This results in numerous parameter sets for the individual load models. Typical parameters of the load models discussed in this section can be found in the Appendix A.2, Tables A.10 to A.13.

5.3.1 *Static Load Models*

Static load models represent the active and reactive power load using algebraic functions of the system variables voltage and frequency. Static models are primarily suitable for loads where the power reference is directly related to these quantities or for steady-state analysis. However, for more complex loads with significant short-term dynamics, static models should only be employed in long-term studies [148]. Some frequently used load models are the exponential load model and the polynomial load model.

5.3.1.1 *Exponential Load Model*

A widely used and simple model for load representation is the exponential load model. It serves as a fundamental building block not only for basic load models but also for more complex static models. The relationship between the load's active power demand P_L and reactive power demand Q_L and the system voltage V is described in (5.14).

$$P_\mathrm{L}(V) = P_\mathrm{r} \cdot (V/V_\mathrm{n})^{k_\mathrm{pv}} \qquad Q_\mathrm{L}(V) = Q_\mathrm{r} \cdot (V/V_\mathrm{n})^{k_\mathrm{qv}} \tag{5.14}$$

Here, k_pv and k_qv are the active and reactive power-voltage exponents, which are determined through experimental analysis. V_n is the power system nominal voltage and P_r and Q_r are the rated active and reactive power respectively. The frequency-dependent behaviour is disregarded in this model. By selecting the voltage exponents as 2, 1 or 0, the represented load corresponds to constant impedance, constant current, or constant power consumption, respectively. In the following, the exponential load model is referred to as *exp* load model.

A popular extension of the voltage-dependent *exp* load model is the frequency-dependent exponential model (*f-exp*). The presented *exp* model is simply extended by one term each for the active and reactive power calculation, which considers the additional dependency on the frequency. This model is expressed by (5.15) and (5.16).

$$P_\mathrm{L}(V, f) = P_\mathrm{r} \cdot (V/V_\mathrm{n})^{k_\mathrm{pv}} \cdot (f/f_\mathrm{n})^{k_\mathrm{pf}} \tag{5.15}$$

$$Q_\mathrm{L}(V, f) = Q_\mathrm{r} \cdot (V/V_\mathrm{n})^{k_\mathrm{qv}} \cdot (f/f_\mathrm{n})^{k_\mathrm{qf}} \tag{5.16}$$

k_pf and k_qf are the active and reactive power-frequency exponent and take into account the relationship of the load power consumption with the power system frequency f. The exponents k_pf and k_qf are determined experimentally. Typical parameters for the *exp* and *f-exp* load model are given in Table A.10.

5.3.1.2 *Polynomial Load Model*

Another widely used static load model is the polynomial model, also known as the *ZIP* model. It characterises loads based on their similarity to three ideal loads: constant impedance Z, constant current I, and constant power P as presented in (5.17) and (5.18).

$$P_\mathrm{L}(V) = P_\mathrm{r} \cdot [\, p_1 \cdot (V/V_\mathrm{n})^2 + p_2 \cdot (V/V_\mathrm{n}) + p_3 \,] \tag{5.17}$$

$$Q_\mathrm{L}(V) = Q_\mathrm{r} \cdot [\, q_1 \cdot (V/V_\mathrm{n})^2 + q_2 \cdot (V/V_\mathrm{n}) + q_3 \,] \tag{5.18}$$

Here, p_i and q_i correspond to the shares of the different load types in the total load. An additional restriction of these parameters can be made according to (5.19), which limits the relative shares to the range $[0,\ 1]$.

$$p_1 + p_2 + p_3 = q_1 + q_2 + q_3 = 1 \tag{5.19}$$

Typical parameters are given in Table A.11. Even though the *ZIP* load model shows no dependency on the frequency, it serves as a part of the composite model, which is described in Chapter 5.3.3.

5.3.2 *Dynamic Load Models*

If dynamic loads account for a large share of the total load or if the transient load behaviour is a particular focus of the investigation, the use of a dynamic model is evident. If loads with dynamic properties are only represented to a small extent, static models can be sufficient [148]. Here, two dynamic models are described: The dynamic exponential and the IM load model.

5.3.2.1 *Dynamic Exponential Load Model*

One possible model to represent dynamic load behaviour is the dynamic exponential model (*dyn-exp*). This model assumes exponential recovery behaviour after voltage disturbances and is mainly used in long-term stability investigations. The *dyn-exp* load model can be applied for residential loads with few rotating machines and is defined by (5.20) to (5.22).

$$T_{\mathrm{P,rec}} \frac{\mathrm{d}P_{\mathrm{rec}}}{\mathrm{d}t} + P_{\mathrm{rec}} = P_{\mathrm{r}} \cdot (V/V_{\mathrm{n}})^{\alpha_{\mathrm{Ps}}} - P_{\mathrm{r}} \cdot (V/V_{\mathrm{n}})^{\alpha_{\mathrm{Pt}}} \tag{5.20}$$

$$T_{\mathrm{Q,rec}} \frac{\mathrm{d}Q_{\mathrm{rec}}}{\mathrm{d}t} + Q_{\mathrm{rec}} = Q_{\mathrm{r}} \cdot (V/V_{\mathrm{n}})^{\alpha_{\mathrm{Qs}}} - P_{\mathrm{r}} \cdot (V/V_{\mathrm{n}})^{\alpha_{\mathrm{Qt}}} \tag{5.21}$$

$$P_{\mathrm{L}}(V) = P_{\mathrm{rec}} + P_{\mathrm{r}} \cdot (V/V_{\mathrm{n}})^{\alpha_{\mathrm{Pt}}} \qquad Q_{\mathrm{L}}(V) = Q_{\mathrm{rec}} + Q_{\mathrm{r}} \cdot (V/V_{\mathrm{n}})^{\alpha_{\mathrm{Qt}}} \tag{5.22}$$

with $T_{\mathrm{P,rec}}$, $T_{\mathrm{Q,rec}}$, P_{rec}, Q_{rec}, α_{Ps}, α_{Pt}, α_{Qs} and α_{Qt} being the active and reactive power recovery time constant, the active and reactive power recovery and the steady-state and transient active and reactive power voltage exponents. Typical parameters for the *dyn-exp* are given in Table A.12. As the dynamic exponential load model shows no dependency on the frequency and is not recommended for short-term dynamic studies, it is not considered in this work.

5.3.2.2 *Dynamic Induction Motor Load Model*

In case the total load has a significant amount of IM also referred to as asynchronous motors in the load mix, the IM should be modelled individually [148].

As previously described in Chapter 5.2 for the SG, the IM can be modelled by electrical and mechanical states. In this work, a sixth-order IM is modelled with four electrical and two mechanical states as shown in (5.23) to (5.28).

$$v_{\mathrm{dS}} = R_{\mathrm{S}} \cdot i_{\mathrm{dS}} + \frac{\mathrm{d}\Psi_{\mathrm{dS}}}{\mathrm{d}t} - \omega \cdot \Psi_{\mathrm{qS}} \tag{5.23}$$

$$v_{\mathrm{qS}} = R_{\mathrm{S}} \cdot i_{\mathrm{qS}} + \frac{\mathrm{d}\Psi_{\mathrm{qS}}}{\mathrm{d}t} - \omega \cdot \Psi_{\mathrm{dS}} \tag{5.24}$$

$$v_{\mathrm{dR}} = R_{\mathrm{R}} \cdot i_{\mathrm{dR}} + \frac{\mathrm{d}\Psi_{\mathrm{dR}}}{\mathrm{d}t} - (\omega - \omega_{\mathrm{R}}) \cdot \Psi_{\mathrm{qR}} \tag{5.25}$$

$$v_{\mathrm{qR}} = R_{\mathrm{R}} \cdot i_{\mathrm{qR}} + \frac{\mathrm{d}\Psi_{\mathrm{qR}}}{\mathrm{d}t} - (\omega - \omega_{\mathrm{R}}) \cdot \Psi_{\mathrm{dR}} \tag{5.26}$$

$$\frac{\mathrm{d}\omega_{\mathrm{R}}}{\mathrm{d}t} = \frac{M_{\mathrm{e}} - M}{2 \cdot H} \tag{5.27}$$

$$\frac{\mathrm{d}\theta}{\mathrm{d}t} = \omega_{\mathrm{R}} \tag{5.28}$$

Here, v_{dS}, v_{qS}, v_{dR}, v_{qR}, i_{dS}, i_{qS}, i_{dR} and i_{qR} are the rotor and stator voltages and currents in direct and quadrature axis respectively; Ψ_{dS}, Ψ_{qS}, Ψ_{dR} and Ψ_{qR} are the stator and rotor flux linkages in d and q axis; R_{S} and R_{R} are the stator and rotor resistance respectively; M_{e}, M and H are the electromagnetic torque, the mechanical load torque and the inertia constant, respectively [148]. The magnetic field of the stator winding rotates at synchronous angular speed ω and the rotor speed ω_{R} differs from the synchronous speed [76].

Many aggregated loads - especially industrial loads - consist of high proportions of IM. Especially the dynamic load behaviour is then dominated by these components.

5.3.3 *Composite Load Models*

An adequate representation of power system loads includes characteristics of different static and dynamic load types. A composite load model is a combination of various load components that effectively captures the load demand at a given bus. Typically, composite load models incorporate a dynamic part in the form of an equivalent IM [148] and a parallel static load.

For the composite load model, an IM model in parallel with a *ZIP* or a *f-exp* load model is chosen. The proportion d of the dynamic load model in relation to the total load is given according to the apparent power of each model using (5.29).

$$S_{\mathrm{L}} = d \cdot S_{\mathrm{L,dyn}} + (1 - d) \cdot S_{\mathrm{L,stat}} \tag{5.29}$$

Here, S_{L} is the total load apparent power, $S_{\mathrm{L,dyn}}$ and $S_{\mathrm{L,stat}}$ are the apparent power of the dynamic and static load, respectively. The proportion of the dynamic load $d \in [0, 1]$ depends on the load type and is generally smaller in residential and larger in industrial sectors.

A comparison of the four load models with regard to the behaviour of voltage, frequency, active and reactive power following a loadstep is given in Figure 5.5. For this purpose, the testbench in Figure 5.1 is used, whereby the IBG is disconnected and only the default SG described in Chapter 5.2 and a load with rated apparent power $S_{\mathrm{L1}} = 5$ MVA remain. The load model parameters applied in this work are given in Table 5.3. A loadstep $\Delta P_{\mathrm{L0}} = 10$ MW is applied, which is realised by connecting an additional constant active power at load L0. The larger loadstep compared to the investigation of the SG parameters is chosen to according the relatively small differences and sensitivities of the load models. The dynamic behaviour of the four load models is evaluated regarding the load active and reactive power consumption P_{L1} and Q_{L1} as a reaction of the terminal voltage v and frequency f.

The *exp res-year* model exhibits the smallest voltage drop Δv and the largest frequency drop Δf as the load model shows no dependency on the frequency and therefore no selfregulating effect. The active power following the loadstep increases, which results in worsening the frequency curve. Due to the highest power factor *cosφ*, the *exp res-year* load model has the lowest reactive power consumption. The frequency-dependent load models counteract the frequency drop by reducing the active power P_{L1}. The largest effect is seen for the composite *ind* model with a large share of IM.

The non-frequency dependent static exponential *exp res-year* load model serves as the default for the following analyses against which the other load models can be compared. Different parameters of the *exp*, *exp-f*, *dyn-exp*, *ZIP* and IM load models found in literature are given in the Appendix A.2, Tables A.10 to A.13.

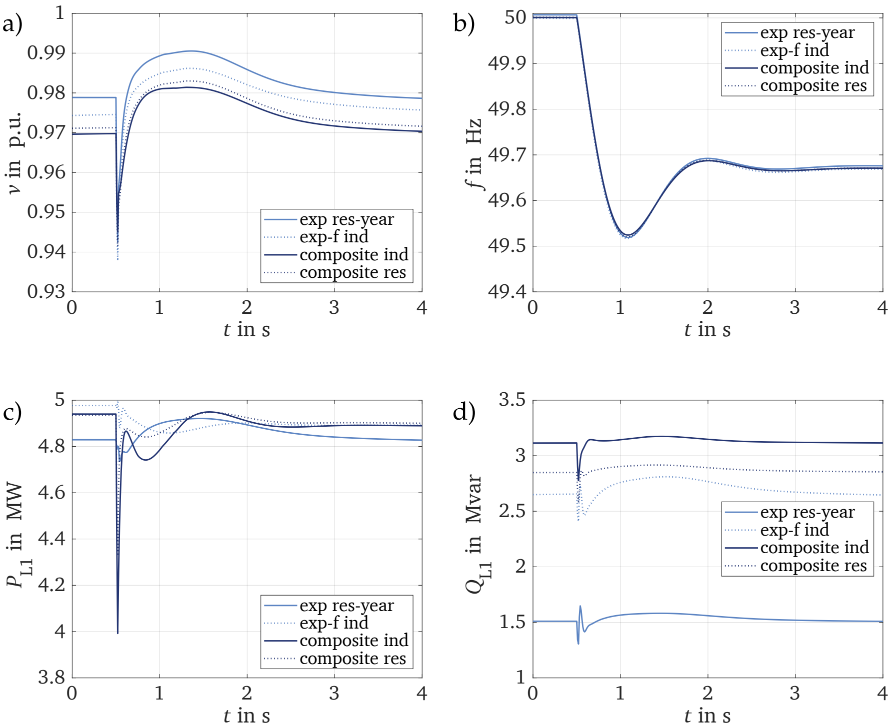

Figure 5.5: Influence of the load model on the a) terminal voltage, b) frequency, c) load L1 active power and d) load L1 reactive power consumption based on the parameters in Table 5.3 for a loadstep $\Delta P_{L0} = 10$ MW.

Selfregulating Effect of Loads: The selfregulating effect of the loads with regard to voltage is relatively pronounced and can also be demonstrated with recent field measurements [175]. With regard to frequency, the role that loads play and will play in the future must continue to be investigated. For this reason, a conservative selfregulation effect of 2 % active power adjustment per frequency deviation $\Delta f = 1$ Hz is assumed in this work. The selfregulating effect of the loads regarding frequency events is included in the frequency-dependent load modelling. In the results shown in Figure 5.5, a load adjustment $\Delta P_{L1} \approx 0.01 \cdot S_{r,L1}/\Delta f = 0.02 \cdot 5$ MVA$/1$ Hz $= 0.1$ MW/Hz is modelled using the *exp-f* load model. However, the effect of loads on the frequency stability is likely to have a larger positive effect in the future.

Table 5.3: Load model parameters for static and composite load models.

type	load model	parameters		
static	*exp* res-year	$k_{\mathrm{pv}} = 1.63$	$k_{\mathrm{qv}} = 3.97$	$cos(\varphi) = 0.95$
static	*exp-f* ind	$k_{\mathrm{pv}} = 0.18$	$k_{\mathrm{qv}} = 6.0$	$cos(\varphi) = 0.85$
		$k_{\mathrm{pf}} = 2.6$	$k_{\mathrm{pf}} = 1.6$	
composite	*ZIP* res	$p_1 = 0.29$	$p_2 = 0.10$	$p_3 = 0.61$
residential	+ IM res-agg	$q_1 = 3.22$	$q_2 = -4.53$	$q_3 = 2.31$
		$d = 0.38$	$R_{\mathrm{s}} = 0.08$ p.u.	$L_{\mathrm{s}} = 0.11$ p.u.
			$R_{\mathrm{r}} = 0.08$ p.u.	$L_{\mathrm{r}} = 0.10$ p.u.
			$L_{\mathrm{m}} = 2.22$ p.u.	$H = 0.74$ s
composite	*ZIP* ind	$p_1 = 0.20$	$p_2 = 0.08$	$p_3 = 0.72$
industrial	+ IM res & ind	$q_1 = 2.76$	$q_2 = -4.03$	$q_3 = 2.27$
		$d = 0.54$	$R_{\mathrm{s}} = 0.04$ p.u.	$L_{\mathrm{s}} = 0.09$ p.u.
			$R_{\mathrm{r}} = 0.05$ p.u.	$L_{\mathrm{r}} = 0.16$ p.u.
			$L_{\mathrm{m}} = 2.80$ p.u.	$H = 0.93$ s

5.4 PASSIVE COMPONENTS

Even though passive components of the power system do not actively control the power system frequency f, the R to X ratio and losses are determined mainly by lines and transformers. The lines are modelled as lumped π-sections [76] based on the series impedance $\underline{Z}$ per phase and the shunt admittance $\underline{Y}$ per phase [76] with the parameters in the Appendix A.3, Table A.14. The transformer models are based on three single-phase transformers using the T-equivalent model [76]. The transformer models include an ideal transformer, which is extended by two resistances R_1, R_2 that take into account the losses in the primary and secondary winding, two inductances L_1, L_2, which account for the leakage flux and a magnetisation inductance L_{m} and a resistance R_{m} taking into account the iron losses P_{Fe} [76]. The transformers are usually equipped with a tap changer, which is specified depending on the benchmark grid and voltage level. The transformer parameters and configurations for different voltage levels can be found in the Appendix A.4, Table A.15 for the IBG transformer, in the Appendix A.5, Table A.18 for the HV/MV transformer and in Table A.20 for the UHV/HV transformer and the windfarm transformer.

5.5 SUMMARY

This chapter introduces a simple generic medium-voltage testbench model for testing the dynamic behaviour of the individual grid components. The external grid in this work is modelled as a sixth order synchronous generator including a power system stabiliser, automatic voltage regulator with exciter and a governor control. The dynamic behaviour of the SG turbine is simplified as a first-order time delay. In order to represent an external overlying grid, the synchronous generator's parameters are chosen to match typical characteristics on the medium-voltage and high-voltage level. The aggregated synchronous generator is the grid-forming component in the grids studied in this work. Characteristics of the dynamic frequency curve following a loadstep can be estimated using rules of thumb in a power system relying on synchronous generators.

Load models can be divided into static and dynamic load models, each type being relevant for different studies. These models represent typical aggregated load behaviour based on the knowledge of the load components and parameters or based on field measurements, e.g. in [175]. Dynamic studies usually use composite models that include a certain proportion of dynamic models. In this work, four different load models - two static and two composite ones - are investigated. The frequency dependency of the load models is referred to as the selfregulation of loads and adapts the active power load demand by approximately 1 % per frequency deviation $\Delta f = 1$ Hz.

The transformers and lines are passive components and modelled using the π-section equivalent for lines and the T-equivalent circuit for transformers.

6 INVERTER-BASED GENERATION MODEL

In recent years, the integration of renewable energy sources into power systems has surged, leading to an increased use of IBG. While these technologies offer numerous environmental and economic benefits, they also introduce unique challenges to the stability and overall performance of power systems. To address these challenges, the modelling of IBG has become a critical aspect of power system stability studies. Different approaches exist for generic IBG models, that can represent the fundamental behaviour independent of the manufacturer and with a reasonable degree of detail, see Chapter 3.2. In this work, the IBG is based on a full-size power VSC and modelled as a type 6 AVM with cascaded vector control and grid-supporting characteristics. It fulfils the German grid code requirements [132, 133] for voltage and frequency support and extends the control by a FFR. The IBG model can be devided into an electrical part, which represents the physical components and a control part, which applies the control strategy. Parameters of the electrical and control model are given in Appendix A.4, Table A.15. This chapter describes the electrical model in Chapter 6.1, the grid-supporting control in Chapter 6.2 and the direct voltage control in Chapter 6.3 as well as the differences of RMS and EMT modelling in Chapter 6.4. For all investigations in this chapter, the medium-voltage testbench as introduced in Chapter 5.1 is used with a closed switch S1. The load is modelled as static exponential *exp res year* model with the parameters presented in Table 5.3.

6.1 ELECTRICAL MODEL

The IBG is modelled as a type 6 AVM, cf. Chapter 3.2. The electrical model of the IBG is reduced to a controlled three-phase voltage source of fundamental frequency that is adjusted by the IBG control. Only the grid-side converter and its control are modelled under the assumption of a constant power infeed during the time interval of interest of a few seconds. The upper part of Figure 6.1 shows the electrical model as presented in Chapter 3.1 and consists of the simplified grid-side VSC, the DC-side, which is modelled as a constant voltage source V_{dc} and a DC-link capacitor C_{dc}, the IBG transformer T and LC-filter for smoothing of the output voltage. The filter is modelled as the filter inductance L_{f} with associated losses through the resistance R_{f} and the filter capacitor C_{f}. On the grid side, the IBG transformer impedance $R_{\mathrm{T}} + \mathrm{j}\omega L_{\mathrm{T}}$ completes the LCL-filter.

The voltage and current measurements for the IBG control are implemented on the low-voltage side of the transformer T. The control of the grid-side VSC relies on this local measurement. As the grid-supporting control is implemented in dq coordinates, the frequency f_{est} and angle θ_{est} estimation play major roles. The estimated angle derived from the voltage measurement is used for the coordinate transformation at the start and the end of the cascaded vector control.

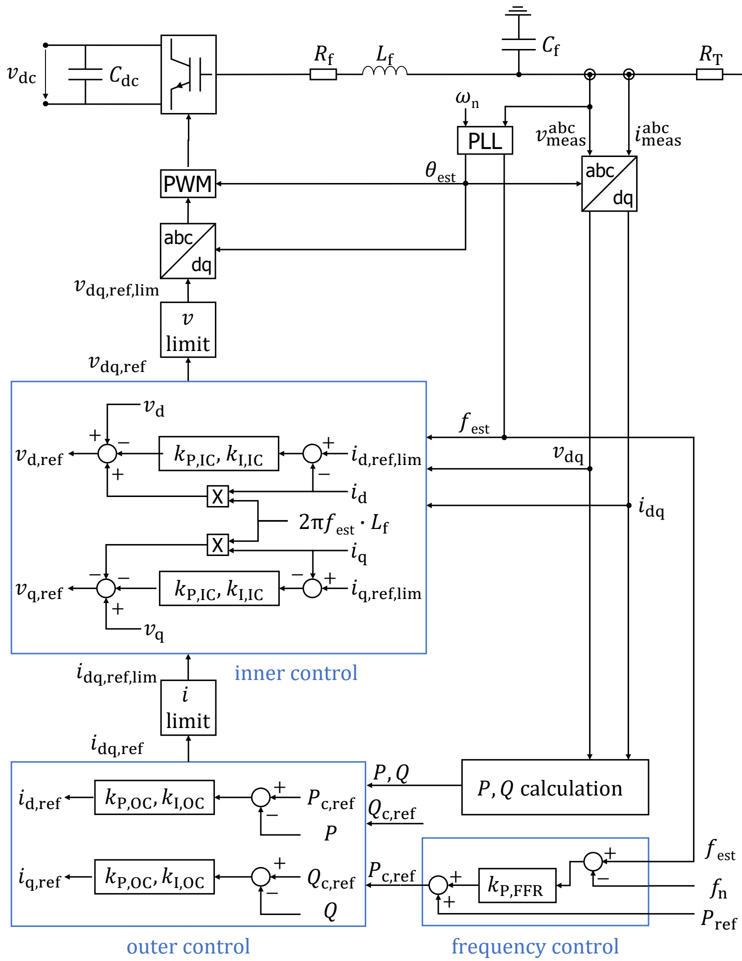

Figure 6.1: Electrical model and grid-supporting control model for an inverter-based generation (IBG) plant.

6.2 GRID-SUPPORTING CONTROL MODEL

The cascaded vector control of the grid-side VSC is implemented in a synchronous referece frame (SRF) in dq coordinates as presented in Figure 6.1. The main blocks of the control are the frequency support, the outer control, the current limiter, the inner control and the voltage limiter. The frequency support control implements the FFR with an active power-frequency *P-f* control as presented in Chapter 2.3.3. The high-level control or outer control is based on two proportional-integral (PI) controllers that compare the measured active and reactive power P and Q with the reference values $P_{\mathrm{c,ref}}$ and $Q_{\mathrm{c,ref}}$. The outer control outputs the reference values of direct and quadrature current $i_{\mathrm{d,ref}}$ and $i_{\mathrm{q,ref}}$, which are passed to the current limiter. The current limiting is described in Chapter 6.2.4 in detail. Through different approaches, the currents are limited to $i_{\mathrm{d,ref,lim}}$ and $i_{\mathrm{q,ref,lim}}$ in order to cope with the physical characteristics of power electronics. The low-level control or inner control compares the currents $i_{\mathrm{d,ref,lim}}$ and $i_{\mathrm{q,ref,lim}}$ with the measured currents i_{d} and i_{q}, leading to the reference values for direct and quadrature voltage $v_{\mathrm{d,ref}}$ and $v_{\mathrm{q,ref}}$. Additionally, the cross coupling in the inner current control takes into account that due to the filter inductance L_{f}, the currents in orthogonal dq coordinates are coupled [176]. Further details about cross-coupling control can be found e.g. in [177]. The voltage limiter limits the voltage magnitude to $V_max = 1.2$ p.u., but has no impact on the studies carried out in this work. Finally, the PWM controls the individual switches of the converter. Since the AVM does not include a detailed converter model, the PWM is assumed to be ideal, and the controlled voltage output of the inner control is directly fed to the three-phase voltage source that represents grid-side VSC. In the following, the individual control blocks are described in more detail. The frequency support is realised as FFR with the linear and constant implementation described in Chapter 2.3.3.

6.2.1 *Signal Processing*

The signal processing includes the signal acquisition through measurements, the derivation of relevant signals for the IBG control and the generation of signals for the electrical model from the output of the control. The blocks involved are the PLL, the transformation from abc to dq coordinates and vice versa and the PWM. As stated above, the PWM is assumed to be ideal and is not modelled specifically. The PLL is implemented as described in Chapter 2.4.1 with the parameters given in Table 6.1. Two parameter sets are compared: The standard PLL parametrisation as proposed by the standard library in Matlab/Simulink and the optimised parametrisation described in [74].

Table 6.1: Standard and optimal parametrisation of the phase-locked loop (PLL).

parameter		standard	optimised
proportional gain	$k_{\mathrm{P,PLL}}$	180	30
integral gain	$k_{\mathrm{I,PLL}}$	3200 s^{-1}	1 s^{-1}
derivative gain	$k_{\mathrm{D,PLL}}$	1 s	0.04 s
rate limit	RL	12 Hz/s	0.88 Hz/s
filter cutoff frequency	f_{cutoff}	25 Hz	25 Hz
sample time	T_{s}	5 μs	5 μs

A comparison of the standard and optimal PLL parametrisation is given in Figure 6.2. Both are compared to the SG rotational speed as a reference. While the quasi-steady states before and shortly after the loadstep are well met with both PLL parametrisations, the limits of the standard parameters are within the subtransient time range. The large oscillations seen in Figure 6.2 arise from the rate limiter settings. Issues with the PLL modelling in low-inertia power systems are discussed in [178].

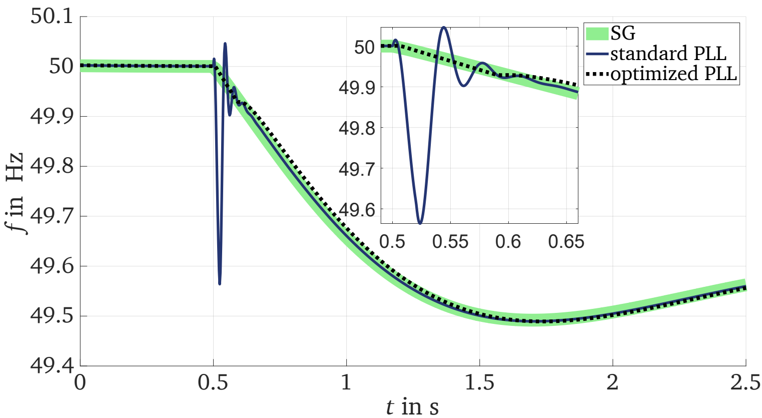

Figure 6.2: Comparison of the frequency estimation with variation of the phase-locked loop (PLL) parameters according to Table 6.1.

Frequency Estimation: Accurate frequency measurement or estimation is crucial for the frequency control of grid-supporting inverters, particularly in scenarios where a communication infrastructure is unavailable. The difficulty of estimating the frequency from a voltage or current measurement becomes even more pronounced in low-inertia systems characterised by rapid and steep frequency changes.

6.2.2 *Outer Control*

The outer control determines the current references $i_{\mathrm{d,ref}}$ and $i_{\mathrm{q,ref}}$ from the instantaneous power infeed P and Q and the power references $P_{\mathrm{c,ref}}$ and $Q_{\mathrm{c,ref}}$ that are usually provided by the system operator. Based on the measured voltage v and current i, the instantaneous values of the active power P and reactive power Q fed in by the IBG are calculated in the power calculation block using (6.1) and (6.2). The derivation of the dq quantities from the three-phase measurements of voltage v and current i is done using Clarke and Park transformation and is explained e.g. in [179].

$$P = v_{\mathrm{d}} \cdot i_{\mathrm{d}} + v_{\mathrm{q}} \cdot i_{\mathrm{q}} \tag{6.1}$$

$$Q = v_{\mathrm{q}} \cdot i_{\mathrm{d}} + v_{\mathrm{d}} \cdot i_{\mathrm{q}} \tag{6.2}$$

The outer control is implemented as control loop based on PI controllers and shown in Figure 6.1. From the control block, the control variable, which is the current reference $i_{\mathrm{ref}}(t)$ can be calculated by (6.3) and (6.4) with the active and reactive power deviation $\Delta P(t) = P_{\mathrm{c,ref}} - P(t)$ and $\Delta Q(t) = Q_{\mathrm{c,ref}} - Q(t)$.

$$i_{\mathrm{d,ref}} = k_{\mathrm{P,OC}} \cdot \Delta P(t) + k_{\mathrm{I,OC}} \cdot \int \Delta P(t)\ \mathrm{d}t \tag{6.3}$$

$$i_{\mathrm{q,ref}} = k_{\mathrm{P,OC}} \cdot \Delta Q(t) + k_{\mathrm{I,OC}} \cdot \int \Delta Q(t)\ \mathrm{d}t \tag{6.4}$$

With $T_{\mathrm{I,OC}} = k_{\mathrm{P,OC}} / k_{\mathrm{I,OC}}$, the open-loop transfer function $G_{\mathrm{o,OC}}$ is given in (6.5).

$$G_{\mathrm{o,OC}}(s) = k_{\mathrm{P,OC}} + \frac{k_{\mathrm{I,OC}}}{\mathrm{s}} = k_{\mathrm{P,OC}} \cdot \left(1 + \frac{1}{T_{\mathrm{I,OC}} \cdot \mathrm{s}} \right) \tag{6.5}$$

Tuning of the outer control PI controllers is relevant for the stability, robustness and dynamic performance of the control [180]. The outer control is tuned based on the symmetrical optimum for a good disturbance rejection [181]. The symmetrical optimum is based on loop shaping of the transfer function with the aim to maximise the phase margin [182]. Typically, the outer control is operated slower than the inner control, so that the outer control does not become active until the inner control is settled. The outer control closed-loop time constant is typically within the range $T_{\mathrm{OC}} = 100$ ms ... 1 s [14].

6.2.3 *Inner Control*

The inner control or inner current control controls the reference currents $i_{\mathrm{dq,ref,lim}}$ given by the outer control and limited by the current limiter. Similar to the outer control, the inner control usually is realised as two PI controllers with identical parameter settings in both axes, cf. Figure 6.1. The PI controllers control the error between reference and measured currents $\Delta i = i_{\mathrm{dq,ref,lim}} - i_{\mathrm{dq}}$. The inner control takes into account the cross-coupling between d and q axis due to the filter inductance L_{F} with the additional term in (6.6) and (6.7).

$$v_{\mathrm{d,ref}} = v_{\mathrm{d}} - \left(k_{\mathrm{P,IC}} \cdot \Delta i_{\mathrm{d}}(t) + k_{\mathrm{I,IC}} \cdot \int \Delta i_{\mathrm{d}}(t)\ \mathrm{d}t \right) + 2\pi f_{\mathrm{est}} \cdot L_{\mathrm{F}} \cdot i_{\mathrm{q}} \tag{6.6}$$

$$v_{\mathrm{q,ref}} = v_{\mathrm{q}} - \left(k_{\mathrm{P,IC}} \cdot \Delta i_{\mathrm{q}}(t) + k_{\mathrm{I,IC}} \cdot \int \Delta i_{\mathrm{q}}(t)\ \mathrm{d}t \right) - 2\pi f_{\mathrm{est}} \cdot L_{\mathrm{F}} \cdot i_{\mathrm{d}} \tag{6.7}$$

The inner control with high dynamics and a fast settling time ensures that the limited currents $i_{\mathrm{dq,ref,lim}}$ from the superimposed outer control and the current limiter are controlled sufficiently fast. In contrast, the inner control open-loop time constant $T_{\mathrm{I,IC}} = k_{\mathrm{P,IC}} / k_{\mathrm{I,IC}}$ cannot be chosen arbitrarily small as the measurement of voltage v and current i is filtered to avoid aliasing effects and the bandwidth of the PWM is limited. According to [17, 138], the closed-loop transfer function of the inner control can be reduced to a first order time delay. The settling time T_{IC} can be chosen within the limits as given in (6.8) [14] with the inverter switching frequency f_{sw} and the maximum settling time of the additive reactive current $t_{\mathrm{e,max}} = 60$ ms required in the German grid code [132].

$$\frac{10}{2 \cdot f_{\mathrm{sw}}} < T_{\mathrm{IC}} < \frac{t_{\mathrm{e,max}}}{3} \tag{6.8}$$

The controller parameters are determined by (6.9) with the filter inductance L_{f} and the inner control closed-loop time constant T_{IC}. This approach is a simplified magnitude optimum criterion as described in [14]. The magnitude optimum criterion [183] also referred to as loop-shaping approach [184] shapes the open-loop transfer function in order to compensate the critical largest time constant of the controlled system [185].

A reference frequency response $G(s) = P/P_{\mathrm{ref}} = Q/Q_{\mathrm{ref}} = 1$ is established over a frequency range as wide as possible, indicating that the controlled variable can follow the value of the reference variable with little time delay [185, 186]. Tuning or optimisation in this context refers to the optimisation of the settling time. Further explanation of the loop-shaping approach is given in [184, 187, 188].

$$k_{\mathrm{P,IC}} = \frac{L_{\mathrm{f}}}{T_{\mathrm{IC}}} \qquad k_{\mathrm{I,IC}} = \frac{R_{\mathrm{f}}}{T_{\mathrm{IC}}} \tag{6.9}$$

6.2.4 *Current Limiter*

Limiting the reference current output of the outer control $i_{dq,ref}$ includes the maximum overcurrent capacity of real converters as described in Chapter 3.1 to the model. Different approaches to limit the IBG current magnitude exist. Besides the classical limit for the controlled current $i_{dq,ref}$, the limitation can also be realised by a virtual impedance or by adjusting the output voltage, see [189]. In this work, four different current limiters are presented and compared that directly limit the current magnitude $I_{ref} = |\underline{i}_{dq}| = \sqrt{i_{d,ref}^2 + i_{q,ref}^2}$:

1. Current limitation with i_d priority.
2. Current limitation with i_q priority.
3. Equal limitation of i_d and i_q without angle change.
4. No current limitation.

Figure 6.3 gives a schematic representation of the approaches one to three. The current magnitude I_{ref} is limited to a maximum magnitude of $I_{max} = 1.1$ p.u., which forms a circle with the radius I_{max} around the origin in the dq plane. The fourth approach serves as a comparative case to observe the impact of the current limiter and does not involve any current limiting.

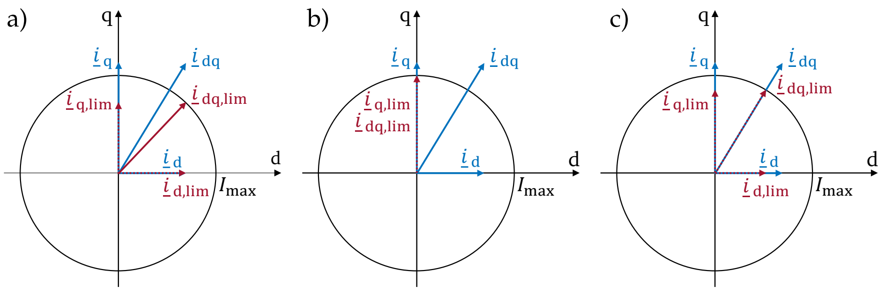

Figure 6.3: Current limiting approaches for the inverter-based generator (IBG) model: a) i_d priority, b) i_q priority and c) current limitation without angle change in accordance with [189].

In the first implementation, the current d component i_d has higher priority, so it is not limited unless the current i_d is larger than the permissible magnitude $i_{d,ref} > I_{max}$ as given in (6.10). If the reference current amplitude $I_{ref} > I_{max}$, the q component of the reference current $i_{q,ref}$ is limited to the maximum permissible value while keeping the d component $i_{\mathrm{d,ref}}$ constant. This relation is given in (6.11). If the current magnitude is $I_{\mathrm{ref}} \leq I_{\max}$, neither the current d component $i_{\mathrm{d,ref}}$ nor the q component $i_{\mathrm{q,ref}}$ need to be limited.

$$i_{\mathrm{d,ref,lim}} = \begin{cases} I_{\max} & \text{if} \quad i_{\mathrm{d,ref}} \geq I_{\max} \\ i_{\mathrm{d,ref}} & \text{if} \quad i_{\mathrm{d,ref}} < I_{\max} \end{cases} \tag{6.10}$$

$$i_{\mathrm{q,ref,lim}} = \begin{cases} \sqrt{I_{\max}^2 - i_{\mathrm{d,ref,lim}}^2} & \text{if} \quad I_{\mathrm{ref}} \geq I_{\max} \\ i_{\mathrm{q,ref}} & \text{if} \quad I_{\mathrm{ref}} < I_{\max} \end{cases} \tag{6.11}$$

The second implementation switches the reference current d and q components $i_{\mathrm{d,ref}}$ and $i_{\mathrm{q,ref}}$ and prioritises the q component $i_{\mathrm{q,ref}}$. Analogous to (6.10) and (6.11), the q axis reference current $i_{\mathrm{q,ref}}$ is only limited if $i_{\mathrm{q,ref}} > I_{\max}$ and the d component is limited accordingly.

The third current limiter implementation does not prioritise a current component, but limits the reference current magnitude I_{ref} without angle change as shown in Figure 6.3 c) in polar form. The magnitude is then limited to $I_{\mathrm{ref}} \leq I_{\max}$. From the magnitude and angle, the limited d and q axis reference current $i_{\mathrm{dq,ref,lim}}$ can be calculated using (6.12) and (6.13). In this work, the current limiter without angle change is the default limiter as during operation, the IBG must provide both, frequency and voltage support and the i_{d} priority can lead to disadvantages during low-voltage ride-through events [14].

$$i_{\mathrm{d,ref,lim}} = \begin{cases} i_{\mathrm{d,ref}} \cdot \frac{I_{\max}}{\sqrt{i_{\mathrm{d,ref}}^2 + i_{\mathrm{q,ref}}^2}} = i_{\mathrm{d,ref}} \cdot \frac{I_{\max}}{I_{\mathrm{ref}}} & \text{if} \quad I_{\mathrm{ref}} \geq I_{\max} \\ i_{\mathrm{d,ref}} & \text{if} \quad I_{\mathrm{ref}} < I_{\max} \end{cases} \tag{6.12}$$

$$i_{\mathrm{q,ref,lim}} = \begin{cases} i_{\mathrm{q,ref}} \cdot \frac{I_{\max}}{\sqrt{i_{\mathrm{d,ref}}^2 + i_{\mathrm{q,ref}}^2}} = i_{\mathrm{q,ref}} \cdot \frac{I_{\max}}{I_{\mathrm{ref}}} & \text{if} \quad I_{\mathrm{ref}} \geq I_{\max} \\ i_{\mathrm{q,ref}} & \text{if} \quad I_{\mathrm{ref}} < I_{\max} \end{cases} \tag{6.13}$$

An exemplary comparison of the four current limiter implementations and their impact on the IBG limited current references $i_{\mathrm{dq,ref,lim}}$ is presented in Figure 6.4. The testbench presented in Chapter 5.1 is simulated with closed switch S1 and the SG and loads in default parametrisation. A loadstep $\Delta P_{\mathrm{L0}} = 5$ MW is applied to load L0 and the IBG control is investigated. The IBG current limiting becomes active when the current phasor I_{ref} reaches the maximum admissible current limit $I_{\max}$, which occurs approximately at $t = 900$ ms. Up to this time instant, the current curves do not differ and are not limited. Additionally, in quasi-steady state, the reference current phasor I_{ref} is smaller than the current limit $I_{\max}$, and no current limiting occurs.

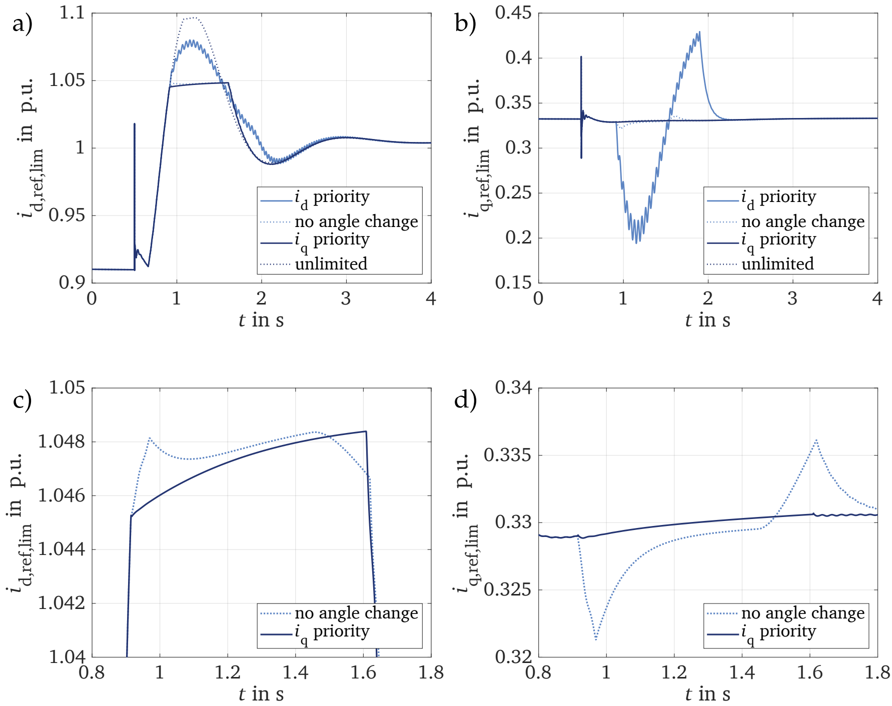

Figure 6.4: Comparison of current limiters:
a) Limited direct current reference,
b) limited quadrature current reference,
c) zoom into the limited direct current reference and
d) zoom into the limited quadrature current reference.

In Figure 6.4 a), the i_{d} priority implementation exhibits a proportional course of the direct current reference $i_{\mathrm{d,ref,lim}}$ with respect to the frequency deviation Δf. In Figure 6.4 b), the quadrature current reference $i_{\mathrm{q,ref,lim}}$ is reduced in favour of the direct current reference $i_{\mathrm{d,ref,lim}}$ and shows an overshoot after the direct current reference $i_{\mathrm{d,ref,lim}}$ reaches its peak and is reduced again. A small high-frequency oscillation is visible in both the direct and quadrature current when using the i_{d} priority current limiter. This is due to the limiter including a rate limit for the current adaptation in order to avoid fast transients. The current limiting implementation without angle change, as well as the i_{q} priority implementation, show a clear reduction in the direct current reference $i_{\mathrm{d,ref,lim}}$. These similar curves can be explained by the quadrature current reference $i_{\mathrm{q,ref,lim}}$, which remains unchanged, because of the loadstep being implemented as an active power disturbance with only minor effects on the voltage. However, in cases of short circuits and FRT, the adaptation of the quadrature current reference $i_{\mathrm{q,ref,lim}}$ is more relevant, as shown in [14]. The i_{q} priority implementation maintains the quadrature current reference $i_{\mathrm{q,ref,lim}}$ constant, and the current limiting without angle change shows a slight deviation towards the i_{d} priority curve. On the other hand, the implementation without current limiting keeps the quadrature current reference $i_{\mathrm{q,ref,lim}}$ constant but allows the direct current reference $i_{\mathrm{d,ref,lim}}$ to reach higher values, resulting in a large current phasor $I_{\mathrm{ref}} \approx \sqrt{1.095^2 + 0.33^2}$ p.u. $= 1.14$ p.u. $> I_{\max}$.

Current Limitation: Despite the fact that the current limiting with i_{d} priority represents the best current limiter for the frequency analysis, the equal limiting of i_{d} and i_{q} is used as the default current limiter. The reason for this is that decentralised inverter-based generators usually also take over the local voltage control and fault ride-through functions. With the no-angle-change limiter, both the voltage and frequency support, can be equally applied.

6.2.5 *Voltage Limiter*

The voltage references $v_{\mathrm{dq,ref}}$ are the output of the inner control. These references are limited as is done for the reference currents in order to cope with the requirements for the DC voltage V_{dc}. The limit is implemented as a saturation with a magnitude limit $V_{\max} = 1.2$ p.u., but does not become relevant in the studies of this work.

6.3 DIRECT VOLTAGE CONTROL MODEL

Direct voltage control has first been proposed in [190, 191] for wind turbine application. It provides direct, fast and continuous voltage control and is commonly considered a grid-forming control regarding voltage stability [18]. The control concept relies on the cascaded vector control and a frequency and angle measurement comparable to the described grid-supporting control. The signal processing, outer control and voltage limiting remain unchanged. The basic concept of the direct voltage control is to remove the integral part of the inner current control, thereby controlling the AC voltage directly through a feed-forward controller. The integral part can be removed yielding $k_{\mathrm{I,IC}} = 0$ because of the PI controller upstream in the outer control, which counteracts control deviations. An additional high-pass washout filter extends the inner control as depicted in Figure 6.5. The high-pass filter time constant τ_{HP} is chosen to $\tau_{HP} = 1/\omega_n$ [14, 191], where ω_n is the nominal frequency. The high-pass filter acts similar to an additional transient virtual resistor [191] and damps transient processes [14, 18].

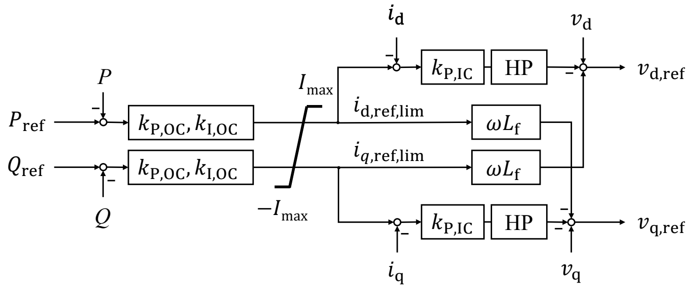

Figure 6.5: Overview of the direct voltage control concept, based on [192].

Additionally, the cross-coupling is carried out based on the limited current references $i_{dq,ref,lim}$ instead of using the measured currents i_{dq}. The calculation of the voltage reference $v_{dq,ref}$ can be reduced to (6.14) and (6.15).

$$v_{d,ref} = v_d - k_{P,IC} \cdot \Delta i_d(t) + \omega \cdot L_F \cdot i_{q,ref,lim} \tag{6.14}$$

$$v_{q,ref} = v_q - k_{P,IC} \cdot \Delta i_q(t) - \omega \cdot L_F \cdot i_{d,ref,lim} \tag{6.15}$$

Due to the missing integral part in the inner current control, the current limiter is adapted with a dynamic maximum current limit $I_{max,dvc}$ given in (6.16). The basic implementation of the current limiter is similar to the equal limitation without angle change presented in Chapter 6.2.4. The factor k_{red} is the gain of the adaptive current limit. The limited current for the direct voltage control can be described as follows [190]:

$$I_{max,dvc} = \begin{cases} I_{max} - k_{red} \cdot \left(\sqrt{i_{d,ref}^2 + i_{q,ref}^2} - I_{max} \right) & \text{if} \quad I_{ref} > I_{max} \\ I_{max} & \text{if} \quad I_{ref} \leq I_{max} \end{cases} \tag{6.16}$$

A comparison of the direct voltage control and the grid-supporting control using the current limiter without angle change is given in Figure 6.6. A load-step ΔP_{L0} is applied to the testbench with standard parametrisation described in Chapter 5.1 with switch S1 being closed. The settings in Figure 6.6 a) and b) are identical to the comparison of current limiters of the grid-supporting control in Figure 6.4. In Figure 6.6 c) and d) the IBG is set to partial-load operation of 70 %, which presents a case where no current limiting is necessary. The direct current reference shown in Figure 6.6 a) is limited to $i_{\mathrm{d,ref,lim}} = 0.98$ p.u. for the direct voltage control. The quadrature current reference $i_{\mathrm{q,ref,lim}}$ is only marginally deflected by the current limiter. When reaching the quasi-steady-state operation, the reference current phasor $I_{\mathrm{ref,lim}} = \sqrt{i_{\mathrm{d,ref,lim}}^2 + i_{\mathrm{q,ref,lim}}^2} = 1.03$ p.u. and the maximum admissible current $I_{\mathrm{max}} = 1.1$ p.u. is not reached. This is due to the adaptive current limit $I_{\mathrm{max,dvc}}$, which is reduced as presented in (6.16). The curves in Figure 6.6 c) and d) show that the impact of the direct voltage control is smaller compared to the grid-support if the current limit is not reached.

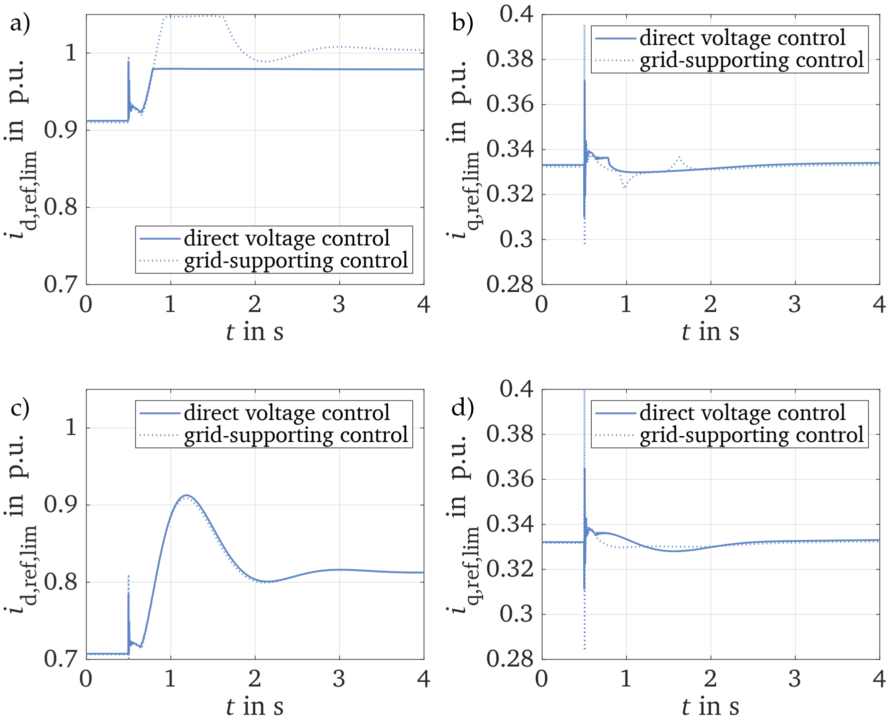

Figure 6.6: Current limitation of the direct voltage control compared to the grid-supporting control using a current limiter without angle change in the medium-voltage (MV) testbench with the default parametrisation in Chapter 5.1 and a loadstep $\Delta P_{\mathrm{L0}} = 5$ MW:
a) Limited direct current reference and
b) limited quadrature current reference when reaching the current limit.
c) Limited direct current reference and
d) limited quadrature current reference whithout reaching the current limit.

Direct Voltage Control: Depending on the definition, the direct voltage control is classified as grid-forming in terms of its voltage behaviour. This is because the inner PI controller is replaced by a P controller and the voltage is therefore controlled directly and without delay. However, the dynamic adjustment of the current limit has a major disadvantage in terms of the active power behaviour compared to grid-supporting control.

6.4 RMS AND EMT MODELLING

Annotation: Parts of this chapter have already been published in [193]. To improve the reading flow, self-citations are omitted.

In EMT simulations, detailed switching devices and transients in power systems can be adequately modelled taking into account time-varying quantities. In contrast, the computational effort is relatively high. RMS simulation tools calculate the phasors of sinusoidal quantities, which adequately models slower dynamics with less computation time and a numerical integration time step in the range of 1...10 ms [111]. In SG-dominated systems, RMS simulation tools are the preferred option for power system stability studies, because of the low computational burden and fast simulation speed. In return, the RMS simulation forces model developers to implement simplifications compared to the control design of the real components. Depending on the type of study, this can lead to inaccuracies and is therefore not suitable for every investigation [128]. EMT simulations can be more accurate, but with small integration time steps in the range of 50 μs, they take significantly more execution time than RMS simulations. In literature, different studies show that the choice of simulation type is not clear for power systems with high shares of IBG. Although the increasing number of decentralised IBG must be modelled in a reduced and easy way with low computational burden, the faster dynamics in low-inertia power systems can lead to the need of EMT models. In [111], the choice of simulation type is made according to the grid strength measured as short-circuit ratio (SCR) at the IBG connection point.

Figure 6.7 shows the frequency at busbar BB1 f_{BB1} and IBG active power P_{IBG} following a loadstep $\Delta P_{\mathrm{L0}} = 10$ MW for the RMS and EMT implementation of the medium-voltage testbench. The setup corresponds to the default MV testbench presented in Chapter 5.1. The IBG inner control is neglected in the RMS model based on the assumption that its settling time is faster than the RMS integration time step. Both models are of type 6 as described in Chapter 3.2. While in EMT, the frequency measurement by a PLL relies on the three-phase voltage measurement, in RMS the frequency is measured using the voltage phasor and calculating the derivative of the phase angle change.

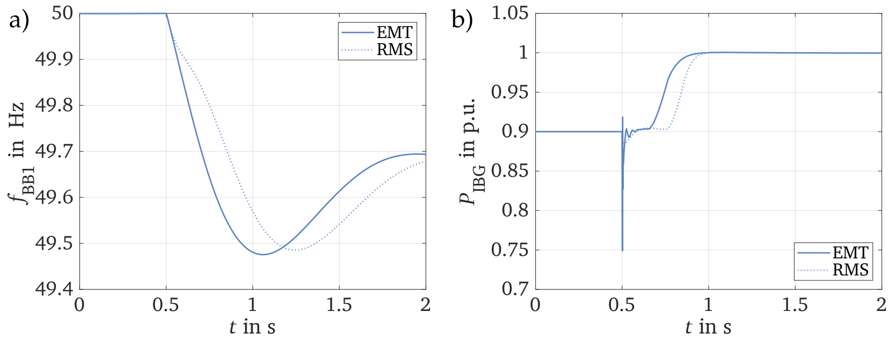

Figure 6.7: Comparison of the medium-voltage (MV) testbench results in RMS and EMT simulation based on the default parametrisation in Chapter 5.1 with a loadstep $\Delta P_{\mathrm{L0}} = 10$ MW.
a) Frequency at busbar BB1 and
b) IBG active power infeed using a linear fast frequency response (FFR).

The dynamic active power response of the IBG model in RMS exhibits a time delay to the loadstep and the EMT active power curve. This delay results from the frequency measurement for RMS simulations due to a relatively large time constant compared to the EMT frequency measurement by a PLL. Besides the distinct time delay, the transient peak and oscillation during the first 100 ms are not represented in RMS due to its characteristic phasor solution that does not solve the components' differential equations and has larger integration time steps. Due to this time delay, the dynamic frequency curve cannot be met by the RMS simulation and this work focuses solely on investigations in EMT simulation. Further details on the comparison of RMS and EMT dynamic frequency investigations can be found in [193] and on the modelling approaches in [111].

6.5 SUMMARY

The inverter-based generator model can be divided into an electrical part and a control part. The electrical part consists of the DC-side capacitor and a constant DC voltage source. The grid-side inverter is modelled as an average-value model, which is a controllable AC voltage source. The inverter model is connected through an LC-filter and a transformer to the grid. The cascaded vector control with grid-supporting functions is based on a local voltage, current and frequency measurement. Its output is the control signal for the AC voltage source representing the grid-side inverter. The frequency measurement through a phase-locked loop (PLL) is a frequency control input and is sensitive to the parametrisation of the PLL during transient processes. The outer power control and inner current control are based on two proportional-integral controllers each. A current limiter restricts the current magnitude to $I_{\mathrm{max}} = 1.1$ p.u.. In the default implementation, the direct and quadrature current are limited equally, so that voltage and frequency support take place evenly.

As a comparison against the standard grid-supporting control, the direct voltage control is implemented in this work. The direct voltage control is partly considered a grid-forming control regarding the voltage control due to its very fast inner control. In contrast, for frequency events, a dynamic current limit due to the missing integral part of the inner control reduces the maximum power infeed and as a consequence shows disadvantages compared to the grid-supporting control.

All investigations and analyses in this work are carried out in electromagnetic transients (EMT) simulations as the phasor (RMS) simulations show large disadvantages concerning the frequency measurement during transients.

7 DISTRIBUTION GRID MODELS

Apart from the simple MV testbench presented in Chapter 5.1, the impact of IBG in distribution grids on the frequency support and system stability is studied in two benchmark grid models: A medium-voltage benchmark grid with six busbars and three IBG, which is a simplified version of the Cigré European medium-voltage benchmark grid [194] and a high-voltage grid in ring configuration taken from the power system transients (PST) 16-machine dynamic test system [73]. The distribution grid models are described here in brief and different levels of IBG integration are introduced for each grid. The aggregation or dynamic equivalent models, which are used to simplify the distribution grids are presented in Chapter 7.3.

7.1 MEDIUM-VOLTAGE BENCHMARK GRID

The medium-voltage benchmark grid model is shown in Figure 7.1 and taken from [195]. It is a simplified radial Cigré European medium-voltage benchmark grid [194] based on two feeders, which are fed by a transformer each. The original grid is simplified by network reduction to six loads L0 to L5, six busbars BB0 to BB5, three lines L1 to L3 and three IBG IBG1 to IBG3.

The external high-voltage grid consists of a sixth-order symmetrical three-phase SG as described in Chapter 5.2 with the parameters in Appendix A.1.2. The external grid is modelled as a weak high-voltage grid with a short-circuit power $S''_{\mathrm{SC}} = 800$ MVA. The SG is equipped with an excitation system, which implements a type-1 static excitation according to [196] including an automatic voltage regulator AVR. A power system stabiliser PSS counteracts the rotor oscillations and the governor Gov implements a speed droop characteristic as given in (5.7) [141]. A loadstep $\Delta P_{\mathrm{L0}} = 50$ MVA of the load L0 on the high-voltage side is carried out, which increases the load L0 by 50 %. The lines are modelled as cables of type NA2XS2Y 120 mm^2 with the line lengths given in Table 7.1.

The loads are represented as static *exp res-year* models, cf. Table 5.3 as default, but the impact of the frequency-dependent and dynamic load modelling is investigated. A total load apparent power $\sum S_{\mathrm{L1,3...5}} = 25.5$ MVA for feeder 1 and $S_{\mathrm{L2}} = 21.7$ MVA for feeder 2 is applied. The 110 kV / 20 kV transformers T1 and T2 have a rated power $S_{\mathrm{r,T}} = 30$ MVA each. The detailed parameters of lines and transformers are given in [194].

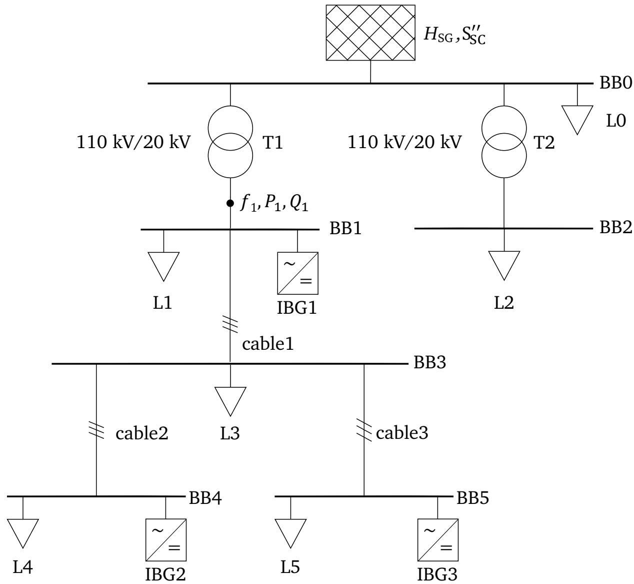

Figure 7.1: Medium-voltage benchmark grid based on the Cigré European medium-voltage benchmark grid [194].

The impact of the IBG on the frequency dynamics is investigated through different scenarios. The first scenario does not include any IBG and serves as a reference scenario against which the others are compared. The basic scenario includes a total installed IBG power $S_{\text{IBG}} = S_{\text{r,IBG1}} + S_{\text{r,IBG2}} + S_{\text{r,IBG3}} = 6.24$ MVA as defined in [14, 194]. This corresponds to about 25 % of the rated load power demand in feeder 1. The third scenario increases the share of IBG to the maximum permissible installed power $S_{\text{IBG}} = 28$ MVA according to the 2-%-voltage rule defined in the German grid code [132]. Due to all installed generation plants in a string, the voltage in the grid must not change more than 2 % at any busbar compared to the grid without any generation. The IBG1 with a rated power $S_{\text{r,IBG1}} = 18$ MVA is realised as three individual plants with a rated power of 6 MVA each.

The maximum installed IBG power $S_{\text{IBG}} = 28$ MVA exceeds the load $\sum S_{\text{L1,3...5}} = 25.5$ MVA in feeder 1. However, since the IBG are operated with a power factor $\cos\varphi \neq 1$ and in 80 % partial load operation, power flow reversal only occurs in the event of severe frequency drops and the frequency support from the IBG. For the aggregation of the medium-voltage benchmark grid, frequency and power measurements are taken at busbar BB1. As the feeder supplied by transformer T2 represents an industrial load without installed IBG, the focus is on the feeder 1.

Table 7.1: Default parameters of the medium-voltage benchmark grid.

component	part	parameters	
external	SG	$H_{SG} = 6$ s	$S_{r,SG} = 200$ MVA
	SG	$d_{Gov} = 2$ %	$S''_{SC} \approx 800$ MVA
loads	ΔL0	$\Delta P_{L0} = 50$ MW	
	L0	$P_{L0} = 100$ MW $+ \Delta P_{L0}$	$Q_{L0} = 0$ Mvar
	L1	$P_{L1} = 19.84$ MW	$Q_{L1} = 6.43$ Mvar
	L2	$P_{L2} = 20.58$ MW	$Q_{L2} = 6.76$ Mvar
	L3	$P_{L3} = 0.50$ MW	$Q_{L3} = 0.22$ Mvar
	L4	$P_{L4} = 1.71$ MW	$Q_{L4} = 0.56$ Mvar
	L5	$P_{L5} = 2.11$ MW	$Q_{L5} = 0.86$ Mvar
lines	cable1	$l = 7.24$ km	
	cable2	$l = 0.61$ km	
	cable3	$l = 1.3$ km	
transformers	T1,T2	$S_{r,T} = 30$ MVA	Dyn1
	T1	tap changer +6.25 %	
	T2	tap changer +3.125 %	

Table 7.2: Scenario definition for the medium-voltage benchmark grid. Power factors are given as overexcited (oe) or underexcited (ue).

scenario	IBG1	IBG2	IBG3
no IBG	$S_r = 0$ MVA	$S_r = 0$ MVA	$S_r = 0$ MVA
basic IBG	$S_r = 2.08$ MVA	$S_r = 2.08$ MVA	$S_r = 2.08$ MVA
	$\cos\varphi = 1$	$\cos\varphi = 0.95$ (ue)	$\cos\varphi = 0.95$ (ue)
max IBG	$S_r = 18$ MVA	$S_r = 5$ MVA	$S_r = 5$ MVA
	$\cos\varphi = 0.98$ (oe)	$\cos\varphi = 0.9$ (ue)	$\cos\varphi = 0.9$ (ue)

Within the max IBG scenario with $S_{\mathrm{IBG}} = 28$ MVA, four variations of the FFR implementation for each IBG are distinguished as presented in Table 7.3. The variations are done in the max IBG scenario as the absolute differences are larger for larger installed IBG powers. The default variation is the homogeneous frequency control using linear FFR only. The homogeneous constant FFR variation employs the constant FFR solely. Finally, two inhomogeneous variations apply a combination of both FFR implementations: The mixed FFR 1 variation models IBG1 utilising linear FFR and IBG2 and IBG3 implementing constant FFR and the mixed FFR 2 variation applies the FFR implementations vice versa. The constant FFR of IBG1 with three individual plants is implemented such that the active power adaptation ΔP_{FFR} is shared equally between the plants.

Table 7.3: Definition of the fast-frequency response (FFR) variations within the medium-voltage benchmark grid.

FFR variation	IBG1	IBG2	IBG3
linear FFR	linear	linear	linear
constant FFR	constant	constant	constant
mixed FFR 1	linear	constant	constant
mixed FFR 2	constant	linear	linear

7.2 HIGH-VOLTAGE BENCHMARK GRID

The high-voltage benchmark grid in ring configuration as shown in Figure 7.2 is taken from the PST 16-machine dynamic test system presented in [73]. The high-voltage grid consists of six loads L1 to L6, six overhead lines OHL1 to OHL6 and up to six windfarms WF1 to WF6. The loads are connected to the high-voltage busbars BB1 to BB6 with a total apparent power $\sum S_{\mathrm{L1...L6}} = 150$ MVA and are modelled as ZIP models as default. The external ultra-high voltage grid is connected to busbar BB1 via a transformer T1 and modelled as a SG with the parameters given in Appendix A.1.3 and a short-circuit power $S''_{\mathrm{SC}} \approx 2300$ MVA. The basic parameters of the high-voltage benchmark grid are given in Table 7.4.

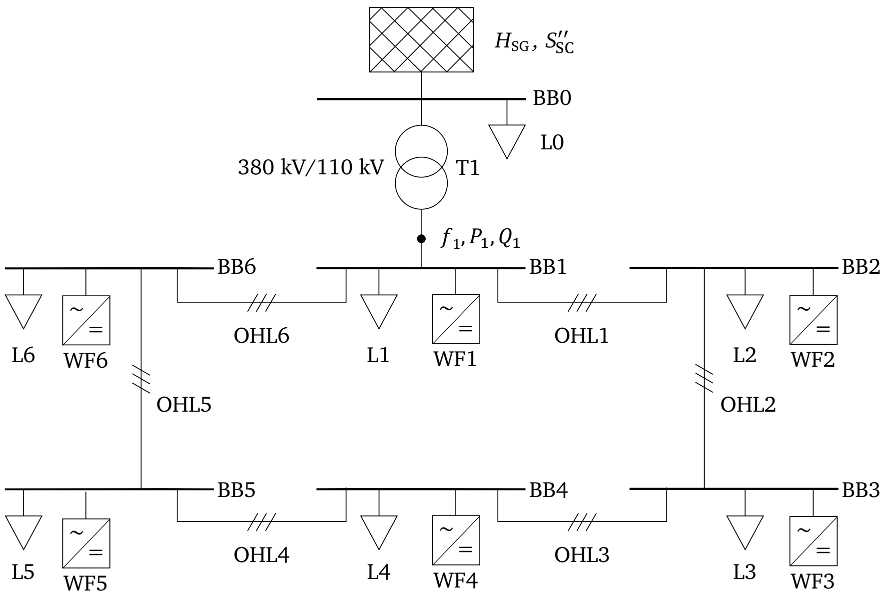

Figure 7.2: High-voltage benchmark grid based on the PST 16-machine dynamic test system [73].

The windfarm model consists of a radial or string configuration [197] depicted in Figure 7.3 with the parallel connection of five wind turbines with a rated power $S_{\mathrm{r,WT}} = 6$ MVA each. The wind turbines are modelled as IBG described in Chapter 6. Between each wind turbine is a cable with a line length $l = 0.8$ km. A transformer 110-kV/20-kV connects the windfarm to the high-voltage grid. The windfarm is modelled such that all wind turbines of a windfarm apply the same

Table 7.4: Default parameters of the high-voltage benchmark grid.

component	part	parameters	
external	SG	$H = 6.5$ s	$S_{\text{r,SG}} = 500$ MVA
grid	SG	$d_{\text{Gov}} = 2$ %	$S''_{\text{SC}} \approx 2300$ MVA
loads	ΔL0	$\Delta P_{\text{L0}} = 100$ MW	
	L0	$P_{\text{L0}} = 200 \text{ MW} + \Delta P_{\text{L0}}$	$Q_{\text{L0}} = 0$ Mvar
	L1, L5, L6	$P_{\text{L}} = 28.5$ MW	$Q_{\text{L}} = 9.368$ Mvar
	L2, L3, L4	$P_{\text{L}} = 17$ MW	$Q_{\text{L}} = 10.54$ Mvar
lines	OHL1	$l = 30$ km	
	OHL2 to OHL6	$l = 20$ km	
transformer	T1	$S_{\text{r,T}} = 300$ MVA	Dyn1
	T1	$V_{\text{HV}}/V_{\text{LV}} = 380 \text{ kV}/110 \text{ kV}$	
	T1	tapchanger + 5 %	
windfarm	WF	$V_{\text{WF}} = 23$ kV	$S_{\text{r,WF}} = 30$ MVA
	WF	$n = 5$	$S_{\text{r,WT}} = 6$ MVA
	T_{WF}	$S_{\text{r,T,WF}} = 40$ MVA	Dy11

control and frequency support. The windfarm operates at a voltage $V_{\text{WF}} = 23$ kV and with a transformer rated power $S_{\text{r,T,WF}} = 40$ MVA. Further parameters of the windfarm are given in Table 7.4.

Three scenarios according to Table 7.5 are distinguished: In the first scenario no IBG are connected for reference purposes. The second scenario includes a windfarm at bus BB4 with the rated power $S_{\text{r,WF4}} = 30$ MVA. In the third scenario, a windfarm is connected to each high-voltage busbar with a total installed IBG power $\sum S_{\text{WF1...6}} = 180$ MVA.

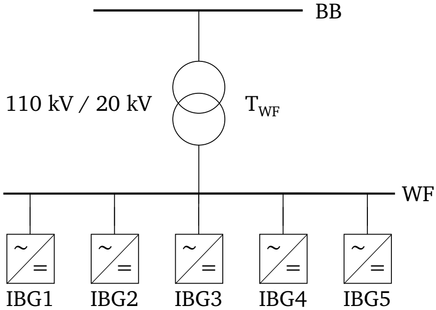

Figure 7.3: Windfarm model in string configuration, based on [197].

Table 7.5: Scenario definition for the high-voltage benchmark grid.

scenario	windfarm
no IBG	none
basic IBG	$S_{\mathrm{r,WF4}} = 30$ MVA and $S_{\mathrm{r,WF1,2,3,5,6}} = 0$ MVA each
max IBG	$S_{\mathrm{r,WF1,2,3,4,5,6}} = 30$ MVA each

7.3 DYNAMIC EQUIVALENT MODELS

For the aggregation of the distribution grids, a single machine model as shown in Figure 7.4 is chosen as the fitting model. It consists of a single aggregated load and a single aggregated IBG that are connected to busbar BB1 via a variable line. The external grid, its transformer, the frequency and power measurements as well as the load L0 and load step ΔP_{L0} are not changed. The aggregated load, the aggregated IBG and the two lines only differ in terms of the parameters applied, the model structures remain unchanged. The parameters to be obtained by the greybox approach are summarised in the parameter vector $\mathbf{x} = [\mathbf{x}_{\mathrm{IBG}} \;\; \mathbf{x}_{\mathrm{line}} \;\; \mathbf{x}_{\mathrm{L}}]$ in (7.1) to (7.3) with S_{IBG}, $\cos\varphi_{\mathrm{IBG}}$, d_{FFR}, db_{FFR}, $k_{\mathrm{P,OC}}$, $k_{\mathrm{I,OC}}$, l_{line}, $R^{'}_{\mathrm{line}}$, $L^{'}_{\mathrm{line}}$, $C^{'}_{\mathrm{line}}$, P_{L1} and Q_{L1} being the IBG aggregated rated power and power factor, the IBG linear FFR droop and deadband, the IBG outer control proportional and integral controller, the line length and length-dependent resistance and inductance as well as the aggregated load active and reactive power. Further details on the limits of each parameter are given in Chapter 10.1. The load $\mathrm{L1}_{\mathrm{agg}}$ is modelled as a constant impedance load model, which corresponds to the static exponential load model described in Chapter 5.3.1.1 with the active and reactive power-voltage exponents in (5.14) being $k_{\mathrm{pv}} = k_{\mathrm{qv}} = 2$.

$$\mathbf{x}_{\mathrm{IBG}} = [S_{\mathrm{IBG}} \;\; cos\varphi_{\mathrm{IBG}} \;\; d_{\mathrm{FFR}} \;\; db_{\mathrm{FFR}} \;\; k_{\mathrm{P,OC}} \;\; k_{\mathrm{I,OC}}] \tag{7.1}$$

$$\mathbf{x}_{\mathrm{line}} = [l_{\mathrm{line1}} \;\; R'_{\mathrm{line1}} \;\; L'_{\mathrm{line1}} \;\; l_{\mathrm{line2}} \;\; R'_{\mathrm{line2}} \;\; L'_{\mathrm{line2}}] \tag{7.2}$$

$$\mathbf{x}_{\mathrm{L1}} = [P_{\mathrm{L1}} \;\; Q_{\mathrm{L1}}] \tag{7.3}$$

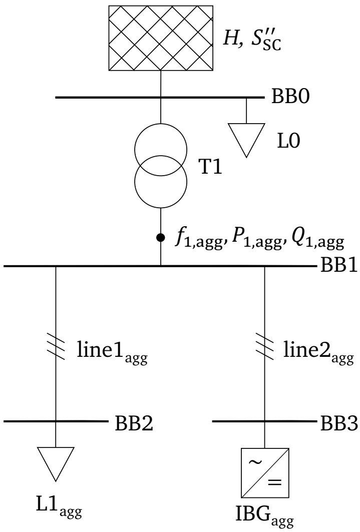

Figure 7.4: Fitting model for the greybox aggregation.

7.4 MODEL PARAMETER FITTING

As shown in Chapter 4.1, it is assumed that the reactions of a dynamic equivalent model correspond to the reactions of the detailed distribution grid. To fulfil this condition, the parameters of the dynamic equivalent model must be identified. The parameters of the vector x given in (7.1) to (7.3) are searched for and optimised using the PSO and DE algorithms. The aim of this process is that for each discrete time t, the active power $P_{1,\mathrm{agg}}(x,t)$ and the reactive power $Q_{1,\mathrm{agg}}(x,t)$ of the dynamic equivalent can reproduce the active and reactive power curves $P_1(t)$ and $Q_1(t)$ of the detailed distribution grid. Before optimisation, the minimisation problem can be formulated using the mean squared error for the active power P and reactive power Q according to equations (7.4), (7.5) and (7.6) [67, 152]. The objective function $\epsilon(\boldsymbol{x})$ has the unit MVA^2. The smaller the resulting value from the objective function, the better the model parameters are estimated and the better the dynamic equivalent reproduces the original power curves.

$$\epsilon_P(\boldsymbol{x}) = \frac{1}{n}\sum_{t=0}^{n}[P_1(t) - P_{1,\text{agg}}(\boldsymbol{x}, t)]^2 \tag{7.4}$$

$$\epsilon_Q(\boldsymbol{x}) = \frac{1}{n}\sum_{t=0}^{n}[Q_1(t) - Q_{1,\text{agg}}(\boldsymbol{x}, t)]^2 \tag{7.5}$$

$$\min_{\boldsymbol{x}} \epsilon(\boldsymbol{x}) = \min_{\boldsymbol{x}}[\epsilon_P(\boldsymbol{x}) + a \cdot \epsilon_Q(\boldsymbol{x})] \tag{7.6}$$

The objective function $\epsilon(\boldsymbol{x})$ is also known as the minimisation of the least-square minimisation problem and has the task of comparing and evaluating the power curves P_1, Q_1 of the reduced and detailed grid. The factor a is the weight assigned to the reactive power Q compared to the active power P. In the context of this thesis, $a = 1$ is assumed. Since the analytical expression of the first and second order derivative of the objective function $\epsilon(\boldsymbol{x})$ cannot be derived, the standard mathematical methods cannot be used unless these derivatives are estimated numerically [67, 152]. For this reason, a metaheuristic optimisation method according to Chapter 4.1 is used and executed until the difference between the simulation results of the dynamic equivalent and the detailed network is as minimal as possible. The default maximum number of iterations of the optimisation is chosen to 50 as a compromise between simulation effort and quality of the results.

7.5 SUMMARY

This chapter focuses on the distribution grid models, specifically the medium-voltage and high-voltage benchmark grid studied in this work. The generic medium-voltage testbench for testing of individual grid components is presented in Chapter 5.1. The medium-voltage benchmark grid, derived from the Cigré European medium-voltage benchmark grid, is presented with details on its components and parameters. Three different scenarios are examined, including variations in the share of inverter-based generators (IBG). For the max IBG scenario, four variations regarding the distribution of the linear and constant fast-frequency response at each IBG are defined. The high-voltage benchmark grid, based on the PST 16-machine dynamic test system, is introduced, including details on the components with a focus on the windfarm model. Again, three scenarios according to the share of IBG, respectively windfarms, are outlined.

The chapter also discusses the dynamic equivalent model used for the greybox aggregation. A fitting model is proposed, consisting of an aggregated load and an aggregated IBG connected to a busbar through a variable line each. The parameters to be optimised using the metaheuristic algorithms particle swarm optimisation (PSO) and Differential Evolution (DE) algorithm are presented. The goal is to minimise the mean square deviation between the aggregated model and the detailed distribution grid in terms of active and reactive power. The chapter provides insights into the optimisation process and the progression of the objective function.

Part III

DYNAMICS OF ACTIVE DISTRIBUTION GRIDS

The power system is a highly complex system, which is never in steady state, but undergoes changes in power demand and supply. With the integration of high shares of inverter-based generation, the dynamic analysis of active distribution grids becomes indispensable.

8 DYNAMIC FREQUENCY RESPONSE OF AN INDIVIDUAL IMVERTER-BASED GENERATOR

The increasing integration of renewable energy sources into power systems necessitates a thorough understanding of the behaviour of individual IBG. Accurate analysis of IBG behaviour and its interaction with the grid is crucial for ensuring grid stability and efficient utilisation of renewable energy resources.

This chapter investigates the behaviour of an individual IBG using the medium-voltage testbench described in Chapter 5.1. The objectives of this investigation are threefold:

1. to examine the IBG behaviour, relevant sensitivities and operational limits for dynamic frequency studies with a minimal computational burden,
2. to validate the frequency measurement and evaluation approaches, such as the RoCoF and frequency nadir calculation, and
3. to establish an understanding of the simple testbench, which resembles the aggregation model presented in Chapter 7.3.

This chapter is structured as follows: The medium-voltage testbench in its standard parametrisation is presented in Chapter 8.1. An evaluation of frequency measurement, RoCoF and frequency nadir calculation is elaborated in Chapter 8.2. Chapter 8.3 evaluates possible sensitivities of the testbench, which influence the frequency and/or the IBG behaviour. An overview of the investigations carried out in the medium-voltage testbench is given in Figure 8.1.

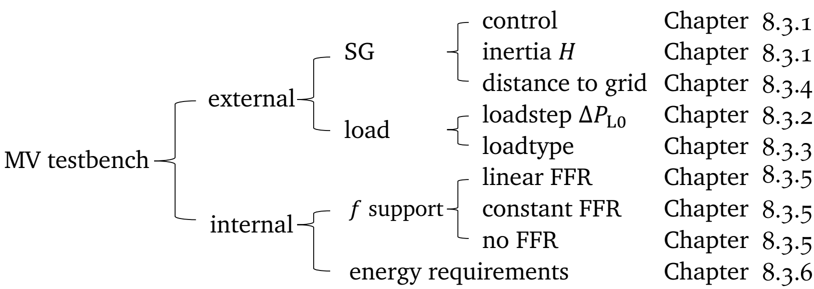

Figure 8.1: Overview of the investigations carried out in the medium-voltage testbench.

8.1 MEDIUM-VOLTAGE TESTBENCH IN DEFAULT PARAMETRISATION

In this section, the simple medium-voltage testbench in its standard parameterisation as presented in Chapter 5.1 and Figure 5.1 and its dynamic processes in response to a loadstep are presented. The fundamental default parameters of the medium-voltage testbench are given in the Appendix A.5, Table A.16 and for the grid-supporting IBG control in the Appendix A.4, Table A.15. The IBG is modelled with a rated power $S_{\mathrm{r,IBG}} = 3$ MVA, which corresponds to an average wind turbine or a small PV park. The SG is connected with a rated power $S_{\mathrm{r,SG}} = 30$ MVA, which corresponds to a subtransient short-circuit power $S''_{\mathrm{SC}} = 110$ MVA. According to [166], this is at the lower end of typical German medium-voltage grids. The load L1 is modelled as static exponential load *exp res-year* by default with a rated power $S_{\mathrm{r,L1}} = 5$ MVA. A loadstep $\Delta P_{\mathrm{L0}} = 5$ MW is applied and the line between busbar BB0 and busbar BB1 is neglected. Further parameters are given in the Appendix A.5, Table A.16 and in the Appendix A.4, Table A.15. The resulting frequency f, voltage v, currents i and powers P, Q in the medium-voltage testbench with default parametrisation are discussed here.

Figure 8.2 a) shows the SG rotational frequency f_{SG}. The frequency metrics can be observed as follows: A $\mathrm{RoCoF}_{500\mathrm{ms}} \approx -0.5$ Hz/s, a quasi-steady-state frequency deviation $\Delta f_{\mathrm{qss}} \approx 0.17$ Hz and a frequency nadir $f_{\min} \approx 49.75$ Hz can be calculated from the frequency curve. The quasi-steady-state frequency deviation Δf_{qss} is identical to the one calculated in (5.13) for the medium-voltage testbench without IBG. This is because the quasi-steady-state frequency is within the deadband of the IBG frequency control. No active power adjustment of the IBG applies during that time instant. Solely the SG defines the quasi-steady-state frequency deviation in this scenario. The RoCoF is smaller than the one calculated in (5.12) without IBG, which can be explained by the inherent behaviour of the IBG filter capacitance C_{f}. The corresponding current infeed is explained below.

The voltage v_1 at busbar BB1 is shown in Figure 8.2 b) and stays in a narrow band with the first transient peak being less than 2 % of the pre-fault voltage. There is no line between the SG and the loadstep. This is why the inductive behaviour of the SG dominates and decouples active and reactive power control. Since a pure active power is switched for the loadstep, the voltage deviation is relatively small and the SG automatic voltage regulator quickly counteracts the small deviation.

The currents in Figure 8.2 c) and d) show the IBG limited reference currents $i_{\mathrm{dq,ref,lim}}$. The IBG, SG and load power curves are shown in the Appendix A.6, Figure A.1. During pre- and post-fault quasi-steady state, the IBG control feeds the same constant power. The FFR does not become active as long as the frequency is within the deadband $db_{\mathrm{FFR}} = 200$ mHz. The outer control

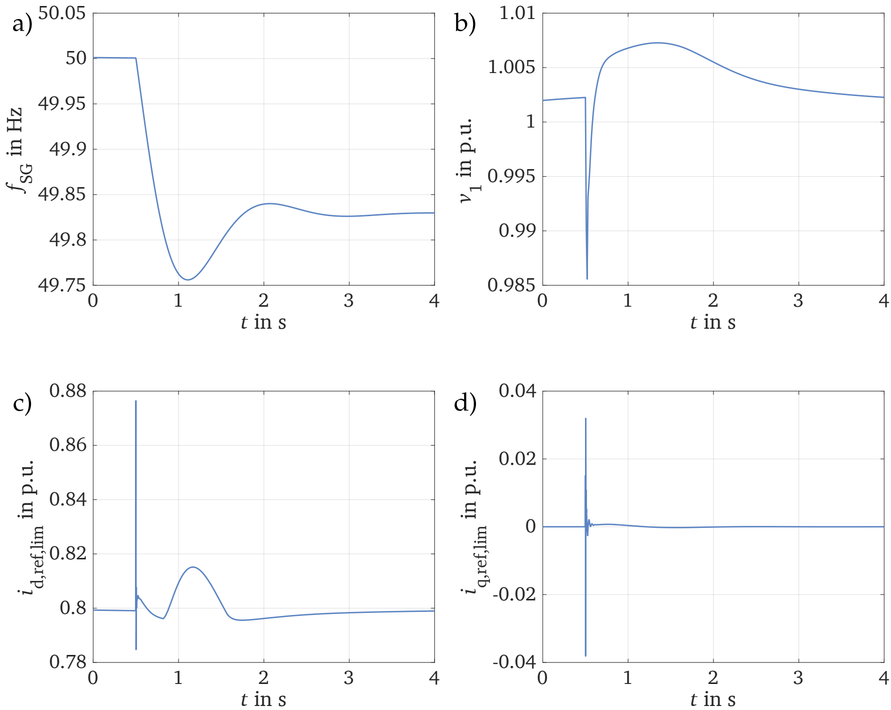

Figure 8.2: Dynamic reaction of the inverter-based generation (IBG) in the medium-voltage testbench following a loadstep $\Delta P_{L0} = 5$ MW:
a) frequency of the synchronous generator (SG),
b) voltage at busbar BB1,
c) IBG d axis current infeed and
d) IBG q axis current infeed.

adapts the currents accordingly to the measured voltage v_1, so that a constant power is fed into the grid.

At the time instant of the loadstep $t = 0.5$ s, a sudden additional d axis current occurs, which mainly results from the IBG filter capacitance C_f acting like an energy storage with instantaneous reaction. After a few miliseconds, the inner control reduces both the d axis and q axis currents towards the pre-fault values. As soon as the frequency reaches the deadband $db_{FFR} = 200$ mHz, an adaptation of the IBG active power proportional to the frequency deviation is realised by the FFR control, cf. Chapter 3.4. With the FFR droop $d_{FFR} = 0.05$ and a frequency difference between FFR frequency deadband and the frequency nadir $f_{\mathrm{db,FFR}} - f_{\mathrm{min}} \approx 49.8$ Hz $- 49.75$ Hz $= 0.05$ Hz, the IBG active power increase can be calculated using (8.1).

$$\Delta P_{\mathrm{IBG}} = \frac{\Delta f}{d_{\mathrm{FFR}}} = \frac{0.001 \text{ p.u.}}{0.05} = 0.02 \text{ p.u.} \tag{8.1}$$

The IBG active power P_{IBG} follows the limited d axis reference current $i_{\mathrm{d,ref,lim}}$ as the voltage remains approximately constant. The active power consumption of the loads L0 and L1 as well as the SG governor control P_{Gov} and the SG active power infeed P_{SG} are given in the Appendix in Figure A.1. The loadstep $\Delta P_{\mathrm{L0}} =$ 5 MW is clearly visible. The load L1 is modelled as static *exp res-year* model, cf. Chapter 5.3.3 and adapts its active power consumption in dependency of the voltage. The SG governor control shows a typical active power curve proportional to the frequency. The SG active power output follows the loadstep $\Delta P_{\mathrm{L0}} = 5$ MW and includes the inertial reponse that immediately follows the additional active power demand of load L0.

8.2 FREQUENCY METRICS EVALUATION

The $\mathrm{RoCoF}_{500\mathrm{ms}}$, the frequency nadir f_{min} and the quasi-steady-state frequency deviation Δf_{qss} are calculated to evaluate the dynamic frequency. The method of the RoCoF calculation has a major impact on the results, whereas the latter two are straightforward to calculate from a given frequency curve $f(t)$.

The frequency nadir f_{min} is calculated as the minimum of the frequency curve $f(t)$ using (8.2). The quasi-steady-state frequency deviation Δf_{qss} is calculated by (8.3) as the difference between the quasi-steady-state frequency f_{qss} and the nominal frequency $f_{\mathrm{n}} = 50$ Hz.

The RoCoF can be calculated by differentiating the frequency curve $f(t)$ with respect to time. Differentiation yields the slope of the curve at each point, indicating how fast the frequency is changing at that specific time instant. Since the simulation leads to a discrete frequency measurement for each simulation time step, the slope is calculated between two consecutive time steps using (8.4). Due to transient processes, the slope between two consecutive time steps can be very large, e.g. as seen for the standard PLL parametrisation in Figure 6.2. In practice, larger time intervals $\Delta t = 100...1000$ ms are applied [26, 91].

$$f_{\mathrm{min}} = \min(f(t)) \tag{8.2}$$

$$\Delta f_{\mathrm{qss}} = f_{\mathrm{n}} - f_{\mathrm{qss}} \tag{8.3}$$

$$\mathrm{RoCoF} = \frac{f(t_0) - f(t_0 + \Delta t)}{\Delta t} \tag{8.4}$$

Table 8.1 shows the calculated frequency metrics for the basic parametrisation of the medium-voltage testbench and the frequency curve shown in Figure 8.2 a). The frequency nadir f_{min} and quasi-steady-state frequency deviation Δf_{qss} differ only marginally for the different frequency measurements as these quantities are measured after the transient processes have decayed. In contrast, the differences of the RoCoF results are pronounced, especially for the calculation over small time periods Δt. The type of frequency estimation has a major influence on the steepness of the frequency curve during transients and thus on the RoCoF. The PLL with standard parameters leads to a very large $\text{RoCoF}_{50\mu\text{s}}$, while the optimised parameters better approximate the SG frequency curve and RoCoF. The error between the SG rotational frequency and the PLL $\text{RoCoF}_{50\mu\text{s}}$ is 13 % for the optimised PLL parameters and 1366 % for the standard parameters, which is why larger time periods for the RoCoF calculation are usually applied [26, 91]. For a PLL time period $\Delta t = 500$ ms, the differences between PLL and SG based RoCoF calculation are reduced to 3.56 % and 1.45 % for the standard and optimised PLL parameters, respectively. In the following, the optimised parameters are applied for the PLL measurements and the rate limite RL for the RoCoF calculation is adapted depending on the inertia constant H_{SG}.

Table 8.1: Frequency nadir f_{min}, RoCoF and quasi-steady-state deviation Δf_{qss} results of the medium-voltage testbench.

f measurement	f_{min}	Δf_{qss}	$\text{RoCoF}_{50\mu\text{s}}$	$\text{RoCoF}_{500\text{ms}}$
SG	49.753 Hz	0.172 Hz	−0.796 Hz/s	−0.478 Hz/s
PLL standard	49.755 Hz	0.172 Hz	−11.673 Hz/s	−0.495 Hz/s
PLL optimised	49.755 Hz	0.173 Hz	−0.899 Hz/s	−0.485 Hz/s

8.3 SENSITIVITY ANALYSIS

Power system operators and planners of modern power systems must have a deep understanding of how various factors influence the system's performance and stability. Sensitivity analysis is a mathematical and computational technique employed to study the behaviour of power systems in response to variations in input parameters. These parameters can encompass a wide range of variables, including load demand, IBG integration, and control settings. Systematically evaluating how alterations in these parameters influence key performance metrics gives valuable insights into power system dynamics. Here, internal IBG-related and external sensitivities are investigated as presented in Figure 8.1.

8.3.1 *External Grid*

The SG representing the external grid is parametrised by the rated SG power $S_{r,SG}$, which impacts the subtransient short-circuit power S''_{SC}, cf. (5.11), the inertia constant H_{SG}, the turbine time constant T_{Tur} as well as the SG governor droop d_{Gov}, which models the primary frequency response. Further details on the derivation of these parameters as well as the fundamental dependencies of the frequency are given in Chapter 5.2. In addition, the line length between SG and busbar BB1 is varied in Chapter 8.3.4 in order to change the electrical distance between SG and IBG. Here, the focus is on the impact of the SG parameters on the IBG frequency support in form of the d axis current infeed $i_{d,ref,lim}$.

Figure 8.3 shows the IBG d axis current infeed $i_{d,ref,lim}$ in dependency of the four parameters of the external grid for a load step $\Delta P_{L0} = 5$ MW. The default values for each parameter are highlighted in bold in the legends, and the curves corresponding to these bold-marked values are identical within the four subplots. In all four subplots, the IBG current limit I_{max} is not reached. Furthermore, the results in Figure 8.3 can be explained by the impact of the SG parameters on the frequency curve as described in Chapter 5.2.

Figure 8.3 a) presents the impact of the inertia constant H_{SG} of the external grid on the IBG d axis current infeed $i_{d,ref,lim}$. The impact of the inertia constant is visible in the transient time range between the loadstep at $t = 0.5$ s and $t \approx 2$ s. With a smaller inertia constant, the frequency curve becomes steeper as shown in (5.12). The frequency deadband is reached earlier and the current deflection of the IBG occurs earlier and with a larger amplitude. The quasi-steady-state deviation Δf_{qss} is not affected by the inertia constant as shown in (5.13).

Figure 8.3 b) shows that a change in the governor droop d_{Gov} results in a d axis current infeed $i_{d,ref,lim}$, which is proportional to the frequency deviation Δf, cf. (5.13). For the default SG governor droop $d_{Gov} = 0.02$, the quasi-steady-state frequency deviation Δf_{qss} is smaller than the deadband of the IBG frequency support, so that the pre-fault current and with it the pre-fault power setpoint is reached again.

Figure 8.3 c) presents a proportional relation between the turbine time constant T_{Tur} and the IBG d axis current infeed $i_{d,ref,lim}$ peak. The turbine time constant T_{Tur} leads to a delay, but does not affect the quasi-steady state after the loadstep. Finally, the rated SG power $S_{r,SG}$ in Figure 8.3 d) has an influence on both, the transient and the quasi-steady state. This is because the external grid strength in form of the short-circuit power S''_{SC} is changed, cf. Chapter 5.2 and the ratio between loadstep ΔP_{L0} and SG rated power $S_{r,SG}$ increases. For the larger SG rated power, the frequency does not leave the IBG frequency support deadband.

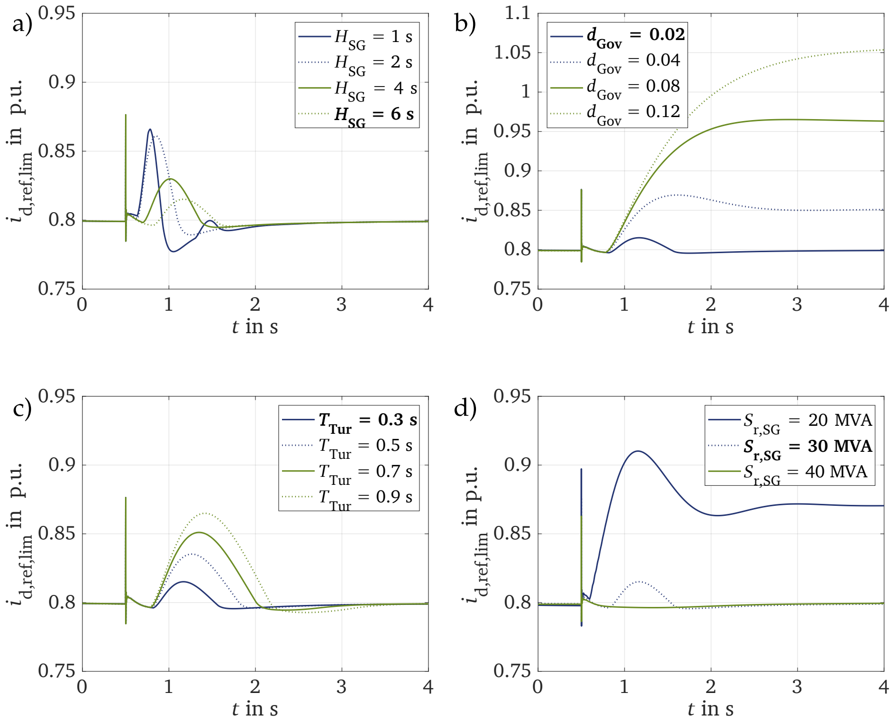

Figure 8.3: Impact of the external grid parameters on the inverter-based generation (IBG) d axis current infeed $i_{d,ref,lim}$ in the medium-voltage testbench following a loadstep $\Delta P_{L0} = 5$ MW:
a) Variation of the synchronous generator (SG) inertia constant H_{SG},
b) variation of the SG governor droop d_{Gov},
c) variation of the SG turbine time constant T_{Tur} and
d) variation of the SG rated power $S_{r,SG}$.

Figure 8.4 repeats the investigation for a loadstep $\Delta P_{L0} = 15$ MW, so that the IBG current limit $I_{max} = 1.1$ p.u. is reached in some cases. In all subplots the d axis current infeed $i_{d,ref,lim}$ is deflected further from its pre-fault value as the larger loadstep ΔP_{L0} leads to a larger frequency deviation. In Figure 8.4 a), the current limit I_{max} is not reached as the inertia constant only impacts the transient frequency course within the first two seconds following the loadstep. During this short time range, the additional current infeed is not as large as for other cases.

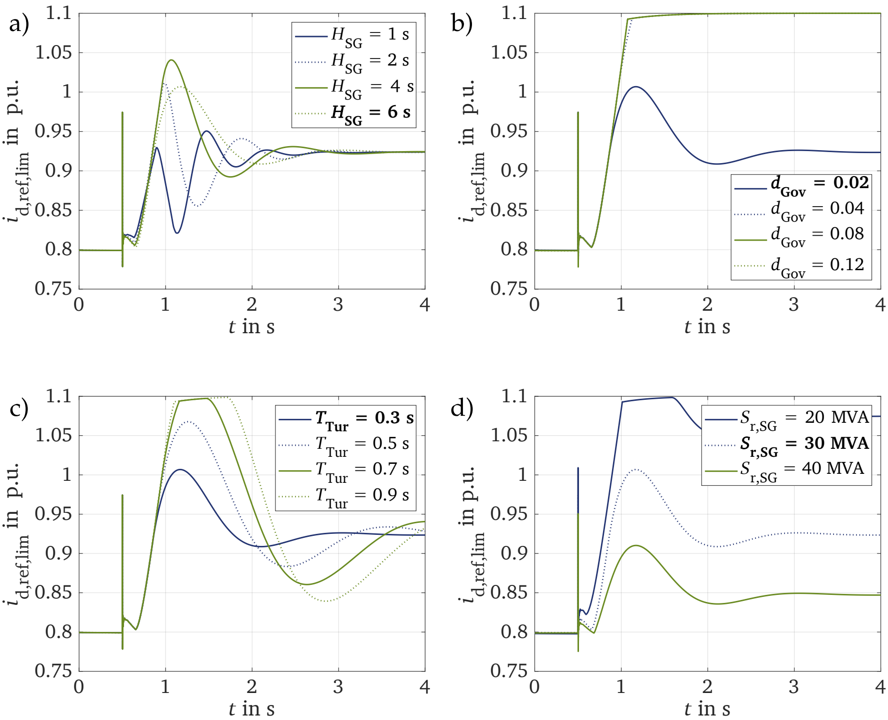

Figure 8.4: Impact of the external grid parameters on the inverter-based generation (IBG) d axis current infeed $i_{d,ref,lim}$ in the medium-voltage testbench following a loadstep $\Delta P_{L0} = 15$ MW:
a) Variation of the synchronous generator (SG) inertia constant H_{SG},
b) variation of the SG governor droop d_{Gov},
c) variation of the SG turbine time constant T_{Tur} and
d) variation of the SG rated power $S_{r,SG}$.

The SG governor droop d_{Gov} in Figure 8.4 b) specifies the impact of the primary frequency control and affects the remaining quasi-steady-state frequency deviation Δf_{qss}. For the default governor droop $d_{Gov} = 0.02$, the typical current curve proportional to the frequency curve can be observed. For larger droops, the SG active power adjustment becomes less steep and the IBG takes over a larger part of the frequency control, which results in the IBG reaching its current limit. When the IBG reaches its current limit, the output current would exceed the maximum allowable current that the power electronics can handle. At this point, the converter's control mechanism detects the overcurrent condition and initiates the current limiting function. This results in the current curves in Figure 8.4 b) being identical for a SG governor droop $d_{\mathrm{Gov}} \geq 0.04$. As the absolute current is limited, the d axis current $i_{\mathrm{d,ref,lim}}$ is initially limited slightly below the limit $I_{\mathrm{max}} = 1.1$ p.u., as the q axis current still has a small non-zero component, cf. Figure 8.2 d).

The SG turbine time constant T_{Tur} and rated power $S_{\mathrm{r,SG}}$ have a significantly smaller impact on the frequency f and therefore also on the IBG d axis current infeed $i_{\mathrm{d,ref,lim}}$ than the governor droop d_{Gov}. While the turbine time constant T_{Tur} in Figure 8.4 c) does affect the settling time, the increase of the rated power $S_{\mathrm{r,SG}}$ in Figure 8.4 d) affects the quasi-steady-state deviation of the IBG d axis current infeed $i_{\mathrm{d,ref,lim}}$.

Impact of the external grid: The synchronous generator (SG), which represents the external overlying grid, has a strong impact on the frequency support of the inverter-based generator (IBG) as its parametrisation strongly impacts the frequency dynamics. Given the fact that conventional power plants are successively being shut down, a decrease of the power system inertia and the installed SG power is anticipated. Also, remaining gas power plants or grid-forming units based on power inverters act on a faster time scale than coal fired ones, leading to a decrease of the turbine time constant. Changing these parameters towards future low-inertia power systems increases the dynamic response of the IBG as faster and/or steeper frequency deviations are provoked by a loadstep. A reduction of the primary control from the overlying grid also ensures that the IBG takes over a larger part of this task until its current limit is reached. Smaller governor droop factors d_{Gov} for the primary control are advantageous, as the active power feed-in is adjusted more strongly as a response to the frequency deviation.

8.3.2 *Loadstep Size*

The size of a loadstep ΔP_{L0} applied to a power system is an indicator of the severeness of the disturbance. A larger loadstep ΔP_{L0} leads to larger dynamic processes resulting in a higher RoCoF, a smaller frequency nadir f_{min} and a larger quasi-steady-state frequency deviation Δf_{qss}, cf. Figure 8.5 a).

The voltage in Figure 8.5 b) initially decreases following the loadstep ΔP_{L0}. This is due to the sudden additional active power consumption. Shortly after the loadstep, the SG automatic voltage regulator and the IBG inner control counteract the voltage drop resulting in a small overshoot until the pre-fault voltage level is reached. The voltage drop and overshoot increase with increasing loadstep size, but remain within a tolerable range even for strong disturbances. The IBG currents $i_{\mathrm{dq,ref,lim}}$ are presented in Figure 8.5 c) and d). For the smallest

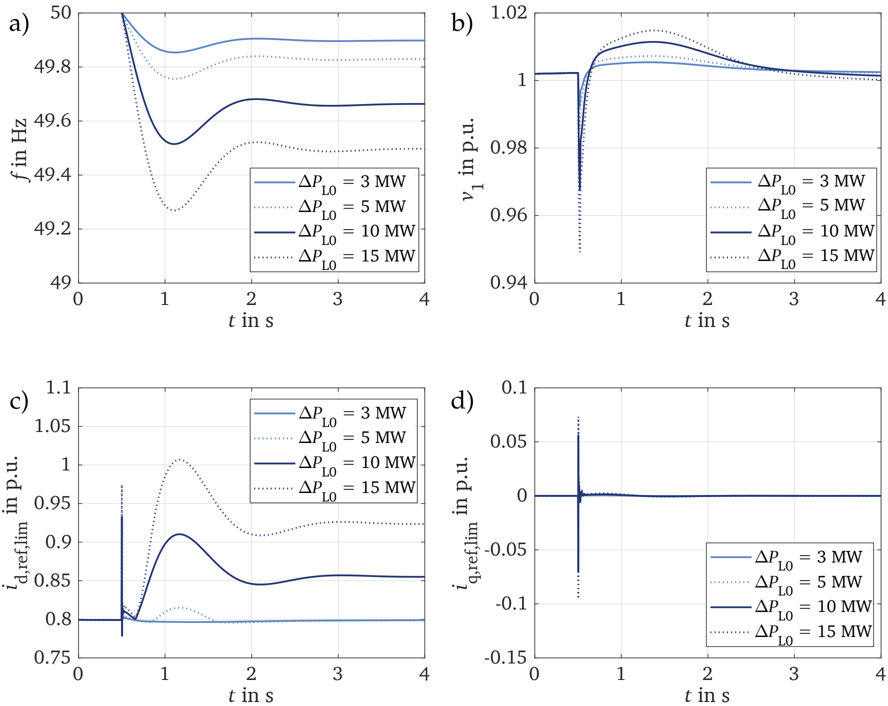

Figure 8.5: Impact of the loadstep size ΔP_{L0} on the inverter-based generation (IBG) in the medium-voltage testbench.
a) frequency of the synchronous generator (SG),
b) voltage at busbar BB1,
c) IBG d axis current infeed and
d) IBG q axis current infeed.

loadstep $\Delta P_{L0} = 3$ MW, the frequency deviation does not reach the IBG FFR deadband $db_{f,IBG} = 200$ mHz and no additional d axis current $i_{d,ref,lim}$ is fed into the grid. For the larger loadsteps $\Delta P_{L0} \geq 5$ MW, the d axis current $i_{d,ref,lim}$ is adapted with a linear correlation to the frequency deviation. The q axis current $i_{q,ref,lim}$ is not largely affected, but in principle counteracts the voltage deviation.

8.3.3 *Load Type*

The impact of a load type variation on the voltage v, frequency f and active and reactive power consumption P, Q is shown in Figure 5.5 and the load data is given in Table 5.3 and in Appendix A.2. The load type has only a small effect on the frequency f with a selfregulating effect of the loads being less than 1 % adaptation of the active power per 1 Hz frequency deviation. For this reason, the IBG current infeed does not vary widely as presented in Figure 8.6. A more severe loadstep $\Delta P_{L0} = 10$ MW is chosen in order to increase the absolute differences between the load models. A small deviation between the frequency-dependent load models *exp-f*, *composite ind*, *composite res* and the static load model *exp res-year* can be observed: The frequency-dependent load models counteract the frequency drop and the IBG frequency support does not increase the d axis current $i_{d,ref,lim}$ as much. Regarding the q axis current $i_{q,ref,lim}$, the rotating asynchronous machine in the composite load models decreases the initial transient peak.

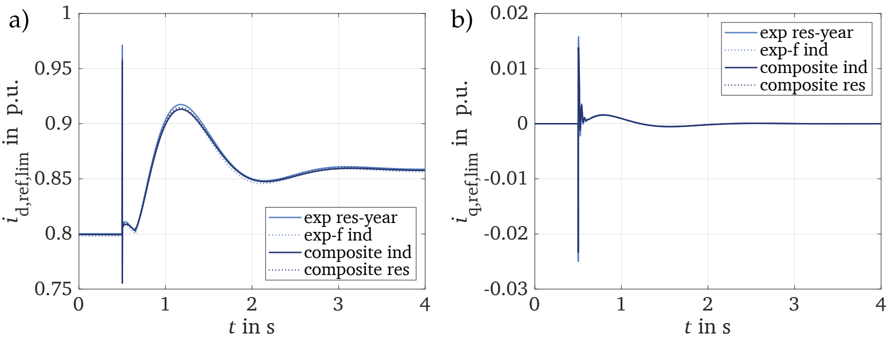

Figure 8.6: Impact of the load model type defined in Table 5.3 on the inverter-based generation (IBG) current infeed in the medium-voltage testbench following a loadstep $\Delta P_{L0} = 10$ MW:
IBG a) d axis and b) q axis current infeed.

Impact of the load model: Even for the severe loadstep $\Delta P_{L0} = 10$ MW, only minor differences between the dynamic load models and the static load models can be identified with the parameters researched in Chapter 5.3. The load self-regulation effect is relatively small and the frequency dependency of the load models used in this work is therefore almost negligible compared to other sensitivities. In future scenarios, e.g. demand-side management could lead to a larger positive impact of loads on the frequency dynamics.

8.3.4 *Distance of the External Grid*

The additional cable represents an additional impedance $\underline{Z}_{\text{line}}$ between busbar BB0 and busbar BB1, i.e. the electrical distance between the IBG and the external grid increases. The longer the cable length l, the larger the effective impedance $\underline{Z}_{\text{line}}$. This has an influence on the load flow and on the short-circuit power S''_{SC} available at busbar BB1. At busbar BB0, the SG provides a short-circuit power $S''_{\text{SC}} \approx 106$ MVA. The short-circuit power S''_{SC} reduces antiproportional with the cable impedance $\underline{Z}_{\text{line}} \approx (R'_1 + \text{j}X'_1) \cdot l = (0.343 + \text{j}0.275)\Omega/\text{km} \cdot l$. The cable parameters are given in the Appendix A.5, Table A.19.

Since the SG is the grid-forming component in the testbench and the load $L1$ at busbar BB1 is larger than the infeed of the IBG, the voltage at busbar BB1 v_1 decreases as a result of the voltage drop across the cable. Figure 8.7 b) and c) show the different voltage levels and the adjustment of the IBG d axis current infeed $i_{\text{d,ref,lim}}$ in order to keep the active power infeed P_{IBG} in Figure 8.7 d) constant. As the SG is further away from the loadstep ΔP_{L0}, the active power infeed P_{SG} as a response to the frequency deviation decreases slightly and the IBG active power infeed P_{IBG} increases slightly with increasing line length l.

The frequency in Figure 8.7 a) does not change significantly with the line length l. A small worsening of the RoCoF and frequency nadir $f_{\min}$ can be observed as a result of the increased electrical distance and the associated delay of travelling wave propagation to the SG. However, this effect is negligible in the medium-voltage testbench.

8.3.5 *Frequency Support of the Inverter-Based Generation*

Two different implementations of the FFR according to Figure 2.5 are distinguished in this work: The linear FFR, which is the default implementation, and the constant FFR, which feeds a predefined constant additional active power $\Delta P_{\text{FFR}} = 0.5$ MW, which corresponds to 0.17 p.u. with the rated base apparent power $S_{\text{IBG}} = 3$ MVA. The active power adjustment following the loadstep has a time delay $T_{\text{delay}} = 1$ s and a duration $T_{\text{dur}} = 6$ s. The parametrisation is based on [97] and corresponds to typical values from grid codes worldwide. The frequency support of IBG during underfrequency events requires the availability of additional energy and adequately dimensioned IBG as discussed in Chapter 2.3.3. The energy requirements are discussed and calculated in the next section. A comparison of both FFR implementations is presented in Figure 8.8.

The linear FFR shows an additional d axis current infeed $i_{\text{d,ref,lim}}$, which is proportional to the frequency deviation Δf as soon as the frequency dead-

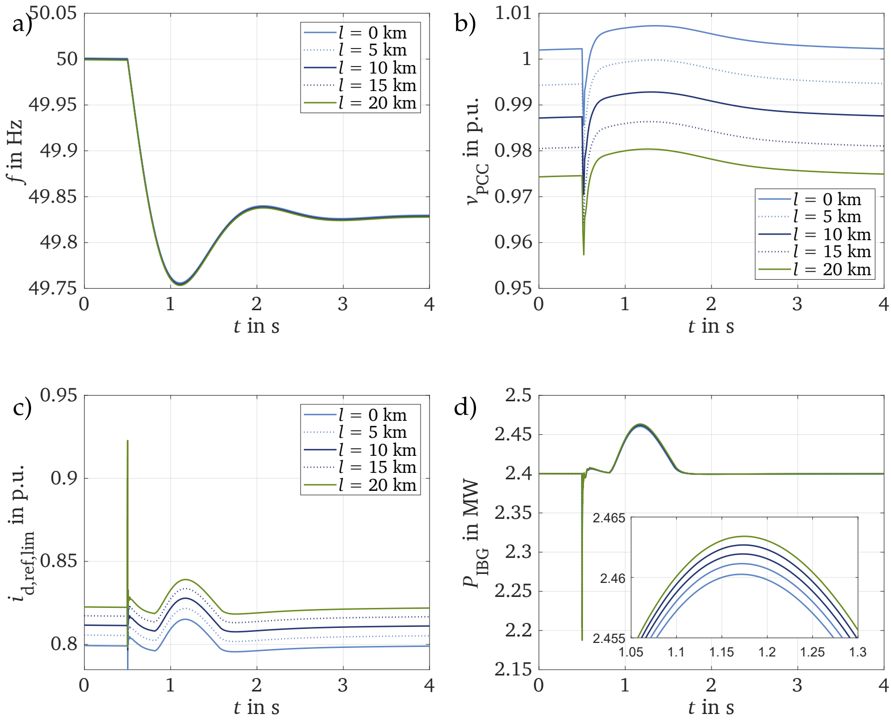

Figure 8.7: Impact of the cable length l on the inverter-based generation (IBG) dynamics in the medium-voltage testbench following a loadstep $\Delta P_{L0} = 5$ MW:
a) frequency of the synchronous generator (SG),
b) voltage at busbar BB1,
c) IBG d axis current infeed and
d) IBG active power infeed.

band $db_{FFR} = 200$ mHz is reached. The FFR droop d_{FFR} increases the additional d axis current $i_{d,ref,lim}$ and active power infeed P_{IBG} per frequency deviation Δf, but does not significantly affect the SG frequency f_{SG} and the voltage at busbar BB1 v_1. The active power peak at $t \approx 1.2$ s is 2.55 MW and 2.47 MW for the FFR droop $d_{FFR} = 0.02$ and $d_{FFR} = 0.05$, respectively.

The constant FFR implementation shows a significantly larger additional active power infeed $\Delta P_{IBG} = 0.5$ MW with a delay $T_{delay} = 1$ s following the loadstep. Therefore, the reaction of this implementation is delayed, but significantly stronger and remains even if the frequency reaches a tolerance band of ± 200 mHz again. After the six seconds of additional active power

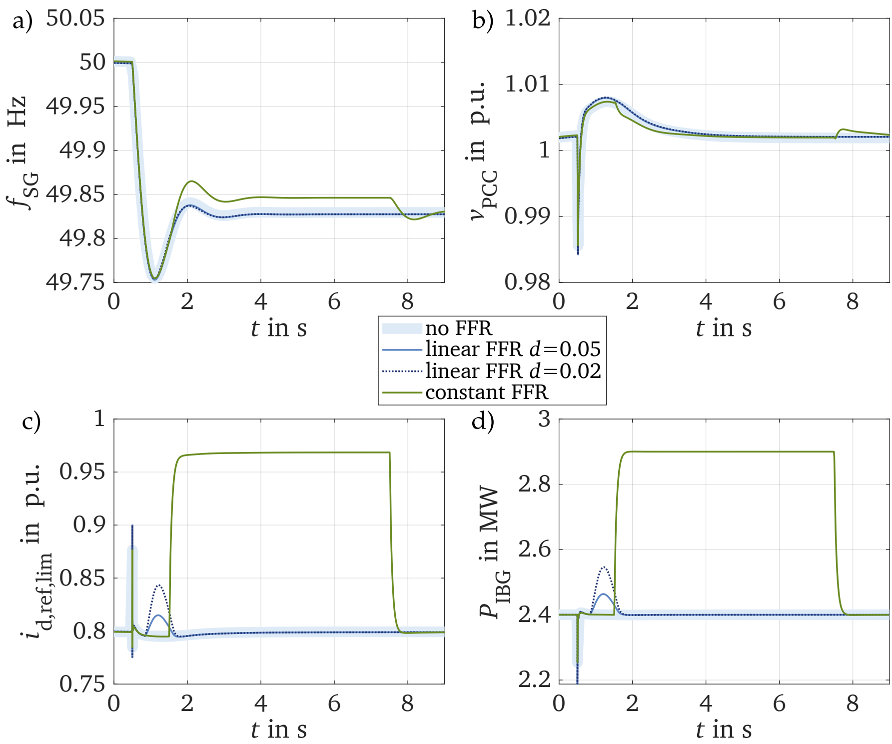

Figure 8.8: Impact of the fast-frequency response (FFR) control implementation in the IBG control on the dynamics in the medium-voltage testbench following a loadstep $\Delta P_{L0} = 5$ MW:
a) frequency of the synchronous generator (SG),
b) voltage at busbar BB1,
c) IBG d axis current infeed and
d) IBG active power infeed.

injection, a clear bend can be observed in both the SG frequency f_{SG} and the voltage v_1 curves.

The linear FFR implementation is characterised by the deadband db_{FFR} and droop d_{FFR}. A variation of these parameters and their impact on the IBG active power injection P_{IBG} is shown in Figure 8.9.

Decreasing the deadband db_{FFR} reduces the range around the nominal frequency f_n where no corrective action is taken by the IBG frequency control. This results in the IBG active power infeed P_{IBG} being adapted as soon as the

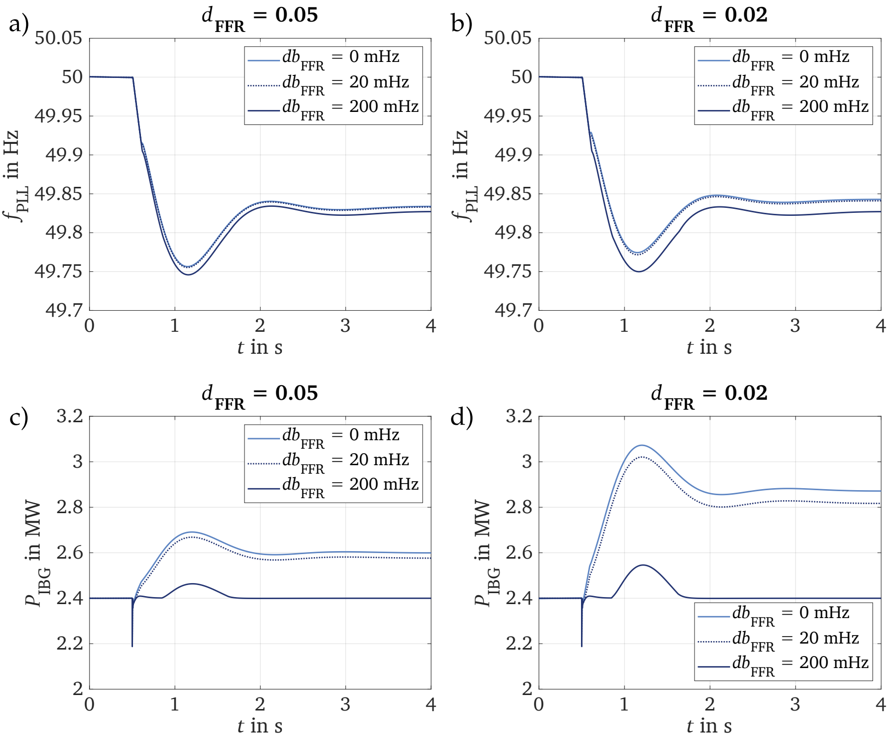

Figure 8.9: Impact of the fast frequency response (FFR) droop d_{FFR} and deadband db_{FFR} on the dynamics in the medium-voltage testbench following a load-step $\Delta P_{\text{L0}} = 5$ MW:
a), b) phase-locked loop (PLL) frequency measurement at busbar BB1,
c) and d) inverter-based generation (IBG) active power infeed.

frequency deviation $\Delta f_{\text{SG}} \geq 0$ mHz is reached, which is significantly earlier than for the larger deadband $db_{\text{FFR}} = 200$ mHz. The SG frequency curve f_{SG} is positively influenced by the smaller deadband db_{FFR}, as the IBG active power P_{IBG} adjustment starts earlier for a constant FFR droop d_{FFR}. The parallel shift of the linear characteristic in Figure 2.5 ensures that for the same frequency deviation Δf there is a stronger adaptation of the IBG active power P_{IBG} for smaller deadbands db_{FFR}.

The FFR droop d_{FFR} is the proportional relation between frequency deviation Δf and IBG active power P_{IBG} adaptation. Decreasing the droop d_{FFR} leads to a steeper and larger adaptation of the IBG active power P_{IBG}. The small bend in the IBG active power P_{IBG} arises from the optimised PLL parametrisation, cf. Figure 6.2. The standard PLL parameters lead to a strong oscillations in the frequency measurement. As a result the IBG active power P_{IBG} oscillates. For comparison, the results with standard PLL parameters are given in Appendix A.6 in Figure A.2. The identical frequency drop can be explained by the rate limit $RL = 0.88$ Hz/s as described in Chapter 6.2.1. The PLL frequency estimation shows strong dynamics, cf. Figure A.2. The rate limit cuts these dynamics to a steady frequency drop accordingly to a $\mathrm{RoCoF}_{500\ \mathrm{ms}} = 0.88$ Hz/s. The frequency curve shortly after the loadstep is therefore strongly dependent on the selected PLL parameters. The latter can also determine whether a control is stable or not, e.g. when comparing Figure 8.9 and Appendix A.6, Figure A.2.

Frequency Support of the Inverter-Based Generation: The choice of PLL parameters is crucial for the stability of the IBG frequency control. For the grid-supporting control, robust local frequency estimation remains a fundamental prerequisite for stable operation. As an alternative, the communication of a frequency signal, e.g. from rotating equipment, can be discussed. However, this leads to additional time delays. For very low inertia systems, oscillatory behaviour can be observed stating that the grid-supporting control reaches its limits. In general, a faster and stronger adaptation of the active power infeed is to be favoured.

8.3.6 *Energy requirements for the fast-frequency response*

The additional energy ΔE_{FFR} required for the different FFR implementations is calculated based on Figure 8.8 c). A scenario without additional FFR control is chosen as a reference. The energy required for the FFR ΔE_{FFR} is calculated as the difference between the total IBG energy fed into the grid in the scenario with FFR $E^{\mathrm{FFR}}_{\mathrm{IBG,tot}}$ minus the IBG energy in the scenario without FFR $E^{\mathrm{no\ FFR}}_{\mathrm{IBG,tot}}$ using (8.5).

$$\Delta E_{\mathrm{FFR}} = E^{\mathrm{FFR}}_{\mathrm{IBG,tot}} - E^{\mathrm{no\ FFR}}_{\mathrm{IBG,tot}} = \int\limits_{t=0\ \mathrm{s}}^{t=9\ \mathrm{s}} S^{\mathrm{FFR}}_{\mathrm{IBG}}(t)\ \mathrm{d}t \ - \int\limits_{t=0\ \mathrm{s}}^{t=9\ \mathrm{s}} S^{\mathrm{no\ FFR}}_{\mathrm{IBG}}(t)\ \mathrm{d}t \quad (8.5)$$

Table 8.2 gives an overview of the total energy $E^{\mathrm{FFR}}_{\mathrm{IBG,tot}}$, which is fed from the IBG into the grid during the simulation of nine seconds and the part of the energy required for the FFR ΔE_{FFR}. The total energy $E^{\mathrm{no\ FFR}}_{\mathrm{IBG,tot}}$ of the scenario without FFR can be approximated by $E^{\mathrm{no\ FFR}}_{\mathrm{IBG,tot}} \approx 0.8 \cdot S_{\mathrm{r,IBG}} \cdot 9\ \mathrm{s} = 21.6\ \mathrm{MJ} = 6\ \mathrm{kWh}$. The simulation leads to a slightly smaller energy $\Delta E_{\mathrm{FFR}} = 21.51\ \mathrm{MJ} \approx 6\ \mathrm{kWh}$, as the IBG power shows a transient peak downwards following the loadstep. The linear FFR requires an additional energy $\Delta E_{\mathrm{FFR}} \approx 14.5\ \mathrm{kJ} \approx 4\ \mathrm{Wh}$ and

33.8 kJ $\approx$ 9 Wh for a droop $d_{\text{FFR}} = 0.05$ and $d_{\text{FFR}}0.02$, respectively. The constant FFR implementation has a significantly larger energy demand ΔE_{FFR}, as the predefined additional active power $\Delta P_{\text{FFR}} = 0.5$ MW is fed in for six seconds resulting in an additional energy demand $\Delta E_{\text{FFR}} = 2.59$ MJ $\approx$ 0.7 kWh.

Table 8.2: Energy requirement for the fast-frequency response (FFR).

FFR implementation	total energy $E^{\text{FFR}}_{\text{IBG,tot}}$	FFR energy ΔE_{FFR}
linear $d = 0.05$	21.52 MJ $\approx$ 6.0 kWh	0.01 MJ $\approx$ 3.0 Wh
linear $d = 0.02$	21.54 MJ $\approx$ 6.0 kWh	0.03 MJ $\approx$ 8.0 Wh
constant	24.10 MJ $\approx$ 6.7 kWh	2.59 MJ $\approx$ 0.7 kWh

Energy Requirements for the FFR: Frequency support from IBG in the form of FFR in underfrequency scenarios can only be provided if sufficient additional energy ΔE_{FFR} is available. For this purpose, the IBG must either be operated in partial load mode or an additional storage system must provide the control energy sufficiently fast. In the scenarios analysed, the demand for control energy is significantly lower for the linear FFR than for constant FFR implementation.

8.4 SUMMARY

This chapter investigates the behaviour of an individual inverter-based generator (IBG) in the context of increasing renewable energy integration into power systems. The study aims to understand the IBG behaviour, sensitivities, and operational limits for dynamic frequency studies, validate frequency measurement approaches, and establish an understanding of a testbench resembling the fitting model for the greybox aggregation. The medium-voltage testbench in its standard parametrisation is presented, detailing the IBG, synchronous generator (SG), and load characteristics in an active distribution grid connected to a low-inertia power system. The evaluation of frequency metrics, including the Rate of Change of Frequency (RoCoF), the frequency nadir f_{min}, and the quasi-steady-state frequency deviation Δf_{qss}, is discussed. Differences in RoCoF calculations using standard and optimised Phase-Locked Loop (PLL) parameters are highlighted and the frequency metrics results for the medium-voltage testbench in its default parametrisation are presented.

A sensitivity analysis explores various factors influencing the power system performance. It studies the impact of parameters such as external grid characteristics, load step size, load type, cable length, and fast-frequency response

(FFR) on the IBG dynamics. Notable findings include the significant influence of the external grid parameters on the IBG frequency support, the role of the load step size, and the limited impact of the load model variations. The analysis also assesses the effect of cable length on IBG dynamics and highlights the importance of FFR in supporting the grid during frequency events. The energy requirements for the FFR are quantified, emphasising its role in enhancing system stability.

9 FREQUENCY DYNAMICS OF ACTIVE DISTRIBUTION GRIDS

As the installed power plants increasingly shift into the distribution grid with the increasing integration of renewable energy plants and the associated IBG, dynamic investigations of these active distribution grids and their contribution to the dynamic frequency support become relevant. In the pursuit of a sustainable and resilient power system, understanding the power system dynamic frequency stability becomes indispensable.

This chapter presents the outcomes of dynamic frequency investigations within typical benchmark distribution grids with varying shares of IBG. The frequency dynamic metrics, which are the frequency nadir f_{min}, the RoCoF and the quasi-steady-state frequency deviation Δf_{qss} are evaluated as described in Chapter 2.3 and applied in Chapter 8.2. The primary objective of this research is to provide valuable insights into the frequency behaviour of active distribution grids under various operational scenarios. By subjecting the system to diverse disturbances in the form of loadsteps ΔP_{L0}, load variations, and SG dynamics, the study discusses the impact of these sensitivities. Such insights are crucial for devising effective strategies to enhance frequency stability, design resilient control mechanisms, and develop adaptive dynamic equivalents.

This chapter is structured as follows: Chapter 9.1 provides an overview of the results obtained from the radial medium-voltage benchmark grid and the impact of different shares of IBG, external grid settings and frequency support control parameters. Chapter 9.2 delves into the analysis of the high-voltage grid, which allows very large shares of IBG. Again, multiple sensitivities are identified, which impact the frequency response of the distribution grid.

9.1 MEDIUM-VOLTAGE BENCHMARK GRID

The medium-voltage benchmark grid introduced in Chapter 7.1 is investigated here in detail. Three scenarios according to Table 7.2 are distinguished: A scenario without IBG as reference scenario, a basic IBG scenario with a total IBG installed power $S_{\text{r,IBG,basic}} = 6.24$ MVA and a max IBG scenario with a maximum share of IBG and a total IBG installed power $S_{\text{r,IBG,max}} = 28$ MVA. The simulation results of the medium-voltage benchmark grid with its standard parametrisation are given in Figure 9.1 for the three scenarios. All IBG are equipped with the linear FFR and the curves are measured at busbar BB1 on the low-voltage side of the HV/MV-transformer T1, cf. Figure 7.1.

There are two different ways to adapt the representation of the external grid as SG to different penetration levels of IBG. The first case is to adapt the SG active power setpoint P_{ref}, which has to supply a smaller part of the load at higher IBG penetrations. Adjusting the SG active power setpoint P_{ref} also changes its contribution to the primary frequency control to compensate for short-term load changes and frequency fluctuations. With high IBG penetrations, the SG active power feed-in P_{SG} is therefore reduced. This scenario corresponds to the classic energy transition scenario, in which the SG infeed is replaced by IBG as shown in Figure 9.1.

The frequencies in Figure 9.1 show that due to the larger share of IBG, the dynamic frequency drop becomes steeper and stronger in response to the loadstep $\Delta P_{\text{L0}} = 50$ MW. This is due to the decreasing part of the SG in the primary frequency control. The IBG with linear FFR operate using a FFR droop $d_{\text{FFR}} = 0.05$ and the SG governor with a droop $d_{\text{Gov}} = 0.02$. Therefore, less primary frequency reserve is released in the basic and max IBG scenarios compared to the scenario without IBG. The inertia remains identical for all scenarios in this case. The impact of the mechanical inertia within the power system on the frequency dynamics as shown in (5.10) is presented in Chapter 9.1.1.

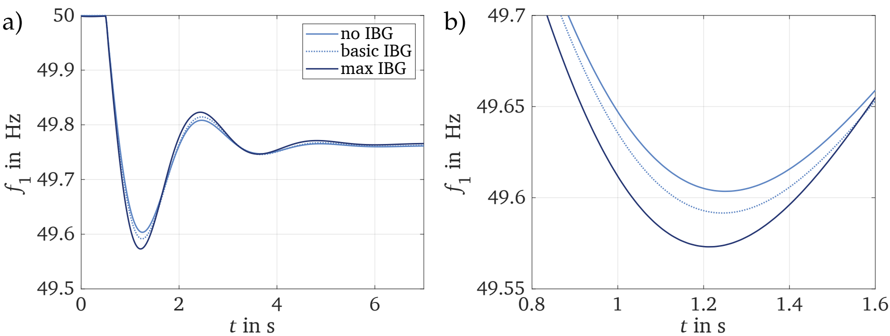

Figure 9.1: Dynamic frequency response for different inverter-based generation (IBG) scenarios according to Table 7.2 in the medium-voltage benchmark grid (case 1) applying a loadstep $\Delta P_{\text{L0}} = 50$ MW.
a) Frequency and b) zoom into the frequency nadir at BB1 at the low-voltage side of the HV/MV-transformer T1.

Using (5.12) and (5.13), the RoCoF and quasi-steady-state frequency deviation Δf_{qss} can be estimated to (9.1) and (9.2). For the scenario without IBG, the term $S_{\text{SG}}/P_{\text{L}} = 1$ can be neglected as the total load demand is fed from the SG.

$$\text{RoCoF}_{50\mu s} \approx \frac{f_\text{n} \cdot \Delta P_\text{L0}}{2 \cdot \frac{S_\text{SG}}{S_\text{L}} \cdot \sum_{i=1}^{n} H_i \cdot S_i} = \frac{50\text{ Hz} \cdot 50\text{ MVA}}{2 \cdot 6.5\text{ s} \cdot 200\text{ MVA}} = 0.96\text{ Hz/s} \tag{9.1}$$

$$\Delta f_\text{qss} = \frac{\Delta P_\text{L0}}{S_\text{r,SG}} \cdot \frac{d_\text{Gov}}{100\ \%} \cdot f_\text{n} = \frac{50\text{ MW}}{200\text{ MVA}} \cdot \frac{2\ \%}{100\ \%} \cdot 50\text{ Hz} = 0.25\text{ Hz} \tag{9.2}$$

The RoCoF of the basic and max IBG scenario can be estimated to 0.99 Hz/s and 1.13 Hz/s, respectively. For the calculation, a total load demand $S_\text{L} = \sum_{n=0}^{5} S_{\text{L}n} = 147.5$ MVA is assumed and the SG power infeed is approximated to $S_\text{SG} = S_\text{L} - S_\text{IBG}$. The simulation leads to similar results with $\text{RoCoF}_{50\mu s} = 0.94$ and a quasi-steady-state frequency deviation $\Delta f_\text{qss} \approx 0.24$ Hz for the scenario without IBG. The small differences are due to the voltage- and frequency-dependent load representation, which is not considered in (9.1) and (9.2). For the basic and max IBG scenario, the additional filter capacitance C_F of the IBG leads to a further improvement of the RoCoF. For this reason, the calculation gives a conservative estimate.

If, in contrast to the first case being the energy transition scenario, the effect of the IBG is to be investigated with constant inertial and primary frequency response of the SG, the parametrisation of the SG is not changed, but the load L0 is increased so that the additional IBG power infeed is compensated. In this second case, the dynamic response of the SG remains constant and the sole effect of the IBG is investigated. The effects of increasing IBG penetration for constant inertia are shown in Figure 9.2. The additional IBG power infeed S_IBG, for a constant dynamic behaviour of the external grid SG, improves the frequency nadir f_min in particular. The FFR control acts as an additional primary control, counteracting the frequency drop. The voltage-reducing behaviour due to the IBG power factor $cos\varphi = 0.9$ (overexcited) is more significant than the voltage increase due to the active power infeed, which reduces the voltage v_1 for higher shares of IBG. For the same reason, the reactive power that flows into the medium-voltage grid increases for the max IBG scenario.

The active power P_1 that is provided by the high-voltage grid to feeder 1 of the medium-voltage bechmark grid is reduced during steady state due to the addidional IBG active power infeed $P_\text{IBG,basic} = 0.8 \cdot P_\text{r,IBG,basic} = 5$ MW and $P_\text{IBG,max} = 0.8 \cdot P_\text{r,IBG,max} = 22$ MW for the two scenarios. The IBG are operated at 80 % partial load. Following the loadstep, a first small decrease of the active power P_1 is visible, which results from the frequency-dependency of the loads. As soon as the frequency curve drops below 49.8 Hz, a further reduction of P_1 can be observed, which is due to the linear FFR of the IBG. The FFR active power adaptation can be estimated by $\Delta P_\text{IBG} = \Delta f / d_\text{FFR} = 0.008\text{ p.u.}/0.05 \approx 0.16$ %,

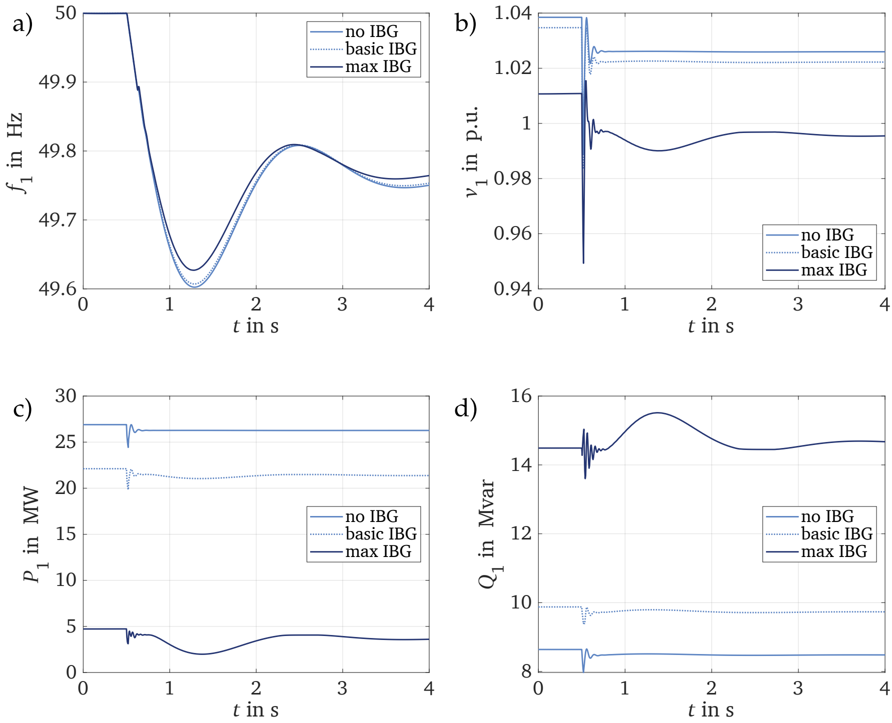

Figure 9.2: Dynamic frequency response for different inverter-based generation (IBG) scenarios according to Table 7.2 in the medium-voltage benchmark grid (case 2) applying a loadstep $\Delta P_{L0} = 50$ MW.
a) Frequency, b) voltage, c) active power and d) reactive power at BB1 at the low-voltage side of the HV/MV-transformer T1.

which corresponds to 0.8 MW for the basic IBG scenario and 3.5 MW for the max IBG scenario.

The measured RoCoF based on two time windows $\Delta t = 50$ μs and $\Delta t = 500$ ms, the frequency nadir $f_{\min}$ as well as the quasi-steady-state frequency deviation Δf_{qss} of each scenario are presented in Table 9.1. Increasing the share of IBG improves all frequency metrics in the second case.

In the following part of this chapter, different sensitivities in the medium-voltage benchmark grid are investigated: Chapter 9.1.1 compares different implementations of the FFR in the IBG control. Chapter 9.1.2 compares the direct voltage control with grid-supporting control, Chapter 9.1.3 lists the influence of

Table 9.1: Frequency nadir f_{min}, RoCoF and quasi-steady-state deviation Δf_{qss} results of the medium-voltage benchmark grid in default parametrisation shown in Figure 9.2.

scenario	f_{min}	Δf_{qss}	$\text{RoCoF}_{50\mu\text{s}}$	$\text{RoCoF}_{500\text{ms}}$
no IBG	49.603 Hz	0.249 Hz	−0.94 Hz/s	−0.68 Hz/s
basic IBG	49.605 Hz	0.248 Hz	−0.94 Hz/s	−0.67 Hz/s
max IBG	49.618 Hz	0.241 Hz	−0.99 Hz/s	−0.66 Hz/s

the external grid parameters and Chapter 9.1.4 adds the variation of the load model to the investigations.

The spatial distribution of the individual IBG has been proven in a case study to have a negligible impact on the dynamic frequency response of the active medium-voltage grid [192]. A delay occurs mainly due to long line lengths, as the frequency change and associated phase jump propagates by means of travelling waves. Due to the relatively short lines in the medium-voltage grid, the spatial distribution is not further investigated. For the following sensitivity analysis, the second case is considered.

Energy Transition Scenarios: Three inverter-based generators (IBG) are connected to the medium-voltage benchmark grid to reveal possible interactions between the individual systems. However, these are not recognised in the investigations carried out. A replacement of synchronous generators (SG) by IBG leads to a worsening of the frequency stability (case 1). In contrast, for a constant system inertia and short-circuit power, the grid-supporting functions of the IBG control improve the dynamic short-term frequency stability (case 2).

9.1.1 *Frequency Control*

The investigations on the IBG frequency control are divided into the influence of the droop d_{FFR} and the deadband db_{FFR} of the linear FFR, the comparison of the two different FFR implementations - linear and constant - and two scenario variations with mixed FFR controls, cf. Table 7.3.

Figure 9.3 presents the impact of the droop d_{FFR} and the deadband db_{FFR} of the linear FFR on the frequency metrics in the basic IBG scenario. The $\text{RoCoF}_{500\text{ms}}$ measured over a time window $\Delta t = 500$ ms and the quasi-steady-state frequency deviation Δf_{qss} increase with increasing FFR droop d_{FFR} and increasing deadband db_{FFR}. This is because of the antiproportional relation between additional active power infeed ΔP_{IBG} and FFR droop d_{FFR} as shown in (2.7). The frequency nadir f_{min} decreases with increasing FFR droop d_{FFR} and increasing deadband db_{FFR}. All curves run into saturation at the larger values of the FFR droop d_{FFR}, since here the relatively small adjustment of the active power has only a marginal effect on the frequency metrics. In addition, the results for a FFR deadband db_{FFR} are significantly worse than for the smaller deadbands. Overall, all frequency metrics deteriorate as the FFR droop and deadband db_{FFR} increase.

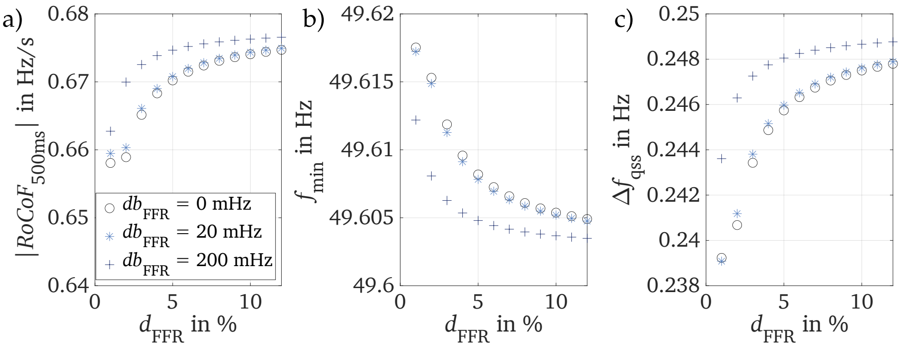

Figure 9.3: Impact of the fast-frequency response (FFR) droop d_{FFR} and deadband db_{FFR} on the frequency metrics in the basic IBG scenario of the medium-voltage benchmark grid when applying a loadstep $\Delta P_{\mathrm{L0}} = 50$ MW:
a) Rate of change of frequency (RoCoF) for a time window $\Delta t = 500$ ms,
b) frequency nadir f_{min} and
c) quasi-steady-state frequency deviation Δf_{qss}.

The impact of the constant FFR implementation is depicted in Figure 9.4 and Figure 9.5. Figure 9.4 displays the dynamic measurements of frequency f_1, voltage v_1, and active/reactive power P_1, Q_1 at busbar BB1 within the medium-voltage benchmark grid. In contrast to the outcomes shown in Figure 9.2, all IBG are equipped with constant FFR control, along with an additional active power infeed $\Delta P_{\mathrm{FFR}} = 3$ MW at each IBG. Theoretically, it is therefore possible to adjust the active power of the three IBG by a total of $\Delta P_{\mathrm{FFR,feeder1}} = 3 \cdot \Delta P_{\mathrm{FFR}} = 9$ MW in feeder 1 for the basic IBG scenario. However, this theoretical active power adaptation can be reduced by the current limitation of the IBG control.

The simulation results show that due to the FFR time delay $T_{\mathrm{delay}} = 1$ s, the IBG frequency support initiates at $t = 1.5$ s and the initial frequency curve remains unaffected by the alteration in the IBG share. The additional active power ΔP_{IBG} significantly impacts all the curves shown in Figure 9.4 from $t = 1.5$ s onwards. In the basic IBG scenario, an approximate active power increase $\Delta P_{\mathrm{IBG}} \approx 2$ MW is observed in the simulation, which results in lowering the active power provided by the high-voltage grid at busbar BB1. The active power increase ΔP_{IBG} can be estimated using the IBG's normal operation at 80 % partial load, a potential 10 % overload, and a power factor $\cos\varphi = 0.9$. The IBG feed $P_{\mathrm{IBG}} = 0.8 \cdot S_{\mathrm{r,IBG}} \cdot \cos\varphi \approx 4.0$ MW during the pre-fault steady state. The IBG current magnitude is limited to $I_{\max} = 1.1$ p.u., which yields (9.3) for the basic IBG scenario and $P_{\mathrm{IBG,lim}} \approx 27.7$ MW for the max IBG scenario. Finally, the IBG active power increase in feeder 1 can be estimated as the difference between the active power limit $P_{\mathrm{IBG,lim}}$ and the pre-fault active power infeed P_{IBG} as shown in (9.4). These calculations give a rough estimate as simplifications apply, such as a constant voltage $v = 1$ p.u. at all busbars and a constant power factor $\cos\varphi = 0.9$ for all IBG during transients.

$$P_{\mathrm{IBG,lim}} = S_{\mathrm{IBG,lim}} \cdot \cos\varphi \approx 1.1 \cdot S_{\mathrm{r,IBG}} \cdot \cos\varphi \approx 6.2 \text{ MW} \tag{9.3}$$

$$\Delta P_{\mathrm{IBG}} \approx P_{\mathrm{IBG,lim}} - P_{\mathrm{IBG}} \approx 2.2 \text{ MW} \tag{9.4}$$

The max IBG scenario shows the largest impact on the frequency f_1 and active power P_1. A theoretical adaptation of the active power $\Delta P_{\mathrm{FFR,feeder1}} = 3 \cdot \Delta P_{\mathrm{FFR}} = 9$ MW in feeder 1 remains. Due to the current limitation, an additional active power $\Delta P_{\mathrm{IBG}} \approx 7.5$ MW is observed in the simulation. The fast IBG active power adaptation ΔP_{IBG} leads to a clear jump of the frequency curve f_1. Power flow revearsal occurs and the medium-voltage benchmark grid exports 2 MW of active power to the high-voltage grid. As for the basic scenario, the IBG active power increase ΔP_{IBG} can be estimated to $\Delta P_{\mathrm{IBG}} \approx P_{\mathrm{IBG,lim}} - P_{\mathrm{IBG}} \approx 27.7 \text{ MW} - 20.2 \text{ MW} = 7.5$ MW. The frequency reacts with a clear cut to the change in active power at $t = 1.5$ s. The reactive power demand Q_1 from the high-voltage grid increases due to IBG1 having a voltage-increasing behaviour, which is reduced in favour to the active power infeed, cf. Chapter 6.2.4. In the max IBG scenario, IBG1 is significantly larger than IBG2 and IBG3 and therefore has the largest impact. As a response to the reactive power change, the voltage v_1 decreases. Further reasons for a voltage drop during reverse power flow are described in [198, 199].

Figure 9.5 presents the results for a variation of the additional constant FFR active power ΔP_{FFR} per IBG. Due to the default FFR time delay $T_{\mathrm{delay}} = 1$ s required in nowadays grid codes [97], the RoCoF and the frequency nadir $f_{\min}$ show no dependency on a change in the additional active power infeed ΔP_{FFR}. Also, the differences between the scenarios are negligible and correspond to the frequency curve of the scenario without IBG as shown in Figure 9.4 a). In contrast, the quasi-steady-state frequency deviation Δf_{qss} is measured at $t = 5$ s during the increase of the active power infeed ΔP_{FFR}. For this reason, the quasi-steady-state frequency deviation Δf_{qss} is affected by the constant FFR control.

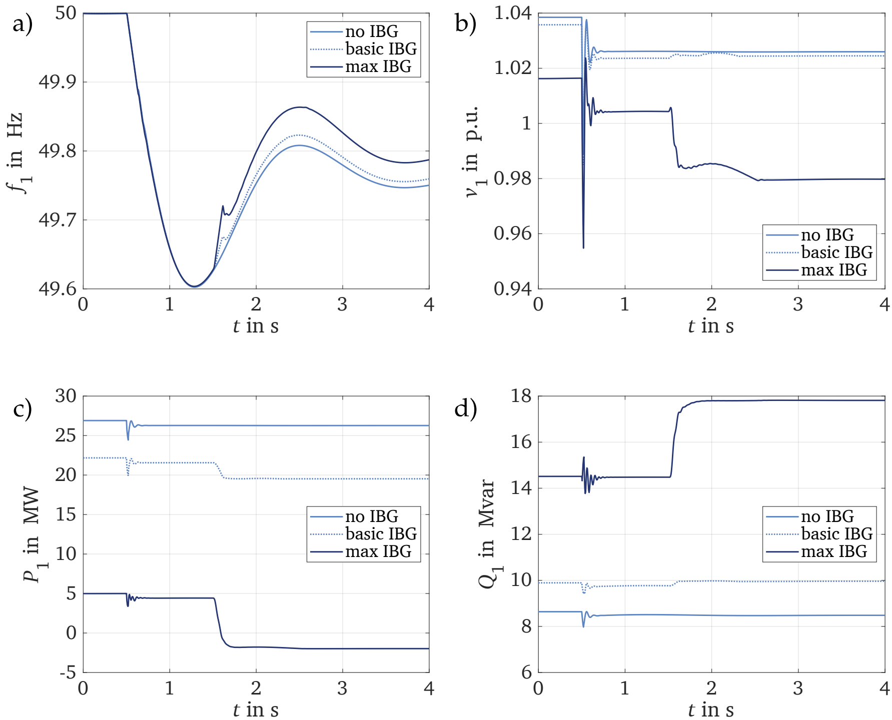

Figure 9.4: Dynamics of the medium-voltage benchmark grid for different inverter-based generation (IBG) scenarios with constant fast-frequency response (FFR) with $\Delta P_{\text{FFR}} = 3$ MW per IBG for a loadstep $\Delta P_{\text{L0}} = 50$ MW:
a) Frequency, b) voltage, c) active power and d) reactive power at BB1 at the low-voltage side of the HV/MV-transformer T1.

For an installed IBG power $S_{\text{IBG}} = 6.24$ MVA, the quasi-steady-state frequency deviation Δf_{qss} decreases until $\Delta P_{\text{FFR}} = 1$ MW. Subsequently, the current limit $I_{\text{max}} = 1.1$ p.u. is reached, and no further effect is observed upon increasing the additional active power infeed ΔP_{FFR}. In the max IBG scenario, a steady decrease in Δf_{qss} is observed. Among the IBG units, IBG2 and IBG3 reach their current limit I_{max} at $\Delta P_{\text{FFR}} = 1.5$ MW, while only the contribution of IBG1 leads to a further decrease in the quasi-steady-state frequency deviation Δf_{qss}. The quasi-steady-state frequency deviation Δf_{qss} can be estimated using (9.2) and subtracting the FFR active power ΔP_{FFR} from the loadstep as long as no IBG reaches its current limit I_{max}. In (9.5) the estimation of the quasi-steady-state frequency deviation Δf_{qss} including the constant FFR is shown. It yields a quasi-steady-state frequency deviation $\Delta f_{qss} = 0.243$ Hz for $\Delta P_{FFR} = 0.5$ MW per IBG or a total $\Delta P_{FFR,feeder1} = 3 \cdot \Delta P_{FFR} = 1.5$ MW, which is identical for both, the basic and max IBG scenario and matches the simulation results in Figure 9.5.

$$\Delta f_{qss} = \frac{(\Delta P_{L0} - \Delta P_{FFR,feeder1})}{S_{r,SG}} \cdot \frac{d_{Gov}}{100\ \%} \cdot f_n \quad \text{if} \quad I_{IBG1}, I_{IBG2}, I_{IBG3} \leq I_{max} \quad (9.5)$$

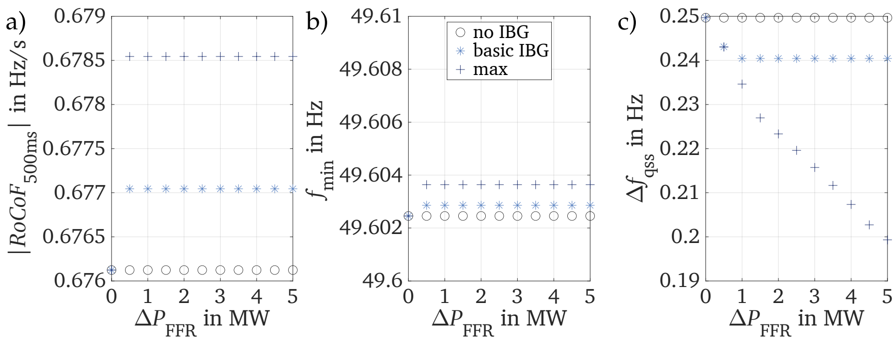

Figure 9.5: Impact of the constant fast-frequency response (FFR) parametrisation with a delay $T_{delay} = 1$ s on the frequency metrics for varying additional active power infeed ΔP_{FFR} and a loadstep $\Delta P_{L0} = 50$ MW:
a) Rate of change of frequency (RoCoF) with a time window $\Delta t = 500$ ms,
b) frequency nadir f_{min} and
c) quasi-steady-state frequency deviation Δf_{qss}.

The investigation is repeated with a shorter FFR time delay $T_{delay} = 0.1$ s, so that the frequency support is activated during the initial frequency drop following the loadstep. The results are presented in Figure 9.6. The results of the quasi-steady-state frequency deviation Δf_{qss} are identical to the ones explained above. This is because the additional active power infeed ΔP_{FFR} remains unchanged and the measurement at $t = 5$ s still includes the FFR.

The RoCoF_{500ms} in Figure 9.6 a) shows a dependency on the FFR with shorter delay as the active power adaptation now occurs within the relevant time interval. As seen for the quasi-steady-state frequency deviation Δf_{qss}, in the basic IBG scenario all IBG reach their current limitation for $\Delta P_{FFR} = 1$ MW. The additional maximum IBG power $\Delta P_{IBG} = 2.2$ MW, see (9.4), decreases the RoCoF_{500ms} by 0.22 Hz/s. In the max IBG scenario, IBG2 and IBG3 reach their current limit I_{max} at $\Delta P_{FFR} = 1.5$ MW and IBG1 due to its size with $S_{r,IBG1} =$ 18 MVA continues increasing its active power adaptation and a linear correlation between RoCoF_{500ms} and ΔP_{FFR} can be observed. Using (9.1), the instantaneous

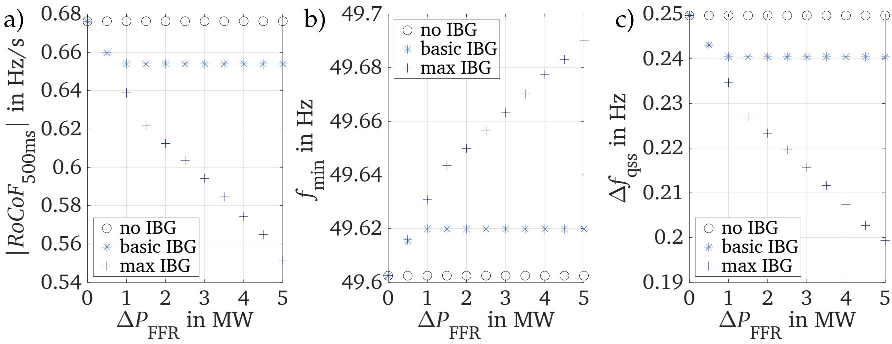

Figure 9.6: Impact of the constant fast-frequency response (FFR) parametrisation with a delay $T_{delay} = 100$ ms on the frequency metrics for varying additional active power infeed ΔP_{FFR} and a loadstep $\Delta P_{L0} = 50$ MW:
a) Rate of change of frequency (RoCoF) with a time window $\Delta t = 500$ ms,
b) frequency nadir f_{min} and
c) quasi-steady-state frequency deviation Δf_{qss}.

RoCoF$_{50\mu s}$ can be estimated. As seen in Table 9.1, the RoCoF$_{50\mu s}$ deteriorates with increasing share of IBG. This is because the FFR is activated with a certain delay and therefore cannot replace the inertial behaviour of SG. Including the constant FFR in (9.1) is therefore disregarded here.

The frequency nadir f_{min} in Figure 9.6 can be explained as the RoCoF: The shorter FFR time delay $T_{delay} = 0.1$ s results in an improvement of the frequency nadir. Due to the additional active power infeed, the frequency nadir f_{min} is increased by 0.19 Hz in the basic IBG scenario and shows a linear correlation with the FFR active power infeed ΔP_{FFR} in the max IBG scenario.

Frequency Support from IBG: The IBG constant fast-frequency response (FFR) time delay is typically chosen to be at least 500 ms as shown in Table 3.2. However, the activation of the additional active power is then too late to have an influence on the RoCoF and the frequency nadir in very fast low-inertia systems. IBG can adapt their power output on a much faster time scale, cf. Figure 2.4. Time delays for the FFR should therefore be revised.

To conclude the investigation into IBG frequency control, four variations within the max IBG scenario are considered as described in Table 7.3:

1. Homogeneous frequency control using linear FFR only,

2. homogeneous frequency control employing constant FFR solely,
3. a combination of both FFR implementations with IBG1 utilising linear FFR and IBG2 and IBG3 implementing constant FFR (mixed FFR 1), and
4. the reverse of the previous combination (mixed FFR 2).

The outcomes are illustrated in Figure 9.7. The linear FFR implementation employs a droop $d_{\mathrm{FFR}} = 5$ % and a deadband $db_{\mathrm{FFR}} = 200$ mHz. The constant FFR implementation is modelled with an additional active power infeed $\Delta P_{\mathrm{FFR}} = 3$ MW per IBG and a time delay $T_{\mathrm{delay}} = 1$ s. Figure 9.7 displays the frequency metrics across variations of the inertia constant H_{SG} alongside the four aforementioned FFR variations. The RoCoF consistently decreases with rising inertia constant H_{SG}. Differences between the variations of FFR can be observed especially for low-inertia systems with the pure constant FFR implementation leading to the largest RoCoF due to the missing active power support within the first second following the loadstep. Comparable results are obtained for the frequency nadir f_{min}, which is lowest for the constant FFR scenario. For low-inertia scenarios with $H_{\mathrm{SG}} \leq 3$ s, the frequency curve exhibits oscillations, which can lead to outliers in the RoCoF and frequency nadir f_{min}. An exemplary frequency course for an inertia constant $H_{\mathrm{SG}} = 2$ s is shown in the Appendix A.7, Figure A.3. The quasi-steady-state frequency deviation Δf_{qss} is measured at $t = 10$ s and is largest for the constant FFR and decreases with an increasing share of linear FFR implementations. This is valid as the constant FFR time duration T_{dur} of the additional active power infeed is exceeded, cf. Chapter 2.3.3.

9.1.2 *Grid-Supporting vs. Direct Voltage Control*

So far, all investigations are carried out based on the grid-supporting control concept described in Chapter 6.2. Here, the impact of the control concept is discussed with a comparison of the grid-supporting and direct voltage control. Figure 9.8 shows the effect of the control concept on the active power P_1 and frequency f_1. Both the linear and the constant FFR implementation are considered for each control concept. Compared to the grid-supporting control, the direct voltage control provides only a limited frequency support regardless of the FFR implementation. The results for the linear FFR with a droop $d_{\mathrm{FFR}} = 5$ % and a deadband $db_{\mathrm{FFR}} = 200$ mHz in Figure 9.8 a) and b) show that the active power P_1 drawn from the high-voltage grid following the loadstep ΔP_{L0} is not reduced as much as for the grid-supporting control. This is due to the dynamic adjustment of the current limitation as already discussed in Chapter 6.3. The lowering of the current limits due to the missing integral part $k_{\mathrm{I,IC}} = 0$ in the inner control of the direct voltage control leads to a capping of the IBG active power infeed.

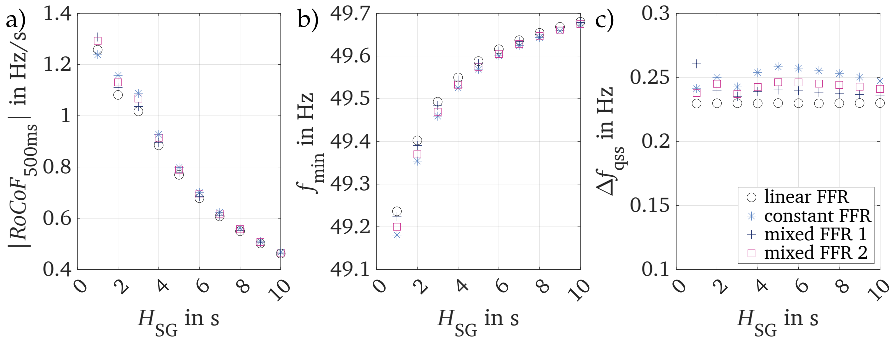

Figure 9.7: Comparison of homogeneous and inhomogeneous distribution of linear and constant fast-frequency response (FFR) implementation on the frequency metrics for a loadstep $\Delta P_{\mathrm{L0}} = 50$ MW and a varying inertia constant H_{SG}:
a) Rate of change of frequency $\mathrm{RoCoF}_{500\mathrm{ms}}$,
b) frequency nadir $f_{\min}$ and
c) quasi-steady-state frequency deviation Δf_{qss}.

The frequency curve only shows a slightly steeper RoCoF and lower frequency nadir $f_{\min}$. The effect is even more pronounced for the constant FFR depicted in Figure 9.8 c) and d) for an additional active power $\Delta P_{\mathrm{FFR}} = 3$ MW per IBG. While the power flow is reversed for the grid-supporting control, the direct voltage control shows a significantly smaller adaptation of the output power due to the dynamic current limit reduction.

Figure 9.9 shows the frequency metrics for a varying inertia constant H_{SG} and for the grid-supporting control and the direct voltage control in the max IBG scenario. Both control concepts are either equipped with a linear FFR implementation with a droop $d_{\mathrm{FFR}} = 5$ % and a deadband $db_{\mathrm{FFR}} = 200$ mHz or with a constant FFR implementation with an additional active power $\Delta P_{\mathrm{FFR}} = 3$ MW per IBG and a time delay $T_{\mathrm{delay}} = 1$ s.

In principle, the linear FFR leads to better results for the RoCoF and frequency nadir $f_{\min}$ and the constant FFR gives the best results regarding the interim quasi-steady-state frequency deviation Δf_{qss}. When comparing the control concepts, it is noticeable that the grid-supporting control with linear FFR gives the better results, i.e. the smaller values, for the RoCoF. For the constant FFR, both control concepts lead to similar results as the constant FFR does not become active in the first second following the loadstep. For the very-low-inertia system with $H_{\mathrm{SG}} = 1$, there is a distortion of the RoCoF results due to oscillations in the frequency curve. However, the basic trend is still visible.

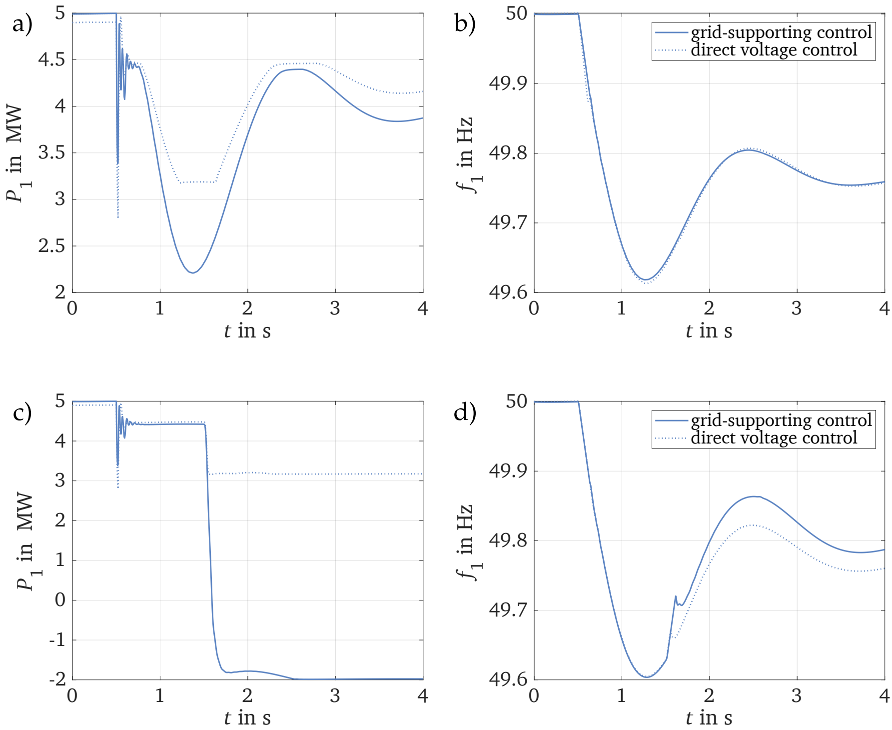

Figure 9.8: Comparison of the grid-supporting and direct voltage control for inverter-based generators (IBG) in the medium-voltage benchmark grid for a load-step $\Delta P_{L0} = 50$ MW in the max IBG scenario with $S_{IBG} = 28$ MVA:
a) Active power P_1 and b) frequency f_1 for the linear fast-frequency response (FFR) control,
c) Active power P_1 and d) frequency f_1 for the constant FFR control at BB1 at the low-voltage side of the HV/MV-transformer T1.

The frequency nadir f_{min} is worst for the constant FFR, while the direct voltage control leads to slightly better results. This can be explained by the faster inner control of the direct voltage control, which adjusts the output current without time delay. The linear FFR results show the disadvantage of the dynamic current limitation in the direct voltage control that can also be seen in Figure 9.8 c). The quasi-steady-state frequency deviation Δf_{qss} at $t = 10$ s is smallest for the grid-supporting control with linear FFR, then increased due to the dynamic current limitation for the direct voltage control with constant FFR, and further increased for the direct voltage control with constant FFR. The grid-supporting

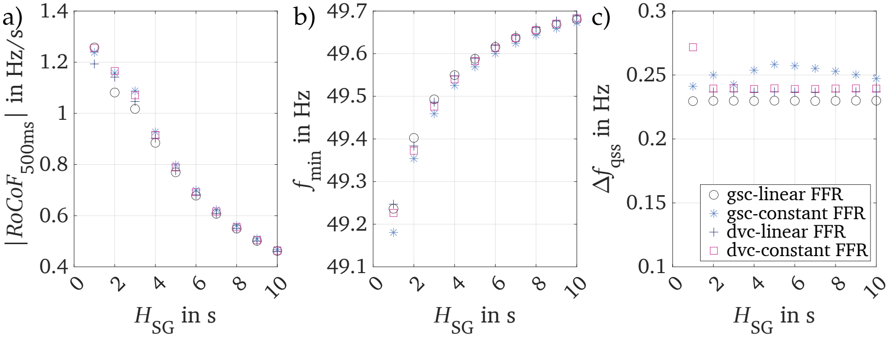

Figure 9.9: Comparison of grid-supporting control (gsc) and direct voltage control (dvc) equippend with a linear fast-frequency response (FFR) or constant FFR implementation regarding the frequency metrics for varying inertia constant H_{SG} and a loadstep $\Delta P_{L0} = 50$ MW in the max IBG scenario:
a) Rate of change of frequency (RoCoF) for a time window $\Delta t = 500$ ms,
b) frequency nadir f_{min} and
c) quasi-steady-state frequency deviation Δf_{qss}.

control with constant FFR leads to the largest quasi-steady-state frequency deviation Δf_{qss}.

Direct voltage control: The IBG direct voltage control is considered a grid-forming control regarding its voltage support. Also during frequency events, it shows a larger first active power reduction at $t = 0.5$ s than the grid-supporting control. Due its dynamic current limit adaptation, the direct voltage control reaches earlier its current limit and therefore the frequency support through an FFR is significantly reduced compared to the grid-supporting control.

9.1.3 *Impact of the External Grid*

The influence of the external high-voltage grid is investigated by means of the inertia constant H_{SG} and the size of the loadstep ΔP_{L0}. Figure 9.10 shows the frequency f_1 of the max IBG scenario depending on the two variables mentioned. The results show that decreasing the system inertia constant H_{SG} or increasing the loadstep ΔP_{L0} leads to a worsening of the frequency curve. The inertia constant H_{SG} affects the RoCoF and frequency nadir f_{min}. Very small values $H_{SG} \leq 3$ s, which represent a very low-inertia power system, show oscillations in the frequency curve. The oscillations occur due to the fast frequency dynamics and associated larger voltage variations, which both can lead to instability of the SG and IBG control. The oscillations are damped relatively fast and the system is stabilised. The variation of the loadstep ΔP_{L0} shows comparable results to the ones obtained for the medium-voltage testbench in Figure 8.5. Increasing the loadstep ΔP_{L0} leads to steeper and more severe frequency drops and a difference in the quasi-steady-state frequency deviation Δf_{qss}.

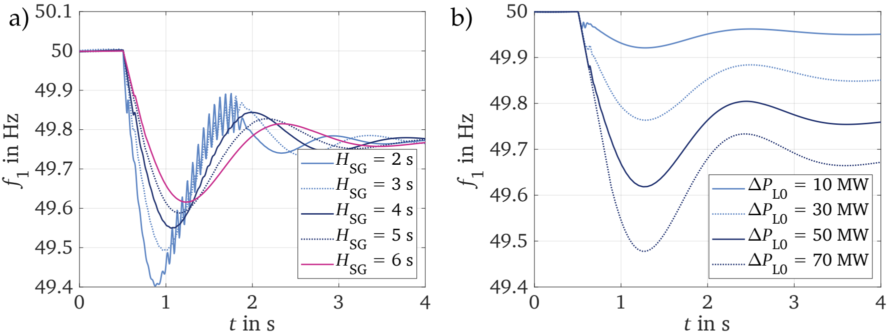

Figure 9.10: Impact of the external inertia constant H_{SG} and loadstep size ΔP_{L0} on the frequency in the medium-voltage benchmark grid for the max IBG scenario with $S_{IBG} = 28$ MVA:
a) Frequency f_1 for varying inertia constant H_{SG} and
b) frequency f_1 for varying loadstep size ΔP_{L0}.

9.1.4 *Impact of the Load Modelling*

The load models defined in Table 5.3 are applied to the medium-voltage benchmark grid in order to achieve a frequency dependency not only in the IBG, but also in the load models. As already shown in Chaper 8.3.3, the impact of the load modelling is rather small compared to the IBG. Figure 9.11 shows the results for the two static and two dynamic composite load models. The load models are applied to the loads L1-L5. The load L0 in the high-voltage grid and the loadstep remain unchanged in order to identify the sole contribution from the medium-voltage benchmark grid.

The active and reactive power P_1, Q_1 exchanged with the high-voltage grid are affected by the choice of load modelling: The active power P_1 drawn from the high-voltage grid decreases with increasing frequency dependency of the load model and is largest for the static *exp* res-year model and smallest for the composite res and *exp-f* ind load models. The reactive power Q_1 also varies, which can be explained by the different power factors $\cos\varphi$ applied to the

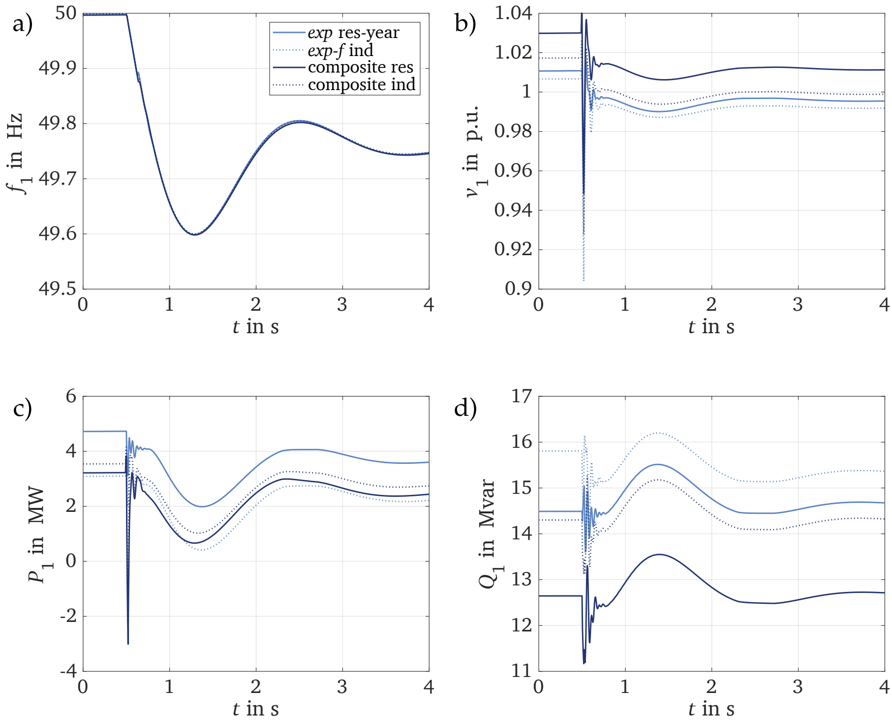

Figure 9.11: Dynamics of the medium-voltage benchmark grid for different static and dynamic load models for a loadstep $\Delta P_{L0} = 50$ MW:
a) Frequency, b) voltage, c) active power and d) reactive power at the low-voltage side of the HV/MV-transformer $T1$ at busbar BB1).

load models, cf. Table 5.3. As a consequence, the voltage v_1 adapts to the reactive power Q_1. The frequency in Figure 9.11 does not change significantly when applying different frequency-dependent and static load models. In future scenarios, a stronger adaptation of the loads as a response to frequency changes can be assumed especially for loads based on power electronics that can quickly adapt their active power consumption, e.g. charging of electric vehicles or on a larger scale industrial processes that can be postponed.

9.2 HIGH-VOLTAGE GRID

While both medium- and high-voltage grids engage in dynamic frequency studies to ensure the stability of the grid, there exist substantial differences. The high-voltage grid features larger generation units and covers larger spatial distances. While the medium-voltage grid typically assumes the task of energy distribution, the high-voltage grid is rather used for energy transmission, owing to its higher voltage level. Only very large solar PV parks and large windfarms are connected to the high-voltage grid. The frequency within interconnected power systems primarily manifests as a variable within the transmission grid. In this context, high-voltage grids have a particularly high capacity to provide essential frequency support through large installed IBG power.

Figure 9.12 illustrates the outcomes corresponding to the scenarios outlined in Table 7.5. These scenarios employ grid-supporting control with linear FFR for all IBG within the windfarms. The results for a constant FFR are shown in the Appendix A.7, Figure A.4. Notably, modifications in the parameters of the SG control lead to a momentary voltage drop, lasting several seconds, in response to a loadstep $\Delta P_{L0} = 150$ MW. This response occurs at a slower rate compared to investigations conducted within the medium-voltage grid. As a result of this voltage dip, a slight distortion is observable in the frequency curve. This distortion can be attributed to the voltage dip itself, rather than to the frequency measurement method. The active and reactive power P_1, Q_1 drawn from the transmission grid are caused by the characteristics of the frequency and voltage-dependent loads. Subsequently, there is an increase in the active power injection from the IBG around $t = 0.8$ s, prompted by the attainment of the deadband threshold, $db_{\mathrm{FFR}} = 200$ mHz. Consequently, the active power P_1 drawn from the transmission grid experiences further reduction. In the max IBG scenario, involving six windfarms with a cumulative IBG rated power $S_{\mathrm{IBG}} = 180$ MVA, power flow reversal occurs during the frequency support phase. This circumstance leads to a minor reduction in the IBG reactive power to favour the active power increase, thereby resulting in a short increase in the reactive power drawn from the transmission grid. Due to the presence of a quasi-steady-state frequency deviation $\Delta f_{\mathrm{qss}} \geq 200$ mHz, both active and reactive power P_1, Q_1 persist as part of the frequency support mechanism.

The frequency curve f_1 shows larger and faster frequency drops for an increasing share of IBG. This is due to the fact that the SG active power infeed is significantly reduced, i.e. adaptation of the SG reference active power P_{ref} in favour to the IBG power infeed. As the IBG in standard parametrisation are equipped with a droop $d_{\mathrm{FFR}} = 0.05$ and a deadband $db_{\mathrm{FFR}} = 200$ mHz, the frequency reponse to the loadstep ΔP_{L0} is worse than for the larger SG share with a governor droop $d_{\mathrm{Gov}} = 0.02$ and the provision of inertia.

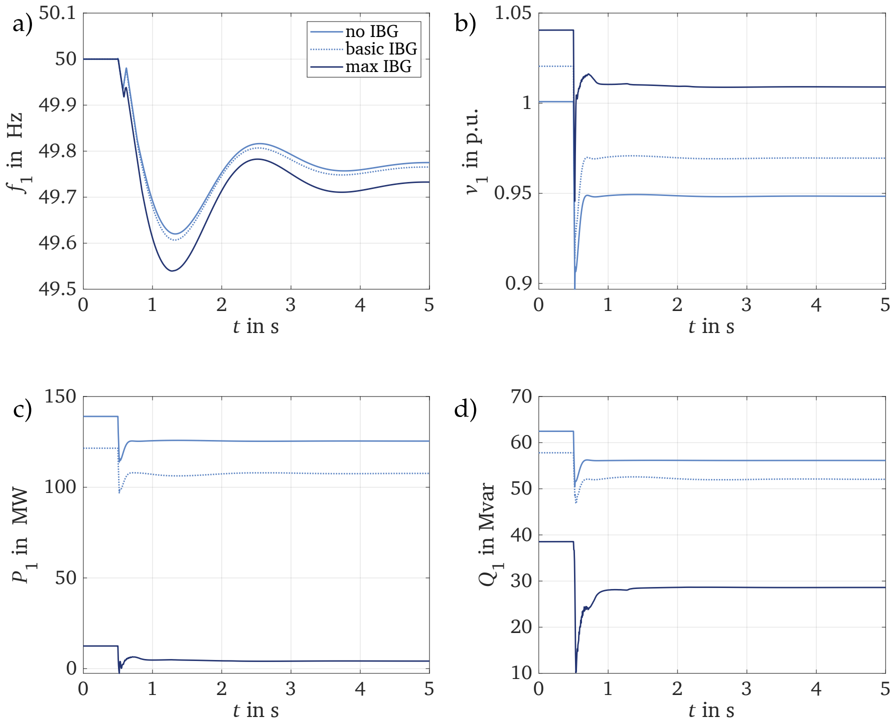

Figure 9.12: Dynamics of the high-voltage grid for different inverter-based generation (IBG) scenarios for a loadstep $\Delta P_{L0} = 150$ MW:
a) Frequency, b) voltage, c) active power and d) reactive power at the low-voltage side of the HV/MV-transformer T1 at busbar BB1.

9.2.1 *Power System Inertia*

The impact of the inertia constant H_{SG} on the high-voltage grid's frequency metrics is depicted in Figure 9.13, mirroring trends observed within the medium-voltage grid. However, notable differences emerge due to the increased short-circuit power S''_{SC}, resulting in better, i.e. less oscillatory frequency responses within very low-inertia systems. Due to the very fast dynamics for small inertia constants, the time window Δt for the RoCoF calculation is reduced to 100 ms. Notably, the implementation of a linear FFR engenders reduced RoCoF and elevated frequency nadir f_{min} values in the high-voltage grid compared to a constant FFR implementation. The strong influence of the constant FFR becomes evident regarding the quasi-steady-state frequency deviations Δf_{qss}.

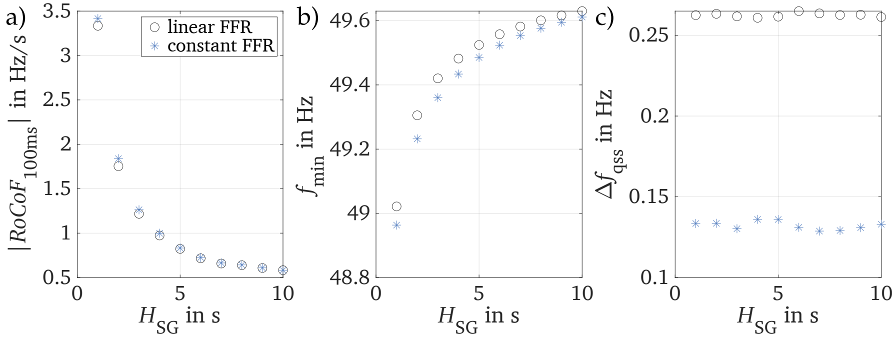

Figure 9.13: Variation of the system inertia constant H_{SG} and the fast-frequency response (FFR) implementation of the windfarms for a loadstep $\Delta P_{\text{L0}} = 150$ MW:
a) Rate of change of frequency (RoCoF) for a time window $\Delta t = 100$ ms,
b) frequency nadir f_{min} and
c) quasi-steady-state frequency deviation Δf_{qss}.

9.2.2 *Spatial Distribution*

Figure 9.14 illustrates the impact of the grid connection point of a windfarm comprising 10 turbines, each with a rated power $S_{\text{r,WT}} = 6$ MVA in the basic IBG scenario. In relation to other sensitivity factors, the effect of the grid connection point is small. The degradation in both frequency nadir f_{min} and quasi-steady-state frequency deviation Δf_{qss} becomes apparent as the electrical distance to the busbar BB1 increases. This degradation occurs because individual IBG experience the frequency drop with a certain delay, due to travelling wave propagation, resulting in a slightly diminished response.

9.3 SUMMARY

This chapter explores the frequency dynamics of active distribution grids, emphasising the growing integration of inverter-based generation (IBG) and its impact on the frequency stability. The study evaluates the three key frequency metrics, frequency nadir, Rate of Change of Frequency (RoCoF), and quasi-steady-state frequency deviation, in two typical benchmark distribution grids under various operational scenarios.

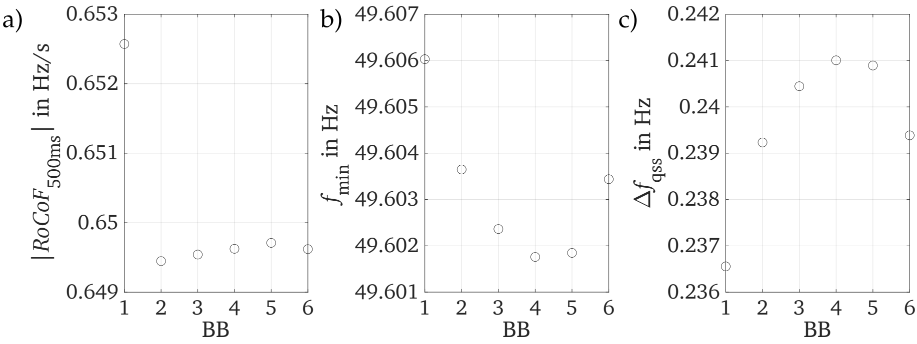

Figure 9.14: Variation of the connection point of the windfarm from busbar BB1 to BB6 in the basic IBG scenario with a loadstep $\Delta P_{\mathrm{L0}} = 150$ MW:
a) Rate of Change of Frequency (RoCoF) for a time window $\Delta t = 500$ ms,
b) frequency nadir f_{min} and
c) quasi-steady-state frequency deviation Δf_{qss}.

The medium-voltage benchmark grid, studied in detail, reveals that an increasing share of IBG leads to a steeper frequency drop during disturbances due to reduced system inertia. The results highlight the importance of the frequency support from IBG in response to a decreasing system inertia and share of conventional power plants. Additionally, the chapter introduces sensitivity analyses, considering factors like IBG control strategies, external grid parameters, and load modelling.

Scenarios with an increasing share of IBG show that replacing synchronous generators (SG) with IBG might initially worsen frequency stability. However, IBG equipped with grid-supporting functions can enhance frequency stability when using advanced control mechanisms. Two IBG control concepts, the grid-supporting and the direct voltage control are compared regarding the frequency support. The simulation results show that, compared to the grid-supporting control, the direct voltage control offers limited frequency support, particularly with both linear and constant fast-frequency response (FFR) implementations. The study emphasises the dynamic adjustment of current limitation in direct voltage control, leading to a capped active power infeed from IBG. The load modelling with a conservative frequency dependency shows only negligible impact on the dynamic frequency.

The results can be validated in the high-voltage benchmark grid, where larger windparks lead to comparable results as for the medium-voltage benchmark grid. Due to the larger installed power of grid components and larger distances, variations in the high-voltage grid lead to larger differences between scenarios.

However, the spatial distribution, i.e. the grid connection point of the windpark within the high-voltage benchmark grid does not lead to significant changes.

10 DERIVATION OF DYNAMIC AGGREGATED MODELS FOR FREQUENCY INVESTIGATIONS

With the increasing share of IBG in distribution grids, this technology must increasingly contribute to power system stability [93]. Frequency studies, which are usually carried out on transmission system level, must implement the frequency behaviour of the underlying active distribution grids. For this reason, it is necessary to model active distribution grids appropriately for dynamic frequency investigations. A complete representation of all underlying grids is impossible due to the vast number of components, the expansion of the grids and due to a lack of available data [76]. Therefore, efforts are being made to develop dynamic equivalent models that replicate the dynamic behaviour of the detailed distribution grid while requiring less data and computation time [67].

The objective of this chapter's study is to apply the greybox approach to the medium-voltage and high-voltage benchmark grid presented in Chapter 7. A greybox approach based on the PSO and DE algorithms as described in Chapter 4.3 is implemented and applied to the single-machine dynamic equivalent fitting model as shown in Chapter 7.3. The parameter optimisation for the equivalent model is described in Chapter 7.4 and implements a least-square approach of the active and reactive powers exchanged with the overlying grid. The parameters to be optimised include the load, IBG and line parameters given in (7.1), (7.2) and (7.3). The limits for each parameter are discussed in Chapter 10.1.

The scenarios investigated are introduced in Chapter 10.2. The results of the greybox aggregation are presented and discussed in Chapter 10.3 for the medium-voltage benchmark grid and in Chapter 10.4 for the high-voltage benchmark grid.

10.1 PARAMETER LIMITS

For the greybox aggregation of the medium-voltage and high-voltage benchmark grid, the dynamic equivalent fitting model described in Chapter 7.3 is considered and parametrised. The fitting model as well as the parameter vector $\mathbf{x}$ to be optimised and the objective function $\epsilon(\boldsymbol{x})$ presented in Chapter 7.4 are identical for the medium-voltage and high-voltage benchmark grid aggregation. The parameter limits are adapted depending on the benchmark grid and the scenario and are presented here in brief.

The allowable ranges of each parameter to be optimised within the greybox aggregation are given in Table 10.1. The aggregated IBG apparent power $S_{\mathrm{IBG,agg}}$

is chosen within the limits $0.2 \cdot \sum S_{\mathrm{IBG}} < S_{\mathrm{IBG,agg}} < 1.1 \cdot \sum S_{\mathrm{IBG}}$ and depends on the total installed rated IBG power $\sum S_{\mathrm{IBG}}$ in each benchmark grid and scenario. For example, the medium-voltage benchmark grid with a basic share of IBG has a total installed IBG power $\sum S_{\mathrm{IBG}} = 6.24$ MVA and the lower and upper limit for the parameter optimisation are chosen to 0.62 MVA and 6.86 MVA, respectively. The power factor $\cos\varphi_{\mathrm{IBG,agg}}$ is chosen to be between 0.8 and 1.0 as all installed IBG exhibit an inductive, i.e. voltage-reducing behaviour, in order to counteract the increased voltage due to their power infeed. If IBG with capacitive reactive power behaviour are connected in the grid to be aggregated, the limit must be adjusted accordingly. The FFR parameters of the linear FFR are chosen to be within the limits given in [132] and [133] and discussed in Chapter 3.4. The impact of different forms of FFR implementations is discussed in Chapter 9.1.1.

Table 10.1: Parameter limits for the aggregation models.

grid	medium-voltage grid				high-voltage grid			
scenario	basic IBG		max IBG		basic IBG		max IBG	
parameter	lower limit	upper limit	lower limit	upper limit	lower limit	upper limit	lower limit	upper limit
S_{IBG} in MVA	0.62	6.86	5.6	30.8	6	33	72	396
$\cos\varphi_{\mathrm{IBG}}$	0.8	1.0	0.8	1.0	0.8	1.0	0.8	1.0
d_{FFR} in %	2	12	2	12	2	12	2	12
db_{FFR} in mHz	0	200	0	200	0	200	0	200
$k_{\mathrm{P,OC}}$	0.1	1.5	0.1	1.5	0.1	1.5	0.1	1.5
$k_{\mathrm{I,OC}}$ in s^{-1}	5.5	88	5.5	88	5.5	88	5.5	88
l_{line1} in km	1	10	1	10	1	70	1	70
R'_{line1} in Ω/km	0	1	0	1	0	0.1	0	0.1
L'_{line1} in mH/km	0	2	0	2	0	2.5	0	2.5
l_{line2} in km	1	10	1	10	1	70	1	70
R'_{line2} in Ω/km	0	1	0	1	0	0.1	0	0.1
L'_{line2} in mH/km	0	2	0	2	0	2.5	0	2.5
P_{L} in MW	0	30	0	30	0	740	0	740
Q_{L} in MVar	0	20	0	20	0	370	0	370

The outer control PI controller parameters are also part of the optimisation and chosen to be roughly in the range $0.25 \cdot k_{\mathrm{P,OC}} < k_{\mathrm{P,OC,agg}} < 4 \cdot k_{\mathrm{P,OC}}$ as well as $0.25 \cdot k_{\mathrm{I,OC}} < k_{\mathrm{I,OC,agg}} < 4 \cdot k_{\mathrm{I,OC}}$, so that the dynamic behaviour can be optimised.

The line parameters differ between the medium-voltage and high-voltage benchmark grid, but remain identical when applying different scenarios. The aggregated line lengths $l_{\mathrm{line1,agg}}$, $l_{\mathrm{line2,agg}}$ get assigned a lower limit of 1 km for a minimum decoupling of the external grid and the aggregated distribution grid model. The upper limit is chosen to the longest electrical distance any busbar in the benchmark grid has to the UHV/HV transformer. The line dependent resistances and inductances $R'_{\mathrm{line,agg}}$, $L'_{\mathrm{line,agg}}$ of each line are chosen between zero and twice the original value.

The aggregated load is modelled as a static load model without voltage or frequency dependency as the results in Chapter 9.1.4 show only very little dependency on the load modelling. The limits for the aggregated load active power consumption $P_{\mathrm{L,agg}}$ are set from zero to the total rated load apparent power $\sum S_{\mathrm{L}}$ and for the reactive power $Q_{\mathrm{L,agg}}$ from zero to two thirds of the total rated load apparent power $\sum S_{\mathrm{L}}$ in the benchmark grid.

10.2 SCENARIO DEFINITION

The greybox aggregation is carried out for the medium-voltage and high-voltage benchmark grids. For both, the max IBG scenario is in focus as it represents the maximum impact of the active distribution grid on the frequency dynamics. Apart from the greybox aggregation, an additional reduced-order model is considered for the comparison and assessment of the quality of the aggregation: The negative load model summarises the active and reactive power fed in by all IBG connected to the distribution grid and represents the power infeed as a static load with negative sign and constant active and reactive power. The same procedure is repeated for the aggregation of loads. This static model is the simplest representation of the aggregated IBG power, but cannot represent its dynamic behaviour. According to [200], more than a third of the transmission system operator (TSO) surveyed in 2017 still use such static models to represent the downstream IBG plants.

Various influences on the quality of the aggregation results are analysed below. The impact of the optimisation algorithm settings are studied. The PSO and DE best and DE rand algorithms are compared against the results of the detailed grid as well as the negative load model. The number of iterations and the swarm size are also varied.

Subsequently, the impact of the unsymmetric distribution of IBG control is applied: A mix of grid-supporting and direct voltage control as well as the two variations of the FFR. These scenarios show the limits of the aggregation method when using heterogeneous controls.

The reduced-order models of the medium-voltage grid replace the loads representing the underlying grids. This way, the impact of the max IBG scenario from two voltage levels can be investigated. Finally, this high-voltage grid is investigated regarding its impact on the frequency dynamics at the transformer to the transmission grid.

10.3 EQUIVALENT MEDIUM-VOLTAGE GRID

The medium-voltage benchmark grid is aggregated using the power measurements P_1, Q_1 at busbar BB1 and therefore only feeder 1 is considered here, see Chapter 7.1 and Figure 7.1. In the following, the measurements at busbar BB1 from the detailed medium-voltage benchmark grid are referred to as the reference and variables from the aggregated model are given the additional index 'agg'. Furthermore, only the max IBG scenario, cf. Table 7.2, is considered, as this is where the effect of the IBG is most evident. As described in Chapter 10.2, in addition to the greybox approaches, a comparative case is examined which models the IBG feed-in as a single static negative load.

This chapter presents the results of the medium-voltage benchmark grid aggregation. After a brief comparison of the different aggregation approaches and the optimisation methods for the greybox approach, the influencing parameters of the optimisers are examined. The aggregation approach is then tested for homogeneous and inhomogeneous cases, i.e. different controls and control parameters are applied to the IBG controls. The aggregation model is adapted for the aggregation of heterogeneous cases.

10.3.1 *Comparison of Aggregation Approaches*

The comparison of the active and reactive power curves P_1, Q_1 of the detailed grid as a reference case and the aggregation as a negative load and as a single machine equivalent using the greybox approach is shown in Figure 10.1. Figure 10.1 a) and b) show the power curves of the negative load model and the greybox approach with PSO algorithm. Figures 10.1 c) and d) show the curves for a greybox aggregation with the two variations of the DE algorithm. The max IBG scenario of the medium-voltage benchmark grid in the default implementation, i.e. with grid-supporting control and a linear FFR control with a droop $d_{\mathrm{FFR}} = 5$ % and a deadband $db_{\mathrm{FFR}} = 200$ mHz, is used for this investigation. The disturbance is a load step of load L0 with $\Delta P_{\mathrm{L0}} = 50$ MW at $t = 0.5$ s.

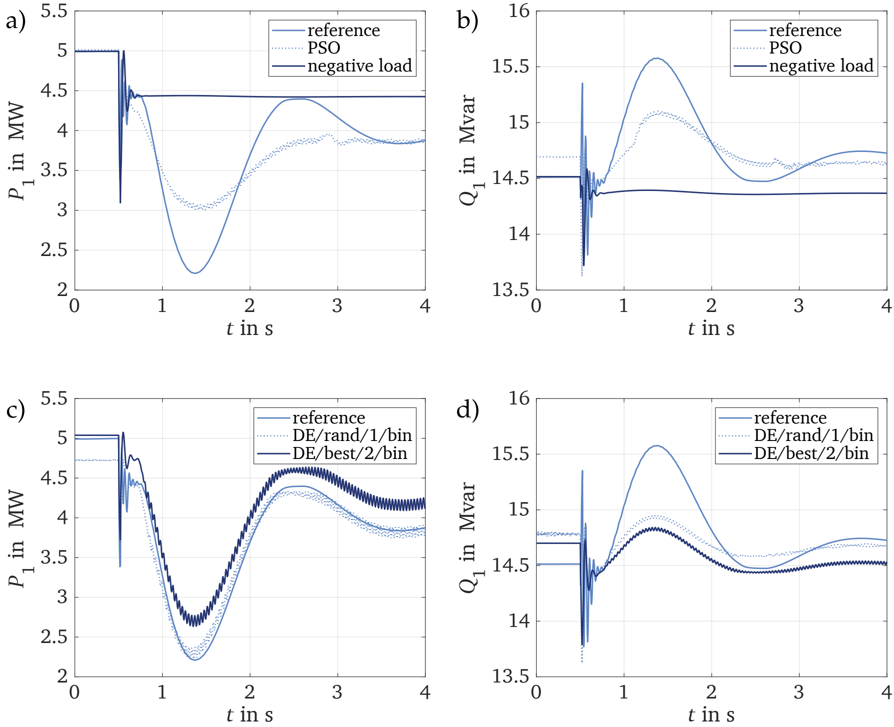

Figure 10.1: Dynamics of the MV benchmark grid aggregation for the max inverter-based generation (IBG) scenario with linear fast-frequency response (FFR) with a droop $d_{\mathrm{FFR}} = 5$ % and deadband $db_{\mathrm{FFR}} = 200$ mHz and for a load-step $\Delta P_{\mathrm{L0}} = 50$ MW:
a) Active power P_1 and b) reactive power Q_1 for the particle swarm optimisation (PSO) and negative load aggregation.
c) Active power P_1 and d) reactive power Q_1 for the two variants of the differential evolution (DE) algorithm.

The power curves of the negative load model show that the static model cannot simulate the dynamic active power adjustment of the FFR control. After the active power drawn from the high-voltage grid drops due to the voltage-dependent behaviour of the aggregated load, the active power remains at a constant value $P_1 \approx 4.45$ MW. The advantage of the FFR control, i.e. the increased active power feed-in of the IBG, cannot be reproduced by the negative load aggregation. The same behaviour can also be observed with regard to the reactive power Q_1.

The results of the greybox aggregation using the PSO algorithm show a dynamic adaptation of the active and reactive power P_1, Q_1. The PSO underestimates the dynamic influence of the FFR by around one third. In contrast to the negative load model, however, the PSO estimates the quasi-steady state before and following the disturbance with only a slight deviation. Table 10.2 shows the optimised parameters on which the simulated curves in Figure 10.1 are based. The PSO algorithm uses the smallest installed IBG power S_{IBG} and therefore underestimates the dynamic contribution of the FFR even though a droop $d_{\mathrm{FFR}} = 0.02$ strongly adjusts the IBG active power output.

Table 10.2: Optimised parameters for the dynamic equivalent of the medium-voltage benchmark grid.

	PSO	DE/rand/1/bin	DE/best/2/bin
S_{IBG}	5.24 MVA	11.31 MVA	11.02 MVA
$cos\varphi_{\mathrm{IBG}}$	0.8	1.0	0.8
d_{FFR}	0.020	0.024	0.057
db_{FFR}	6 mHz	160 mHz	200 mHz
$k_{\mathrm{P,OC}}$	20.0	4.34	0.01
$k_{\mathrm{I,OC}}$	0.01 s^{-1}	20.0 s^{-1}	7.6 s^{-1}
l_{line1}	1.0 km	5.26 km	3.86 km
R'_{line1}	0.69 Ω/km	0.0 Ω/km	0.82 Ω/km
L'_{line1}	0.12 mH/km	1.0 mH/km	1.0 mH/km
l_{line2}	10.0 km	1.19 km	10.0 km
R'_{line2}	0.19 Ω/km	0.76 Ω/km	1 Ω/km
L'_{line2}	1.0 mH/km	1.0 mH/km	0.29 mH/km
P_{L}	8.03 MW	17.52 MW	7.41 MW
Q_{L}	16.99 Mvar	13.58 Mvar	18.23 Mvar

In Figure 10.1 c), the two DE variants DE/rand/1/bin and DE/best/2/bin show a much stronger dynamic adjustment of the active power than the PSO. Due to the higher installed IBG power and a relatively weak decoupling, oscillations occur due to interactions between the SG and IBG controls. The weak decoupling occurs in the DE/rand/1/bin variant due to the short cable length. In the DE/best/2/bin variant, the line-dependent inductance L_{line2} is low and therefore the R/X ratio is relatively high. Apart from the oscillation, the DE/rand/1/bin variant matches the dynamic active power curve P_1 and the quasi-steady state following the loadstep with only minor deviations. However, the steady state before the loadstep $0 < t < 0.5$ s is estimated with a mean absolute error (MAE) larger than 5 %. The variant DE/best/2/bin estimates a very similar active power curve P_1 with an offset of approximately 0.3 MW. The increase of the reactive power Q_1 drawn from the overlying high-voltage grid is underestimated for both the DE/rand/1/bin and DE/best/2/bin variant.

In order to better compare the different aggregation approaches, the results are presented in the form of boxplots in Figure 10.2. The boxplots give a graphical representation of the distribution of the absolute error (AE) for each time step of the simulation. It provides a visual summary of key statistics: The blue box represents the interquartile range, which indicates the spread of the central 50 % of the data. The red line inside the box represents the median. The black lines indicate the whiskers, which define the range of 150 % of the interquartile range with the exception being here that no negative AE can occur and the lower whisker is zero. Individual AE beyond the whiskers are considered outliers and represented and individual red crosses. Further details on boxplots can be found in [201].

The results shown in Figure 10.2 correspond to the ones from Figure 10.1 and compare the four different aggregations in comparison to the reference case using the detailed grid model. Again, it can be seen that the negative load aggregation does not meet the requirements and reaches an active power AE larger than 40 %. The large number of outlier corresponds to the missing dynamic active power adaptation as seen in Figure 10.1 a). The PSO exhibits a relatively constant deviation from the reference curve. For this reason, the deviations are included in the interquartile range and no outliers occur for the active power AE. In contrast, the reactive power boxplot for the PSO is scattered, mainly due to the differences in the transient time range following the loadstep. The two DE approaches show promising results with a AE median for the active power P_1 of 2.5 % and 4.6 %. The AE of the reactive power is relatively scattered for all four aggregations due to the larger deviations during the dynamics following the loadstep. The AE of the frequency f_1 is very small with the maximum error being less than 1 ‰ for all aggregations. The DE/rand/1/bin algorithm obtains the best results, while the negative load aggregation is worst.

Figure 10.3 shows the performance of each optimisation algorithm over the iterations. The minimisation of the objective function $\min \epsilon(x)$ as defined in (7.6) is plotted after each iteration and for a swarm size of 90. The course of the objective functions shows a steep reduction of the PSO algorithm during the first iteration. This is due to the randomised choice of the start parameters. The PSO algorithm then shows a steady improvement of the objective function until iteration 72 and then stagnates. The DE/rand/1/bin algorithm exhibits larger jumps and reaches the smallest objective function with an average deviation of 0.15 MVA^2. The DE/best/2/bin algorithm reaches similar results as the PSO after 100 iterations, but starts at a better objective function.

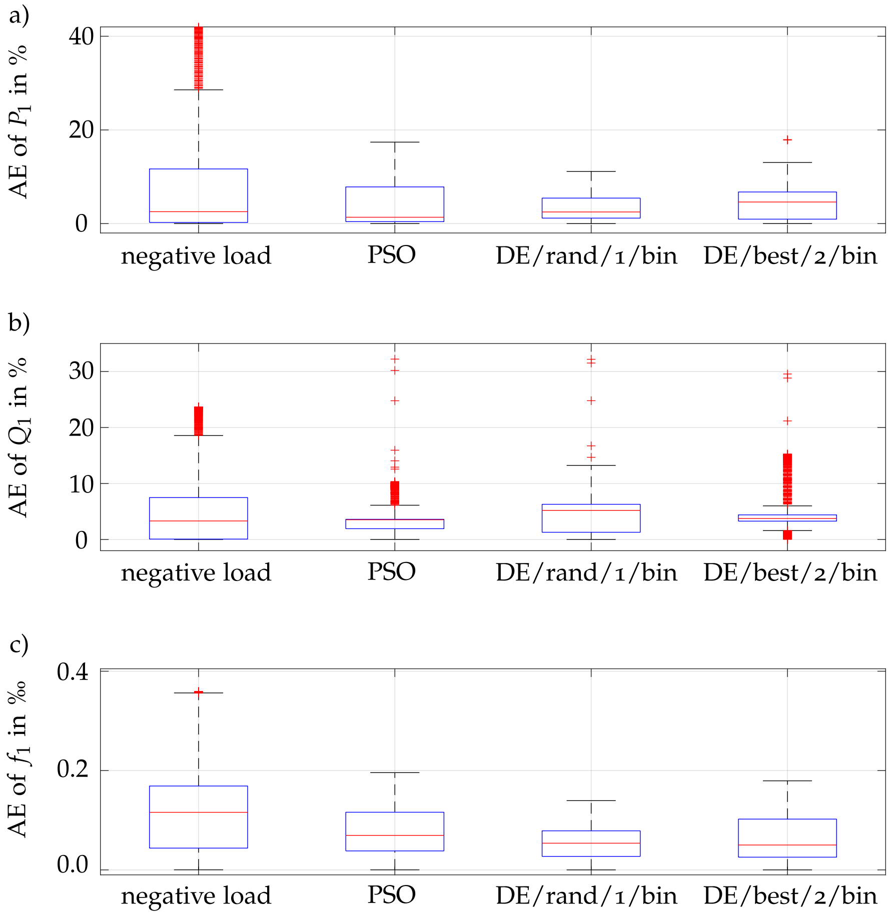

Figure 10.2: Distribution of the relative mean absolute error for the different aggregation methods of the MV benchmark grid based on 100 iterations and a population $POP = 90$. The relative AE is evaluated for
a) the active power P_1,
b) the reactive power Q_1 and
c) the frequency f_1 measured at busbar BB1.

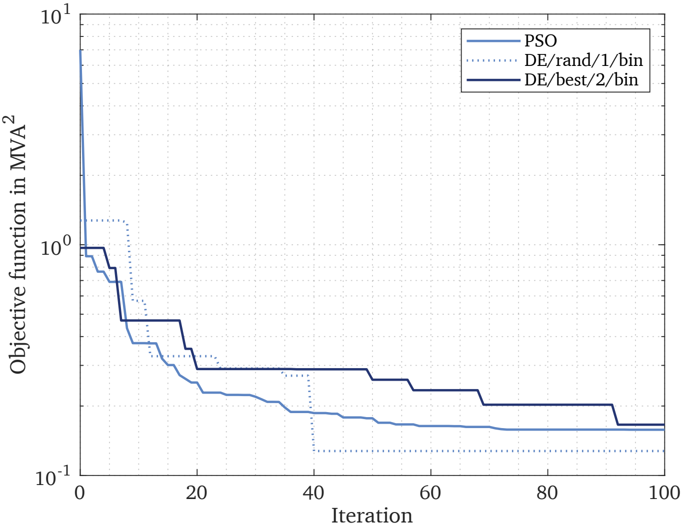

Figure 10.3: Comparison of the objective function $\epsilon(\mathbf{x})$ for the particle swarm optimisation (PSO) and the differential evolution (DE) algorithm using a population $POP = 90$.

Aggregation Approaches: The results in Figures 10.1 through 10.3 show that selecting an appropriate aggregation algorithm is crucial. Among the algorithms evaluated, the DE/rand/1/bin algorithm excels, particularly in its objective function performance. This is supported by the boxplot analysis, which highlights its effective dynamic representation of the detailed medium-voltage grid. Despite these strengths, this algorithm falls short in accurately reflecting the pre-fault steady-state. Conversely, the PSO algorithm aligns more closely with the steady-state conditions but lacks the dynamic adaptability found in the DE/best/2/bin algorithm. Given these considerations, the DE/best/2/bin algorithm emerges as the most balanced choice. It handles both the dynamic adaptation and steady-state representation, even though its objective function performance is not as good as the other algorithms.

10.3.2 *Optimisation settings*

Figure 10.4 shows the results of the aggregation using the DE/best/2/bin algorithm. The distribution of the AE for each simulation time step is presented for the active power P_1, the reactive power Q_1 as well as the frequency f_1 at busbar BB1. Further, the settings of the optimiser, i.e. the maximum number of iterations IT and the population size or number of particle POP are varied.

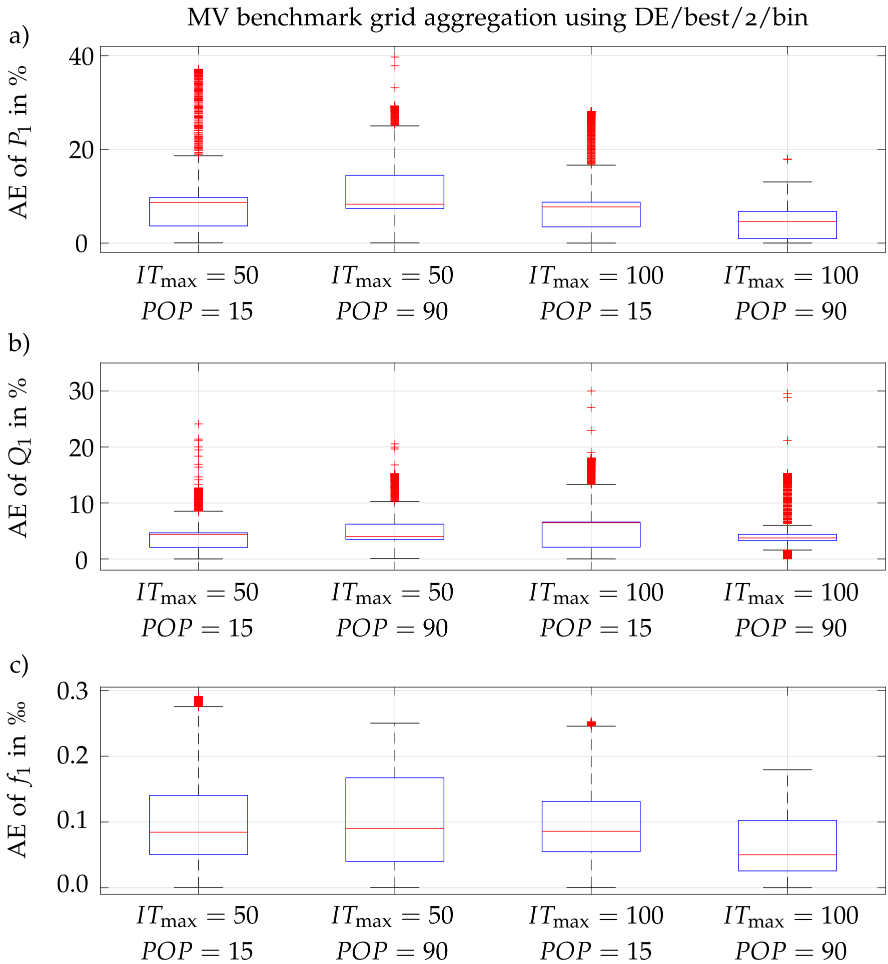

Figure 10.4: Distribution of the relative absolute error (AE) for the aggregation of the medium-voltage benchmark grid using the diffenrential evolution DE/best/2/bin algorithm for a varying maximum number of iterations $IT_{\max}$ and population size POP. The AE is evaluated for
a) the active power P_1,
b) the reactive power Q_1 and
c) the frequency f_1 measured at busbar BB1.

The results presented in Figure 10.4 indicate that an increase in the number of iterations IT does not consistently enhance the aggregation outcomes, especially in scenarios where the population is fixed at 15. On the other hand, for larger populations, augmenting the number of iterations, or conversely, increasing the population size when a sufficient number of iterations are already in place, tends to improve the aggregation results. The data shows that the smallest values for the median, interquartile range, and whiskers are observed at the highest iteration count combined with the largest population size. There are only a few outliers in the reactive power AE that resemble those observed with smaller populations. The DE/best/2/bin algorithm is influenced solely by the results of the initial random selection of start parameters, as it does not involve randomised parameter choices in subsequent iterations.

For the DE/rand/1/bin algorithm, the results are documented in the Appendix A.8, Figure A.5. Similarly, results for the PSO are shown in the Appendix A.8, Figure A.6. In contrast to the DE/best/2/bin algorithm, these two algorithms incorporate a partially randomised selection of parameters in each iteration. Consequently, their outcomes do not consistently demonstrate improved performance with larger populations or increased iterations.

10.3.3 *Aggregation results for varying inertia constant*

By reducing the system inertia, the contribution of IBG to the frequency stability becomes more relevant. This section therefore discusses the aggregation results for a varying inertia constant H_{SG} of the external grid. The results of the greybox aggregation using the DE/best/2/bin algorithm with a population of 90 and 100 iterations are shown in Figure 10.5.

The aggregation models can reflect the influence of decreasing inertia and in principle show a stronger adjustment of the active power for lower inertia values. For the aggregation at an inertia $H_{SG} = 8$ s, the current limit of the IBG is reached, which is why the flat curve occurs and the active power P_1 does not drop below 3.5 MW. The frequency also shows the desired dependency on the inertia and becomes more critical at low inertia constants. Compared to the results found in Figure 9.10, the frequency curves are modelled more critically than simulated in the detailed medium-voltage benchmark grid. The curves in Figure 9.10 b) and d) for an inertia constant $H_{SG} = 5$ s differ largely from the other curves, but also reproduces the behaviour shown in Figure 9.10 at very low inertia. Due to a very low inertia and high rated power of the grid-supporting IBG, undesired oscillations occur, which can be attributed to an interaction between the control of the IBG and the SG.

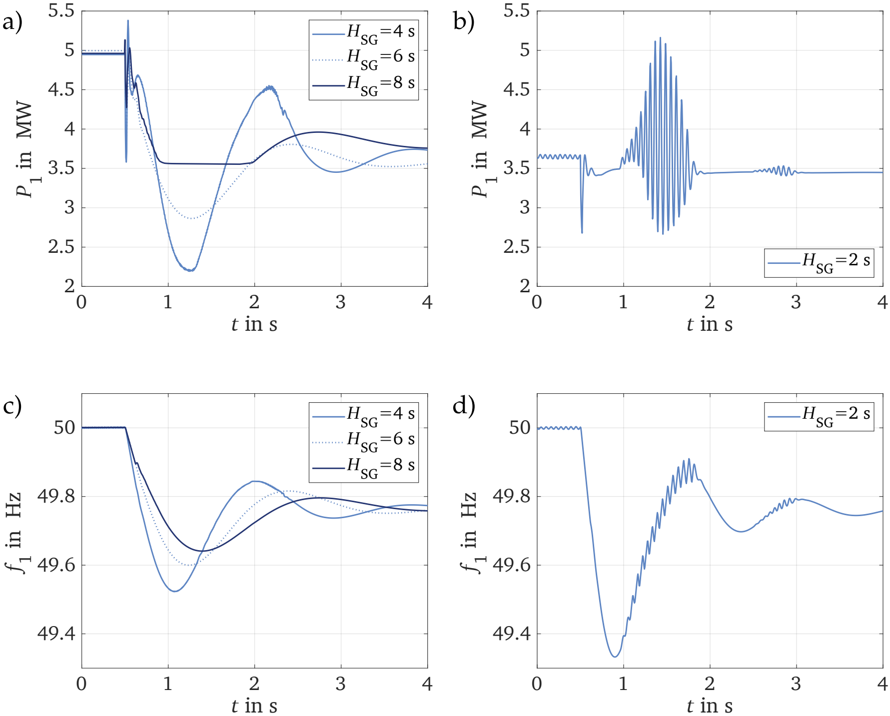

Figure 10.5: Dynamics of the medium-voltage benchmark grid aggregation for the high inverter-based generation (IBG) scenario with linear fast-frequency response (FFR) with a droop $d_{\mathrm{FFR}} = 5$ % and deadband $db_{\mathrm{FFR}} = 200$ mHz and for a loadstep $\Delta P_{\mathrm{L0}} = 50$ MW using the DE/best/2/bin algorithm for varying inertia constant H_{SG}:
a) and b) Active power P_1,
c) and d) frequency f_1.

10.3.4 *Inhomogeneous inverter control*

So far, only homogeneous scenarios in the medium-voltage benchmark grid are aggregated, i.e. all IBG are modelled uniformly with linear FFR and grid-supporting control. Inhomogeneous scenarios are now to be aggregated here, namely a mixed use of the linear and constant FFR implementations within the medium-voltage benchmark grid. Additionally, the impact of the direct voltage control and the extent to which the aggregation can take into account the two control concepts is investigated.

For this purpose, the classical greybox approach as presented in Chapter 7.3 is adapted to handle inhomogeneous IBG control scenarios. In addition, the parameter vectors presented in (7.1) through (7.3) are simplified. In order to avoid an additional IBG model with corresponding control in the fitting model, changes are only made to the control of the existing IBG model, see Figure 7.4. Figure 10.6 shows that the two implementations of the FFR are run in parallel and a weighting factor $k_{\mathrm{linFFR}} \in [0,\ 1]$ is used to optimise the proportion of control to be included in each case. The weighting factor as well as the additional active power infeed ΔP_{FFR} of the constant FFR are added to the parameters to be optimised by the greybox aggregation. These two new parameters replace the parameters of the outer control PI controller $k_{\mathrm{P,OC}}$ and $k_{\mathrm{I,OC}}$, which are considered to be less decisive for the optimisation results.

For the direct voltage control, which mainly differs from the grid-supporting control in terms of the current limiting, the current limit I_{max} is added as an additional parameter to the optimisation problem. The current limiter remains set to the limiting without angle change, cf. Chapter 6.2.4 and the control concept of the grid-supporting control is not changed either. Therefore, the IBG parameter vector $\mathbf{x}_{\mathrm{IBG}}$ for the greybox aggregation given in (7.1) changes to the adapted vector $\mathbf{x}^*_{\mathrm{IBG}}$ in (10.1), which adds the three parameters mentioned.

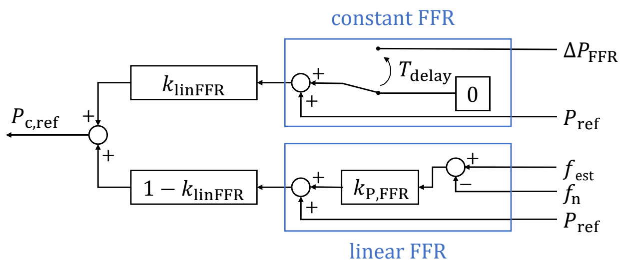

Figure 10.6: Adaptation of the inverter-based generation (IBG) control in order to represent inhomogeneous IBG control scenarios within a single IBG fitting model.

The parameter vector $\mathbf{x}^*_{\mathrm{line}}$ of the two lines connecting the equivalent IBG and load model to the transformer T1 is reduced to only the two line lengths l_{line1} and l_{line2}. The reason behind is the redundancy as the active and reactive power of IBG and load can be adapted individually. For this reason, only the line lengths, which indicate the absolute impedance between aggregation model and the overlying grid remains for optimisation. The length-dependent resistance and inductance are set to the default values of the 20-kV NA2XS2Y cable given in the Appendix A.3, Table A.14. The load parameter vector $\mathbf{x}^*_{\mathrm{L1}}$ remains identical to the one presented in Chapter 7.3 resulting in the adapted parameter vectors (10.1) to (10.3).

$$\mathbf{x}^*_{\mathrm{IBG}} = [S_{\mathrm{IBG}} \;\; cos\varphi_{\mathrm{IBG}} \;\; d_{\mathrm{FFR}} \;\; db_{\mathrm{FFR}} \;\; \Delta P_{\mathrm{FFR}} \;\; k_{\mathrm{linFFR}} \;\; I_{\mathrm{max}}] \tag{10.1}$$

$$\mathbf{x}^*_{\mathrm{line}} = [l_{\mathrm{line1}} \;\; l_{\mathrm{line2}}] \tag{10.2}$$

$$\mathbf{x}^*_{\mathrm{L1}} = \mathbf{x}_{\mathrm{L1}} = [P_{\mathrm{L1}} \;\; Q_{\mathrm{L1}}] \tag{10.3}$$

The results of the aggregation using mixed FFR implementations are shown in Figure 10.7. The plots show the reference curve from the detailed medium-voltage benchmark grid, the aggregation based on the classic greybox approach using a single IBG with only grid-supporting control and linear FFR and the new approach with the adapted control structure and parameter vectors including both FFR implementations as shown in Figure 10.6. Figure 10.7 a) and b) show the results for the mixed FFR 1 variation and Figure 10.7 c) and d) for the mixed FFR 2 variation according to Table 7.3. The results show that the classic greybox approach cannot represent the active power jump of the constant FFR. Neither the steady-state nor the dynamic behaviour are sufficiently met. In contrast, changing the fitting model to allow for a partial constant FFR strongly improves the aggregation result. The differences are less pronounced in the frequency curves, but can be observed especially when the constant FFR sets in.

The aggregation results for the direct voltage control using the adapted new greybox approach as well as the classical one are presented in Figure 10.8 and compared against the reference detailed simulation of the medium-voltage benchmark grid as presented in Chapter 9.1.2. The results show very good result using the adapted greybox approach. Reducing the current limit I_{max} enables the grid-supporting control to mimic the direct voltage control active power adaptation. A drawback of the solution found is the oscillation that occurs due to a relatively large installed IBG capacity $S_{\mathrm{IBG}} = 27$ MVA and the small line impedance with a line length $l_{\mathrm{line2}} \approx 2$ km. This configuration favours interactions between the controls of the SG and the IBG.

Overall, the dynamic behaviour of the inhomogeneous control in the medium-voltage benchmark grid can be replicated effectively with the adaptations in the IBG control and the reduced parameter vectors presented.

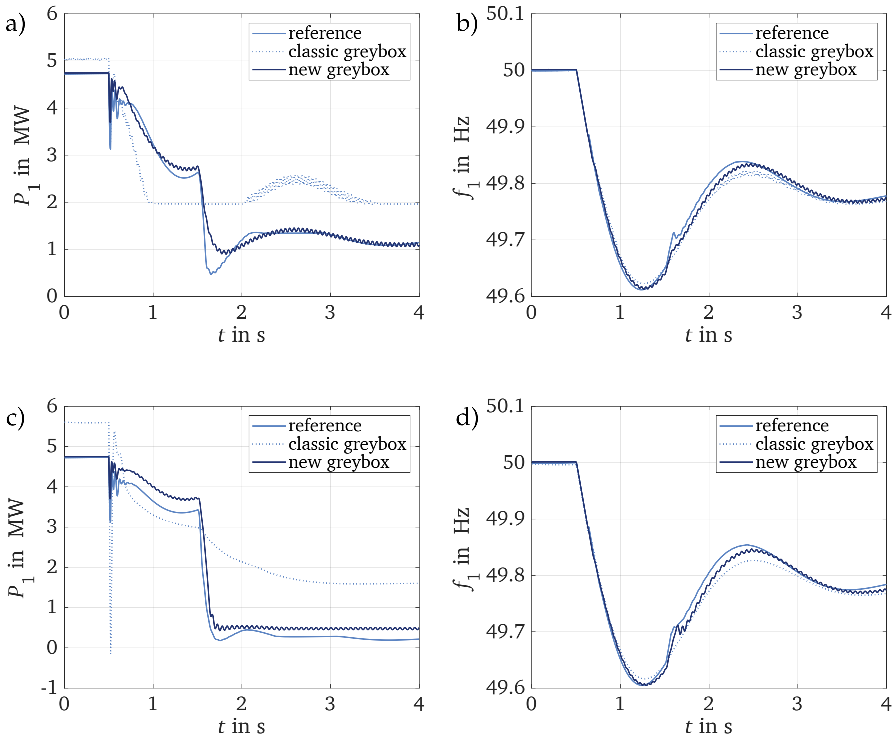

Figure 10.7: Dynamics of the medium-voltage benchmark grid greybox aggregation for the max IBG scenario with mixed fast-frequency response (FFR) implementations according to Table 7.3 for a loadstep $\Delta P_{L0} = 50$ MW using the DE/best/2/bin algorithm.
a) Active power P_1 and b) frequency f_1 for the mixed FFR 1 variation.
c) Active power P_1 and b) frequency f_1 for the mixed FFR 2 variation.

Aggregation of Inhomogeneous Scenarios: A fitting model using only a single inverter-based generator (IBG) and a single control concept does not meet the dynamics of inhomogeneous grids with divers IBG controls. In order to avoid an additional IBG model in the fitting model for each individual control, only the control of the existing IBG is adapted in this work to allow different implementations of the fast-frequency response (FFR) and to be able to include direct voltage control. The reduced parameter vectors are also sufficient to aggregate the dynamic behaviour of the inhomogeneous medium-voltage benchmark grid.

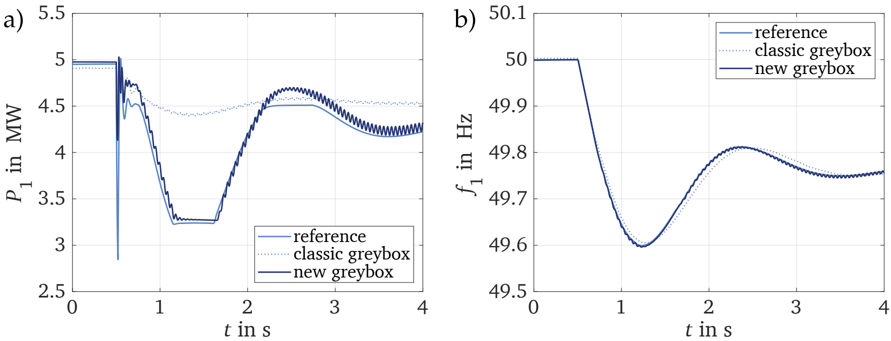

Figure 10.8: Dynamics of the medium-voltage benchmark grid greybox aggregation for the max IBG scenario using the direct voltage control for a loadstep $\Delta P_{L0} = 50$ MW using the DE/best/2/bin algorithm.
a) Active power P_1 and b) frequency f_1.

10.4 EQUIVALENT HIGH-VOLTAGE GRID

The high-voltage grid serves as a detailed overlying grid to test the medium-voltage grid dynamic equivalents. For this reason, Chapter 10.4.1 presents the results of the detailed high-voltage benchmark grid substituting the representation of the connected loads by the medium-voltage grid dynamic equivalent found in Chapter 10.3. For both, the medium-voltage dynamic equivalents as well as the high-voltage benchmark grid, the max IBG scenarios are applied leading to an enormous share of IBG in the active distribution grid. In a last step, the high-voltage benchmark grid is aggregated to serve as a reduced-order model for dynamic frequency studies in the transmission grid. The results of the aggregation are shown in Chapter 10.4.2.

10.4.1 *High-voltage benchmark grid with dynamic equivalent medium-voltage grids*

The influence of the underlying medium-voltage grids on the frequency dynamics is analysed using the dynamic equivalents determined in Chapter 10.3. The dynamic equivalents are inserted into the high-voltage benchmark grid presented in Chapter 7.2 for this purpose. As the loads have no dynamics and load demand may vary strongly, only the IBG dynamic equivalent models are used and the existing static loads are left unchanged. The dynamic equivalent IBG are each inserted in parallel to the existing six loads in the high-voltage benchmark grid, see Figure 7.2. Due to substantial changes in load flow, the load L0 is adjusted to match the new high-voltage grid's load flow conditions. The SG, which represents the external grid, and all components in the high-voltage benchmark grid remain unaltered. The analysis focuses on the max IBG scenario for both the high-voltage benchmark grid and the dynamic equivalent medium-voltage benchmark grid. The dynamic equivalents are based on the DE/best/2/bin algorithm's outcomes, with parameters detailed in Table 10.2. Six IBG, each with a rated power of $S_{\mathrm{r,IBG1,\ldots,6}} = 11$ MVA, are connected at busbars BB1 to BB6, culminating in a total IBG capacity of approximately 250 MVA across the medium-voltage and high-voltage grids.

The effects of employing dynamic equivalents compared to the static load representation of underlying medium-voltage grids are depicted in Figure 10.9. The findings indicate a pronounced shift in both active and reactive power exchanged with the overlying transmission grid. The inclusion of IBG infeeds from the medium-voltage grids leads to a power flow reversal in steady-state conditions, leading the distribution grid to export nearly 40 MW to the transmission grid. The reactive power diminishes owing to the power factor $\cos\varphi = 0.8$ of the dynamic equivalent IBG, which also causes a reduction in voltage at busbar BB1. The frequency curve, as shown in Figure 10.9 a), reveals a significant change when dynamic equivalents are used, as opposed to the scenario with static loads. This positive effect on the frequency dynamics is attributed to the application of the linear FFR. The inclusion of dynamic equivalents results in a delayed active power adjustment, caused by the dynamic equivalent IBG FFR droop $d_{\mathrm{FFR}} = 0.057$, which exceeds the standard FFR droop of windfarms connected to the high-voltage grid.

10.4.2 *Reduced-order active distribution grid*

The high-voltage benchmark grid is aggregated using the greybox approach with the DE/best/2/bin algorithm as it achieves the best results in the previous studies. The adapted greybox approach presented in Chapter 10.3.4 is applied. As for the medium-voltage grid aggregation, measurements are taken at busbar BB1, which is on the low-voltage side of the 380-/110-kV-transformer T1, see Figure 7.2. The aggregation results are compared to the reference curves obtained from the detailed grid and presented in Chapter 9.2.

The comparison of the active and reactive power curves P_1, Q_1 of the detailed high-voltage benchmark grid in its standard parametrisation and the aggregation using the greybox approach is presented in Figure 10.10. For the greybox approach, the fitting model applied for the medium-voltage benchmark grid aggregation, see Figure 7.4, is used here. The analysis reveals that the dynamic adaptation of the active power can be approximated, albeit with an underestimation of 8 MW at $t = 1.3$ s, accompanied by a small time delay of approximately

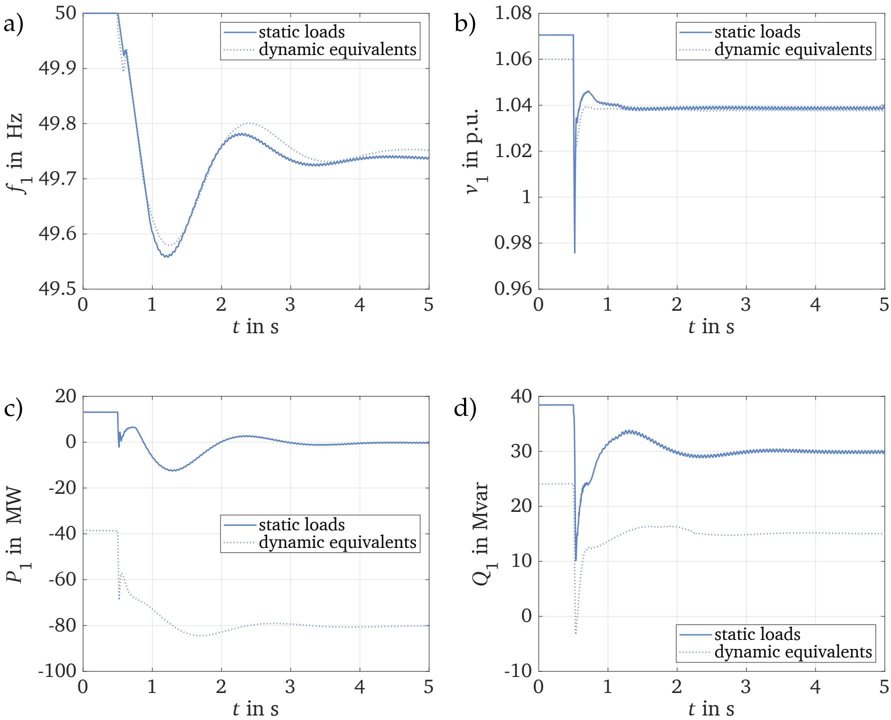

Figure 10.9: Comparison of the dynamics of the detailed high-voltage benchmark grid using static loads and aggregated active medium-voltage grids for a load-step $\Delta P_{L0} = 150$ MW.
a) Frequency f_1,
b) voltage v_1,
c) active power P_1 and
b) reactive power Q_1 at busbar BB1.

200 ms. The dynamic behaviour of the reactive power Q_1 shows an offset of 3.5 Mvar following the loadstep. These aggregated curves align significantly more closely with the reference curves, particularly when compared with the results from the negative load model.

The resulting frequency curves are depicted in Figure 10.11. The missing active power adaptation from the IBG FFR leads to a delay in the frequency curve when simulated with negative load models. The greybox approach reproduces the reference frequency curve more accurately with only small deviations. A small oscillation occurs in both, the reference frequency curve and the one of

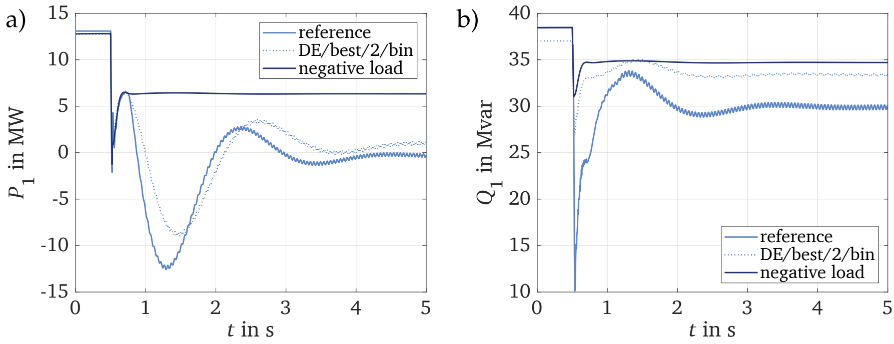

Figure 10.10: Comparison of the dynamics of the detailed high-voltage benchmark grid and the dynamic equivalent based on the greybox approach and the negative load model for a loadstep $\Delta P_{L0} = 150$ MW.
a) Active Power P_1,
b) reactive power Q_1.

the aggregated model. This is due to an interaction of the SG and IBG controls and cannot be observed for the negative load model without IBG.

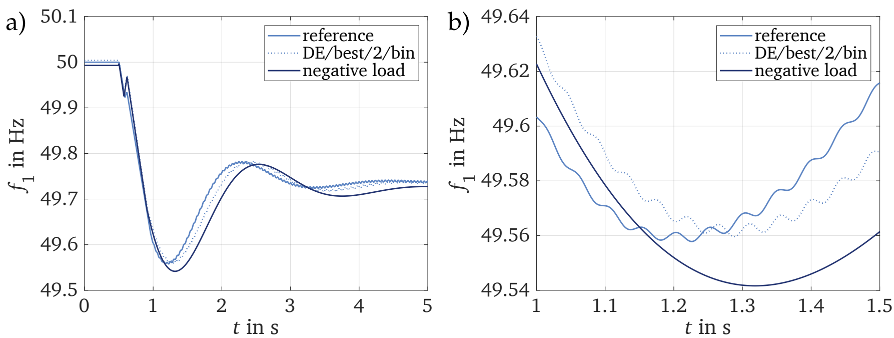

Figure 10.11: Comparison of the frequency dynamics of the detailed high-voltage benchmark grid and the dynamic equivalent based on the greybox approach and the negative load model for a loadstep $\Delta P_{L0} = 150$ MW.
a) Frequency f_1 and
b) zoom into the frequency nadir.

Aggregation of the high-voltage benchmark grid: The results in the high-voltage benchmark grid not only validate the precision of the greybox approach but also emphasise its potential to enhance grid modelling for dynamic stability studies. By offering a more accurate representation of the underlying grid dynamic behaviour, this approach paves the way for more efficient and reliable dynamic power system simulation studies.

10.5 SUMMARY

This chapter presents the results of employing the greybox aggregation to derive dynamic equivalents of active distribution grids. The three algorithms, two based on the differential evolution (DE) and one using the particle swarm optimisation (PSO), reveal varying results.

Differences in the resultant dynamic active and reactive power curves can be observed in the optimised parameters, boxplots of the absolute errors when compared to a reference case. Despite the considerable variance in the active and reactive power exchanged with the overlying grid, the frequency curve remains relatively unaffected. The DE/best/2/bin algorithm is identified as providing the overall best performance within this study. A basic knowledge of the grid and its components slated for aggregation simplifies the selection of parameters and the fitting model.

The fitting model is adapted in order to aggregate IBG with diverse controls within a distribution grid. This adaptation allows for the simultaneous adjustment of active power input by both linear and constant fast-frequency response (FFR), offering the capability to weight the influence of linear versus constant FFR. Moreover, for the simulation of the direct voltage control, the current limit within the control algorithm is optimised as a parameter. This optimisation permits the simulation of the dynamic current limit adjustments, thereby augmenting the model's precision and applicability. The aforementioned enhancements also enable the aggregation of heterogeneous grids, using a single IBG in the fitting model for the greybox approach.

The integration of aggregated medium-voltage grids into the high-voltage grid highlights the considerable impact of underlying grids. Such integration evidences the substantial contributions these grids make, emphasising that their roles should not be ignored in overlying grid studies. Finally, the greybox appraoch can be applied to the high-voltage benchmark grid yielding a dynamic equivalent of the active distribution grid for dynamic frequency studies in the transmission grid.

Part IV

CONCLUSION AND OUTLOOK

11 SUMMARY AND CONCLUSION

The environmental impact of carbon dioxide (CO_2) emissions on global warming and climate change emphasises the transition from fossil fuels to renewable energy sources to mitigate these effects. Challenges arise when integrating a large amount of smaller renewable energy sources, such as wind and solar power plants, into the existing power system. The shift from conventional large-scale power plants to decentralised renewable energy plants leads to a more complex and highly dynamic power system. The introduction of renewable energy sources, mainly based on inverter-based generators (IBG), challenges traditional power system structures. Unlike conventional generators, IBG lack rotating masses and rely on fast-switching power electronic inverters.

The aim of this thesis is to study the impact of transforming passive distribution grids into active ones, incorporating a high share of IBG equipped with an appropriate frequency control. The thesis explores the impact of IBG within the distribution grid on the power system's frequency dynamics and emphasises the need for innovative control strategies to ensure frequency stability. Beyond that, the thesis introduces a nonlinear greybox dynamic equivalencing method as a solution to incorporate reduced yet accurate models of the large number of active distribution grids for accurate frequency stability analysis on the transmission level.

The outcomes of this work are as follows:

1. **For nonlinear dynamic frequency simulations in active distribution grids, a synchronous generator is essential to model the external overlying grid.** Simulation-based dynamic frequency investigations in the distribution grid within the interconnected power system require a SG or another grid-forming unit to reproduce the overlying transmission system inertia and frequency behaviour. The transient frequency measurement using a PLL and its parametrisation must be adapted to the faster frequency dynamics in low-inertia power systems. The IBG can be modelled as state-of-the-art average-value models (AVM).

2. **A high share of IBG with fast-frequency control (FFR) can have a significant impact on the frequency dynamics:** An extensive sensitivity analysis shows the impact of IBG on grid nonlinear dynamic processes in various scenarios and in different distribution grids. IBG with appropriate control in distribution grids can contribute to frequency stability to a non-negligible extent and their inclusion in power system studies becomes more relevant

with increasing share of IBG and decreasing grid strength and inertia. The impact of the connecting point of IBG to the grid is negligble regarding its contribution to the frequency stability. The control concept and installed power have a significant influence on the frequency dynamics.

3. **The increasing share of IBG in distribution grids necessitates the derivation of dynamic equivalents for nonlinear dynamic frequency studies.** The thesis proposes a simulation-based methodology for deriving reduced-order, equivalent models of active distribution grids that can be attached to the transmission system model for dynamic studies by the transmission system operator (TSO). Using a greybox approach, dynamic equivalents are parametrised for various scenarios using three different optimisation techniques with a focus on the impact of the IBG control. The models are benchmarked against detailed distribution grid models and the accuracies are evaluated. The aggregation models can reproduce the frequency-dependent behaviour of active distribution grids using a single load and a single IBG model.

4. **The greybox equivalents can match the dynamic frequency response of detailed distribution grids with homogeneous or inhomogeneous IBG control.** Dissimilar IBG controls - fundamental control concepts as well as variations of the fast-frequency response control - require an adaptation of the reduced-order distribution grid fitting model. This work presents an approach on how to include inhomogeneities to the aggregation model using a single IBG model.

In conclusion, the contribution of distributed IBG plays a significant role when evaluating frequency stability, especially in future low-inertia systems. The IBG contribution to frequency support in distribution grids can be modelled in simulations in the form of generic component models. These models cope with both the confidential data and the many manufacturer details. Due to the large number of IBG, active distribution grids are reduced to aggregated models, which take into account their contribution to transmission system frequency studies.

The following restrictions apply to this study: This thesis investigates only symmetrical faults. All components are modelled in positive sequence assuming balanced three-phase voltages and currents. As a consequence, single-phase inverters, e.g. for photovoltaic rooftop units on the low-voltage level cannot be considered properly. Additionally, only the fundamental frequency is studied. The IBG are modelled as controlled voltage sources or AVM, which do not model the individual power electronic switches. For this reason, harmonics are not included in this work. The investigations focus on short-term dynamics. Long-term frequency stability, e.g. considering poorly tuned controls is not considered.

12 OUTLOOK AND FURTHER RESEARCH

The phases during which the majority of electricity is derived from renewable energy sources are becoming more pronounced worldwide. These changing characteristics of power systems must be represented in simulation models and system stability must be achieved with little to no contribution from conventional power plants. The development towards a more decentralised system must be considered and simplifications should be applied where possible in order to cope with the increasing complexity. In this context, this thesis provides a detailed discussion on the control of inverter-based generation (IBG), e.g. wind and PV power plants. Extensive scenarios are tested using both benchmark active distribution grids and the dynamic equivalents of those grids. Subsequent investigations and research fields can be addressed as follows.

The control of IBG is intensely studied in current research. Some of the proposed control concepts are tested in hardware-in-the-loop simulations. However, only a limited number of these controls are implemented in real power systems. Notably, grid-forming control with virtual inertia holds the potential for positively affecting frequency stability additionally to the fast-frequency response (FFR) control studied in this work. The implementation and study of these control concepts in real interconnected power systems needs to gain momentum. The controller interactions between synchronous generators and IBG in the context of converter-driven stability are to be studied in detail. Additionally, more in-depth load models, e.g. inverter-based loads as electric vehicle chargers or heat pumps, can expand the investigations of this thesis. Demand side management can achieve further contribution to frequency stability. The interplay of multiple components, IBG, synchronous generators, storage systems, loads and their controls needs to be considered when discussing the impact of active distribution grids to the system stability. The reduced-order models should then be connected to detailed transmission system models to study the implications of the increasing dependency of frequency stability on the proliferation of IBG.

In the context of reduced-order modelling, additional control concepts can be integrated into the algorithm, either as additional IBG with grid-forming control or as part of the existing IBG model. The quality of the dynamic equivalent models at various operating points needs thorough investigation. Moreover, in high-voltage grids, it is common to have multiple tie lines or boundaries to the overlying transmission grid. The impact of multiple tie lines on the dynamic equivalent needs to be examined, necessitating a detailed representation of the transmission grid. The results of this thesis are based on three benchmark distribution grid models. The development of well-defined and widely accepted generic dynamic reduced-order distribution grid models is indispensable for future dynamic frequency stability studies of the transmission system and requires the measurement of real distribution grids under various operating conditions.

Part V

APPENDIX

A

APPENDIX

A.1 SYNCHRONOUS GENERATOR MODEL PARAMETERS

The external overlying grid is modelled as a sixth-order synchronous generator (SG). For the medium-voltage testbench described in Chapter 5.1 a medium-voltage SG is modelled with the data given in Chapter A.1.1. The data of the SG, which represents the overlying high-voltage grid in the medium-voltage benchmark grid is given in Chapter A.1.2. For the high-voltage benchmark grid a SG with the data in Chapter A.1.3 is modelled. The parameters of the power system stabiliser as well as the excitation system are identical for all SG models with the data given in Table A.1.

Table A.1: Parameters of the SG power system stabiliser (PSS) and excitation system.

excitation system		
transducer time constant	T_{transd}	20 ms
proportional gain	$k_{\mathrm{P,exc}}$	200
exciter time constant	T_{exc}	1 ms
field voltage limits	$V_{\mathrm{f,max}}$, $V_{\mathrm{f,min}}$	±12.3 p.u.
power system stabiliser		
sensor time constant	$T_{\mathrm{sensor,PSS}}$	30 ms
proportional gain	$k_{\mathrm{P,PSS}}$	20
washout time constant	T_{PSS}	2 s
numerator time constant of 1st lead-lag	$T_{\mathrm{num,1}}$	50 ms
denominator time constant of 1st lead-lag	$T_{\mathrm{den,1}}$	20 ms
numerator time constant of 2nd lead-lag	$T_{\mathrm{num,2}}$	3 s
denominator time constant of 2nd lead-lag	$T_{\mathrm{den,2}}$	5.4 s
lower output voltage limit	$V_{\mathrm{PSS,min}}$	0 p.u.
upper output voltage limit	$V_{\mathrm{PSS,max}}$	4 p.u.

A.1.1 *Medium-Voltage Synchronous Generator Model*

Table A.2: Parameters of the medium-voltage (MV) synchronous generator (SG) model.

synchronous generator electrical model					
S_{r}	V_{n}	f_{n}	H	F	p
24 ... 50 MVA	20 kV	50 Hz	0.2 ... 10 s	0	4
X_{d}	X_{d}'	X_{d}''	X_{q}	X_{q}'	X_{q}''
1.8 p.u.	0.3 p.u.	0.2 p.u.	1.7 p.u.	0.55 p.u.	0.25 p.u.
X_{l}	T_{d}'	T_{d}''	T_{q}'	T_{q}''	R_{s}
0.2 p.u.	8 s	0.03 s	0.4 s	0.05 s	0.0379 p.u.

Table A.3: Parameters of the medium-voltage synchronous generator (SG) governor (Gov) and turbine (Tur) model.

governor droop	d_{Gov}	0.02
turbine time constant	T_{Tur}	0.3 s

A.1.2 *High-Voltage Synchronous Generator Model*

Table A.4: Parameters of the high-voltage (HV) synchronous generator (SG) model.

synchronous generator electrical model					
S_r	V_n	f_n	H	F	p
200 MVA	20 kV	50 Hz	1 ... 10 s	0	4
X_d	$X_d^{'}$	$X_d^{''}$	X_q	$X_q^{'}$	$X_q^{''}$
2.0 p.u.	0.4 p.u.	0.25 p.u.	1.8 p.u.	0.55 p.u.	0.25 p.u.
X_l	$T_d^{'}$	$T_d^{''}$	$T_q^{'}$	$T_q^{''}$	R_s
0.2 p.u.	1.0 s	0.03 s	0.4 s	0.05 s	0.0379 p.u.

Table A.5: Parameters of the high-voltage synchronous generator (SG) governor (Gov) and turbine (Tur) model.

governor droop	d_{Gov}	0.02
turbine time constant	T_{Tur}	0.5 s

Table A.6: Parameters of the high-voltage (HV) synchronous generator (SG) transformer model based on [76].

rated power	$S_{r,T}$	220 MVA
vector group		Dyn1
transformation	V_{HV}/V_{LV}	110 kV / 20 kV
copper losses	P_{cu}	0.3 %
iron losses	P_{Fe}	0.06 %
tap changer		+3 %

A.1.3 *Ultra-High-Voltage Synchronous Generator Model*

Table A.7: Parameters of the ultra-high-voltage (UHV) synchronous generator (SG) model.

synchronous generator electrical model					
S_r	V_n	f_n	H	F	p
500 MVA	20 kV	50 Hz	1 ... 10 s	0	4
X_d	X_d'	X_d''	X_q	X_q'	X_q''
3.0 p.u.	0.35 p.u.	0.22 p.u.	3.0 p.u.	0.55 p.u.	0.22 p.u.
X_l	T_d'	T_d''	T_q'	T_q''	R_s
0.2 p.u.	0.8 s	0.02 s	0.4 s	0.02 s	0.0379 p.u.

Table A.8: Parameters of the ultra-high voltage (UHV) synchronous generator (SG) governor (Gov) and turbine (Tur) model.

governor droop	d_Gov	0.02
turbine time constant	T_Tur	0.5 s

Table A.9: Parameters of the ultra-high-voltage (UHV) synchronous generator (SG) transformer model based on [76].

rated power	$S_\mathrm{r,T}$	300 MVA
vector group		Dyn1
transformation	$V_\mathrm{HV}/V_\mathrm{LV}$	380 kV / 20 kV
copper losses	P_cu	0.3 %
iron losses	P_Fe	0.06 %
tap changer		+5 %

A.2 LOAD MODEL PARAMETERS

The load models are described in Chapter 5.3. The parameters for the static exponential load model are described in Table A.10, for the static ZIP model in Table A.11, for the dynamic exponential model in Table A.12 and for the dynamic induction motor in Table A.13.

Table A.10: Parameters for the static exponential load model.

sector	$\cos\varphi$	k_{pv}	k_{qv}	k_{pf}	k_{qf}	reference
res-s	0.90	1.20	2.9	0.8	−2.2	[168]
res-w	0.99	1.50	3.2	1.0	−1.2	[168]
comm-s	0.85	0.99	3.5	1.2	−1.6	[168]
comm-w	0.90	1.30	3.1	1.5	−1.1	[168]
ind	0.85	0.18	6.0	2.6	1.6	[168]
res-s	-	1.57	4.10	-	-	[202]
res-w	-	1.76	4.66	-	-	[202]

Table A.11: Parameters for the static ZIP load model.

sector	p_1	p_2	p_3	q_1	q_2	q_3	reference
res-s	0.88	−0.21	0.34	14.95	−26.35	12.40	[202]
res-w	1.09	−0.45	0.36	11.10	−18.94	8.85	[202]
comm	0.44	−0.04	0.59	3.76	−5.18	2.42	[203]
comm/ind	0.39	0.12	0.49	3.61	−4.98	2.37	[203]

Table A.12: Parameters for the dynamic exponential (dyn-exp) load model.

sector	α_{Ps}	α_{Pt}	$T_{P,rec}$	α_{Qs}	α_{Qt}	$T_{Q,rec}$	reference
res-s	1.35	1.76	169 s	3.43	3.71	138 s	[204]
res-w	1.19	1.63	142 s	3.93	4.15	127 s	[204]
res-year	1.24	1.67	150 s	3.74	3.98	131 s	[204]

Table A.13: Parameters for the dynamic induction motor (IM) load model.
* Impedances are given in per Unit (p.u.).
type 1: large industrial motor
type 2: small industrial motor
type 3: aggregated residential motors
type 4: aggregated residential and industrial motors
type 5: mixed aggregated - 25 % residential, 45 % commercial, 30 % industrial

type	R_S*	L_S*	L_m*	R_R*	L_R*	H	reference
1	0.013	0.067	3.80	0.009	0.17	1.50 s	[203]
2	0.031	0.100	3.20	0.018	0.180	0.70 s	[203]
3	0.077	0.107	2.22	0.079	0.098	0.74 s	[203]
4	0.035	0.094	2.80	0.048	0.163	0.93 s	[45]
5	0.046	0.097	2.57	0.056	0.115	0.63 s	[45]

A.3 LINE PARAMETERS

Table A.14: Medium-voltage line parameters.

parameter		value
type	3 NA2XS2Y 1x120 mm^2 [194]	
nominal frequency	f_n	50 Hz
resistance	R_1'	0.343 Ω/km
resistance	R_0'	0.817 Ω/km
inductance	L_1'	$\frac{0.275}{2\cdot\pi\cdot f_n}$ H/km
inductance	L_0'	$\frac{1.598}{2\cdot\pi\cdot f_n}$ H/km
capacitance	C_1'	$\frac{47.493}{2\cdot\pi\cdot f_N}$ μF/km
capacitance	C_0'	$\frac{47.492}{2\cdot\pi\cdot f_N}$ μF/km
type	Al/St 240/40 mm^2	
nominal frequency	f_n	50 Hz
resistance	R_1'	0.051 Ω/km
resistance	R_0'	0.192 Ω/km
inductance	L_1'	$\frac{0.395}{2\cdot\pi\cdot f_n}$ H/km
inductance	L_0'	$\frac{1.345}{2\cdot\pi\cdot f_n}$ H/km
capacitance	C_1'	9 nF/km
capacitance	C_0'	8 nF/km

A.4 INVERTER-BASED GENERATION MODEL PARAMETERS

Table A.15: Default parameters of the grid-supporting inverter-based generator (IBG) model.

electrical system		
nominal voltage	V_{n}	400 V
rated power	$S_{\mathrm{r,VSC}}$	3 MVA
arm resistance	R_{arm}	0.03 p.u.
arm reactance	X_{arm}	0.15 p.u.
DC voltage	V_{dc}	360 V
DC capacitor	C_{dc}	1 mF
control system		
outer control proportional gain	$k_{\mathrm{P,OC,d}} = k_{\mathrm{P,OC,q}}$	0.38
outer control integral gain	$k_{\mathrm{I,OC,d}} = k_{\mathrm{I,OC,q}}$	22.05
frequency support deadband	$db_{\mathrm{f,VSC}}$	20 mHz
frequency support droop	d_{FFR}	5 %
current limiter maximum current	I_{max}	1.1 p.u.
inner control proportional gain	$k_{\mathrm{P,IC,d}} = k_{\mathrm{P,IC,q}}$	0.6
inner control integral gain	$k_{\mathrm{I,IC,d}} = k_{\mathrm{I,IC,q}}$	1.6
voltage limiter maximum voltage	V_{max}	1.2 p.u.
transformer		
rated power	$S_{\mathrm{r,T}} = 1.1 \cdot S_{\mathrm{r,VSC}}$	3.3 MVA
high-voltage level	$V_{\mathrm{T,HV}}$	20 kV
low-voltage level	$V_{\mathrm{T,LV}}$	0.4 kV
primary winding resistance	R_1	0.8 Ω
primary winding inductance	L_1	0.04 H
secondary winding resistance	R_2	0.32 mΩ
secondary winding inductance	L_2	15.3 μH
magnitisation reactance	X_{m}	6000 H
core or iron losses	R_{m}	20 kΩ

A.5 BENCHMARK MODEL PARAMETERS

A.5.1 *Medium-Voltage Benchmark Model Parameters*

Table A.16: Default parameters of the medium-voltage testbench.

inverter-based generation	control	grid-supporting
current limiter		no angle change
partial load operation		80 %
rated power	$S_{r,IBG}$	3 MVA
power factor	$\cos\varphi$	1
frequency support, cf. Figure 2.5	FFR	linear
frequency support droop	$d_{f,IBG}$	5 %
frequency support deadband	$db_{f,IBG}$	200 mHz
current limiter maximum current	I_{max}	1.1 p.u.
synchronous generator		
rated power	$S_{r,SG}$	30 MVA
onsite load rated power	$S_{L,onsite}$	8 MVA
nominal voltage	$V_{n,SG}$	20 kV
inertia constant	H_{SG}	6 s
turbine time constant	T_{Tur}	0.3 s
governor droop	d_{Gov}	2 %
dynamic load *f-exp ind*		
rated power	$S_{r,L}$	5 MVA
power factor	$\cos\varphi$	0.85
active power-voltage exponent	k_{pv}	0.18
reactive power-voltage exponent	k_{qv}	6
active power-frequency exponent	k_{pf}	2.6
reactive power-frequency exponent	k_{qf}	1.6
loadstep *constant P*	ΔP_{L0}	5 MW

Table A.17: Load parameters of the medium-voltage benchmark grid.

	S_L in MVA		$\cos\varphi$	
	residual	industrial	residual	industrial
L1	15.3	5.1	0.98	0.95
L2	15.514	5.7	0.98	0.944
L3	0.285	0.265	0.97	0.85
L4	1.76	–	0.97	–
L5	1.435	0.845	0.97	0.85

Table A.18: Parameters of the medium-voltage benchmark model external grid and transformers.

component	parameter	value
ext	S''_{SC}	800 MVA
	X to R ratio	10
T1, T2	$S_{r,T}$	25 MVA
	vector group	Dyn1
	transformation	110 kV / 20 kV
	u_{kr}	12 %
	P_{Fe}	25 kW
T1	tap changer	+6.25 %
T2	tap changer	+3.125 %

Table A.19: Cable parameters of the medium-voltage benchmark grid.

parameter		value
line 1, line2, line3	type	3 NA2XS2Y 1x120 mm^2
length line 1	l_{line1}	7.240 km
length line 2	l_{line2}	0.610 km
length line 3	l_{line3}	1.300 km

A.5.2 *High-Voltage Benchmark Model Parameters*

Table A.20: Parameters of the high-voltage benchmark grid components.

component	parameter	value
ext	S_{SC}	500 MVA
	X to R	10
	V_{ext}	380 kV
T1	$S_{r,T}$	300 MVA
	V_{HV}	380 kV
	V_{LV}	110 kV
	u_{kr}	12 %
	P_{Fe}	180 kW
T2	$S_{r,T}$	25 MVA
	V_{HV}	110 kV
	V_{LV}	20 kV
	u_{kr}	12 %
	P_{Fe}	25 kW
OHL1 - OHL6	type	Al/St 240/40 mm^2
OHL1	length	30 km
OHL2	length	20 km
OHL3	length	20 km
OHL4	length	20 km
OHL5	length	20 km
OHL6	length	204 km
L1, L5, L6	S_L	30 MVA
	$\cos\varphi$	0.95
L2, L3, L4	S_L	20 MVA
	$\cos\varphi$	0.85

A.6 SUPPLEMENTARY RESULTS TO CHAPTER 8

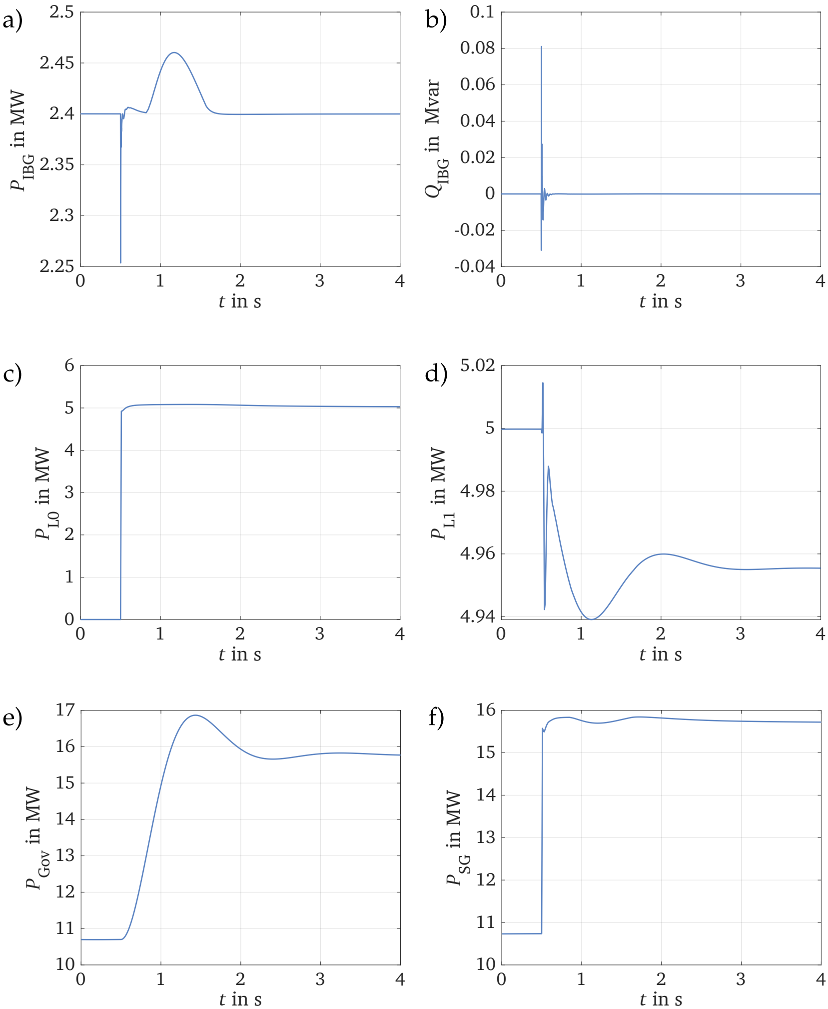

Figure A.1: Dynamic active power sharing in the medium-voltage testbench following a loadstep $\Delta P_L = 5$ MW:
a) Inverter-based generation (IBG) active and b) reactive power output,
c) active power consumption of load L0 and d) of load L1,
e) synchronous generator (SG) governor control and f) SG active power.
Additional results as a supplement to Figure 8.2

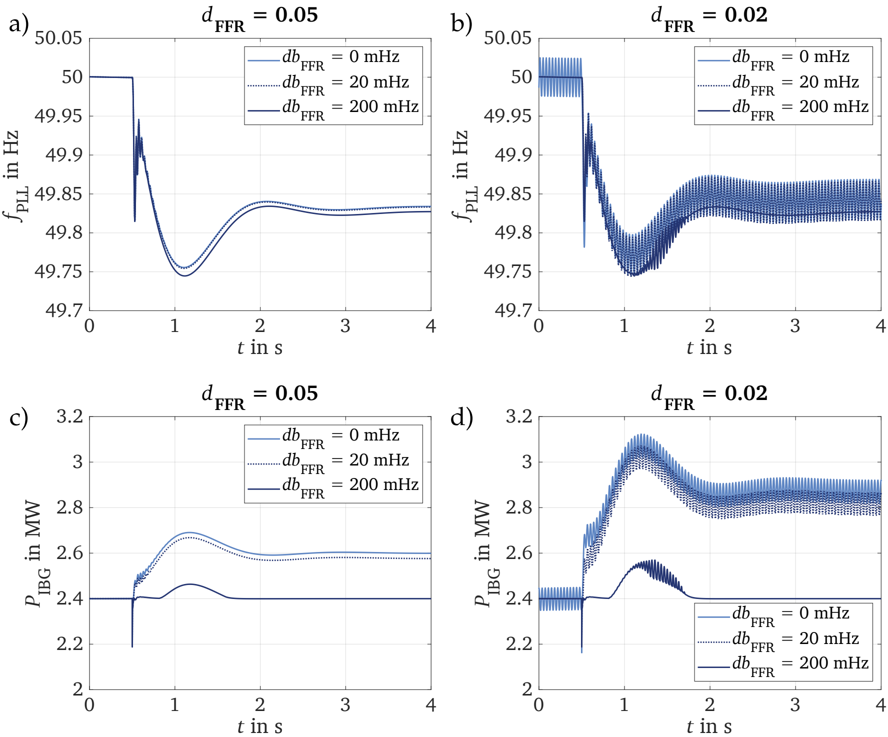

Figure A.2: Impact of the fast frequency response (FFR) droop d_{FFR} and deadband db_{FFR} on the dynamics in the medium-voltage testbench using the standard PLL parametrisation, cf. Table 6.1 following a loadstep $\Delta P_{\text{L0}} = 5$ MW: a), b) inverter-based generation (IBG) active power infeed,
c) and d) phase-locked loop (PLL) frequency measurement at busbar BB1 for different FFR droops.
Additional results as a supplement to Figure 8.9.

A.7 SUPPLEMENTARY RESULTS TO CHAPTER 9

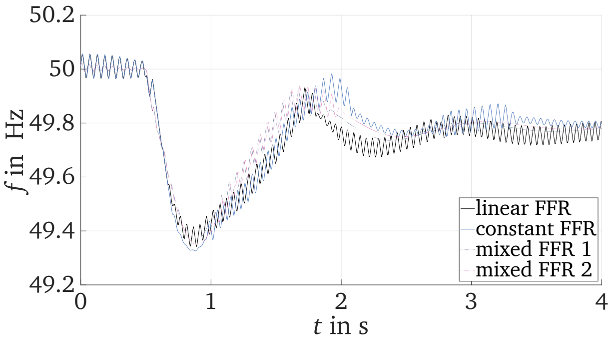

Figure A.3: Frequency curves in a low-inertia system with $H = 2$ s for different FFR implementations. Additional results as a supplement to Figure 9.7.

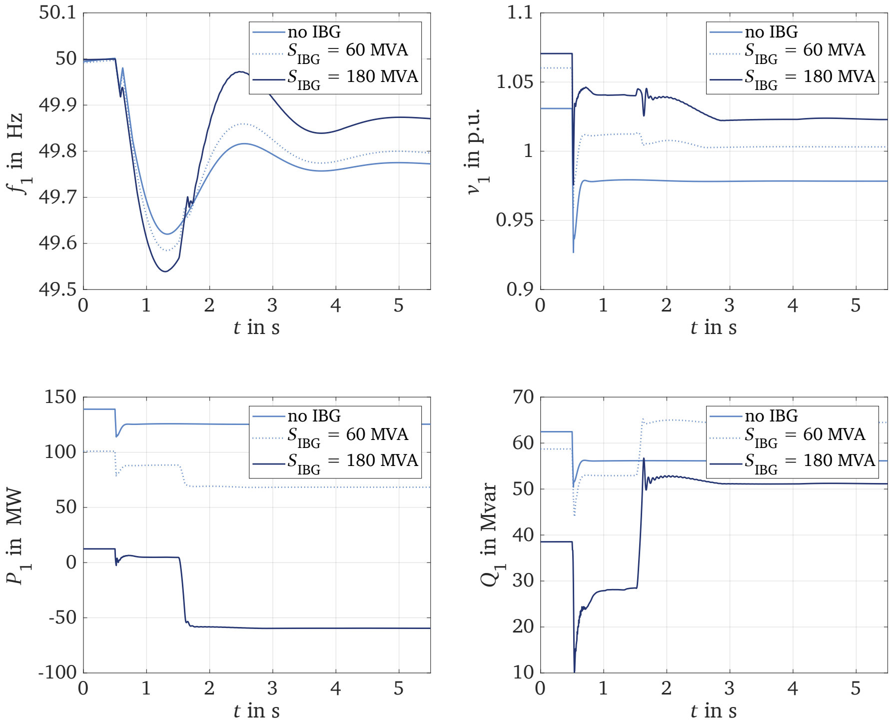

Figure A.4: Supplementary result to Figure 9.12: Dynamics of the high-voltage grid for different shares of inverter-based generation (IBG) for the constant FFR and a loadstep $\Delta P_{L0} = 150$ MW:
a) Frequency, b) voltage, c) active power and d) reactive power at the low-voltage side of the HV/MV-transformer T1 (bus BB1).

A.8 SUPPLEMENTARY RESULTS TO CHAPTER 10

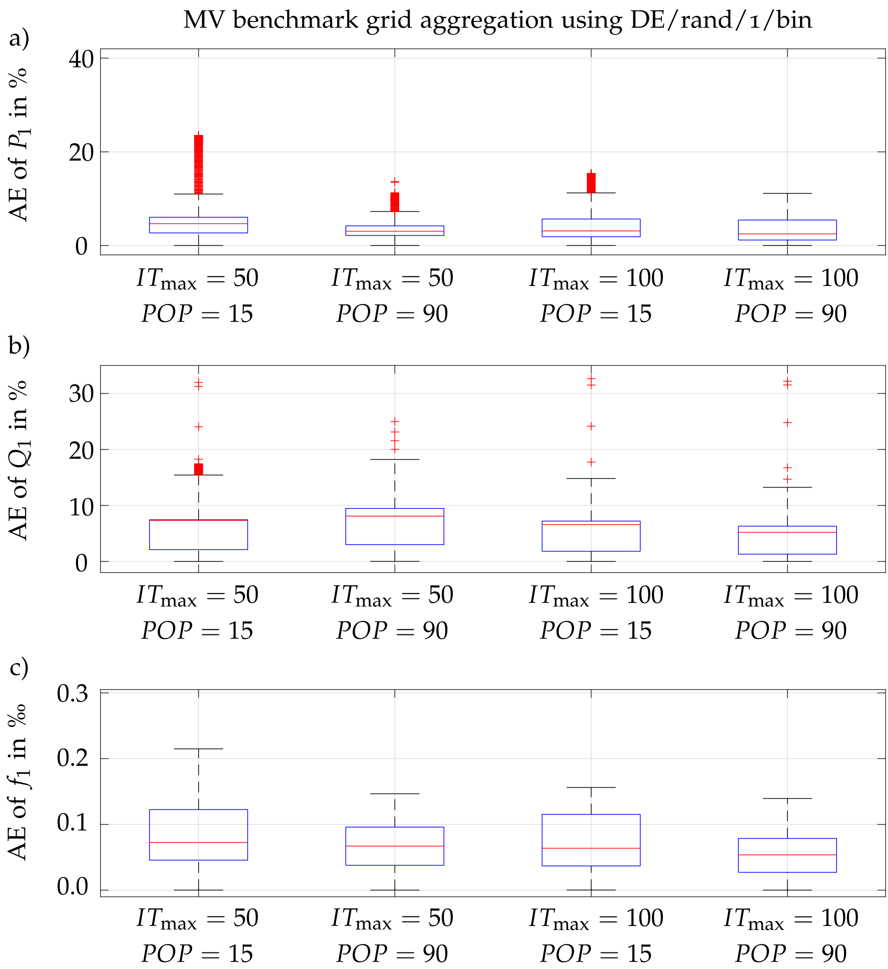

Figure A.5: Distribution of the absolute error (AE) for the aggregation of the medium-voltage benchmark grid using the differential evolution DE/rand/1/bin algorithm for a varying maximum number of iterations IT_{max} and population size POP. The AE is evaluated for
a) the active power P_1,
b) the reactive power Q_1 and
c) the frequency f_1 measured at busbar BB1.

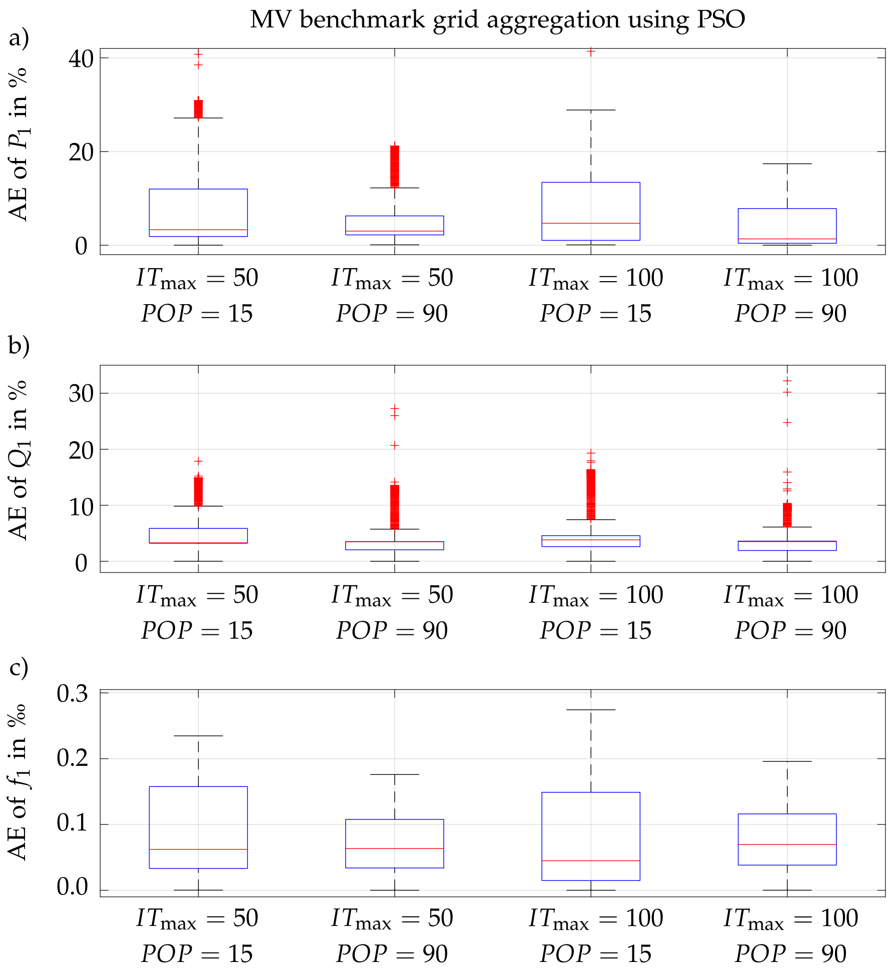

Figure A.6: Distribution of the absolute error (AE) for the aggregation of the medium-voltage benchmark grid using the particle swarm optimisation (PSO) algorithm for a varying maximum number of iterations $IT_{\max}$ and population size POP. The AE is evaluated for
a) the active power P_1,
b) the reactive power Q_1 and
c) the frequency f_1 measured at busbar BB1.

BIBLIOGRAPHY

[1] Arvydas Lebedys et al. *Renewable capacity statistics 2022*. International Renewable Energy Agency (IRENA), 2022. URL: www.irena.org/Publications.

[2] *EEG in numbers 2019*. 2019. URL: www.bundesnetzagentur.de.

[3] German system operators. *System master data under the German Renewable Energy Sources Act (EEG)*. 2022. URL: netztransparenz.de.

[4] Xiaolong Jin et al. "Alleviation of overloads in transmission network: A multi-level framework using the capability from active distribution network." In: *International Journal of Electrical Power and Energy Systems* 112 (2019), pp. 232–251. DOI: https://doi.org/10.1016/j.ijepes.2019.05.007.

[5] Gianluigi Migliavacca. "Introduction." In: *TSO-DSO Interactions and Ancillary Services in Electricity Transmission and Distribution Networks*. Cham: Springer International Publishing, 2020.

[6] Alexander Fuchs, Turhan Demiray, and Mats Larsson. "Aggregated models of active distribution networks for stability studies of large transmission systems." In: *Electric Power Systems Research* 212 (2022), p. 108607. DOI: https://doi.org/10.1016/j.epsr.2022.108607.

[7] Pouyan Pourbeik et al. "Generic Dynamic Models for Modeling Wind Power Plants and Other Renewable Technologies in Large-Scale Power System Studies." In: *IEEE Transactions on Energy Conversion* 32.3 (2017), pp. 1108–1116. DOI: 10.1109/TEC.2016.2639050.

[8] Poul Sorensen et al. "Next Edition of IEC 61400-27: Electrical simulation models for wind power plants." In: *1st International Conference on Large-Scale Grid Integration of Renewable Energy*. Sept. 2017.

[9] International Electrotechnical Commission (IEC). *IEC 61400-27-1:2020 Wind energy generation systems - Part 27-1: Electrical simulation models - Generic models*. 2020.

[10] WECC REMTF. "WECC second generation of wind turbines models guidelines." In: *WECC, USA* (2014).

[11] A. Ellis et al. "Generic models for simulation of wind power plants in bulk system planning studies." In: *2011 IEEE Power and Energy Society General Meeting*. 2011, pp. 1–8. DOI: 10.1109/PES.2011.6039844.

[12] Cigré. *Modeling and Dynamic Behavior of Wind Generation as it relates to Power system Control and Dynamic Performance: Technical Brochure 328*. Paris: CIGRÉ, 2007. ISBN: 978-2-85873-016-2.

[13] A. Honrubia-Escribano et al. "Generic dynamic wind turbine models for power system stability analysis: A comprehensive review." In: *Renewable and Sustainable Energy Reviews* 81 (2018), pp. 1939–1952. DOI: https://doi.org/10.1016/j.rser.2017.06.005.

[14] Martin Albrecht Coumont. "Dynamik und Modellierung aktiver Verteilnetze unter Berücksichtigung netzbildender Regelung." PhD thesis. Darmstadt: Technische Universität Darmstadt, 2022. DOI: https://doi.org/10.26083/tuprints-00022021. URL: http://tuprints.ulb.tu-darmstadt.de/22021/.

[15] Pouyan Pourbeik, Nathan Etzel, and Song Wang. "Model Validation of Large Wind Power Plants Through Field Testing." In: *IEEE Transactions on Sustainable Energy* 9.3 (2018), pp. 1212–1219. DOI: 10.1109/TSTE.2017.2776751.

[16] Electric Power Research Institute (EPRI). *Generic Models and Model Validation for Wind and Solar PV Generation: Technical Update*. 2010.

[17] Aris Gkountaras. "Modeling techniques and control strategies for inverter dominated microgrids." English. PhD thesis. Technische Universität Berlin, 2017.

[18] Peter Unruh et al. "Overview on Grid-Forming Inverter Control Methods." In: *Energies* 13.10 (2020). DOI: 10.3390/en13102589.

[19] Bala Kameshwar Poolla, Dominic Groß, and Florian Dörfler. "Placement and Implementation of Grid-Forming and Grid-Following Virtual Inertia and Fast Frequency Response." In: *IEEE Transactions on Power Systems* 34.4 (2019), pp. 3035–3046. DOI: 10.1109/TPWRS.2019.2892290.

[20] Robert H. Lasseter, Zhe Chen, and Dinesh Pattabiraman. "Grid-Forming Inverters: A Critical Asset for the Power Grid." In: *IEEE Journal of Emerging and Selected Topics in Power Electronics* 8.2 (2020), pp. 925–935. DOI: 10.1109/JESTPE.2019.2959271.

[21] Dinesh Pattabiraman, R. H. Lasseter., and T. M. Jahns. "Comparison of Grid Following and Grid Forming Control for a High Inverter Penetration Power System." In: *2018 IEEE Powerand and Energy Society General Meeting (PESGM)*. 2018. DOI: 10.1109/PESGM.2018.8586162.

[22] Fei Teng and Goran Strbac. "Assessment of the Role and Value of Frequency Response Support From Wind Plants." In: *IEEE Transactions on Sustainable Energy* 7.2 (2016), pp. 586–595. DOI: 10.1109/TSTE.2015.2505085.

[23] Jaber Alipoor, Yushi Miura, and Toshifumi Ise. "Power System Stabilization Using Virtual Synchronous Generator With Alternating Moment of Inertia." In: *IEEE Journal of Emerging and Selected Topics in Power Electronics* 3.2 (2015), pp. 451–458. DOI: 10.1109/JESTPE.2014.2362530.

[24] Johan Driesen and Klaas Visscher. "Virtual synchronous generators." In: *2008 IEEE Power and Energy Society General Meeting - Conversion and Delivery of Electrical Energy in the 21st Century*. 2008. DOI: 10.1109/PES.2008.4596800.

[25] Yamit Lavi and Jay Apt. "Inverter fast frequency response is a low-cost alternative to system inertia." In: *Electric Power Systems Research* 221 (2023). DOI: https://doi.org/10.1016/j.epsr.2023.109422.

[26] NERC Inverter-Based Resource Performance Task Force (IRPTF). *Fast Frequency Response Concepts and Bulk Power System Reliability Needs*. North American Electric Reliability Corp. (NERC), 2020. URL: https://www.nrel.gov/grid/ieee-standard-1547/bulk-power-reliability-needs.html.

[27] Catalin Gavriluta et al. "Storage system requirements for grid supporting PV-power plants." In: *2014 IEEE Energy Conversion Congress and Exposition (ECCE)*. 2014. DOI: 10.1109/ECCE.2014.6954131.

[28] Gauthier Delille, Bruno Francois, and Gilles Malarange. "Dynamic Frequency Control Support by Energy Storage to Reduce the Impact of Wind and Solar Generation on Isolated Power System's Inertia." In: *IEEE Transactions on Sustainable Energy* 3.4 (2012), pp. 931–939. DOI: 10.1109/TSTE.2012.2205025.

[29] Vaclav Knap et al. "Sizing of an Energy Storage System for Grid Inertial Response and Primary Frequency Reserve." In: *IEEE Transactions on Power Systems* 31.5 (2016), pp. 3447–3456. DOI: 10.1109/TPWRS.2015.2503565.

[30] Georgios C. Kryonidis, Charis S. Demoulias, and Grigoris K. Papagiannis. "A Nearly Decentralized Voltage Regulation Algorithm for Loss Minimization in Radial MV Networks With High DG Penetration." In: *IEEE Transactions on Sustainable Energy* 7.4 (2016), pp. 1430–1439. DOI: 10.1109/TSTE.2016.2556009.

[31] Anna Kulmala, Sami Repo, and Pertti Järventausta. "Coordinated Voltage Control in Distribution Networks Including Several Distributed Energy Resources." In: *IEEE Transactions on Smart Grid* 5.4 (2014), pp. 2010–2020. DOI: 10.1109/TSG.2014.2297971.

[32] Yifei Guo et al. "Distributed voltage regulation of smart distribution networks: Consensus-based information synchronization and distributed model predictive control scheme." In: *International Journal of Electrical Power and Energy Systems* 111 (2019), pp. 58–65. DOI: https://doi.org/10.1016/j.ijepes.2019.03.059.

[33] Ye Wang, Vera Silva, and Miguel Lopez-Botet-Zulueta. "Impact of high penetration of variable renewable generation on frequency dynamics in the continental Europe interconnected system." In: *IET Renewable Power Generation* 10 (2016), pp. 10–16. URL: https://api.semanticscholar.org/CorpusID:112103273.

[34] Vahan Gevorgian, Yingchen Zhang, and Erik Ela. "Investigating the Impacts of Wind Generation Participation in Interconnection Frequency Response." In: *IEEE Transactions on Sustainable Energy* 6.3 (2015). DOI: 10.1109/TSTE.2014.2343836.

[35] Mostafa Farrokhabadi et al. "Microgrid Stability Definitions, Analysis, and Examples." In: *IEEE Transactions on Power Systems* 35.1 (2020), pp. 13–29. DOI: 10.1109/TPWRS.2019.2925703.

[36] Joan Rocabert et al. "Control of Power Converters in AC Microgrids." In: *IEEE Transactions on Power Electronics* 27.11 (2012), pp. 4734–4749. DOI: 10.1109/TPEL.2012.2199334.

[37] Zhiyuan Tang et al. "Distributed Control of Active Distribution Networks for Frequency Support." In: *2018 Power Systems Computation Conference (PSCC)*. 2018, pp. 1–7. DOI: 10.23919/PSCC.2018.8442534.

[38] P. Ernst et al. *Verbundnetzstabil - Stabiles Verbundsystemverhalten bei umrichterbasierter Erzeugung: Schlussbericht*. 2022. DOI: 10.2314/KXP:1832906531.

[39] Xiaoya Shang et al. "Equivalent modeling of active distribution network considering the spatial uncertainty of renewable energy resources." In: *International Journal of Electrical Power and Energy Systems* 112 (2019), pp. 83–91. DOI: https://doi.org/10.1016/j.ijepes.2019.04.029.

[40] Georgios C. Kryonidis et al. "Ancillary services in active distribution networks: A review of technological trends from operational and online analysis perspective." In: *Renewable and Sustainable Energy Reviews* 147 (2021), p. 111198. DOI: https://doi.org/10.1016/j.rser.2021.111198.

[41] Daniel Mayorga Gonzalez et al. "Determination of the Time-Dependent Flexibility of Active Distribution Networks to Control Their TSO-DSO Interconnection Power Flow." In: June 2018. DOI: 10.23919/PSCC.2018.8442865.

[42] Florin Capitanescu. "TSO–DSO interaction: Active distribution network power chart for TSO ancillary services provision." In: *Electric Power Systems Research* 163 (2018), pp. 226–230. DOI: https://doi.org/10.1016/j.epsr.2018.06.009.

[43] Paul Cuffe, Paul Smith, and Andrew Keane. "Capability Chart for Distributed Reactive Power Resources." In: *IEEE Transactions on Power Systems* 29.1 (2014), pp. 15–22. DOI: 10.1109/TPWRS.2013.2279478.

[44] João Silva et al. "Estimating the Active and Reactive Power Flexibility Area at the TSO-DSO Interface." In: *IEEE Transactions on Power Systems* 33.5 (2018), pp. 4741–4750. DOI: 10.1109/TPWRS.2018.2805765.

[45] IEEE Taskforce on Load Representation for Dynamic Performance. "Standard load models for power flow and dynamic performance simulation." In: *IEEE Transactions on Power Systems* 10.3 (1995), pp. 1302–1313. DOI: 10.1109/59.466523.

[46] Afshin Samadi et al. "Static Equivalent of Distribution Grids With High Penetration of PV Systems." In: *IEEE Transactions on Smart Grid* 6.4 (2015), pp. 1763–1774. DOI: 10.1109/TSG.2015.2399333.

[47] Wei Dai et al. "Two-tier static equivalent method of active distribution networks considering sensitivity, power loss and static load characteristics." In: *International Journal of Electrical Power and Energy Systems* 100 (2018), pp. 193–200. DOI: https://doi.org/10.1016/j.ijepes.2018.02.032.

[48] Lena Robitzky, Ulf Häger, and Christian Rehtanz. "Modelling of Active Distribution Networks and its Impact on the Performance of Emergency Controls." In: *2018 Power Systems Computation Conference (PSCC)*. 2018, pp. 1–7. DOI: 10.23919/PSCC.2018.8443004.

[49] V. Müller and D. Nelles. "Application of neural networks to static equivalent networks." In: *European Transactions on Electrical Power* 12.3 (2002), pp. 217–223. DOI: https://doi.org/10.1002/etep.4450120308.

[50] Wei Yan et al. "A Black-Box External Equivalent Method Using Tie-Line Power Mutation." In: *IEEE Access* 7 (2019). DOI: 10.1109/ACCESS.2019.2892060.

[51] Wei Yan et al. "A two-port black-box external equivalent method using improved branch outage simulation." In: *International Journal of Electrical Power and Energy Systems* 115 (2020), p. 105437. DOI: https://doi.org/10.1016/j.ijepes.2019.105437.

[52] Eleftherios O. Kontis et al. "Modal analysis of active distribution networks using system identification techniques." In: *International Journal of Electrical Power and Energy Systems* 100 (2018), pp. 365–378. DOI: https://doi.org/10.1016/j.ijepes.2018.02.038.

[53] Feng Ma and Vijay Vittal. “Right-Sized Power System Dynamic Equivalents for Power System Operation.” In: *IEEE Transactions on Power Systems* 26.4 (2011), pp. 1998–2005. DOI: 10.1109/TPWRS.2011.2138725.

[54] F. Conte et al. “Dynamic equivalent modelling of active distribution networks for TSO-DSO interactions.” In: *2017 IEEE PES Innovative Smart Grid Technologies Conference Europe (ISGT-Europe)*. 2017. DOI: 10.1109/ISGTEurope.2017.8260235.

[55] Janek Massmann, Andreas Roehder, and Armin Schnettler. “Modeling approaches for considering active distribution grids in power system stability studies.” In: *Electrical Engineering* 99 (2017). DOI: 10.1007/s00202-016-0398-x.

[56] A. Ishchenko et al. “Dynamic reduction of distribution networks with dispersed generation.” In: *2005 International Conference on Future Power Systems*. 2005. DOI: 10.1109/FPS.2005.204320.

[57] A. Ischchenko, J.M.A. Myrzik, and W.L. Kling. “Dynamic equivalencing of distribution networks with dispersed generation.” In: *2006 IEEE Power Engineering Society General Meeting*. 2006. DOI: 10.1109/PES.2006.1709353.

[58] Eleftherios O. Kontis et al. “Dynamic equivalencing of active distribution grids.” In: *2017 IEEE Manchester PowerTech*. 2017, pp. 1–6. DOI: 10.1109/PTC.2017.7981103.

[59] Panagiotis Papadopoulos et al. “Black-box dynamic equivalent model for microgrids using measurement data.” In: *Generation, Transmission and Distribution, IET* 8 (May 2014), pp. 851–861. DOI: 10.1049/iet-gtd.2013.0524.

[60] X. Feng, Z. Lubosny, and J. W. Bialek. “Identification based Dynamic Equivalencing.” In: *2007 IEEE Lausanne Power Tech*. 2007, pp. 267–272. DOI: 10.1109/PCT.2007.4538328.

[61] Georgios Mitrentsis and Hendrik Lens. “A Dynamic Active Distribution Network Equivalent for Enhancing the Generalization Capability of the Exponential Recovery Model in Stability Studies.” In: *IEEE Transactions on Power Systems* 36.3 (2021), pp. 2709–2712. DOI: 10.1109/TPWRS.2021.3053137.

[62] Luis David Pabón Ospina, Valeria Usuga Salazar, and Daniel Pabón Ospina. “Dynamic Equivalents of Nonlinear Active Distribution Networks Based on Hammerstein-Wiener Models: An Application for Long-Term Power System Phenomena.” In: *IEEE Transactions on Power Systems* 37.6 (2022), pp. 4286–4296. DOI: 10.1109/TPWRS.2022.3153117.

[63] J. V. Milanovic and M. Kayikci. "Transient Responses of Distribution Network Cell with Renewable Generation." In: *2006 IEEE PES Power Systems Conference and Exposition*. 2006, pp. 1919–1925. DOI: 10.1109/PSCE.2006.296207.

[64] Samila Mat Zali and Jovica V. Milanović. "Generic Model of Active Distribution Network for Large Power System Stability Studies." In: *IEEE Transactions on Power Systems* 28.3 (2013), pp. 3126–3133. DOI: 10.1109/TPWRS.2012.2233223.

[65] Jovica V. Milanović and Samila Mat Zali. "Validation of Equivalent Dynamic Model of Active Distribution Network Cell." In: *IEEE Transactions on Power Systems* 28.3 (2013), pp. 2101–2110. DOI: 10.1109/TPWRS.2012.2227844.

[66] F. Conte, F. D'Agostino, and F. Silvestro. "Operational constrained nonlinear modeling and identification of active distribution networks." In: *Electric Power Systems Research* 168 (2019), pp. 92–104. DOI: https://doi.org/10.1016/j.epsr.2018.11.014.

[67] Gilles Chaspierre, Patrick Panciatici, and Thierry Van Cutsem. "Aggregated Dynamic Equivalent of a Distribution System Hosting Inverter-Based Generators." In: *2018 Power Systems Computation Conference (PSCC)* (2018), pp. 1–7. DOI: 10.23919/PSCC.2018.8442968.

[68] Nuno Fulgêncio et al. "Aggregated dynamic model of active distribution networks for large voltage disturbances." In: *Electric Power Systems Research* 178 (2020), p. 106006. DOI: https://doi.org/10.1016/j.epsr.2019.106006.

[69] Hêmin Golpîra, Hossein Seifi, and Mahmoud Reza Haghifam. "Dynamic equivalencing of an active distribution network for large-scale power system frequency stability studies." In: *IET Generation, Transmission and Distribution* 9.15 (2015). DOI: https://doi.org/10.1049/iet-gtd.2015.0484.

[70] Samila Mat Zali and J. V. Milanovic. "Dynamic equivalent model of Distribution Network Cell using Prony analysis and Nonlinear least square optimization." In: *2009 IEEE Bucharest PowerTech*. 2009. DOI: 10.1109/PTC.2009.5282274.

[71] Panagiotis N. Papadopoulos et al. "Measurement-based analysis of the dynamic performance of microgrids using system identification techniques." In: *IET Generation, Transmission and Distribution* 9.1 (2015). DOI: https://doi.org/10.1049/iet-gtd.2014.0555.

[72] Chao Zheng et al. "A Novel Equivalent Model of Active Distribution Networks Based on LSTM." In: *IEEE Transactions on Neural Networks and Learning Systems* 30.9 (2019), pp. 2611–2624. DOI: 10.1109/TNNLS.2018.2885219.

[73] Jens Denecke and István Erlich. "Dynamic equivalents of active distribution networks." In: *2017 IEEE Power and Energy Society General Meeting*. 2017. DOI: 10.1109/PESGM.2017.8274180.

[74] Anna Pfendler, Rafael Steppan, and Jutta Hanson. "Transient Frequency Estimation Methods for the Fast Frequency Response in Converter Control." In: *Electronics* 12.8 (2023). DOI: 10.3390/electronics12081862.

[75] Anna Pfendler, Rafael Steppan, and Jutta Hanson. "Comparison of Transient Frequency Estimation Methods for Evaluating the Frequency Gradient in Active Distribution Grids." In: *2022 57th International Universities Power Engineering Conference (UPEC)*. 2022, pp. 1–6. DOI: 10.1109/UPEC55022.2022.9917822.

[76] Jan Machowski et al. *Power system dynamics: Stability and control*. Third edition. Hoboken, NJ, USA: John Wiley, 2020. ISBN: 978-1-119-52634-6.

[77] Lou van der Sluis. *Transients in Power Systems*. Chichester, UK: John Wiley and Sons, Ltd, 2001. DOI: 10.1002/0470846186.

[78] Liansong Xiong et al. "Modeling and Stability Issues of Voltage-source Converter-dominated Power Systems: A Review." In: *CSEE Journal of Power and Energy Systems* 8.6 (2022), pp. 1530–1549. DOI: 10.17775/CSEEJPES.2020.03590.

[79] *Continental Europe Synchronous Area Separation on 8 January 2021 - Final Report*. 2021. URL: https://www.entsoe.eu/news/2021/07/15/final-report-on-the-separation-of-the-continental-europe-power-system-on-8-january-2021/.

[80] *Continental Europe Synchronous Area Separation on 24 July 2021 - Final Report*. 2021. URL: https://www.entsoe.eu/news/2022/03/28/final-report-on-the-power-system-separation-of-iberia-from-continental-europe-on-24-july-2021/.

[81] Hassan Haes Alhelou et al. "A Survey on Power System Blackout and Cascading Events: Research Motivations and Challenges." In: *Energies* 12.4 (2019). DOI: 10.3390/en12040682.

[82] Nikos Hatziargyriou et al. "Definition and Classification of Power System Stability – Revisited and Extended." In: *IEEE Transactions on Power Systems* 36.4 (2021), pp. 3271–3281. DOI: 10.1109/TPWRS.2020.3041774.

[83] A. Riepnieks et al. "'Frequency' and the PMU standard." In: *To measure is to know*. Piscataway, NJ, USA: IEEE, 2021, pp. 1–6. ISBN: 978-1-7281-9539-1. DOI: 10.1109/I2MTC50364.2021.9459944.

[84] Boualem Boashash. "Estimating and interpreting the instantaneous frequency of a signal. I. Fundamentals." In: *Proceedings of the IEEE* 80.4 (1992), pp. 520–538. DOI: 10.1109/5.135376.

[85] Prabha Kundur et al. "Definition and classification of power system stability IEEE/CIGRE joint task force on stability terms and definitions." In: *IEEE Transactions on Power Systems* 19.3 (2004), pp. 1387–1401. DOI: 10.1109/TPWRS.2004.825981.

[86] DGA Consulting. *International review of frequency control adaptation*. Australian Energy Market Operator, 2016. URL: https://aemo.com.au/-/media/Files/Electricity/NEM/Security_and_Reliability/Reports/2016/FPSS-International-Review-of-Frequency-Control.pdf.

[87] Mariano Ippolito, Rossano Musca, and Gaetano Zizzo. "Analysis and Simulations of the Primary Frequency Control during a System Split in Continental Europe Power System." In: *Energies* 14 (2021). DOI: 10.3390/en14051456.

[88] C.G. Bright. "COROCOF: comparison of rate of change of frequency protection. A solution to the detection of loss of mains." In: *2001 Seventh International Conference on Developments in Power System Protection (IEE)*. 2001, pp. 70–73. DOI: 10.1049/cp:20010102.

[89] Bohan Liu et al. "Advanced ROCOF protection Of synchronous generator." In: *ISGT 2011*. 2011, pp. 1–6. DOI: 10.1109/ISGT.2011.5759125.

[90] Turaj Amraee et al. "Probabilistic Under Frequency Load Shedding Considering RoCoF Relays of Distributed Generators." In: *IEEE Transactions on Power Systems* 33.4 (2018), pp. 3587–3598. DOI: 10.1109/TPWRS.2017.2787861.

[91] John Fradley. "Frequency Containment using Voltage Source Converters in Future Power Systems." English. PhD thesis. The University of Manchester, 2020.

[92] International Electrotechnical Commission (IEC). *IEC Technical Specification 62786-41: 2023 Distributed energy resources connection with the grid - Part 41: Requirements for frequency measurement used to control distributed energy resources (DER) and loads*. 2023.

[93] Federico Milano et al. "Foundations and Challenges of Low-Inertia Systems Invited Paper." In: *2018 Power Systems Computation Conference (PSCC)*. 2018, pp. 1–25. DOI: 10.23919/PSCC.2018.8450880.

[94] Daniel Fernandez-Muñoz et al. "Fast Frequency Control Services in Europe." In: *2018 15th International Conference on the European Energy Market (EEM)*. 2018, pp. 1–5. DOI: 10.1109/EEM.2018.8469973.

[95] Paul Denholm et al. *Inertia and the Power Grid: A Guide Without the Spin*. Golden, 2020. URL: https://www.nrel.gov/docs/fy20osti/73856.pdf..

[96] ENTSO-E. *Technical Requirements for Fast Frequency Reserve Provision in the Nordic Synchronous Area - External document*. 2021.

[97] Lexuan Meng et al. "Fast Frequency Response From Energy Storage Systems—A Review of Grid Standards, Projects and Technical Issues." In: *IEEE Transactions on Smart Grid* 11.2 (2020), pp. 1566–1581. DOI: 10.1109/TSG.2019.2940173.

[98] J. Fang et al. "On the Inertia of Future More-Electronics Power Systems." In: *IEEE Journal of Emerging and Selected Topics in Power Electronics* 7.4 (2019), pp. 2130–2146. DOI: 10.1109/JESTPE.2018.2877766.

[99] Kyoung-Jun Lee et al. "A Novel Grid Synchronization PLL Method Based on Adaptive Low-Pass Notch Filter for Grid-Connected PCS." In: *IEEE Transactions on Industrial Electronics* 61.1 (2014), pp. 292–301. DOI: 10.1109/TIE.2013.2245622.

[100] Chunjiang Zhang et al. "A Grid Synchronization PLL Method Based on Mixed Second- and Third-Order Generalized Integrator for DC Offset Elimination and Frequency Adaptability." In: *IEEE Journal of Emerging and Selected Topics in Power Electronics* 6.3 (2018), pp. 1517–1526. DOI: 10.1109/JESTPE.2018.2810499.

[101] Saeed Golestan, Josep M. Guerrero, and Juan C. Vasquez. "Three-Phase PLLs: A Review of Recent Advances." In: *IEEE Transactions on Power Electronics* 32.3 (2017), pp. 1894–1907. DOI: 10.1109/TPEL.2016.2565642.

[102] Remus Teodorescu, Marco Liserre, and Pedro Rodríguez. *Grid converters for photovoltaic and wind power systems*. Chichester, West Sussex and Piscataway, New Jersey: Wiley and IEEE, 2011. DOI: 10.1002/9780470667057. URL: https://onlinelibrary.wiley.com/doi/book/10.1002/9780470667057.

[103] A. Carcelen-Flores et al. "Comparison of instantaneous frequency estimation algorithms under power system disturbances." In: *2012 IEEE Power and Energy Society General Meeting*. 2012. DOI: 10.1109/PESGM.2012.6345019.

[104] V.V. Terzija. "Improved recursive Newton-type algorithm for frequency and spectra estimation in power systems." In: *IEEE Transactions on Instrumentation and Measurement* 52.5 (2003). DOI: 10.1109/TIM.2003.817152.

[105] Federico Milano. "Rotor Speed-Free Estimation of the Frequency of the Center of Inertia." In: *IEEE Transactions on Power Systems* 33.1 (2018), pp. 1153–1155. DOI: 10.1109/TPWRS.2017.2750423.

[106] Soon-Ryul Nam, Seung-Hwa Kang, and Sang-Hee Kang. "Real-Time Estimation of Power System Frequency Using a Three-Level Discrete Fourier Transform Method." In: *Energies* 8 (Dec. 2014), pp. 79–93. DOI: 10.3390/en8010079.

[107] Frede Blaabjerg et al. "Power Electronics in Renewable Energy Systems." In: *2006 12th International Power Electronics and Motion Control Conference*. 2006, pp. 1–17. DOI: 10.1109/EPEPEMC.2006.4778368.

[108] ENTSO-E. *Need for synthetic inertia (SI) for frequency regulation*. 2018.

[109] Jens Fortmann et al. *Generic simulation model for DFIG and full size converter based wind turbines*. 2010.

[110] Daniel Duckwitz. "Power System Inertia." PhD thesis. Kassel, Universität Kassel, Fachbereich Elektrotechnik/Informatik, 2019. DOI: https:\\doi.org\10.17170/kobra-20190510451.

[111] Cigré. *Modelling of Inverter-Based Generation for Power System Dynamic Studies: Technical Brochure 727*. CIGRÉ, 2018. ISBN: 978-2-85873-429-0.

[112] Giovanni De Carne et al. "Which Deepness Class Is Suited for Modeling Power Electronics?: A Guide for Choosing the Right Model for Grid-Integration Studies." In: *IEEE Industrial Electronics Magazine* 13.2 (2019), pp. 41–55. DOI: 10.1109/MIE.2019.2909799.

[113] Zhongting Tang, Yongheng Yang, and Frede Blaabjerg. "Power electronics: The enabling technology for renewable energy integration." In: *CSEE Journal of Power and Energy Systems* 8.1 (2022), pp. 39–52. DOI: 10.17775/CSEEJPES.2021.02850.

[114] Jose Rodriguez, Jih-Sheng Lai, and Fang Zheng Peng. "Multilevel inverters: a survey of topologies, controls, and applications." In: *IEEE Transactions on Industrial Electronics* 49.4 (2002), pp. 724–738. DOI: 10.1109/TIE.2002.801052.

[115] R. S. Geetha, Ravishankar Deekshit, and G. Lal. "Converter Topologies in VSC-HVDC Systems-an overview." In: *International Journal of Engineering Research and Technology (IJERT* 03 (08 2022). DOI: 10.17577/IJERTV3IS081058.

[116] José Fernando Silva and Sónia F. Pinto. "35 - Linear and Nonlinear Control of Switching Power Converters." In: *Power Electronics Handbook (Fourth Edition)*. Ed. by Muhammad H. Rashid. Fourth Edition. Butterworth-Heinemann, 2018, pp. 1141–1220. DOI: https://doi.org/10.1016/B978-0-12-811407-0.00039-8.

[117] Pradyumn Chaturvedi. "Chapter Three - Conventional Multilevel Inverter: Topologies and Control Strategies." In: *Modeling and Control of Power Electronics Converter System for Power Quality Improvements*. Ed. by Sanjeet Kumar Dwivedi et al. Academic Press, 2018, pp. 85–120. DOI: https://doi.org/10.1016/B978-0-12-814568-5.00003-X.

[118] Sang-Hoon Kim. "Chapter 7 - Pulse width modulation inverters." In: *Electric Motor Control*. Ed. by Sang-Hoon Kim. Elsevier, 2017, pp. 265–340. DOI: https://doi.org/10.1016/B978-0-12-812138-2.00007-6.

[119] Stefanos N. Manias. "Power Electronics Technology." In: *Power Electronics and Motor Drive Systems*. Ed. by Stefanos N. Manias. Academic Press, 2017, pp. 1–22. DOI: https://doi.org/10.1016/B978-0-12-811798-9.00001-9.

[120] Nimrod Vazquez and Joaquin Vaquero Lopez. "11 - Inverters." In: *Power Electronics Handbook (Fourth Edition)*. Ed. by Muhammad H. Rashid. Fourth Edition. Butterworth-Heinemann, 2018, pp. 289–338. DOI: https://doi.org/10.1016/B978-0-12-811407-0.00011-8.

[121] Cigré. *Guide for the development of models for HVDC converters in a HVDC grid: Technical Brochure 604*. Paris: CIGRÉ, 2014. ISBN: 978-2-85873-305-7.

[122] J.G. Slootweg et al. "General model for representing variable speed wind turbines in power system dynamics simulations." In: *IEEE Transactions on Power Systems* 18.1 (2003), pp. 144–151. DOI: 10.1109/TPWRS.2002.807113.

[123] Electric Power Research Institute (EPRI). *Model User Guide for Generic Renewable Energy System Models*. 2010.

[124] Pouyan Pourbeik et al. "Generic stability models for type 3 and 4 wind turbine generators for WECC." In: *2013 IEEE Power and Energy Society General Meeting*. 2013, pp. 1–5. DOI: 10.1109/PESMG.2013.6672398.

[125] R.T. Elliott et al. "Generic photovoltaic system models for WECC - A status report." In: *2015 IEEE Power and Energy Society General Meeting*. 2015, pp. 1–5. DOI: 10.1109/PESGM.2015.7285992.

[126] Juan J. Sanchez-Gasca. "Generic wind turbine generator models for WECC - a second status report." In: *2015 IEEE Power and Energy Society General Meeting*. 2015. DOI: 10.1109/PESGM.2015.7285645.

[127] T. Demiray, G. Andersson, and L. Busarello. "Evaluation study for the simulation of power system transients using dynamic phasor models." In: *2008 IEEE/PES Transmission and Distribution Conference and Exposition: Latin America*. 2008, pp. 1–6. DOI: 10.1109/TDC-LA.2008.4641716.

[128] M. A. Cova Acosta et al. "Wind power plant modelling benchmark of RMS vs EMT simulation models for the electric reliability council of Texas (ERCOT) market." In: *20th International Workshop on Large-Scale Integration of Wind Power into Power Systems as well as on Transmission Networks for Offshore Wind Power Plants (WIW 2021)*. 2021, pp. 503–508. DOI: 10.1049/icp.2021.2653.

[129] Agency for the Cooperation of Energy Regulators (ACER) and ENTSO-E. *Expert group interaction studies and simulation models (EG ISSM) - Final report*. 2021. URL: https://www.entsoe.eu/network_codes/cnc/expert-groups/.

[130] International Renewable Energy Agency (IRENA). *Grid codes for renewable powered systems*. 2022.

[131] VDE Forum Network Technology/Network Operation (FNN). *VDE-AR-N 4105 application rule: 2018-11 Power generation systems connected to the low-voltage distribution network - Technical minimum requirements for the connection to and parallel operation with low-voltage distribution networks*. 2018.

[132] VDE Forum Network Technology/Network Operation (FNN). *VDE-AR-N 4110 application rule: 2018-11 Power generation systems connected to the medium-voltage distribution network - Technical minimum requirements for the connection to and parallel operation with medium-voltage distribution networks*. 2018.

[133] VDE Forum Network Technology/Network Operation (FNN). *VDE-AR-N 4120 application rule: 2018-11 Power generation systems connected to the high-voltage distribution network - Technical minimum requirements for the connection to and parallel operation with high-voltage distribution networks*. 2018.

[134] VDE Forum Network Technology/Network Operation (FNN). *VDE-AR-N 4131 application rule: 2019-03 Technical requirements for grid connection of high voltage direct current systems and direct current-connected power park modules*. 2019.

[135] F. O. Resende, J. Matevosyan, and J. V. Milanovic. "Application of dynamic equivalence techniques to derive aggregated models of active distribution network cells and microgrids." In: *2013 IEEE Grenoble Conference*. 2013, pp. 1–6. DOI: 10.1109/PTC.2013.6652356.

[136] Xin Huang et al. "Decentralized Control of Multi-Parallel Grid-Forming DGs in Islanded Microgrids for Enhanced Transient Performance." In: *IEEE Access* 7 (2019), pp. 17958–17968. DOI: 10.1109/ACCESS.2019.2896594.

[137] Seyed Fariborz Zarei et al. "Reinforcing Fault Ride Through Capability of Grid Forming Voltage Source Converters Using an Enhanced Voltage Control Scheme." In: *IEEE Transactions on Power Delivery* 34.5 (2019), pp. 1827–1842. DOI: 10.1109/TPWRD.2018.2844082.

[138] Martin Coumont, Florian Bennewitz, and Jutta Hanson. "Influence of Different Fault Ride-Through Strategies of Converter-Interfaced Distributed Generation on Short-Term Voltage Stability." In: *2019 IEEE PES Innovative Smart Grid Technologies Europe (ISGT-Europe)*. 2019, pp. 1–5. DOI: 10.1109/ISGTEurope.2019.8905465.

[139] Ali Tayyebi et al. "Grid-Forming Converters – Inevitability, Control Strategies and Challenges in Future Grids Application." In: *CIRED 2018 Ljubljana Workshop*. 2019. DOI: 10.34890/412.

[140] Taoufik Qoria et al. "Critical Clearing Time Determination and Enhancement of Grid-Forming Converters Embedding Virtual Impedance as Current Limitation Algorithm." In: *IEEE Journal of Emerging and Selected Topics in Power Electronics* 8.2 (2020), pp. 1050–1061. DOI: 10.1109/JESTPE.2019.2959085.

[141] Uros Markovic et al. "Understanding Small-Signal Stability of Low-Inertia Systems." In: *IEEE Transactions on Power Systems* 36.5 (2021), pp. 3997–4017. DOI: 10.1109/TPWRS.2021.3061434.

[142] Ali Tayyebi et al. "Frequency Stability of Synchronous Machines and Grid-Forming Power Converters." In: *IEEE Journal of Emerging and Selected Topics in Power Electronics* 8.2 (2020), pp. 1004–1018. DOI: 10.1109/JESTPE.2020.2966524.

[143] J. B. Ward. "Equivalent Circuits for Power-Flow Studies." In: *Transactions of the American Institute of Electrical Engineers* 68.1 (1949), pp. 373–382. DOI: 10.1109/T-AIEE.1949.5059947.

[144] WF Tinney and WL Powell. "The REI approach to power network equivalents." In: *Proc. PICA Conference*. Vol. 314. 1977.

[145] Federico Milano and Kailash Srivastava. "Dynamic REI equivalents for short circuit and transient stability analyses." In: *Electric Power Systems Research* 79.6 (2009), pp. 878–887. DOI: https://doi.org/10.1016/j.epsr.2008.11.007.

[146] S. Deckmann et al. "Studies on Power System Load Flow Equivalencing." In: *IEEE Transactions on Power Apparatus and Systems* PAS-99.6 (1980), pp. 2301–2310. DOI: 10.1109/TPAS.1980.319798.

[147] U. D. Annakkage et al. "Dynamic System Equivalents: A Survey of Available Techniques." In: *IEEE Transactions on Power Delivery* 27.1 (2012), pp. 411–420. DOI: 10.1109/TPWRD.2011.2167351.

[148] Cigré. *Modelling and Aggregation of Loads in Flexible Power Networks: Technical Brochure 566*. Paris: CIGRÉ, 2014.

[149] Octavio Loyola-González. "Black-Box vs. White-Box: Understanding Their Advantages and Weaknesses From a Practical Point of View." In: *IEEE Access* 7 (2019). DOI: 10.1109/ACCESS.2019.2949286.

[150] R. Podmore. "A Comprehensive Program For Computing Coherency-based Dynamic Equivalents." In: *IEEE Conference Proceedings Power Industry Computer Applications Conference, 1979. PICA-79.* 1979, pp. 298–306. DOI: 10.1109/PICA.1979.720081.

[151] Donghua Pan et al. "Transient Stability of Voltage-Source Converters With Grid-Forming Control: A Design-Oriented Study." In: *IEEE Journal of Emerging and Selected Topics in Power Electronics* 8.2 (2020), pp. 1019–1033. DOI: 10.1109/JESTPE.2019.2946310.

[152] Gilles Chaspierre. "Reduced-order modelling of active distribution networks for large-disturbance simulations." English. PhD thesis. ULiège - Université de Liège, 14 December 2020.

[153] F. O. Resende and J. A. Pecas Lopes. "Development of Dynamic Equivalents for MicroGrids using System Identification Theory." In: *2007 IEEE Lausanne Power Tech.* 2007, pp. 1033–1038. DOI: 10.1109/PCT.2007.4538457.

[154] Qi Wang et al. "Synthetic load modelling considering the influence of distributed generation." In: *Energy Reports* 9 (2023). 2022 9th International Conference on Power and Energy Systems Engineering, pp. 662–669. DOI: https://doi.org/10.1016/j.egyr.2022.11.036.

[155] Mohamed Abdel-Basset, Laila Abdel-Fatah, and Arun Kumar Sangaiah. "Chapter 10 - Metaheuristic Algorithms: A Comprehensive Review." In: *Computational Intelligence for Multimedia Big Data on the Cloud with Engineering Applications*. Ed. by Arun Kumar Sangaiah, Michael Sheng, and Zhiyong Zhang. Intelligent Data-Centric Systems. Academic Press, 2018, pp. 185–231. ISBN: 978-0-12-813314-9. DOI: https://doi.org/10.1016/B978-0-12-813314-9.00010-4.

[156] Jakob Vesterstrø m and René Thomsen. "A Comparative Study of Differential Evolution, Particle Swarm Optimization, and Evolutionary Algorithms on Numerical Benchmark Problems." In: *Proceedings of the 2004 Congress on Evolutionary Computation (IEEE Cat. No.04TH8753)* 2 (2004), pp. 1980–1987. DOI: 10.1109/CEC.2004.1331139.

[157] Pakize Erdogmus. "Introductory Chapter: Swarm Intelligence and Particle Swarm Optimization." In: *Particle Swarm Optimization with Applications*. Ed. by Pakize Erdoğmuş. Rijeka: IntechOpen, 2018. Chap. 1. DOI: 10.5772/intechopen.74076. URL: https://doi.org/10.5772/intechopen.74076.

[158] Russel Eberhart and James Kennedy. "A New Optimizer Using Particle Swarm Theory." In: *Sixth International Symposium on Micro Machine and Human Science* (1995), pp. 39–43.

[159] Mostafa Kheshti and Lei Ding. "Particle Swarm Optimization Solution for Power System Operation Problems." In: *Particle Swarm Optimization with Applications*. Ed. by Pakize Erdoğmuş. Rijeka: IntechOpen, 2017. Chap. 3. DOI: 10.5772/intechopen.72409. URL: https://doi.org/10.5772/intechopen.72409.

[160] *Particle Swarm Optimization (PSO) in MATLAB — Video Tutorial*. URL: https://yarpiz.com/440/ytea101-particle-swarm-optimizationpso-in-matlab-video-tutorial.

[161] M. Clerc and J. Kennedy. "The particle swarm - explosion, stability, and convergence in a multidimensional complex space." In: *IEEE Transactions on Evolutionary Computation* 6.1 (2002), pp. 58–73. DOI: 10.1109/4235.985692.

[162] Rainer Storn and Kenneth Price. "Differential Evolution - A Simple and Efficient Heuristic for Global Optimization over Continuous Spaces." In: *Journal of Global Optimization* 11 (1997), pp. 341–359. DOI: https://doi.org/10.1023/A:1008202821328.

[163] Luke Jebaraj. "Applications of Differential Evolution in Electric Power Systems." In: *Differential Evolution: From Theory to Practice* 1009 (Sept. 2021). Ed. by Vinoth Kumar, Diego Oliva, and P.N. Suganthan, pp. 266–296. DOI: https://doi.org/10.1007/978-981-16-8082-3.

[164] James Montgomery and Stephen Chen. "An analysis of the operation of differential evolution at high and low crossover rates." In: July 2010. DOI: 10.1109/CEC.2010.5586128.

[165] S. Sastry and P. Varaiya. "Coherency for interconnected power systems." In: *IEEE Transactions on Automatic Control* 26.1 (1981), pp. 218–226. DOI: 10.1109/TAC.1981.1102569.

[166] Kaveh Malekian et al. “Characteristic Parameters and Reference Networks of German Distribution Grid (LV, MV, and HV) for Power System Studies.” In: *International ETG Congress 2017*. 2017, pp. 1–6.

[167] Saurav Roy Choudhury, Ankul Gupta, and Sandeep Anand. “Simulation of low voltage ride through scheme for inverters connected to distribution system with high R/X ratio.” In: *2016 10th International Conference on Compatibility, Power Electronics and Power Engineering (CPE-POWERENG)*. 2016, pp. 202–207. DOI: 10.1109/CPE.2016.7544185.

[168] Prabha Kundur. *Power System Stability and Control*. 25th reprint. McGraw Hill Education, 1994.

[169] ENTSO-E. *Inertia and Rate of Change of Frequency (RoCoF)*. 2020.

[170] Ana Fernández-Guillamón, Eduard Muljadi, and Ángel Molina-Garcia. “Frequency control studies: A review of power system, conventional and renewable generation unit modeling.” In: *Electric Power Systems Research* 211 (Oct. 2022), p. 108191. DOI: 10.1016/j.epsr.2022.108191.

[171] ENTSO-E. *Rate of Change of Frequency (RoCoF) withstand capability*. 2018.

[172] M. Kurth and E. Welfonder. “Importance of the selfregulating effect within power systems.” In: *IFAC Proceedings Volumes* 39.7 (2006). 5th IFAC Symposium on Power Plants and Power Systems Control, pp. 345–352. DOI: https://doi.org/10.3182/20060625-4-CA-2906.00064.

[173] Berardino Porretta and Steven Porretta. “Self Regulation of Electrical Power Systems.” In: *2019 IEEE Texas Power and Energy Conference (TPEC)* (2019), pp. 1–6.

[174] ENTSO-E. *Load-Frequency Control and Performance*. 2009. URL: https://www.entsoe.eu/publications/system-operations-reports/#continental-europe-operation-handbook.

[175] Hendrik Lens et al. “Measurement data based identification of the contribution of distribution networks to the self-regulating effect.” In: *Power Supply Transformation - Grid Regulation and System Stability; 14. ETG/GMA-Symposium*. 2022.

[176] F. Briz, M.W. Degner, and R.D. Lorenz. “Analysis and design of current regulators using complex vectors.” In: *IEEE Transactions on Industry Applications* 36.3 (2000), pp. 817–825. DOI: 10.1109/28.845057.

[177] Sizhan Zhou et al. “Cross-coupling and decoupling techniques in the current control of grid-connected voltage source converter.” In: *2015 IEEE Applied Power Electronics Conference and Exposition (APEC)*. 2015, pp. 2821–2827. DOI: 10.1109/APEC.2015.7104750.

[178] Matej Krpan et al. “Three-Phase SRF PLL Model for System Frequency Response Studies in Low-Inertia Systems.” In: Nov. 2022, pp. 155–159. DOI: 10.1109/ISGTAsia54193.2022.10003520.

[179] Colm J. O’Rourke et al. “A Geometric Interpretation of Reference Frames and Transformations: dq0, Clarke, and Park.” In: *IEEE Transactions on Energy Conversion* 34.4 (2019), pp. 2070–2083. DOI: 10.1109/TEC.2019.2941175.

[180] Maude Josee Blondin. *Controller Tuning Optimization Methods for Multi-Constraints and Nonlinear Systems - A Metaheuristic Approach*. Switzerland: Springer Nature, 2021. DOI: 10.1007/978-3-030-64541-0.

[181] O. Aydin et al. “Optimum controller design for a multilevel AC-DC converter system.” In: *Twentieth Annual IEEE Applied Power Electronics Conference and Exposition, 2005. APEC 2005.* Vol. 3. 2005. DOI: 10.1109/APEC.2005.1453262.

[182] Chandra Bajracharya et al. “Understanding of Tuning Techniques of Converter Controllers for VSC-HVDC.” In: June 2008.

[183] J.W. Umland and M. Safiuddin. “Magnitude and symmetric optimum criterion for the design of linear control systems: what is it and how does it compare with the others?” In: *IEEE Transactions on Industry Applications* 26.3 (1990), pp. 489–497. DOI: 10.1109/28.55967.

[184] E. Grassi et al. “Integrated system identification and PID controller tuning by frequency loop-shaping.” In: *IEEE Transactions on Control Systems Technology* 9.2 (2001), pp. 285–294. DOI: 10.1109/87.911380.

[185] Martin Pischtschan. *Antriebsregelungstechnik*. 2023. URL: https://bookdown.org/martin_pischtschan/skript_atrt1/.

[186] Damir Vrančić et al. “Improving disturbance rejection of PID controllers by means of the magnitude optimum method.” In: *ISA Transactions* 49.1 (2010), pp. 47–56. DOI: https://doi.org/10.1016/j.isatra.2009.08.002. URL: https://www.sciencedirect.com/science/article/pii/S0019057809000585.

[187] Philippe Feyel. *Loop-shaping robust control*. Automation control and industrial engineering series. Hoboken, NJ and London: Wiley and ISTE, 2013. DOI: 10.1002/9781118575246. URL: https://onlinelibrary.wiley.com/doi/book/10.1002/9781118575246.

[188] Karl J. Aström and Tore Hägglund. *PID Controllers, 2nd Edition*. Instrument Society of America, 1995.

[189] Bo Fan et al. "A Review of Current-Limiting Control of Grid-Forming Inverters Under Symmetrical Disturbances." In: *IEEE Open Journal of Power Electronics* (2022), pp. 955–969. DOI: 10.1109/OJPEL.2022.3227507.

[190] T. Neumann et al. "Novel direct voltage control by wind turbines." In: *2016 IEEE Power and Energy Society General Meeting (PESGM)*. 2016, pp. 1–5. DOI: 10.1109/PESGM.2016.7741744.

[191] Istvan Erlich et al. "New Control of Wind Turbines Ensuring Stable and Secure Operation Following Islanding of Wind Farms." In: *IEEE Transactions on Energy Conversion* 32.3 (2017), pp. 1263–1271. DOI: 10.1109/TEC.2017.2728703.

[192] Anna Pfendler et al. "INFLUENCE OF THE SPATIAL DISTRIBUTION OF GRID-FORMING CONVERTER-BASED GENERATION ON THE FREQUENCY SUPPORT IN A MEDIUM-VOLTAGE BENCHMARK GRID." In: *CIRED 2021 - The 26th International Conference and Exhibition on Electricity Distribution*. Vol. 2021. 2021, pp. 1894–1899. DOI: 10.1049/icp.2021.2042.

[193] Anna Pfendler et al. "Comparison of RMS and EMT Models of an Inverter-Based Generator with Fast-Frequency Response." In: *CIRED 2023 - The 27th International Conference and Exhibition on Electricity Distribution*. 2023.

[194] Cigré. *Benchmark systems for network integration of renewableand distributed energy resources - TB 575*. Paris: CIGRÉ, 2014. ISBN: 9782858732708.

[195] Martin Coumont, Benjamin Braun, and Jutta Hanson. "Influence of Grid-Forming Inverter Control on Short-Term Voltage Stability in Distribution Grids." In: *18th Int'l Wind Integration Workshop*. 2019.

[196] "IEEE Recommended Practice for Excitation System Models for Power System Stability Studies." In: *IEEE Std 421.5-2016 (Revision of IEEE Std 421.5-2005)* (2016), pp. 1–207. DOI: 10.1109/IEEESTD.2016.7553421.

[197] J.G. Slootweg and W.L. Kling. "Aggregated modelling of wind parks in power system dynamics simulations." In: *2003 IEEE Bologna Power Tech Conference Proceedings,* 2003. DOI: 10.1109/PTC.2003.1304458.

[198] Daisuke Iioka et al. "Voltage reduction due to reverse power flow in distribution feeder with photovoltaic system." In: *International Journal of Electrical Power and Energy Systems* 113 (2019), pp. 411–418. DOI: https://doi.org/10.1016/j.ijepes.2019.05.059.

[199] Daisuke Iioka et al. "Voltage Reduction in Medium Voltage Distribution Systems Using Constant Power Factor Control of PV PCS." In: *Energies* 13.20 (2020). DOI: 10.3390/en13205430.

[200] Gustav Lammert et al. "International Industry Practice on Modelling and Dynamic Performance of Inverter Based Generation in Power System Studies." In: *CIGRE Science and Engineering* (June 2017), pp. 25–37.

[201] Ross T. Whitaker, Mahsa Mirzargar, and Robert M. Kirby. "Contour Boxplots: A Method for Characterizing Uncertainty in Feature Sets from Simulation Ensembles." In: *IEEE Transactions on Visualization and Computer Graphics* 19.12 (2013), pp. 2713–2722. DOI: 10.1109/TVCG.2013.143.

[202] Lidija Korunovic, D.P. Stojanovic, and Jovica Milanović. "Identification of static load characteristics based on measurements in medium-voltage distribution network." In: *Generation, Transmission and Distribution, IET* 2 (Apr. 2008), pp. 227 –234. DOI: 10.1049/iet-gtd:20070091.

[203] Electric Power Research Institute (EPRI). *Advanced load modeling*. 2002.

[204] Dobrivoje P. Stojanović, Lidija M. Korunović, and J.V. Milanović. "Dynamic load modelling based on measurements in medium voltage distribution network." In: *Electric Power Systems Research* 78.2 (2008), pp. 228–238. DOI: https://doi.org/10.1016/j.epsr.2007.02.003.

LIST OF PUBLICATIONS

Anna Pfendler, Andreas Saciak, Jutta Hanson and Gerd Balzer, „Fault Location Dependency of Short-Ciruit Currents in MMC based Meshed HVDC Cable Systems," *2019 IEEE Milan PowerTech*, Milan, Italy, 2019, pp. 1-6, doi: 10.1109/PTC.2019.8810935.

acatech/Leopoldina/Akademieunion (Hrsg.) „Zentrale und dezentrale Elemente im Energiesystem: Der richtige Mix für eine stabile und nachhltige Versorgung," *Schriftenreihe zur wissenschaftsbasierten Politikberatung*, 2020.

Anna Pfendler, Martin Coumont, Soham Choudhury and Jutta Hanson, „Influence of the spatial distribution of grid-forming converter-based generation on the frequency support on a medium-voltage benchmark grid," *CIRED 2021 - The 26th International Conference and Exhibition on Electricity Distribution*, 2021, pp. 1894-1899, doi: 10.1049/icp.2021.2042.

Anna Pfendler, Rafael Steppan and Jutta Hanson, „Vergleich transienter Frequenzschätzverfahren zur Auswertung des Frequenzgradienten in aktiven Verteilnetzen," *17. Symposium Energieinnovation: Future of Energy*, 2022.

Anna Pfendler, Christian Bott, Christian Lakenbrink, Thomas Hunger and Jutta Hanson, „Eignung und Auswirkung verschiedener Blindleistungsregelverfahren für Erzeugungsanlagen in generischen Mittelspannungsnetzen," *17. Symposium Energieinnovation: Future of Energy*, 2022.

Anna Pfendler, Rafael Steppan and Jutta Hanson, „Comparison of transient frequency estimation methods for evaluating the frequency gradient in active distribution networks," *UPEC 2022 - 57th International Universities Power Engineering Conference*, Istanbul, Turkey, 2022.

Anna Pfendler, Martin Coumont and Jutta Hanson, „Impact of the PLL Time Constant in Converter Control on the Dynamic Frequency Support," *UPEC 2022 - 57th International Universities Power Engineering Conference*, Istanbul, Turkey, 2022.

Anna Pfendler, Berit Erlach and Jutta Hanson, „Allgemeine technische Aspekte der elektrischen Energieversorgung - ein System im Wandel," *Handbuch Elektrische Energieversorgung. Energietechnik und Wirtschaft im Dialog*, 2022.

Anna Pfendler, Anne Freiberger, Ben Gemsjäger, Charlotte Biele, Christof M. Schneider, Erik Zipperling, Felix Nowak, Frederike Pfeifer, Johannes Legner, Martin Kleimaier, Rainer Speh, Sasan J. Rasti, Sebastian Wingender, Thomas Benz and Wiebke Beerens „Zukunftsbild Energie," VDE Studie, Offenbach am Main, Germany, 2022.

Manuel Schwenke, Rafael Steppan, **Anna Pfendler** and Jutta Hanson, „Parametrierung von Q(P)-und Q(U)-Kennlinien mittels zeitreihenbasierter optimaler Leistungsflussberechnungen," *13. Internationale Energiewirtschaftstagung an der TU Wien*, Vienna, Austria, 2023.

Anna Pfendler, Rafael Steppan and Jutta Hanson, „Transient Frequency Estimation Methods for the Fast Frequency Response in Converter Control," *Electronics* 12, no. 8, 2023, p. 1862, doi:10.3390/electronics12081862.

Anna Pfendler, Lukas Jung, David Nickel and Jutta Hanson, „Aggregation of a generic high-voltage network using the grey-box approach for dynamic frequency investigations," *ETG-Kongress*, Kassel, Germany, 2023.

Anna Pfendler, Ferdinand Keil, Klaus Hofmann and Jutta Hanson, „How to inspire girls for STEM studies through a series of consecutive multi-day hands-on labs," *IEEE German Education Conference (GeCon)*, Berlin, Germany, 2023.

Rafael Steppan, **Anna Pfendler** and Jutta Hanson, „Meter Placement Algorithm for Reliable Distribution System State Estimation," *27th International Conference on Electricity Distribution (CIRED)*, Rome, Italy, 2023.

Anna Pfendler, Patrick Riess, Soham Choudhury, Rafael Steppan, Aaron Hebing and Jutta Hanson, „Comparison of RMS and EMT Models of an Inverter-Based Generator with Fast-Frequency Response," *27th International Conference on Electricity Distribution (CIRED)*, Rome, Italy, 2023.

Manuel Schwenke, Rafael Steppan, **Anna Pfendler** and Jutta Hanson, „Determination of $Q(P)$ and $Q(V)$ Characteristics by means of Time-Series Based Optimal Power Flow Calculation to Optimize Distribution Grid Operation," *27th International Conference on Electricity Distribution (CIRED)*, Rome, Italy, 2023.

Aaron Hebing, Xiong Xiao, **Anna Pfendler** and Jutta Hanson, „Tuning of Cascaded Droop Control Systems for Power Converters Based on the Eigenvalue Analysis," *2023 IEEE Belgrade PowerTech*, Belgrade, Serbia, 2023.

Anna Pfendler, Lukas Jung and Jutta Hanson, „Randnetzmodellierung für dynamische Frequenzuntersuchungen im Verteilnetz," *18. Symposium Energieinnovation 2024 (EnInnov 2024)*, Graz, Austria, 2024.

Lukas Jung, **Anna Pfendler**, Aaron Hebing and Jutta Hanson, „Einflussgrößen auf die Dynamik der netzbildenen Droop-Regelung," *18. Symposium Energieinnovation 2024 (EnInnov 2024)*, Graz, Austria, 2024.

Anna Pfendler, Berit Erlach and Jutta Hanson, „General technical aspects of the electrical power system - a system in transition," *Handbook of Electrical Power Systems: Energy Technology and Management in Dialogue*, 2024.

SUPERVISED STUDENT WORKS

Jael Rebeca Sepúlveda Schweiger, „Aggregation generischer Windkraftanlagenmodelle mit Vollumrichter für dynamische Netzuntersuchungen,“ Bachelor's Thesis, 2019.

Lukas Jung, „Regelstrategien zur Synchronisation von leistungselektronisch angeschlossenen Erzeugungsanlagen ohne PLL,“ Proseminar, 2020.

Aschkan Davoodi Memar, „Energiesystemanalyse und optimierte Integration von solarthermischen Kraftwerken (CSP) in China,“ external Master's Thesis in cooperation with Fraunhofer ISE, 2021.

Agnes Engelter, „Neue Stabilitätsdefinitionen in elektrischen Energiesystemen mit großem Anteil umrichterbasierter Anlagen,“ Proseminar, 2021.

Duc Toan Le, „Dynamisches Verhalten von über VSC-HGÜ angebundenen Offshore-Windparks,“ Master's Thesis, 2021.

Melina Gabriella Vruna, „Umsetzung einer vorausschauenden Netzengpasserkennung für das Hochspannungsnetz der Netze BW mittels Leistungsflussrechnungen,“ external Master's Thesis in cooperation with Netze BW, 2021.

Lukas Jung, „Ersatznetznachbildung für dynamische Untersuchungen zur Frequenzstabilität,“ Bachelor's Thesis, 2021.

Rafael Steppan, „Transiente Frequenzschätzverfahren für dynamische Netzuntersuchungen,“ Master's Thesis, 2021.

Adrian Ripoll Moncho, „Impact of the PLL Time Constant in Converter Control on the Dynamic Frequency Support of Renewable Energy Plants,“ Master's Thesis Erasmus+, 2022.

Patrick Marc Rieß, „Vergleich von RMS und EMT Modellen für umrichterbasierte Erzeugungsanlagen,“ Master's Thesis, 2022.

Bani Pamungkas, **Ekram Amirzad** and **Daniel David Vega Florez**, „Analyse der hohen Grundlast am Campus Lichtwiese," Project Seminar, 2022.

Aaron Hebing, „Tuning der kaskadierten Droop-Regelung von Umrichtern basierend auf der Eigenwertanalyse," Master's Thesis, 2022.

Agnes Engelter, „Aggregation eines generischen Mittelspannungsnetzes für dynamische Untersuchungen zur Frequenzstabilität," Bachelor's Thesis, 2022.

Hendrik Schröder, „Modellierung frequenzabhängiger Lasten für dynamische Netzuntersuchungen," Bachelor's Thesis, 2022.

Julius Stephani, „Anforderungen für den Anschluss von Erneuerbare-Energie-Anlagen im Hochspannungsnetz," Proseminar, 2022.

Dominik Zacharias, „Vergleich von Regelstrategien für VSC-basierte Erzeugungsanlagen hinsichtlich der Auswirkungen auf die dynamische Frequenzstützung," Bachelor's Thesis, 2022.

Mustafa Inkaya, „Die Rolle von großen Batterien in Hochfahrnetzen des Netzwiederaufbaus," external Master's Thesis in cooperation with 50Hertz, 2022.

Jan Deranek, „Anschlussbedingungen für Erzeugungsanlagen an das deutsche Mittelspannungsnetz," Proseminar, 2022.

Julius Stephani, „Dynamische Randnetznachbildung des Übertragungsnetzes für Frequenzuntersuchungen im Hochspannungsnetz," Bachelor's Thesis, 2022.

David Nickel and **Lukas Jung**, „Vergleich von Whitebox- und Greybox-Verfahren zur Aggregation eines generischen Hochspannungsnetzes," Project Seminar, 2022.

Bani Pamungkas, „Dynamische Aggregation eines aktiven Verteilnetzes für Frequenzuntersuchungen im Zeitbereich mithilfe des Greybox-Ansatzes," Master's Thesis, 2022.

Christian Mayer, „Analyse der Stabilitätsgrenzen bei dem Parallelbetrieb von Synchrongeneratoren und Umrichteranlagen," Bachelor's Thesis, 2023.

Tobias Jentsch, „Optimierung und Weiterentwicklung einer netzbildenden Regelung," external Master's Thesis in cooperation with Fraunhofer ISE, 2023.

Lukas Jung, „Einfluss einer virtuellen Impedanz auf das dynamische Verhalten der netzbildenden Regelung von umrichterbasierten Erzeugungsanlagen," Master's Thesis, 2024.

COLOPHON

This document was typeset using the typographical look-and-feel `classicthesis` developed by André Miede and Ivo Pletikosić. The style was inspired by Robert Bringhurst's seminal book on typography *"The Elements of Typographic Style"*. `classicthesis` is available for both LaTeX and LyX:

https://bitbucket.org/amiede/classicthesis/

Happy users of `classicthesis` usually send a real postcard to the author, a collection of postcards received so far is featured here:

http://postcards.miede.de/

Thank you very much for your feedback and contribution.

Final Version as of August 30, 2024.